UNIVERSITY OF LONDON THESIS

Degree PhD Year 2007 Name of Author MATTHEW GRAHAM O'BRIEN

Davy-Faraday Research Laboratory
The Royal Institution of Great Britain

Department of Chemistry
University College London
University of London

Investigations into the Formation of Nanoporous Materials

A thesis submitted in partial fulfilment for the requirements for a degree of Doctor of Philosophy

By

Matthew Graham O'Brien

2007

ProQuest LLC
789 East Eisenhower Parkway
P.O. Box 1346
Ann Arbor, MI 48106-1346

Declaration

I, Matthew Graham O'Brien confirm that the work presented in this thesis is my own.

Where information has been derived from other sources, I confirm that this has been indicated in the thesis.

(Signed Matthew Graham O'Brien, 2007)

Abstract

The formation processes of a number of microporous materials have been investigated using a powerful combination of *ex situ* and *in situ* experimental techniques together with computational modelling. The materials investigated include both zeolites and their aluminophosphate counterparts, which have been previously synthesised and have shown some potential as industrial catalysts. Using an array of techniques has allowed different stages (such as nucleation or crystal growth) to be monitored as well as different aspects of the gel chemistry, such as the geometry of substituted metal ions and the location and conformation of organics within the framework. For MeAPO-34 and AlPO-5, quantum mechanical calculations have examined the early stages of AlPO formation and shown that, unlike silicates, chain growth seems to be preferred. Raman techniques have then identified metal-organic interactions and changes in organic conformation, key to the formation of a particular AlPO over another. For CoAPO-36, energy dispersive X-ray diffraction has been used to monitor crystal growth using three different organic species, and significant differences in the rate of formation have been identified. By combining these observations with crystallographic measurements and molecular mechanical modelling, it has shown that the rate of formation can be affected by both the size and shape of the organic used to form the crystal structure. Combined small angle/wide angle X-ray diffraction has also been used to follow the formation of zeolite-A throughout the nucleation and growth process and, it has been shown, that the insertion of the substituted metal germanium can alter the precise nature of the aggregation and dissolution processes occurring within this system.

Finally, a synthesis project has been initiated to attempt to introduce mesopores into microporous AlPO materials. The synthesis of hierarchical microporous-mesoporous materials is of great interest as they offer advantages over both microporous and mesoporous materials for use in catalytic and other applications. The results from this work are very promising, and both AlPO-5 and MeAlPO-34 have been synthesised with some apparent mesoporosity, using non-ionic surfactants. A mechanistic process for the formation of these materials based on micelle and mesophase formation has also been proposed.

Table of Contents

List of Figures

List of Tables

Acknowledgments

The completion of this thesis and the work within it would not have been possible without the help and assistance of a large number of people, who have supported me in both my work and my life during the course of the past three years.

To this end, I would like to thank my supervisors Prof. Richard Catlow and Dr. Dewi Lewis for their continued support, enthusiasm and ideas throughout this work. I would also like thank Prof. G Sankar whose ideas formed the initial basis of my work and for the use of beam time, equipment and chemicals without which this project would not have been possible. Particular thanks must also go the Dr. Andrew Beale, Dr. Ian Watts and Dr. Simon Jacques for their faith and support in my abilities during difficult times and without whom I would not have got this far.

I am also grateful to many other people at the Davy Faraday Research laboratory who have help and assisted me, and made the laboratory such a great place to work. These include (but are not restricted to!), Simon Carling and Said Gomez for help with many scripts and conversion programs, Mike Sheehee for his technical support and Manuel Sanchez-sanchez for his wealth of knowledge on all things AlPO, as well as Dee, Will, Rob, Amber, Wing, Gareth, Furio, Dave, Martyne and others, for their useful discussions and the odd pint (or two!) at the Goat.

Besides the people from the Royal Institution I would like to thank both Andy (again) and Prof. Bert Weckhuysen for the unique opportunity to work in a foreign country for three months at the university of Utrecht (The Netherlands) and Miguel Mora-Fonz from UCL for the structures and methods, which have made the computational parts of this work possible. I would also like to thank all those at the SRS, Daresbury who have helped me over the years.

Last, but not least, I would like to thank all my family and friends, especially Mum and Dad (for both emotional and financial support) and Vicki, Martin, Phil, Wayne, Adam, Kally, Cheryl, Erica, Colin, Helena, Pete, Rob and Avis for their ability to listen (without appearing too bored) to my explanations of all things chemical after a few pints of beer!

Chapter 1
Introduction

1.1 : Chapter overview

The work in this thesis concerns the mechanisms of formation by which a series of microporous and hierarchical microporous-mesoporous materials are formed. The materials studied include those based on oxygen-bridged silicon and aluminium systems and on oxygen-bridged phosphorus and aluminium systems.

This chapter initially highlights some of the general features of porous materials. It then details the history, classification and experimental conditions of microporous materials and then examines some of the previously presented formation mechanisms.

The discussions in this chapter concentrate generally on microporous materials as these are used in all of the experimental chapters. For mesoporous and hierarchical phases, much of this information (such as the hydrothermal synthesis method and the effect of gel components) is also relevant, but the specific details on these phases are confined to chapter 6, where they are used specifically.

1.2 : Porous materials

Porosity is of immense importance. Indeed, it is very difficult to find or prepare a truly non-porous solid[1]. Pore sizes can range from centimetres to nanometres and they control many important physical properties of materials such as density, strength and thermal conductivity. They are also important factors in the chemical reactivity of solids and the interaction of solids with liquids and gases.

Porous materials are commonly found in nature (e.g. wood and carbon), as part of industrial materials (e.g. foams, ceramics and bricks) and as part of chemical processes (e.g. silicates and alumina supports). They are used in a wide range of applications[2]. For example, electrodes in fuel cells must have large surface areas and interconnected pores of between 1 and 10 μm[3], whilst polypropylene containing 20% calcium phosphate can be used as an orthopaedic bone replacement[4]. Here the pores (100 and 400 μm) allow good bone intergrowth and a rich blood supply and nutrient delivery. Additional examples are given in figure 1.1, and further potential uses include hydrogen storage[5], electroluminescent semi-conduction[6] and photonics[7].

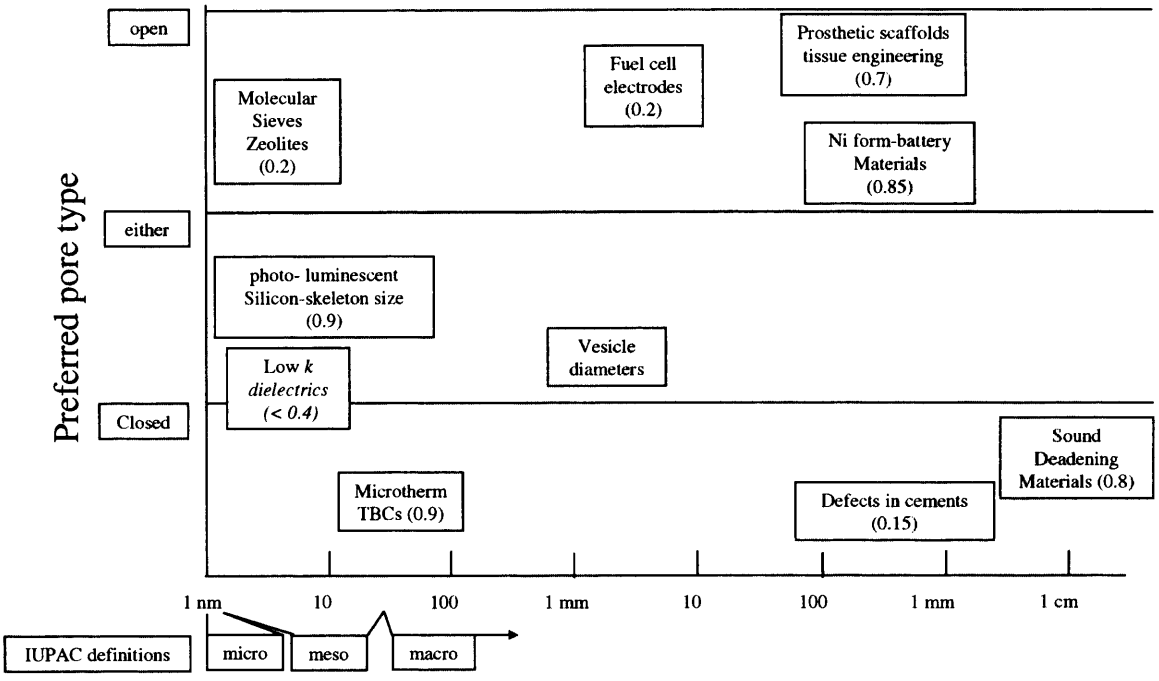

Figure 1.1: Various uses of porous materials with the volume fraction of pores given in brackets and IUPAC definition of pore sizes. Modified from ref. 2.

From figure 1.1 it can be seen that there is one particular class of porous material with very small open pores. These are described as molecular sieve zeolites and can contain pores down to molecular sizes. As such, these materials are particularly good for applications in the chemical industry such as catalysts and molecular sieving (see below).

1.2.1 : Classification

1.2.1.1 : Pore size

When describing any porous material, it is important to have a standardised system of measurement for the size, shape and connectivity of the pores. Currently IUPAC (the International Union of Pure and Applied Chemistry) defines pores sizes as follows[1,8,9]:

- Micropores < 2nm
- Mesopores 2 – 50 nm
- Macropores > 50 nm

1.2.1.2 : Pore type

As the actual shape and connectivity of pores is also important to the applications of the porous material IUPAC have also classified pores according to their availability to interact with an external fluid[1]. The pore types include:

1. Isolated closed pores, which can influence properties such as bulk density and mechanical strength but cannot interact with gases or liquids (figure 1.2, a).
2. Open pores, with a continuous channel of communication to the external surface of the body. These can then be additionally described as either blind, with only a single opening (b and f) or through pores with an opening at both ends (c, d and e).

Classification according to shape has also been performed, with pore shapes considered as cylindrical (c and f), ink bottle (b), funnel (d) or slit shaped. It was also noted that surface irregularities that are wider than they are deep are not classed as porous (g).

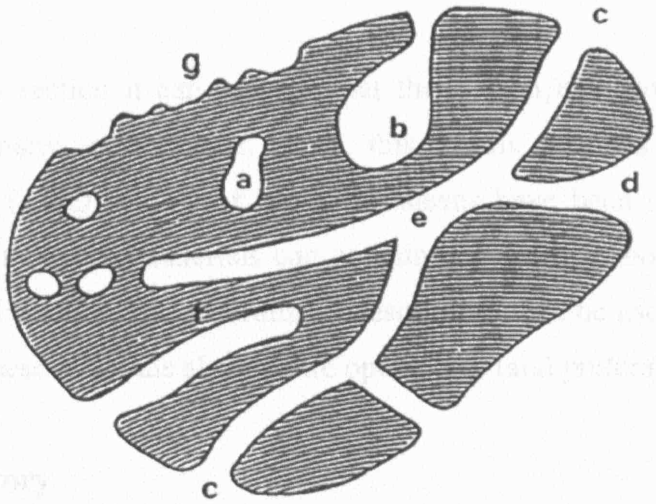

Figure 1.2: Classification of pore type (dependant on liquid accessibility) and pore shape according to IUPAC recommendations. Reproduced from ref. 1.

1.3 : Zeolites and related microporous materials

From the previous section it can be seen that there is an extensive range of porous materials with many applications. In this thesis zeolites and the related aluminophosphate (AlPO) family of molecular sieves have been investigated. From figure 1.1 we see that these materials can contain pores up to about 10 nm; they are therefore classified as either microporous or mesoporous. To be useful as catalysts and molecular sieves these materials also require open pores (and preferably through pores).

1.3.1 : A brief history

The boiling stone or 'zeolite' (from the Greek *–zeo* [to boil] and *lithos* [a stone]), was first described by Crönstedt[10] in 1756, who discovered that the mineral stilbite began to 'dance about' upon heating, as water was released from the material. Little work was performed on these materials until 1840 when Damour[11] observed reversible rehydration without damage to the materials and in 1858 when Eichhorn[12] demonstrated zeolitic ion exchange[12]. An important development was the first successful laboratory synthesis of a zeolite (levynite) by Deville[13] in 1862. The hydrothermal method used in this experiment remains the main synthesis route for zeolites to this day. By 1896 Friedel[14] had begun to develop the idea of spongy open frameworks after observing liquids being occluded by dehydrated zeolites and by 1909 the ability of these materials to adsorb small molecules such as ammonia, air and hydrogen was recorded[15]. In 1925 Weigel and Stienhoff[16] noticed the affinity of zeolites for particular organics (with only certain sized materials adsorbed), however, the actual term "molecular sieve" was not coined until McBain's work in 1932[17].

Despite this previous work, the two people considered to be the founding fathers of modern zeolite synthesis and practice are Richard Barrer and Robert Milton[18]. Barrer's work began in the early 1940s and he made a life time of contributions to all aspects of zeolite science, including, in 1948, the synthesis of the first zeolites with no known natural analogue. The two variants, zeolite-P and Q, were later identified to have the KFI topology[19,20]. By this time the industrial importance of zeolitic materials had been realised and Milton, working for the Linde Corporation, (along with co-workers including Breck) successfully synthesised over 20 zeolites (14 with no natural

analogues) by 1953[21]. Of particular importance was the synthesis of zeolite-A[22] and X[23], which were to become widely used for industrial separation and other applications.

In the next decades, the applications of zeolites grew with the Mobil Oil Company recognising the catalytic potential of these materials, utilising zeolite-X as a cracking catalyst. Henkel also demonstrated the potential of zeolites as an environmentally friendly alternative to harmful chemicals, replacing phosphates in detergents with zeolite-A.

In 1982 Wilson *et al*[24] identified a whole new class of materials. These aluminophosphates (AlPOs) contain oxygen bridged phosphorus and aluminium rather than silicon and aluminium (see below), but could still form topologies identical to zeolites, as well as many novel structures. By 1986 over 13 elements had been incorporated into AlPO structures[25], creating an array of materials potentially very useful as catalysts. The development of AlPOs, zeolites and other related structures continued through out the 80's and into 90's, with a steady increase in the number of new structure types and applications. By 2000 over 125 structure types had been assigned, with publications reaching nearly 4000 per annum (Figure 1.3)[26].

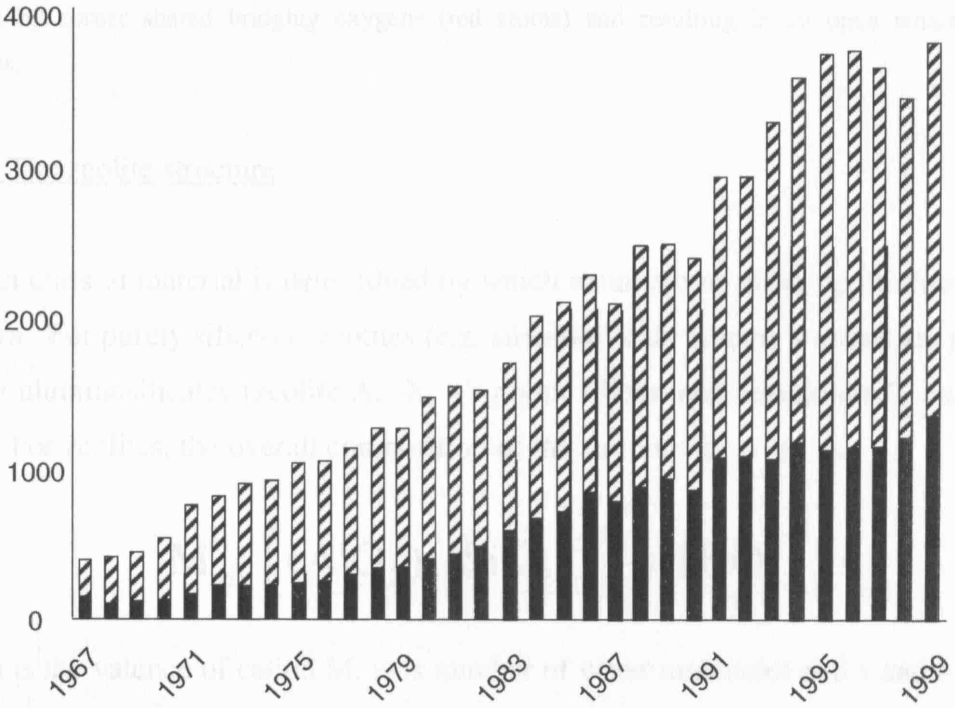

Figure 1.3: The number of papers (dashed bars) and patents (solid bars) published over the last four decades on microporous materials. Modified from ref. 26.

1.3.2 : Structure

1.3.2.1 : Building a zeolitic material

The primary building unit of all zeolitic type frameworks is the tetrahedral unit (Figure 1.4), consisting of a metal centre (or T atom) and coordinated oxygen atoms that are linked together by corner sharing bridging oxygen atoms to form open (porous) crystalline frameworks of repeating unit cells.

.

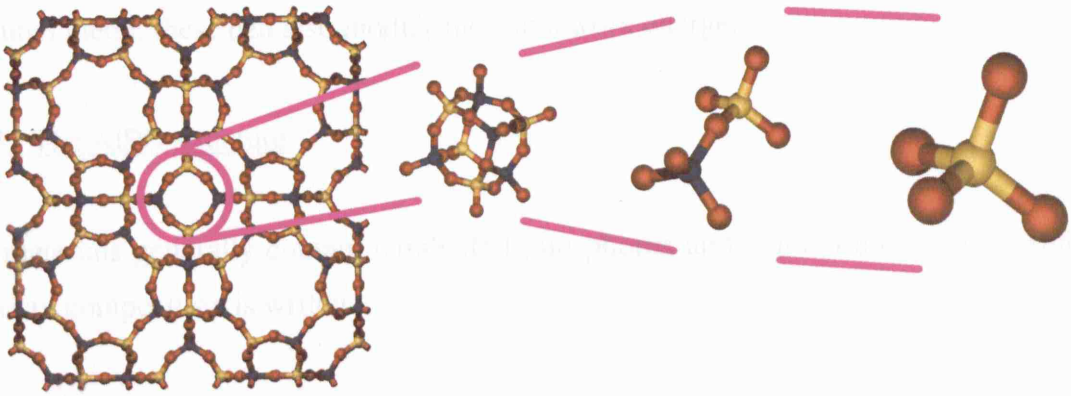

Figure 1.4: A zeolite (LTA) type framework consists of a repeating series of tetrahedral (TO_4) units connected by corner shared bridging oxygens (red atoms) and resulting in an open structure with micropores.

1.3.2.2 : The zeolite structure

The exact class of material is determined by which metal atoms make up the framework tetrahedra. For purely siliceous zeolites (e.g. silicalite) only silicon T atoms are present, whilst in aluminosilicates (zeolite-A, -X, –Y) both silicon and aluminium T atoms are present. For zeolites, the overall composition of the structure is given as:

$$M_{x/n}\left[(AlO_2)_x(SiO_2)_y\right]\cdot wH_2O$$

Where n is the valence of cation M, w is number of water molecules and x and y are the number of Al and Si tetrahedra respectively.

When the zeolite is not purely siliceous (i.e. x = 0), the framework carries a charge, with every Si^{4+}-O-Al^{3+} link increasing the overall atomic charge of the framework by one. This charge can be balanced by the presence of inorganic cations (e.g. sodium and lithium) or organics (e.g. tetraethylammonium cations) held within the pores. It is also essential for the important catalytic properties exhibited by many structures, as the replacement of counter ions with protons results in Brønsted acid sites, allowing acid (or in some cases redox) catalysis.

It is also possible to substitute a percentage of these tetrahedra with other metals (e.g. gallium for silicon or cobalt for aluminium) and depending on the valence of the substituted metal, these can also modify the framework charge.

1.2.2.3 : The AlPO structure

AlPO materials generally contain tetrahedral phosphorus and aluminium T atoms, and the overall composition is written:

$$x\mathrm{R} \cdot \mathrm{Al_2O_3} \cdot 1.0(\pm 0.2)\mathrm{P_2O_5} \cdot y\mathrm{H_2O}$$

Where R is an organic amine or quaternary ammonium ion and counter ion, and x and y are amounts of guest materials required to fill the pores.

Generally, naturally occurring and synthetic zeolitic aluminophosphates tend to have a P:Al ratio = 1 (see Lowenstein's rule below). However, it should be noted that recently, materials containing single, double and triple bonded phosphate groups with terminal oxygen and hydroxyls have been synthesised resulting in variations in this ratio[27].

As with the aluminosilicates it is possible to replace framework atoms with other elements, however, in their un-substituted state aluminophosphates require no balancing cations due to the overall neutrality of the framework. In addition, whilst zeolites frameworks tend always to contain tetrahedral metal centres, some aluminium sites in AlPO structures can coordinate with other ligands such as water or F^- and organics to give 5 and 6-coordinate geometries[28].

1.3.2.4 : Lowenstein's and Dempsey's rules

If examined in detail, it can be seen that the structure in figure 1.4 contains no aluminium-oxygen-aluminium bridges. Lowenstein[29] first noted this phenomenon in zeolites and formulated a series of rules for the linking of silicon and aluminium tetrahedra (and octahedra). These rules state:

- When two tetrahedra are bridged by one oxygen atom, only one will contain aluminium and the other must contain either silicon or another small ion with an electrovalence of 4 or more, such as phosphorus.
- If two aluminium ions are neighbours then one must have a coordination number of oxygen greater than four (e.g. octahedral coordination).

From these rules it can be seen why the minimum Si:Al ratio observed for hydrothermally synthesised zeolitic systems cannot be less than 1:1 (as long as there are no octahedral aluminium atoms), as at this value there is strict ordering of the silicon and aluminium atoms.

An extension to this rule was later demonstrated by Dempsey[30], who argued that electrostatic considerations mean that any framework aluminium atoms will occupy the greatest possible distance from each other, minimising the number of Al-O-Si-O-Al links.

1.3.2.5 : Selectivity and sieving

It is the microporous and open nature of these frameworks that gives rise to the molecular sieving properties of these materials. Depending on the size and shape of the pores, frameworks can be used to allow only certain molecules into the structure[31] (figure 1.5 a), select particular intermediates within the structure (b) and prevent particular products leaving the material (c) during catalytic reactions. The variable pore size of zeolite structures allow us to tailor zeolites to particular applications, resulting in high precision and selectivity in catalytic reactions.

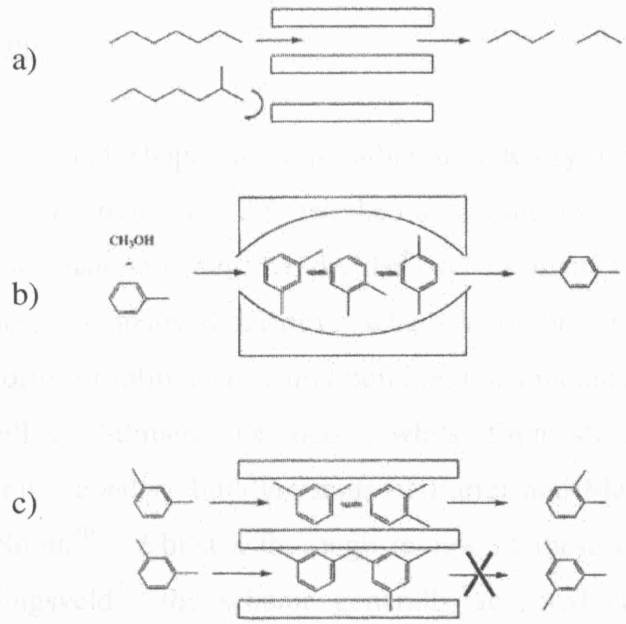

Figure 1.5: Molecular selection properties of a zeolitic type framework with reactant (a), intermediate (b) and product (c) shape selectivity. Modified from ref. 31.

1.3.3 : Classification

1.3.3.1 : pore size, shape and connectivity

Defining zeolitic materials by their structural attributes has been attempted in numerous ways to help group materials with similar physical and chemical characteristics. One of the most useful approaches is to classify materials according to pore size, because as mentioned above, it is the dimension of the pores which determine many of the properties. Historically, zeolites containing no larger than 8-rings (i.e. 8 tetrahedra linked to form a ring) were classified as small pore, 10-rings as medium pore and 12-rings as large pore. However, this classification is very simple as it does not take into account the shape of the pores, the connectivity within the structure or the recently developed materials with far larger ring sizes[32]. When further detail about the structure is required, it is necessary to consider both the dimensions and shape of the pores. The dimensionality of the pore structure can be 1, 2 or 3 and can have important consequences for catalytic reactions, affecting factors such as the selectivity and coking. The shape of the pore is also important. For example, the 12-ring structure mordenite does not exhibit all the properties expected for large pores systems[33], as its pore opening is significantly elongated (6.5 x 7.0 Å) compared to other large pore systems (e.g. faujasite, 7.4 x7.4 Å).

1.3.3.2 : Building units

As well as pore size and shape, it is possible to classify microporous materials according to the connectivity of the tetrahedra within their frameworks. The frameworks of these materials can be divided up in many different ways, and correspondingly, there are many descriptive schemes for building zeolites from the subsequent units. Forms of infinite structural building units include crank shafts[34,35] and saw chains[36] as well as 3-dimensional nets[37], whilst finite structural building units include the non-chiral secondary building units of Barrer and Meier[38,39] and the more complex cages of Smith[40]. Whilst a thorough review of these (and many others) is given by van Koningsveld[36], the scheme generally accepted and used to describe zeolitic materials today is the secondary building unit (SBU) scheme.

The SBUs are based on Pauling's rule of parsimony[41] and allow each zeolite to be constructed from a single SBU type containing no more than 16 T atoms. There are currently 16 different known SBUs (figure 1.6) and by omitting bridging oxygen from a zeolite structure some of these can be clearly seen in a framework.

Often, a zeolite topology can be entirely constructed from different SBU types. For example, the topology MFI can be constructed from either the 6-6, 6-2, 6 or 4 units. There are also a few exceptions to the rule, including zeolite-β which requires two single 4-rings and a 5-3 ring to be described.

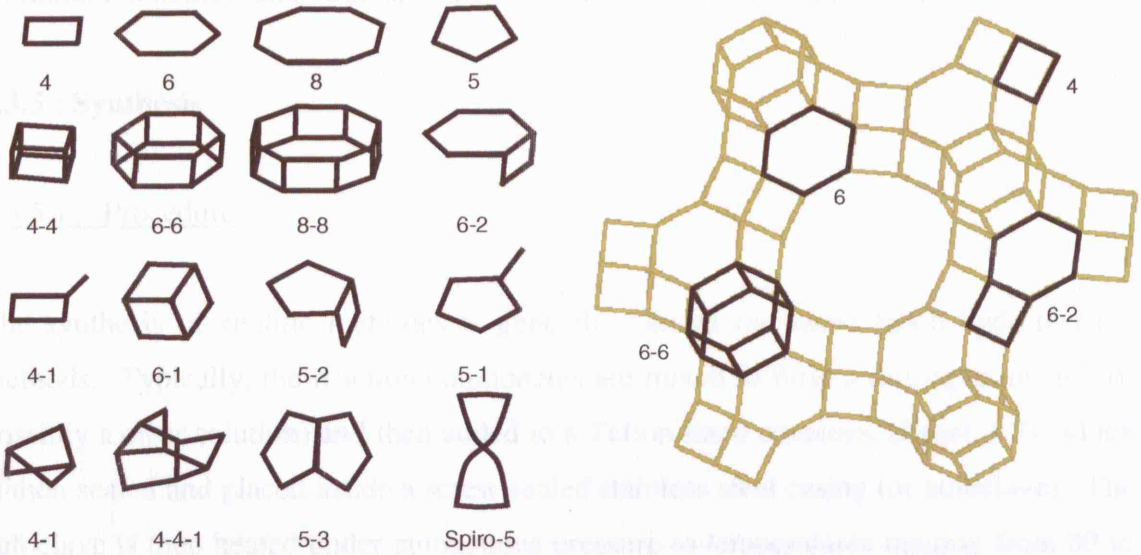

Figure 1.6: Examples of currently used secondary building units (left) modified from ref 32, and the various SBUs that can make up the faujasite structure highlighted within the framework (right).

1.3.4 : Nomenclature

Understanding the nomenclature used for naming zeolites can be confusing, with a number of different systems utilised in the past. Some materials have been named according to differences in framework composition and cation type. For example, the naturally occurring faujasite, zeolite-X and zeolite-Y all have differing compositions, but the same framework topology. Other materials are named after the company that patented the originally structure (e.g. ZSM [**Z**eolite **S**econy **M**obil] and MCM [**M**obil **C**omposition of **M**atter], or the discovering institute (e.g. DAF [**Da**vy **F**araday research laboratory]). Indeed some, such as materials with the MFI topology, have been referred to by dozens of different structural and trade names including, AMS-B, TS-1, AZ-1, TSZ, BOR-C, TSZ-III, Boralite-C, TZ-01, silicalite and ZSM-5.

To try and reduce this confusion the International Zeolite Association (IZA) structural commission[42] has adopted a three-lettered system to identify different zeolite topologies. This three letter code is often based on the name of the naturally occurring zeolite of a particular topology, for example, gismondine (GIS) and analcime (ANA). However, whilst this helps identify frameworks with identical topologies, as can be seen from the examples above, it does not distinguish between different zeolites with the same topology. Therefore, a combination of the topological code and 'common name' are often used to identify a material, which is the system generally used in this work. For example, in chapter 3 chabazite is the zeolitic form of the aluminophosphate AlPO-34 (common names) and both have the CHA (IZA code) topology.

1.3.5 : Synthesis

1.3.5.1 : Procedure

The synthesis of zeolitic materials is generally carried out using batch hydrothermal methods. Typically, the reaction components are mixed to form a homogenous gel (or possibly a clear solution) and then added to a Teflon lined container (figure 1.7), which is then sealed and placed inside a screw sealed stainless steel casing (or autoclave). The autoclave is then heated under autogenous pressure to temperatures ranging from 80 to 200°C. The reaction mix is then left at temperature, from a few hours to many weeks

whilst the microporous material forms. The product is then filtered or centrifuged from the mother liquor, washed in distilled water and dried.

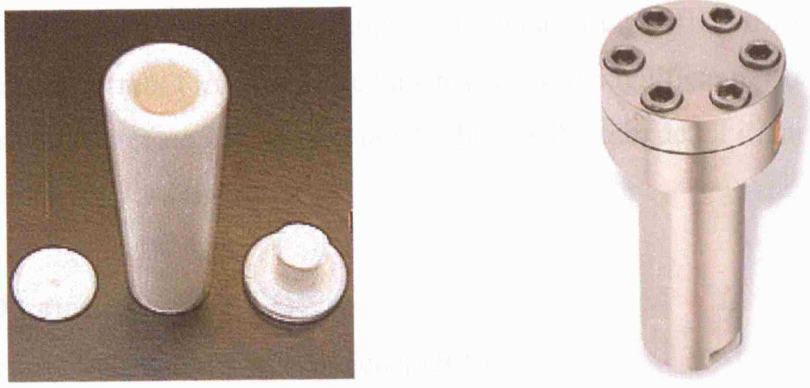

Figure 1.7: An example of the Teflon lined autoclave system used for batch hydrothermal synthesis of zeolitic materials.

1.3.5.2 : Reaction components

The reaction medium can contain a large array of components, including the metals to form the framework (aluminium and silicon or phosphorus), additional metals for framework substitution (e.g. cobalt, zinc or germanium), inorganic cations (e.g. sodium and potassium) and an organic structure directing agent. Each of these components can have an affect on the type and quality of the final crystalline product. For example, Lowe *et al*[43] demonstrated that a simple variation in the Al_2O_3 molar ratio could produce up to four different microporous and disordered phases.

1.3.5.3 : Reaction conditions

The reaction conditions, such as temperature, time and pH are also important and can affect the final products in a similar manner to the components. For example, an increase in pH (concentration of free hydroxide) can reduce both the nucleation and crystallisation time of mordenite[44].

1.3.6 : Formation mechanisms

Currently, one of the most significant challenges in the science of microporous materials concerns their formation mechanisms. This is particularly important as it will

allow control over the synthesis products and lead to the rational design of new porous materials, custom made for particular industrial needs. However, from the previous section it can be seen there are potentially many variables that can affect the mechanism which are often interconnected, making an understanding of their behaviour very complex. Indeed, current formation mechanisms can vary significantly for each specific type of material. Therefore it is appropriate to discuss them in detail in the experimental chapters in which they are used:

- AlPO formation (chapter 3)
- Clear solution zeolite synthesis (chapter 5)
- Combined micro/meso materials (chapter 6)

In this section some more general discussion of zeolite formation is given.

1.3.6.1 : Nucleation and growth curves

Budd *et al*[45] have described the formation of a zeolitic material by dividing it into a number of stages (figure 1.8). In the pre-nucleation stage, dissolution of the initial solid components occurs, forming a gel phase (except in clear solution synthesis) containing a randomly distributed array of the components. Next, some of these components become ordered (*via* some event) into nucleation centres, in either the gel or solution phase. These nucleation centres continue to form (nucleation profile) until, through some aggregation process, viable crystalline materials form. These then grow (growth curve), again either in the gel or solution phase, consuming the nucleation species and giving the final crystalline product.

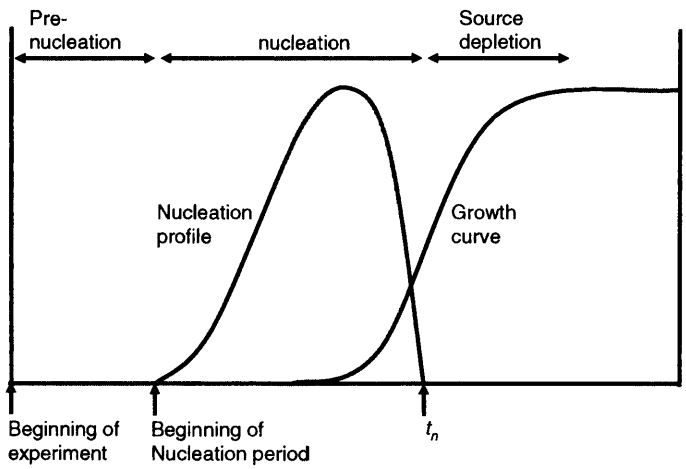

Figure 1.8: The different stages of a hydrothermal synthesis. Reproduced from ref. 45.

During these stages numerous processes can occur on an atomic level, either at specific points or throughout the reaction. These include the formation of polynuclear species, aggregation of species, dissolution of species, formation of long range order and growth of these ordered species.

Detection and measurement of each of these processes and determination of how the synthesis components interact with each other is essential to understand the formation mechanisms of these materials, however, it is also a difficult task. For example, whilst *ex situ* techniques are comparatively easy to perform, the removal of gel components from the reaction environment inevitably alters the species present. The development of *in situ* techniques over the past few decades (see below) has overcome this problem by examining the gel forming in the hydrothermal environment[46]. However, these experiments can still be difficult, costly and time consuming.

1.3.6.2 : Early ideas

Despite the difficulties mentioned above, a large amount of experimental data has been collected on all parts of the zeolitic growth process. As a result there are various mechanisms proposed in the open literature.

Probably the first mechanism was proposed by Flanigen and Breck[47,48]. Here polymerisation / depolymerisation of the gel species occur and rearrangement of the framework anions is controlled by hydrated cationic species. Basic polyhedral units then form around these cations and then link to form massive ordered crystalline structures (figure 1.9). Interestingly, the polyhedral building units described earlier by Barrer[38] were included in this work. Later, Barrer[49] suggested that the addition of small units to the forming structure would result only in dense structures. He therefore concluded that, to form microporous materials, condensation polymerisation of small ring structures must occur. These 'secondary building unit' (SBU) like species were to become integral parts of a number of mechanisms suggested in later years.

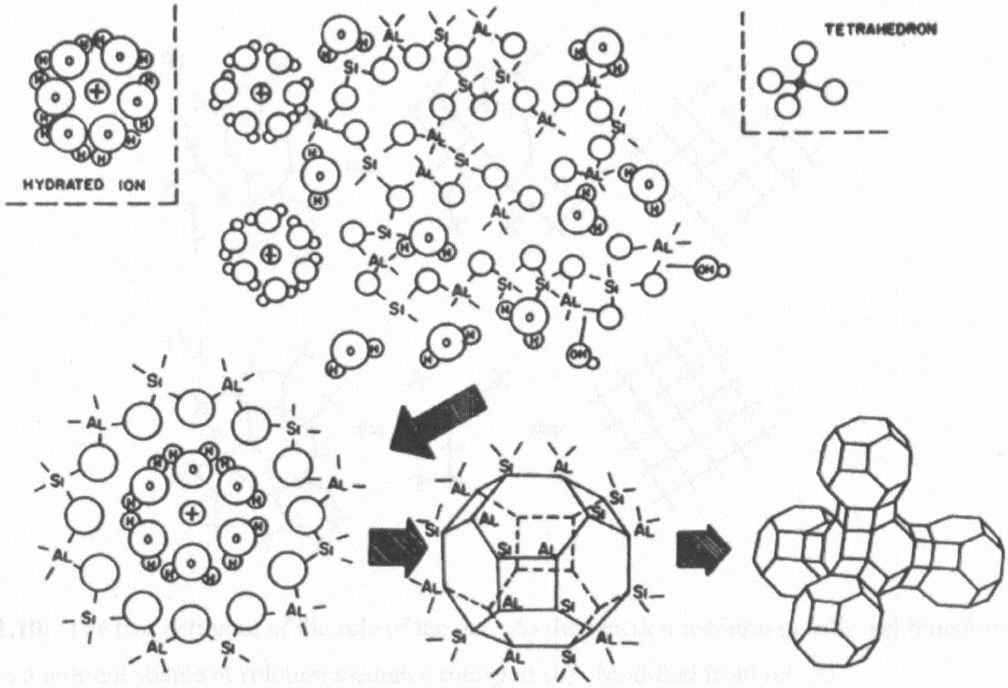

Figure 1.9: The first schematic representation of a zeolite crystallisation as proposed by Flanigen and Breck. Reproduced from ref. 48.

1.3.6.3 : The role of the gel

At this stage it is important to note that two extreme views on the role of the gel had developed by the mid sixties. These are, as illustrated in figure 10[50]:

- The solid-gel transformation, in which the amorphous gel phase is the medium where crystallisation occurs, undergoing a reorganisation to give long range order, with crystals forming by solid-solid transformations.

- The solution mediated transport mechanism, in which the amorphous gel is effectively just a nutrient source, with nucleation and growth occurring by solution mediated crystallisation.

A comprehensive overview of these mechanisms, with further examples, are given elsewhere[50,51]. However, it is important to note that examples of zeolite formation from both solid hydrogel (e.g. Xu *et al*'s[52] amorphous solid transformations) and solution mediated (e.g. Schoeman *et al's*[53,54] clear solutions) have been observed. Indeed, it is likely that in most syntheses a combination of the two mechanisms occurs.

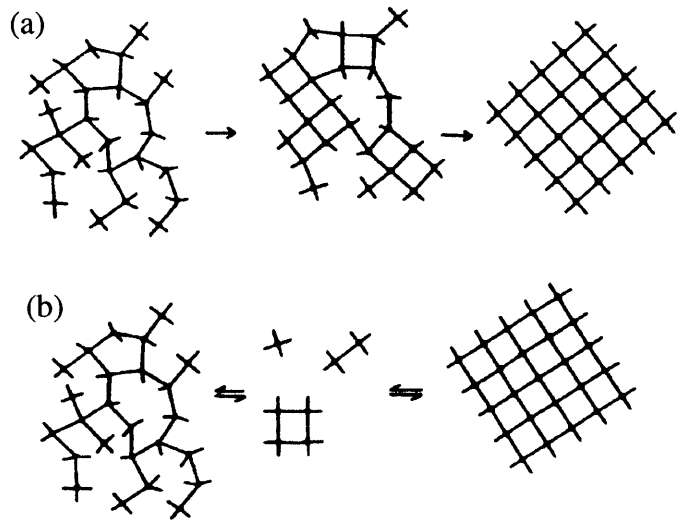

Figure 1.10: The two extremes of the role of the gel. As the reaction medium in solid-gel transformation (a) and as a nutrient source in solution mediated transport (b). Modified from ref. 50.

1.3.6.4 : Principal mechanisms

A large array of mechanisms have been developed from the initial works of Flanigen and Breck[47,48] and Barrer[38,49]. Although there are far too many to detail in this work, some important experiments and suggested mechanisms include:

- The recirculation experiments of Kerr *et al*[55], who demonstrated, by passing sodium hydroxide through amorphous and then crystalline materials, that crystal growth from solution species could occur.

- Detailed experiments by Zhdanov[56] leading to the proposal of a solubility equilibrium between the solid and liquid phases, with a condensation reaction giving rise to 'primary aluminosilicate blocks'. In this work, the gel was viewed as a more dynamic entity, releasing nucleation species into the solution resulting in 'autocatalytic nucleation'.

- The proposal by Derouane *et al*[57,58] of two separate mechanisms for ZSM-5 formation depending on the exact aluminium and silicon content, with pathway (a) indicating small number of nuclei form, which then grow by liquid phase transportation (similar to Zhdanov[56]); whilst pathway (b) suggests that the

formation of microcrystallites occurs from nuclei exclusively within the hydrogel phase.

- The examination by de Moor *et al*[59,60] (and others) of dilute and clear solutions using, among other techniques, light scattering and SAXS, which has lead to a mechanism based on the initial formation of clusters, which then form primary fractal aggregates and undergo a series of aggregation and densification steps, resulting in the crystalline product (see chapter 5).

These and many other studies are discussed in detail in the excellent reviews by Cundy and Cox[18,61] and some are summarised in figure 1.11 (references as given in the original work[61]). Note that the important works of Chang and Bell[62] and Burkett and Davis[63,64] are discussed in relation to the role of the template below.

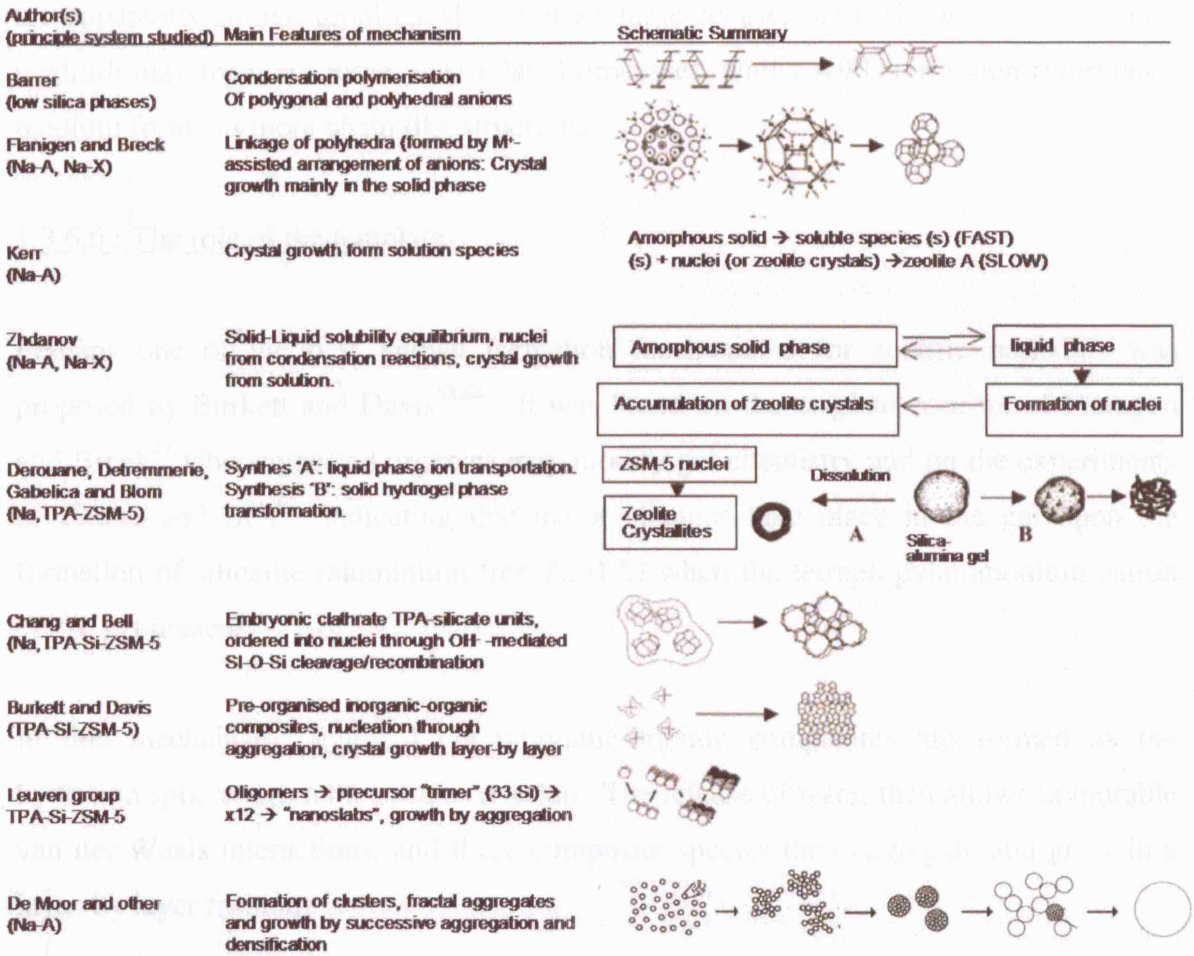

Figure 1.11: Some principal zeolitic formation mechanisms from 1959 – 2005. Modified from ref. 61. Primary references are given in the original work.

1.3.6.5 : SBUs or chains

From figure 1.11 it can be seen that a number of mechanisms propose the formation of individual SBU species within the solution that can form the zeolitic structure. For zeolites there is evidence for the formation of such species in aqueous solutions[65,66]. However, little direct evidence for their conversion to the final zeolite has been observed. Indeed, species such as double 5-rings often observed in these experiments, cannot be located in any known zeolitic structure[32]. For AlPO materials the situation is even more complex, with evidence for both SBU-like and chain-like species in the forming gels (refer to chapter 3 for details). In these materials it appears that the presence of particular ions (e.g. fluoride) in the solution may alter the gel chemistry and change which type of species form.

It therefore seems likely that different mechanisms may be operating in materials that are apparently similar topologically. For example zeolites, and AlPOs in a fluorinated medium may form *via* some SBU related processes, whilst AlPOs in a non-fluorinated medium form *via* more chain like structures.

1.3.6.6 : The role of the template

Perhaps one of the best known formation mechanisms for zeolitic materials was proposed by Burkett and Davis[63,64]. It was based on the original concept of Flanigen and Breck[47] who suggested organics may modify gel chemistry and on the experiments of Chang and Bell[62], indicating that major changes take place in the gel upon the formation of silicalite (aluminium free ZSM-5) when the tetrapropylammonium cation (TPA^+) is present.

In this mechanism (figure 1.12) inorganic-organic composites are formed as the hydration spheres from the species overlap. The release of water then allows favourable van der Waals interactions, and these composite species then aggregate and grow in a layer-by layer fashion.

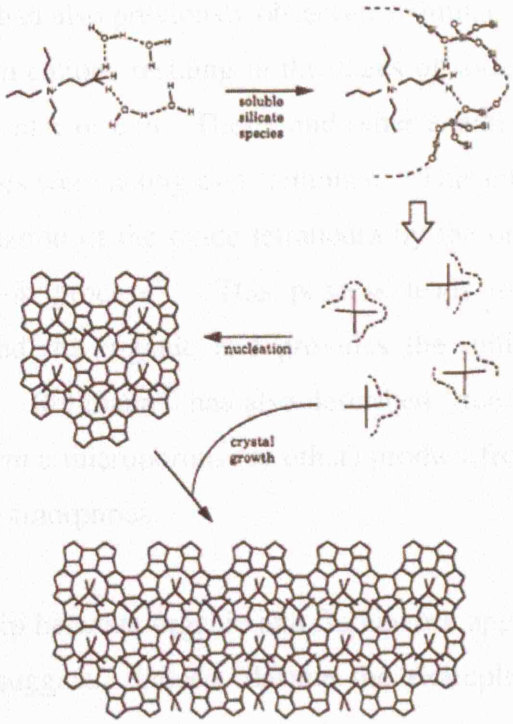

Figure 1.12: The formation silicalite as proposed by Burkett and Davis. Reproduced from ref. 63.

What is clear from this mechanism is the importance of the interaction between the organic and inorganic gel components, suggesting the organic's role within the gel is substantial, and certainly more than just a pH modifier. Certainly, it was already known that the TPA cation was 'trapped' within the silicalite framework, residing at the channel intersections with the propyl chains extending into the channels (Figure 1.13)[67].

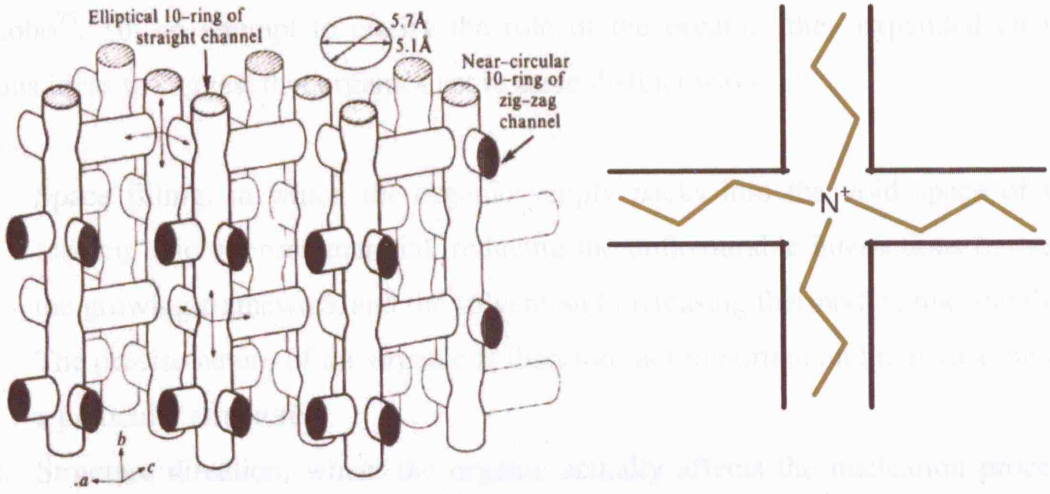

Figure 1.13: The structure of silicaite-1 as described by Flanigen in ref. 67 (left) and a schematical representation of how the TPA cations occupy the channel intersections (right).

Baerlocher and Meier[68] had also previously observed a similar 'trapping' of the organic, with trimethylammonium cations residing in the cages of sodalite, which are too small to allow the organic to enter or exit. These, and other examples, have led to the idea that the organic molecules were acting as a 'template'. This templating action has been described as the organisation of the oxide tetrahedra by the organic species within the gel during the nucleation process[69]. This process leads to a particular geometric topology forming around the organic and provides the initial building block for a particular structure type. Rollmann[70] has also described 'true templating' as occurring when an organic can form a microporous (or other) product from a mixture (gel) which would otherwise remain amorphous.

However, the relationship between organic and framework appears to be more complex than these definitions suggest. Indeed, despite the examples given above, there is generally little correlation between the organic shape and the pore shape. For example, ZSM-5 can be synthesised from over 20 different organic molecules, and the same is true for AlPOs with AlPO-5 forming from 23 organics[71]. Additionally, one organic can often form different structures, depending on the synthesis conditions (see for example AlPO-34 and AlPO-5 formation from triethylamine and tetraethylammonium hydroxide in chapter 3) and very large pore materials can be formed in the presence of small organics[72-74].

Probably the most complete description of the role of the organic was given by Davis and Lobo[75]. In an attempt to clarify the role of the organic, they expanded on the previous ideas to suggest that organics act in three distinct ways:

1. Space filling, in which the organic simply packs into the void space of the forming microporous material, reducing the unfavourable interactions between the growing framework and the solvent and increasing thermodynamic stability. The precise nature of the organic is therefore not important and non-specific for a particular structure.
2. Structure direction, where the organic actually affects the nucleation process, resulting in the formation of unique structures from unique organics.
3. True templating, where enhanced guest-host interactions occur during crystalline ordering, again resulting in unique structures. This is considered by the authors as extremely rare, only occurring in the case of ZSM-18.

Note that in many published works the terms structure directing agent and template are often used interchangeably. For convenience, in this thesis the microporous organic in each experiment has generally been referred to as the structure directing agent (SDA).

1.4 : *In situ* methods

As mentioned in section 1.3.6, a greater understanding of the formation mechanisms of these materials is necessary to allow the design of more advanced materials for industrial applications. To understand the mechanism we need to probe the interactions that are occurring in the gel. Unlike *ex situ* methods, *in situ* methods can allow us to measure the hydrothermal processes with little effect on the reaction medium. Whilst these methods are often costly and time consuming, continued advances in specialist cells (which can maintain integrity under high pressure but also have thin walls allowing sample detection) and the increased use and availability of synchrotron light sources (see chapter 2), have made *in situ* techniques an essential tool in the understanding of these and many other materials.

Today, *in situ* techniques are performed using a whole range of spectroscopic and diffraction instruments including UV-Vis, NMR, XAS, SAXS, WAXS and EDXRD. Combinations of instruments have offered even more flexibility, for example two technique combinations such as EXAFS and XRD, and more recently; three technique combinations such as SAXS, WAXS and EXAFS[76, *].

In this thesis, extensive use of *in situ* techniques has been made, both synchrotron and laboratory based, to increase the understanding of the formation mechanisms of micropores materials. EDXRD has been used to determine kinetic data, whilst Raman spectroscopy has been employed to monitor organic-inorganic interactions and conformation change. SAXS/WAXS has then been used to measure the formation of amorphous entities in relation to the onset of crystallinity.

* Note UV-vis = ultraviolet-visible, NMR = nuclear magnetic resonance, XAS = X-ray absorption spectroscopy, SAXS = small angle X-ray scattering, WAXS = wide angle X-ray scattering, EDXRD = energy dispersive X-ray diffraction and EXAFS = extended X-ray fine structure. Details of these techniques are given in chapter 2.

1.5 : Project overview

During the course of this thesis, both *ex situ* and *in situ* experimental techniques as well as computational methods have been used to follow the formation processes of a number of porous materials. With this powerful combination different components of the formation processes (such as nucleation and crystal growth) have been examined and the interactions of different species within the hydrothermal gels have been monitored.

The formation of metal substituted AlPO-34 has been examined and the need for a divalent metal ion (or fluorine) has been identified. Density functional theory (DFT) has then identified a preference for chain like species (unlike silicates) during the initial moments of synthesis. Raman spectroscopy has shown that a combination of a metal-organic SDA interaction and the conformation of the organic can determine the structure formed. Further investigations into the crystallisation of CoAPO-36, using EDXRD and molecular mechanics calculations, have demonstrated that the orientation and size of the template can significantly affect the kinetics of formation and the final crystalline structure, whilst still producing the same AlPO. Examination of the effect of germanium substitution on a zeolite (zeolite-A) using SAXS/WAXS has shown that metal substitution can effect the size of pre-crystalline species in these materials and the rate of crystallisation. These effects then lead to a propensity for increased crystal intergrowth in the final materials.

Each of these experiments will have important implications for the future of microporous materials as industrial catalysts, as the greater understanding of these interactions in both the AlPOs and zeolites presented in this work will allow greater control of the hydrothermal synthesis processes, resulting in more a rational design process.

Finally, the synthesis of a new hierarchical mesoporous/microporous AlPO material has been developed, using simple organics for microporous formation and cheap readily available non-ionic organic surfactants for mesopore formation. This material is of particular interest as it should combine the high throughput of mesopores and the reactivity and stability of micropores.

1.6 : References

(1) Rouquerol, J.; Avnir, D.; Fairbridge, C. W.; Everett, D. H.; Haynes, J. H.; Pernicone, N.; Ramsay, J. D. F.; Sing, K. S. W.; Unger, K. K. *Pure Appl. Chem.* **1994**, *66*, 1739.

(2) Kelly, A. *Philos. Trans. R. Soc. A-Math. Phys. Eng. Sci.* **2006**, *364*, 5.

(3) Brandon, N. P.; Brett, D. J. *Philos. Trans. R. Soc. A-Math. Phys. Eng. Sci.* **2006**, *364*, 147.

(4) Bobyn, J. D.; Pilliar, R. M.; Cameron, H. U.; Weatherly, G. C. *Clinical Orthopaedics & Related Research* **1980**, *150*, 263

(5) Seayad, A. M.; Antonelli, D. M. *Adv. Mater.* **2004**, *16*, 765.

(6) Cullis, A. G.; Canham, L. T.; Calcott, P. D. J. *J. Appl. Phys.* **1997**, *82*, 909.

(7) Stein, A.; Schroden, R. C. *Curr. Opin. Solid State Mat. Sci.* **2001**, *5*, 553.

(8) Haber, J. *Pure Appl. Chem.* **1991**, *63*, 1227.

(9) Sing, K. S. W.; Everett, D. H.; Haul, R. A. W.; Moscou, L.; Pierotti, R. A.; Rouquerol, J.; Siemieniewska, T. *Pure Appl. Chem.* **1985**, *57*, 603.

(10) Cronstedt, A. F. In *Akad. Hankl.* Stocholm, 1756; Vol. 18, p 120.

(11) Damour, A. *Ann. Mines.* **1840**, *17*, 191.

(12) Eichhorn, H. *Poggendorf Ann. Phys Chem.* **1858**, *105*, 126.

(13) de St. Claire Deville, H. *Compt. Rend.* **1862**, *54*, 324.

(14) Friedel, G. *Bull. Soc. Franc. Mineral. Cristallogr* **1896**, *19*, 94

(15) Grandjean, F. *Compt. Rend.* **1909**, *149*, 866.

(16) Weigel, O.; Steinhoff, E. *Z. Kristallogr.* **1925**, *61*, 125.

(17) McBain, J. W. *The Sorption of Gases and Vapours by Solids*; Rutledge and Sons: London, 1932.

(18) Cundy, C. S.; Cox, P. A. *Chem. Rev.* **2003**, *103*, 663.

(19) Barrer, R. M.; Hinds, L.; White, E. A. *J. Chem. Soc.* **1953**, 1466.

(20) Barrer, R. M. *J. Chem. Soc.* **1948**, 127.

(21) Milton, R. M. In *Zeolite Synthesis*; Occelli, M. L., Robson, H. E., Eds.; The American Chemical Society: 1989; Vol. 398, p 1.

(22) Milton, R. M. US Patent, 1959, p 2882243.

(23) Milton, R. M. US Patent, 1959, p 2882244.

(24) Wilson, S. T.; Lok, B. M.; Messina, C. A.; Cannan, T. R.; Flanigen, E. M. *J. Am. Chem. Soc.* **1982**, *104*, 1146.

(25) Flanigen, E. M.; Lok, B. M.; Patton, R. L.; Wilson, S. T. *Pure Appl. Chem.* **1986**, *58*, 1351.

(26) Van Bekkum, H.; Flanigen, E. M.; Jacobs, P. A.; Jansen, J., C *Introduction to Zeolite Science and Practice*; Elsevier, 2001; Vol. 137.

(27) Oliver, S.; Kuperman, A.; Lough, A.; Ozin, G. A. *Chem. Mat.* **1996**, *8*, 2391.

(28) Meinhold, R. H.; Tapp, N. J. *J. Chem. Soc.-Chem. Commun.* **1990**, 219.

(29) Loewenstein, W. *Am. Miner.* **1954**, *39*, 92.

(30) Dempsey, E.; Kuhl, G. H.; Olson, D. H. *J. Phys. Chem.* **1969**, *73*, 387.

(31) Dyer, A. *An Introduciton to Zeolite Molecular Sieves*; first ed.; John Wiley and Sons: Chichester, 1988.

(32) Szostak, R. *Molecular Sieves*; second ed.; Blackie Academic, 1998.

(33) Jacobs, P. A.; Martens, J. A. In *Introductiion to Zeolite Science and Practice*; van Bekkum, H., Flanigen, E. M., Jansen, J., C, Eds.; Elsevier: Amsterdam, 1991; Vol. 58, p 445.

(34) Keller, E. B.; Meier, W. M.; Kirchner, R. M. *Solid State Ionics* **1990**, *43*, 93.

(35) Richardson, J. W.; Smith, J. V.; Pluth, J. J. *J. Phys. Chem.* **1990**, *94*, 3365.

(36) van Koningsveld, H. In *studies in surface science and catalysis*; Van Bekkum, H., Flanigen, E. M., Jacobs, P. A., Jansen, J., C, Eds.; Elsevier: 2001; Vol. 137, p 69.

(37) Wells, A. F. *Three-dimensional nets and polyhedra*; Wiley-Interscience: New York, 1977.

(38) Barrer, R. M.; Baynham, F. W.; Meier, W. M. *J. Chem. Soc.* **1959**, 195.

(39) Meier, W. M. In *Molecular Sieves*; Society of Chemistry and industry: London, 1968, p 10

(40) Smith, J. V. *Chem. Rev.* **1988**, *88*, 149.

(41) Pauling, L. *J. Am. Chem. Soc.* **1929**, *51*, 1010.

(42) Baerlocher, C.; McCusker, L. B.; Database of Zeolite Structures: http://www.iza-structure.org/databases/: 2005.

(43) Araya, A.; Lowe, B. M. *J. Chem. Res.-S* **1985**, 192.

(44) Barrer, R. M. *Zeolites* **1981**, *1*, 130.

(45) Budd, P. M.; Myatt, G. J.; Price, C.; Carr, S. W. *Zeolites* **1994**, *14*, 198.

(46) Catlow, C. R. A.; Sankar, G. In *Microporous Properties and Processes in Minerals*; Wright, K., Catlow, C. R. A., Eds.; Kluwer Academic: 1999, p 145.

(47) Flanigen, E. M.; Breck, D. W. *Crystalline Zeolites V - Growth of Zeolite Crystals from Gels. 137th Meet. ACS, Div. Inorg. Chem.* **1960**, paper 82.

(48) Breck, D. W. *J. Chem. Educ.* **1964**, *41*, 678.

(49) Barrer, R. M. *Chem. Br.* **1966**, *2*, 380.

(50) Guth, J. L.; Caullet, P. *J. Chim. Phys.-Chim. Biol.* **1986**, *83*, 155.

(51) Guth, J. L.; Kessler, H. In *Catalysis and Zeolites*; Weitkamp, J., Puppe, L., Eds.; Springer-Verlag: Berlin, 1999, p 1.

(52) Xu, W. Y.; Dong, J. X.; Li, J. P.; Li, J. Q.; Wu, F. *J. Chem. Soc.-Chem. Commun.* **1990**, 755.

(53) Schoeman, B. J.; Regev, O. *Zeolites* **1996**, *17*, 447.

(54) Schoeman, B. J. *Zeolites* **1997**, *18*, 97.

(55) Kerr, G. T. *J. Phys. Chem.* **1966**, *70*, 1047.

(56) Zhdanov, S. P. In *The Second International Conference on Molecular Sieves*; Flanigen, E. M., Sand, L. B., Eds.; American Chemical Society: Worchester, 1970; Vol. 101, p 20.

(57) Derouane, E. G.; Detremmerie, S.; Gabelica, Z.; Blom, N. *Appl. Catal.* **1981**, *1*, 201.

(58) Gabelica, Z.; Derouane, E. G. In *Catalytic Materials Relationship between Structure and Reactivity*; The American Chemical Society: 1984; Vol. 248, p 219.

(59) Dokter, W. H., TU Eindhoven, 1994.

(60) Dokter, W. H.; Vangarderen, H. F.; Beelen, T. P. M.; Vansanten, R. A.; Bras, W. *Angew. Chem.-Int. Edit. Engl.* **1995**, *34*, 73.

(61) Cundy, C. S.; Cox, P. A. *Microporous Mesoporous Mat.* **2005**, *82*, 1.

(62) Chang, C. D.; Bell, A. T. *Catal. Lett.* **1991**, *8*, 305.

(63) Burkett, S. L.; Davis, M. E. *J. Phys. Chem.* **1994**, *98*, 4647.

(64) Burkett, S. L.; Davis, M. E. *Chem. Mat.* **1995**, *7*, 1453.

(65) McCormick, A. V.; Bell, A. T.; Radke, C. J. In *Studies in Surface Science and Catalysis*; Murakami, Y., Iijima, A., Ward, J. W., Eds.; Elsevier: Amsterdam, 1986; Vol. 28, p 247.

(66) Groenen, E. J. J.; Kortbeek, A.; Mackay, M.; Sudmeijer, O. *Zeolites* **1986**, *6*, 403.

(67) Flanigen, E. M.; Bennett, J. M.; Grose, R. W.; Cohen, J. P.; Patton, R. L.; Kirchner, R. M. *Nature* **1978**, *271*, 512.

(68) Baerlocher, C.; Meier, W. M. *Helvetica Chemica Acta* **1969**, *52*, 1853.

(69) Flanigen, E. M.; Patton, R. L.; wilson, S. T. *Studies in Surface Science and Catalysis* **1988**, *37*, 13

(70) Rollmann, L. D. *Advances in Chemistry Series* **1979**, 387.

(71) Oliver, S.; Kuperman, A.; Ozin, G. A. *Angew. Chem.-Int. Edit.* **1998**, *37*, 47.

(72) Davis, M. E.; Saldarriaga, C.; Montes, C.; Garces, J.; Crowder, C. *Nature* **1988**, *331*, 698.

(73) Loiseau, T.; Ferey, G. *J. Solid State Chem.* **1994**, *111*, 403.

(74) Estermann, M.; McCusker, L. B.; Baerlocher, C.; Merrouche, A.; Kessler, H. *Nature* **1991**, *352*, 320.

(75) Davis, M. E.; Lobo, R. F. *Chem. Mat.* **1992**, *4*, 756.

(76) Beale, A. M.; van der Eerden, A. M. J.; Jacques, S. D. M.; Leynaud, O.; O'Brien, M. G.; Meneau, F.; Nikitenko, S.; Bras, W.; Weckhuysen, B. M. *J. Am. Chem. Soc.* **2006**, *128*, 12386

Chapter 2

Experimental and computational methods

2.1 : Chapter overview

This chapter outlines the main experimental techniques used during the course of this work. It gives a brief overview of the theory surrounding each technique as well as any detail regarding the experimental equipment. A number of techniques were performed using synchrotron radiation, and the generation of this radiation is also discussed. The chapter is divided into 3 sections, laboratory based, synchrotron based and computational techniques. Other than XRD and EXAFS, which have been used throughout this thesis, the method of data analysis performed on each technique is discussed in the chapter in which it is used.

2.2 : Lab based techniques

2.2.1 : X-ray diffraction

Discovered by Röntgen in 1895, X-rays were found to have the ability to penetrate materials such as skin and bone to varying degrees, which has led to a wide number of applications in fields such as security and medicine. As the X-ray wavelength is of the order of interplanar distances (d-spacings) of crystalline materials X-rays can also been diffracted from these planes. The technique has become routinely used to 'fingerprint' powdered materials (including the porous materials used in this thesis) and for detailed structure determination.

2.2.1.1 : Theory

X-rays can be generated using both standard laboratory based equipment, which produces monochromatic X-rays and synchrotrons, which produce a white beam. Lab based X-rays are produced by generating electrons at a cathode filament, which are then accelerated across a vacuum towards a cooled metal anode target. Upon impact the electrons decelerate producing X-rays of two characteristic types:

- Bremsstrahlung radiation – a continuous spectrum of X-rays.
- K-shell emission - sharp emissions characteristic to the type of target metal.

Bremsstrahlung radiation is generated from the continuous deceleration of the electrons striking the target and its wavelength is dependant on the accelerating voltage. K-shell emission is produced when electrons from the core of the target metal are struck by the electrons accelerated from the cathode. When these are above the 'excitation potential', electrons in the targets K-shell are ionised and those from a higher shell (L or M) drop down, emitting X-rays of a discrete wavelength, which is element specific.

Standard laboratory based diffractometers use these K-shell emissions for pattern generation. Copper and cobalt are two frequently used targets utilising $K_{\alpha 1}$ and $K_{\alpha 2}$ X-rays, the K indicating the radiation comes from electron transitions into a K shell.

Bragg's law provides a qualitative mathematical formula for diffraction, linking the wavelength of the incident radiation with the lattice planes of a crystal (equation 2.1)[1,2]. In the case of X-rays scattered from two Bragg planes (Figure 2.1), constructive inference occurs when distance I is equal to $d\sin\theta$, resulting in an intensity in the diffraction pattern (a reflection).

$$n\lambda = 2d\sin\theta \tag{2.1}$$

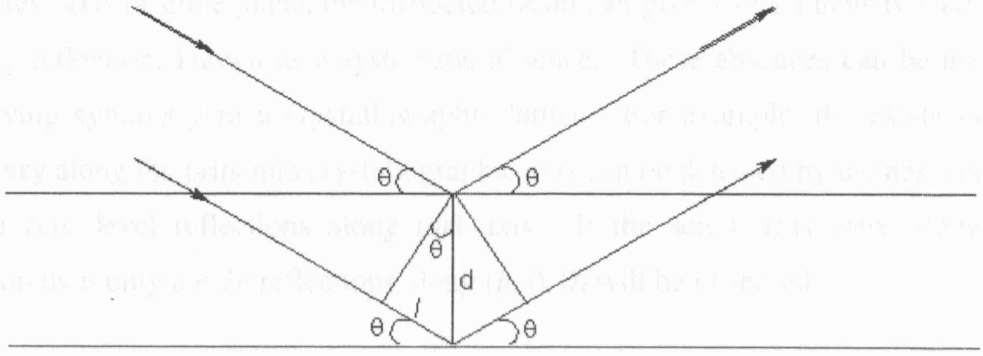

Figure 2.1: Scattering of x-rays from two Bragg planes in a crystal

For a fixed X-ray wavelength (λ) it is possible to determine the plane separation (d) as a function of the angle (θ) for each diffraction intensity, and for each type of unit cell d can be related to a particular lattice plane in the crystal, identified by the Miller indices (h, k, l). In the case of a simple cubic cell, d can be related to the Miller indices by equation 2.2. The quantity a is equal to the length of the unit cell, which in this cubic case is the same along each axis. Note that for more complex systems, the cell edges are no longer equivalent and new terms are introduced, particularly when the cell angles deviate from 90°.

$$d_{hkl} = \frac{a}{\sqrt{h^2 + k^2 + l^2}} \tag{2.2}$$

The experimental values of the Miller indices for the cubic unit cell can be calculated using equation 2.3, and thus it is possible to identify the unit cell parameters of a crystalline material by measuring the angle at which each reflection occurs at a given wavelength (a procedure known as 'indexing').

$$\sin^2\theta = \frac{\lambda}{4a^2}\left(h^2 + k^2 + l^2\right) \tag{2.3}$$

The actual intensity of each reflection depends on the arrangement and atomic number of the atoms in the unit cell. Therefore, whilst the angle of the diffraction signal gives information about the unit cell, the intensity of the signal can yield some information on the contents of the unit cell (see Rietvield refinement below).

In principle, each set of lattice planes gives rise to a diffracted beam, and therefore a reflection. However, in some crystal systems containing, for example, symmetries such as a screw axis or glide plane, the diffracted beam can give a zero intensity leading to a missing reflection, known as a systematic absence. These absences can be useful for identifying symmetry in a crystallographic lattice. For example, the existence of 2_1 symmetry along the principle crystallographic axis can be detected by the absence of the $(2n+1)$ zero level reflections along that axis. If the screw axis were along the *a* direction then only the $2n$ reflections along $(h, 0, 0)$ will be observed.

2.1.1.2 : Geometries and detectors

During the course of this thesis X-ray diffractometers in both the Bragg-Brentano reflection geometry and the Debye-Scherrer transmission geometry[3] have been utilised (figure 2.2 a + b).

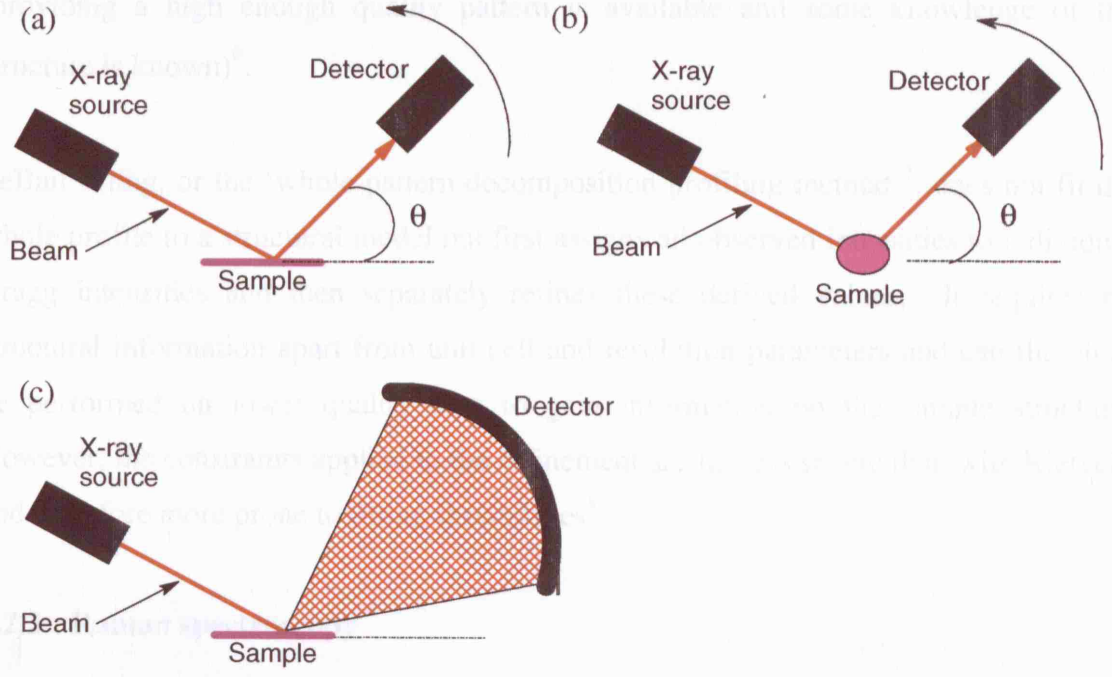

Figure 2.2: The three types of set-up for XRD used in this thesis, (a) Bragg-Brentano reflection, (b) Debye-scherrer transmission, both using a position sensitive detectors and (c) the Bragg-Brentano geometry utilising an angular sensitive detector.

In both of these set-ups the diffracted signal is recorded by a position sensitive detector which moves through each angle of θ required, recording the angle at which in-phase signals are found. For the patterns recorded in chapter 6, a third set up was utilised, again using the Bragg-Brentano geometry, but with an angular dispersive detector, which can record all of the scattered signals and their positions at once (figure 2.2 c).

2.2.1.3 : Data analysis

When a powder is used, the resulting diffraction pattern can be used as a 'finger print' to identify the topology of the structure by simply matching the observed reflections with a known compound. However, it is also possible to obtain more data about the system using a number of fitting techniques.

The Rietveld refinement method[4,5] can make full use of the all the information available in a diffraction pattern, including the intensity (or lack of) at each point in the system. Key to this procedure is the ability to carry out least squares refinements simultaneously on models for the crystal structure, diffraction optics, instrumental factors and other characteristics, calculating the best fit between the observed and calculated models. This procedure can be used to obtain unit cell parameters and unit cell contents (providing a high enough quality pattern is available and some knowledge of the structure is known)[6].

LeBail fitting, or the 'whole-pattern decomposition profiling method'[7], does not fit the whole profile to a structural model but first assigns all observed intensities to individual Bragg intensities and then separately refines these derived values. It requires no structural information apart from unit cell and resolution parameters and can therefore be performed on lower quality data to gain information on the sample structure. However, the constraints applied to the refinement are far less severe than with Rietveld and therefore more prone to fitting instabilities[8].

2.2.2 : Raman spectroscopy

Raman first reported the light scattering phenomenon, which latterly bore his name, in 1928, although some earlier experiments have now been recognised as examples of the

Raman effect. Along with Infrared (IR) radiation, Raman scattering is used to obtain information about the structure and properties of a molecule from vibrational transitions. It is therefore sensitive to the type and orientation of bonds within a structure.

2.2.2.1 : Theory

Although related to IR scattering, Raman scattering is a more complex process. IR absorption occurs when IR radiation interacts with a normal mode of vibration of a molecule, which causes a change in the permanent dipole moment. The interaction then adsorbs the IR photons, and elevates the vibrational energy of the bond to an excited vibrational state (figure 2.3). The particular energy of the photon absorbed is dependant on the vibrational energy of the bond in question, and so different bonds result in absorptions at different energies (and therefore frequencies) in the IR spectrum[9,10].

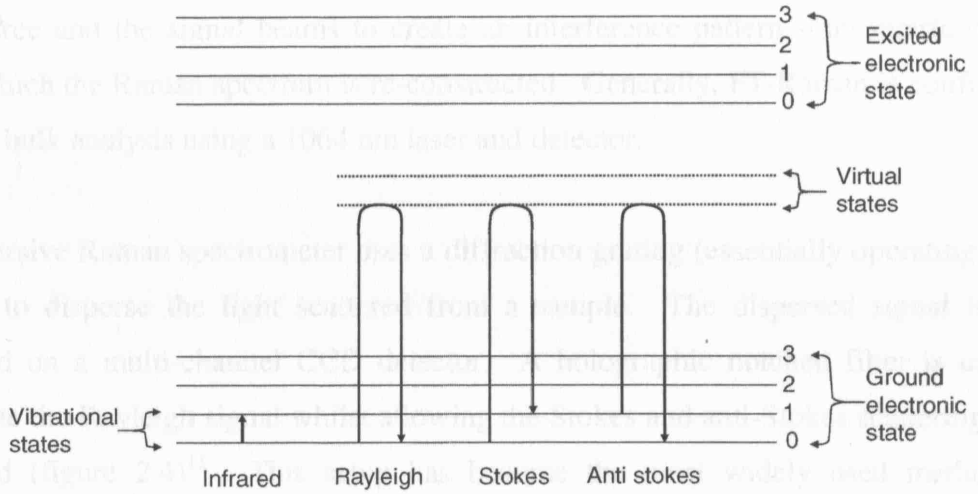

Figure 2.3: The electronic and vibrational term scheme for IR and Raman scattering. Modified from ref. 9.

For Raman scattering, the radiation causes a change in the polarizability of the molecule, resulting in an induced dipole moment, which absorbs photons and elevates an electron to a 'virtual' state, between the ground and excited electronic states. Upon relaxation of the molecule photons are released, resulting in both Rayleigh and Raman scattering. Rayleigh scattering occurs when the molecule relaxes back to its ground vibrational state and results in scattered radiation of an identical frequency to the incident radiation. However, if the molecule relaxes to an excited vibrational energy

state, the scattered radiation is shifted to a lower energy (and lower frequency) with regards to the incident radiation, and this is known as Stokes shift. It is also possible that the molecule was already in an excited vibrational state before excitation and that upon relaxation the molecule enters the ground state. This again results in a change in energy (but this time an increase), resulting in an anti-Stokes shift, with an increase in frequency. Raman scattering is a weak effect resulting from only 10^{-9} parts of the incident radiation (whilst Rayleigh scattering results from with 10^{-4} parts of the radiation).

2.2.2.2 : Experimental setups

Both Fourier-transform and dispersive experimental setups can be used for measuring the Raman spectrum of a sample.

The FT-Raman system uses an interferrometer to introduce a path difference between the source and the signal beams to create an interference pattern – an interferogram, from which the Raman spectrum is re-constructed. Generally, FT-Raman is confined to routine bulk analysis using a 1064 nm laser and detector.

A dispersive Raman spectrometer uses a diffraction grating (essentially operating like a prism) to disperse the light scattered from a sample. The dispersed signal is then detected on a multi-channel CCD detector. A holographic notched filter is used to attenuate the Rayleigh signal whilst allowing the Stokes and anti-Stokes scattering to be detected (figure 2.4)[11]. This setup has become the most widely used method for recording Raman spectra as it is versatile and different lasers and focal lengths can be used depending on the experimental needs. Generally, no modification to the sample environment is required and whole patterns can be recorded rapidly, making it particularly useful for *in situ* studies. The analysis of the Raman data recorded in this thesis is described in chapter 3.

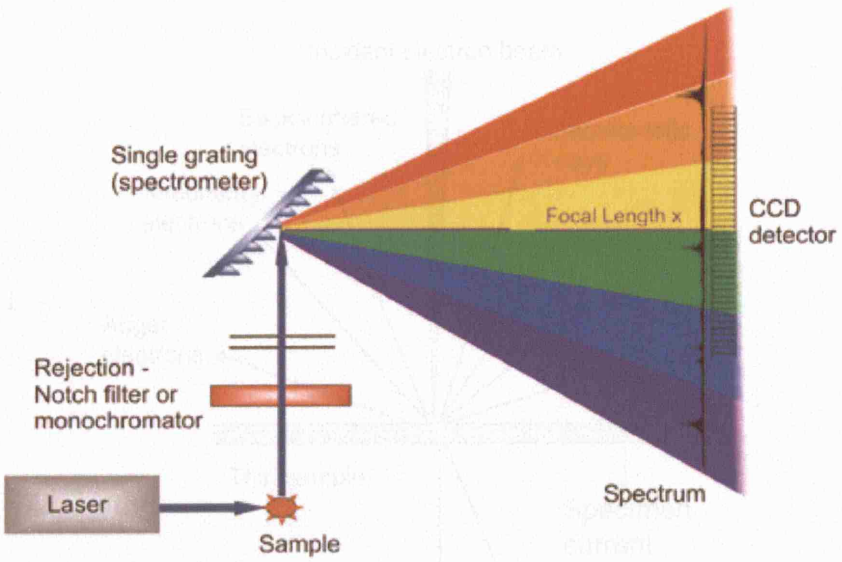

Figure 2.4: A schematical representation of a dispersive Raman detector. Reproduced from ref. 11.

2.2.3 : Electron probe techniques

The resolution of a microscope is partly related to the wavelength of radiation used. For example, ordinary white light has a maximum resolution of about 200 nm when the typical wavelength is 550 nm. Electron beam wavelengths, however, are about 10^5 times shorter allowing resolutions to far closer to the atomic level. Therefore, electron microscopy is widely utilised for obtaining topographical information at a molecular level.

2.2.3.1 : Theory

As with XRD, electrons are produced via an electron gun, containing a filament such as tungsten. The beam produced has energies ranging from a few hundred eV in SEM devices to 250 keV in TEM devices. Note that it is this difference in energies which is the main distinction between SEM and TEM devices, as the exact energy determines the wavelength of the emitted electrons; therefore the higher energy TEM devices have a smaller electron beam resulting in a higher resolution. The electron beam is then focused on to a sample producing a tear drop shaped 'interaction volume' with a depth of about 5 μm. On striking the surface the electrons can interact in either an elastic or inelastic manner to produce a number of scattering and emission events (figure. 2.5)[12].

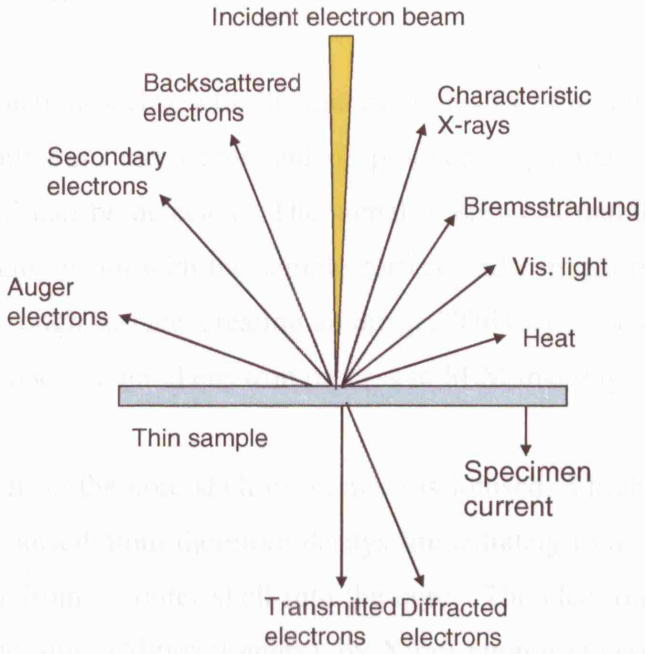

Figure 2.5: The scattering and emission events that can occur upon striking a sample with an electron beam. Reproduced from ref. 12.

For elastic interactions, the energy and momentum of the electrons are conserved but the trajectory of the beam changes. Elastic scattering results in broadening of the electron beam when penetrating a sample and this results in a fraction of the electrons being backscattered. The cross-section for elastic scattering is proportional to Z^2 of the target (where Z is the atomic number)[9]. Therefore, a sample composed of different atoms experiences scatter in different amounts, this creates contrast and so backscattered electrons can be used to produce an image of the sample. This technique is used in scanning electron microscopy (SEM).

If the sample is thin enough, then some electrons are elastically transmitted through the sample, although here the intensity of the transmitted electrons is inversely proportional to Z^2. Therefore, a contrasted image can again be built, dependant on the mean atomic number of the sample, which is referred to as the transmission electron microscopy technique (TEM).

With inelastic processes, the electron beam interacts with the orbital electrons of the atoms in the sample. There are a number of inelastic interactions, including phonon

excitation (heating), cathode luminescence (visible light fluorescence), and continuum radiation (Bremsstrahlung or breaking radiation).

If an inelastic interaction occurs with the electronic levels of an atom, ionisation of an electron to the continuum can occur and, if produced near the sample surface, this 'secondary electron' can be detected. The signal intensity is mainly a function of the angle of the impinging beam with the sample surface and contrast is created as a probe is scanned across a rough surface, creating an image. This secondary electron process is used along side the backscattered electron process in SEM imaging.

When the electron from the core shell of an atom is ionised, a highly energetic atomic state occurs. The ionised atom therefore decays immediately to a more stable state by an electron transfer from an outer shell into the core. The electron can drop from the outermost shell, releasing additional energy by X-ray photon emission, or from a shell closer to the core, releasing energy by the ejection of an electron from the outer shell (Auger electron release)[9]. The energies of any emitted X-ray photons are a function of the difference in binding energies between the two shells involved, and this is characteristic of the atom type. The photon energy can therefore be used to identify the types of atom present in the sample, as is the case with the electron probe X-ray micro analysis (EPXMA) technique, or energy dispersive X-ray analysis (EDX) as it is also referred to[9,13].

2.2.3.2 : Experimental setups

As described in the theory section, a number of processes occur simultaneously upon an electron beam striking a surface. Therefore, the techniques described above can often be combined in one device. For example, SEM and EDX are regularly combined and analytical electron microscopy setups can also combine SEM, TEM and diffraction[9].

In general, a standard experimental setup consists of an electron gun from which the generated electron beam is then focused through a number of magnetic lenses to produce a highly collimated, beam typically a few nanometres wide (figure 2.6). To allow scanning of the sample, a set of coils are also present, allowing the beam to 'sweep' over the sample. Finally, the objective lenses focus the beam onto the desired

part of the sample. Depending on the technique being utilised, various detectors are then placed above and below the sample[9,13].

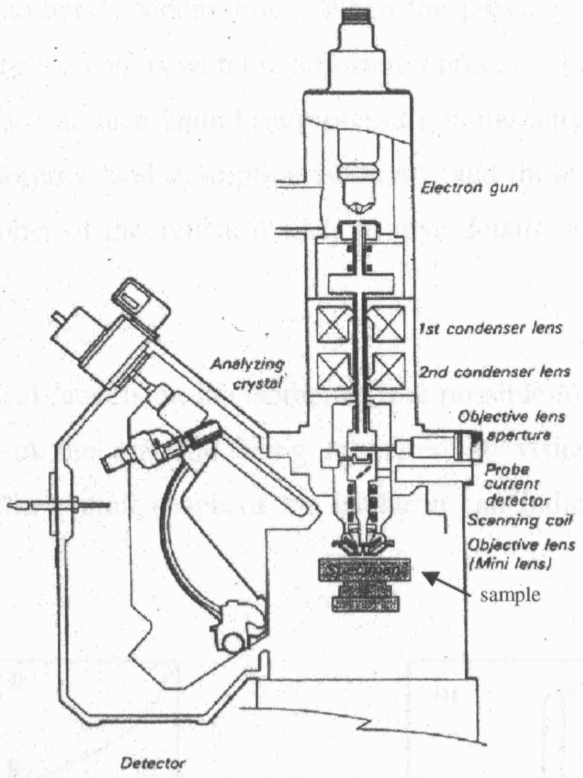

Figure 2.6: A schematic for a combined SEM/EDX setup. A TEM set up is also very similar although the detector is positioned below the sample. Reproduced from ref. 9.

2.2.4 : Adsorption / desorption techniques

Adsorption is the process of a gas or liquid (the adsorbate) accumulating on the surface of a solid, or more rarely a liquid (the adsorbent). The adsorbate then forms a molecular or atomic film which can then be desorbed by changing the conditions in the system (for example decreasing the pressure). As the uptake or release of the adsorbate in porous materials can be related to the size of the pores, the adsorption/desorption process is often used for analysis of porous materials.

2.2.4.1 : Theory

An adsorption/desorption experiment measures the equilibrated pressure (P) inside an evacuated sample holder at precisely controlled pressures, which is then compared with the saturation pressure (P_o) to give the relative pressure (P/P_o) at each stage of the experiment. As the pressure is increased, the adsorbate (e.g. nitrogen) is deposited on

the sample and the thickness of the film increases. Any micropores in the sample are filled first, then the free surface becomes completely covered, and finally the larger pores are filled by capillary condensation. When the pressure is then systematically reduced desorption occurs, and as with the adsorption process, the changing quantity of gas on the solid surface at each equilibrium pressure is measured. These two sets of data describe the adsorption and desorption isotherms and these can be compared and described with a number of theoretical models to give details on the properties of the material (see below)[14].

Before using theoretical models on the isotherms it is possible to estimate qualitatively some characteristics of the material being measured by visual examination of the isotherm shape[15]. The overall shape of the isotherm can indicate the type of pores (figure 2.7).

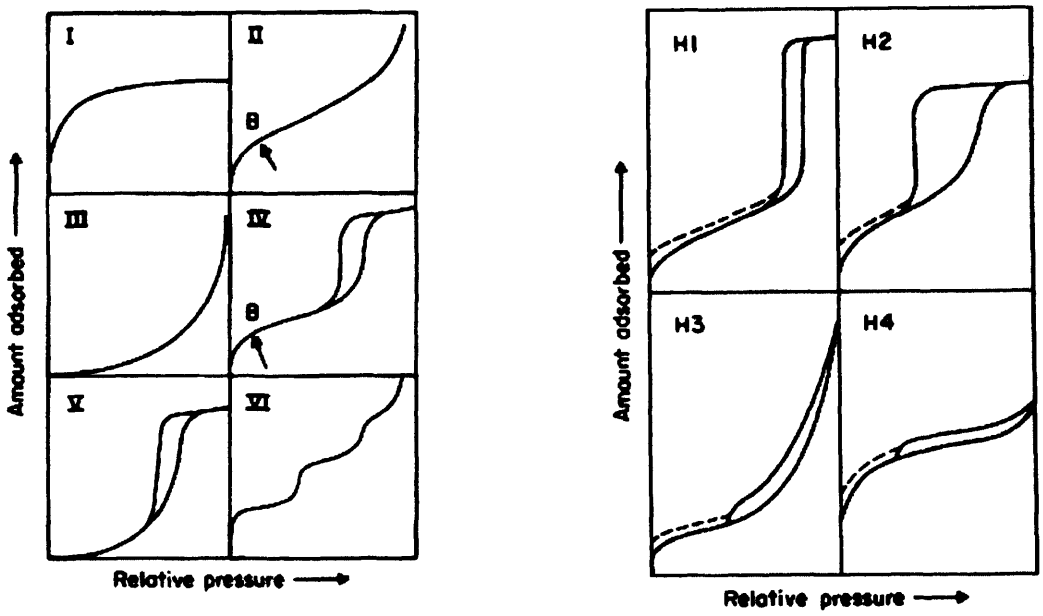

Figure 2.7: The types of isotherm shape (left) and hysteresis loops (right) for porous materials as described by IUPAC standards. Reproduced from ref. 15.

Type I is indicative of small pores systems such as zeolites, type II non-porous or macroporous systems, type III is uncommon but can occur in some systems, (e.g. nitrogen on polyethylene), type IV is indicative of mesoporous materials, type V is also uncommon and related to type III and type VI occurs with step-wise multilayer adsorption on a uniform non-porous surface[15]. The shape of any hysteresis loops

present in the isotherm have also been associated with specific pore structures, although the processes are not fully understood, therefore care must be taken with the interpretation. Currently the H1 isotherm is believed to be associated with uniform spheres in a regular array, whilst H2 can result from many porous adsorbents but is difficult to interpret (formally associated with 'ink Bottle shapes'). Both H3 and H4 are indicative of slit-shaped pores, but H4 with the type I isotherm is indicative of slit like pores in microporous materials[15].

The most common model isotherm used to describe gases adsorption on microporous solids is the Brunauer-Emmett-Teller (BET) isotherm[16]. It is an extension of the Langmuir isotherm[17] which describes the partitioning between gas phase and adsorbed species as a function of applied pressure (at a fixed temperature). However, whilst the Langmuir isotherm cannot describe multilayers on a surface, the BET isotherm extends the description to include this. It can be used to calculate the total surface (S_{total}) and specific surface area (S_{spec}) of a sample (equation 2.4)[18].

$$S_{total} = \frac{(v_m N s)}{M} \qquad S_{spec} = \frac{S_{total}}{a} \qquad \textbf{(2.4)}$$

v_m = monolayer gas quantity
N = Avogadro's No.
s = adsorption cross section
M = mol. weight of adsorbate
a = weight of sample

For calculating the mesoporous distribution in a sample the Barret-Joyner-Halenda (BJH) calculation can be used on either the adsorption and/or desorption branch of the measured isotherms starting from filled pores. The pore size distribution (PSD) then gives the volume of pores as a function of their diameter[14].

2.2.4.2 : Experimental setup

A schematic of a typical static volumetric type gas adsorption/desorption rig is shown in figure 2.8. Effectively, precisely known amounts of the adsorbate gas are introduced into the sample holder (measured using pressure gauge P_1), which is kept at 77 K (under liquid nitrogen). As the gas adsorbs on the surface of the sample, the pressure slowly decreases until equilibrium is reached in the manifold. The pressure in the sample container is then measured (P_2) to give the equilibrium pressure. The pressure in the

container is then increased until saturation occurs, giving the saturation pressure (P_o) and allowing the relative pressure for each point to be calculated.

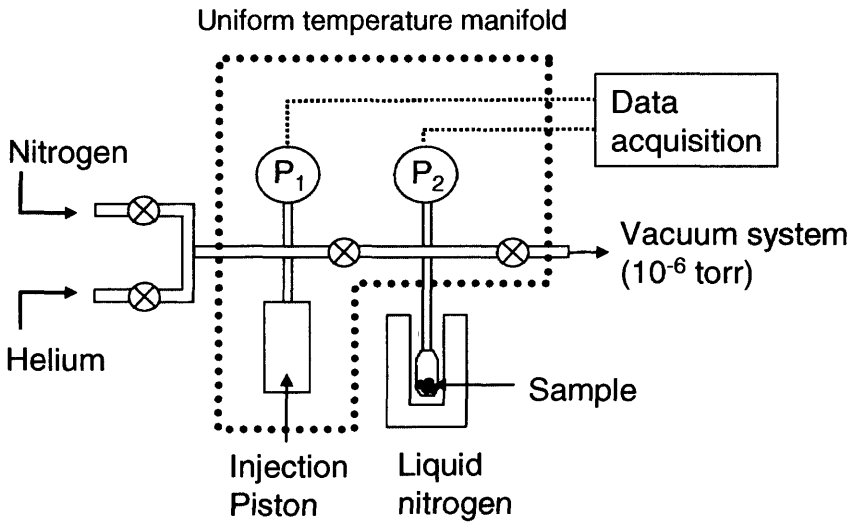

Figure 2.8: A standard volumetric gas adsorption/desorption experimental rig.

2.2.5 : Nuclear magnetic resonance

Discovered in the 1940s, during work on the development of RADAR and the production, detection and absorption of radiofrequency (RF) energy, nuclear magnetic resonance (NMR) has become an important analytical tool for identifying the environment of particular atoms. It allows detail about molecular structure to be ascertained and, for porous materials, solid state NMR (see below) is used to examine the coordination of atoms such as aluminium within the materials framework.

2.2.5.1 : Theory

A basic NMR experiment involves using the resonant absorption of radio frequency radiation of atomic nuclei exposed to a magnetic field. To be sensitive to NMR an atoms nucleus must posses a magnetic moment, requiring a non-zero spin angular momentum. Both electrons and nucleons (protons and neutrons) posses spin of either +1/2 or -1/2 (or up and down) and when these pair up according to the Pauli principle the spin is zero. However, if there are an odd number of electrons or nucleons then a net spin angular momentum is created, which is associated with a magnetic moment. NMR exploits the unpaired spins of the nucleons, whilst the electron spin resonance

technique exploits the unpaired spin of electrons. Molecules containing a net nucleon spin include ^{1}H, ^{13}C ^{29}Si and ^{27}Al[19,20].

When considering nuclei such as ^{1}H, the spin of ½ can either be 'up' or 'down'. Generally, the energy of these states is degenerate and so there is an equal population in each state. However, when place in a magnetic field the energy of the two states alters (i.e. the nuclear Zeeman effect) and those aligned with the field (up spin) become lower in energy and those aligned against (down spin) higher in energy, resulting in a slight population bias towards the more stable 'up' state.

If RF radiation is applied this system, with the same energy as the difference between these two states then resonance occurs and the populations are equalised. If all the nuclei in a system are in the same chemical environment then the energy difference between all states would be identical. However, if nuclei are in different environments (i.e. bonded to different atoms), then each can experience different shielding/deshielding from the magnetic fields of the surrounding atoms, which alters the effective field at the nucleus. This changes the energy difference between the states and so the frequency of RF waves required to achieve resonance becomes different. By measuring these shifts in resonance frequency the local environment of the nuclei being investigated can be identified. Note that when the RF is removed from the system the 'excited' nuclei relax back to their ground state[19,20].

2.2.5.2 : Experimental setup

All modern NMR devices operating above 100MHz require helium cooled superconducting solenoids to provide the magnetic field (figure 2.9). The magnets are specifically designed to minimise variations in the magnetic field during an experiment. The probe then contains the RF transmitter and receiver coils as well as any spinner devices to remove inhomogeneities within the sample. The entire system is then surrounded by a liquid nitrogen cooling system to reduce the helium loss from the device[20]. For the solid state NMR often used in materials science, poor resolution and massive line broadening tends to occur. Two of the main causes of this are anisotropy and dipole-dipole interactions that are not averaged out in the solid static sample. A solution to this is to use magic angle spin NMR (MAS-NMR) which takes note of the fact that both these broadening effects are dependant on a $1-3\cos^2\theta$ relationship. At the

'magic angle' of 54.74° the equation $1\text{-}3\cos^2\theta = 0$, therefore averaging all dipole-dipole and anisotropic interactions to zero[19].

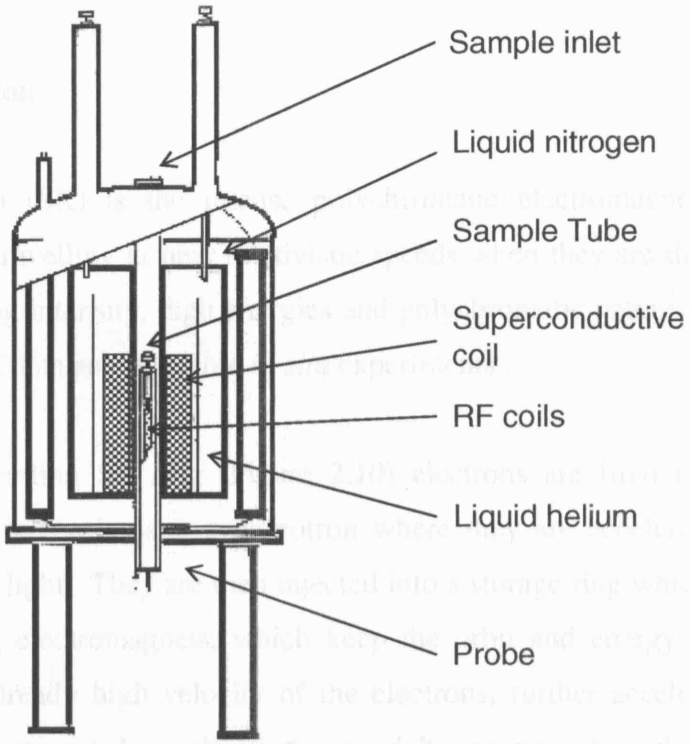

Figure 2.9: Schematic of a typical superconducting cryo-magnetic NMR machine. Reproduced from ref. 20.

2.3 : Synchrotron based techniques

A number of synchrotron based techniques have been used in this thesis. Here the basic operation of a synchrotron is explained and then the techniques utilising the resulting synchrotron radiation are discussed.

2.3.1 : The synchrotron

Synchrotron radiation (SR) is the intense polychromatic electromagnetic radiation emitted by electrons travelling at near relativistic speeds when they are deflected from their course. Its strong intensity, high energies and polychromatic nature make it ideal for quick collection of data and therefore *in situ* experiments.

In a typical 2nd generation SR ring (Figure 2.10) electrons are fired from a linear accelerator (LINAC) into a booster synchrotron where they are accelerated to about 99.999% the speed of light. They are then injected into a storage ring which consists of a number of bending electromagnets, which keep the orbit and energy of the beam stable. Due to the already high velocity of the electrons, further acceleration is not possible and so the attempted acceleration caused by passing through the bending magnets results in emission of electromagnetic radiation. As energy is lost by emitting this SR, a radio frequency klystron is constantly used to replenish the energy of the electrons in the storage ring.

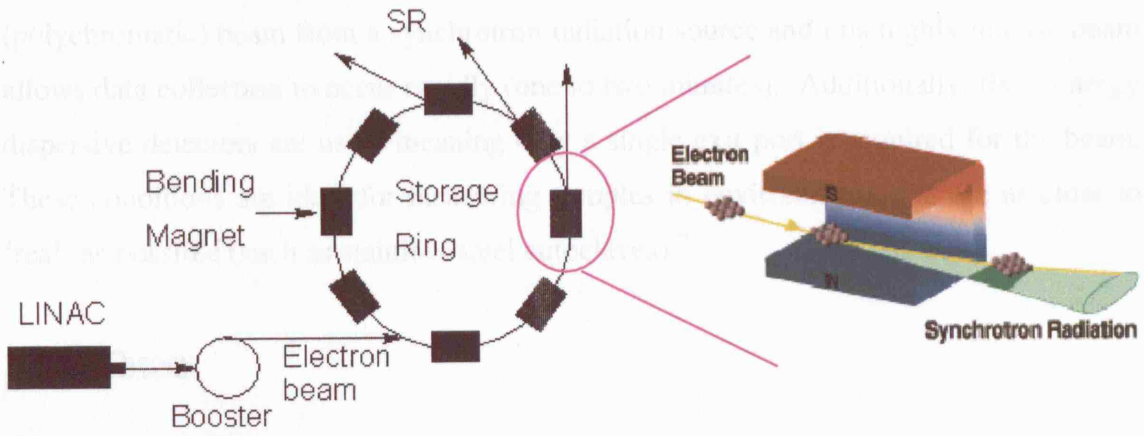

Figure 2.10: A typical 2nd generation synchrotron ring consisting of a LINAC, booster ring and a storage ring with a series of bending magnets (left) and the generation of synchrotron radiation as electrons are bent around a magnet (right).

On its own the storage ring gives a spectrum which rapidly drops off in intensity at higher energies. However, insertion devices such as wigglers and undulators can be placed in the beam allowing increased intensities and extension of the energy range over all or particular parts of the spectrum (figure 2.11)[21]. Wigglers are used to shift the entire spectrum to higher energies, whilst undulators produce very intense radiation at specific energies. Further details of the generation of synchrotron radiation are given by Duke[22].

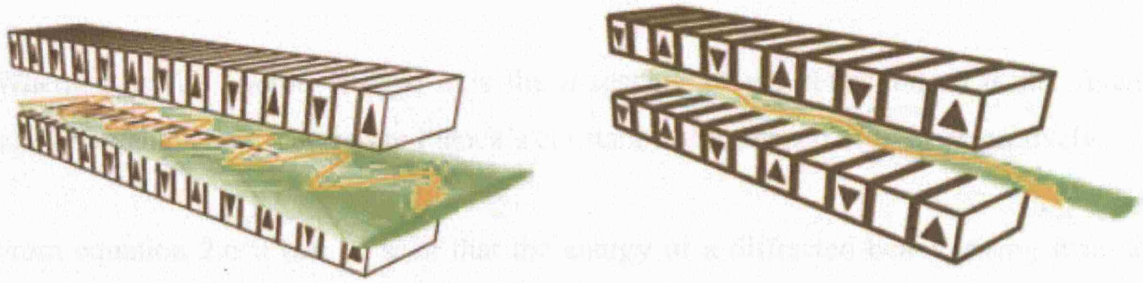

Figure 2.11: Basic schematics of a multipole wiggler (left) and an undulator (right). Note that the undulator produces a narrow coherent beam of synchrotron radiation. Reproduced from ref. 21.

2.3.2 Energy dispersive X-ray diffraction

As described above, laboratory based XRD uses a monochromatic light source and data are collected over a range of angles (2Θ). However, whilst high quality scans can be achieved using this method, the data collection time is too slow for most *in situ* zeolite growth. Energy dispersive X-ray diffraction (EDXRD) uses a full 'white' (polychromatic) beam from a synchrotron radiation source and this highly intense beam allows data collection to occur rapidly (one to two minutes). Additionally, fixed energy dispersive detectors are used, meaning only a single exit port is required for the beam. These conditions are ideal for measuring samples in environments that are as close to 'real' as possible (such as stainless steel autoclaves)[23].

2.3.2.1 Theory

Using a fixed energy dispersive detector and white synchrotron light, an EDXRD setup can collect the whole X-ray diffraction pattern within a limited d-space range. Of the radiation striking the sample, only radiation with the correct energy to satisfy the Bragg

condition will be reflected. Energy can be related directly to wavelength by comparing the Bragg equation (equation 2.1), with the Planck-Einstein equation (equation 2.5).

$$E = \frac{hc}{\lambda} \tag{2.5}$$

Combining equation 2.1 and equation 2.5 then gives equation 2.6:

$$E = \frac{hc}{2d \sin\theta} \tag{2.6}$$

Where E is the photon energy, d is the d-spacing of the reflection, θ is the fixed scattering angle and h and c are Planck's constant and the speed of light respectively.

From equation 2.6 it can be seen that the energy of a diffracted beam arising from a crystallographic d-spacing is inversely proportional to $\sin\theta$. Therefore, as long as the fixed angle of the detector is known, the energy can be directly related to d.

2.3.2.2 Experimental setup

In situ experiments on autoclave systems generally require high energy X-rays. For example, station 16.4 at the synchrotron radiation source (SRS) at the Daresbury laboratory uses a 6 tesla wiggler to boost the energy. The high flux polychromatic light is then passed through a collimator and strikes the sample environment with a foot print of about 0.5 mm, which is ideal for the study of crystallisation within a sample. The scattered beam then passes through post sample collimators with 100 μm gaps and onto a nitrogen cooled germanium solid state energy discriminating detector (Figure 2.12).

The energy distribution on station 16.4 has a useful range of 20 – 70 keV and a peak intensity of 40 – 50 KeV[24,25,*]. Note that to cover the desired range of d-spacing for AlPO samples a triple detector arrangement[26] was used for the measurements in this thesis, as detailed in chapter 4. The analysis of data recorded using this EDXRD setup is also discussed in chapter 4.

* Note that this information was partially derived from the 16.4 website at www.srs.dl.ac.uk/xrd/16.4/ which is no longer available.

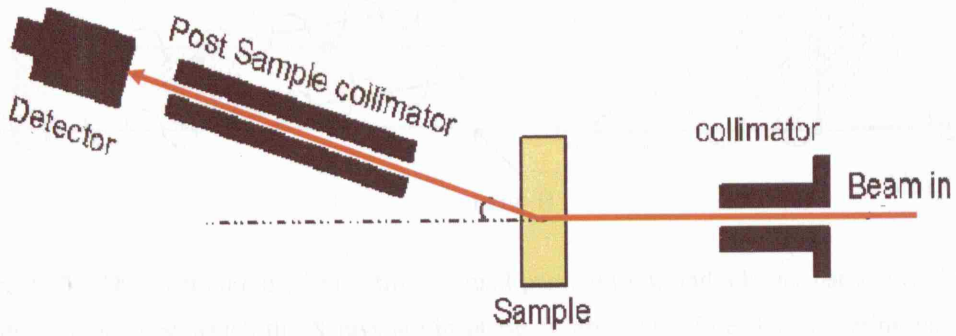

Figure 2.12: A typical synchrotron EDXRD experimental setup using a fixed, energy dispersive detector

2.3.3 : Small angle X-ray scattering

From Bragg's law (equation 2.1) it can be seen that, for a fixed wavelength, as the scattering angle θ decreases the distance between the planes on which the scattering occurs (d-spacing) must increase. For crystalline samples, regular closely spaced planes result in scattering at wide angles ($2\theta \sim 1^{o}$–180^{o}). However, in very small non-crystalline particles, these planes either have no long range order or are not present. Despite this, non-periodic scattering from electrons in the particle still occurs, controlled by the shape and size of the particles with a size limit generally of 10 – 1000 Å. Therefore, by recording the X-ray scattering at very small angles information on the size and (in some circumstances) shape of non-crystalline colloidal particles can be obtained.

2.3.3.1 : Theory

As X-rays are primarily scattered by electrons, scattering is observed when electron inhomogeneities of colloidal size exists in a sample. At low angles only coherent scattering needs to be considered, as incoherent (Compton) scattering is negligible.

As mentioned above, the scattering distance is inversely proportional to the angle. This is due to the fact that as the distance between the two scatterers increases, the point at which the scattered X-rays are in phase (and can therefore be detected) moves towards lower angles (figure 2.13). Therefore, in systems with no Bragg planes the angle at which scattering occurs can yield information regarding the size of the particles[27].

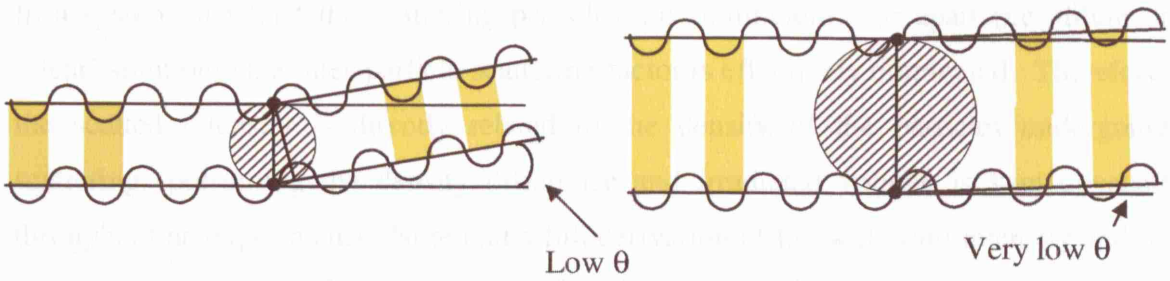

Figure 2.13: The scattering of X-rays from a small particle (left) and a larger particle (right). It can be seen that the angle at which the X-rays are in phase is larger the closer the scattering pair are to each other.

In a SAXS experiment the intensity (see below) is measured as a function of the scattering vector (Q), which is a product of the difference between the vector of incoming radiation and the resulting vector of the X-rays scattered by the electrons. The magnitude of the difference is equal to $2\sin\theta$ and therefore the scattering vector is related to the angle (θ) and the wavelength (λ) (equation 2.7).

$$Q = (4\pi/\lambda)\sin\theta \tag{2.7}$$

By substituting the Bragg equation (equation 2.1) into this equation it is possible to directly relate the scattering vector with the distance between the two scatterers (d) (equation 2.8), and so the scattering from the surface of a colloid will indicate the diameter of the colloid in question.

$$Q = 2\pi/d \tag{2.8}$$

The measured intensity at a point ($I(Q)$) is a combination of the contributions from particle scattering or the 'form factor' ($P(Q)$), inter-particle scattering or 'structure factor' ($S(Q)$) as well as the density of particles (n), the difference in density between the particles and solvent ($\Delta\rho$) and the irradiated volume (V) (equation 2.9).

$$I(Q) = n\Delta\rho^2 V^2 P(Q)S(Q) \tag{2.9}$$

In a system in which the scattering particles are significantly far apart (i.e. dilute or 'clear' solutions) the inter-particle scattering factor is effectively eliminated. Therefore, the scatted intensity is directly related to the density of the particles undergoing scattering (presuming the density difference and irradiated volume is kept constant throughout an experiment). Note that a full derivation of the scattering intensity and its relation to the electron density and wave functions of a particle can be found in the texts by Glatter *et al*[27], Guinier *et al*[28] and Feigin *et al*[29].

From a basic scattering pattern at low angle, there are a large number of techniques that can be used to extract information on particle size, shape and distribution in a system. The validity of each technique depends on various factors, including the dispesivity of the system, the Q-range observed and the size of the particles being studied. Some methods analyse particular parts of the pattern, such as the low-Q 'Guinier' region, which can give details on particle size and shape (through the radius of gyration) or the high-Q 'Porod' region, which can give detail on the 'roughness' of the particles surface and fractal aggregation. Fourier transforms have also been used to give quantities such as the pair distance distribution function (PDDF) or correlation function and indicate the size and distribution of particles. Finally, mathematical modelling has also been used to compare the shape of the scattering curve to ideal geometries. For polydispersed systems undergoing constant change, (such as zeolite crystallisation), many of the methods mentioned are either not valid or are difficult to interpret.

One measurement of particular use is that of the 'invariant' of the system (Q_{inv}). The word invariant is used to describe the fact that shifts or distortions in the structure of the particles will alter the diffraction pattern, but as long as the total internal contrast (i.e. the total internal scattering surface and the electron density difference between these surfaces) remains the same the invariant will remain unchanged (equation 2.10)[27].

$$Q_{inv} = \int_0^\infty Q^2 I(Q) \mathrm{d}Q \qquad \textbf{(2.10)}$$

Therefore, an increase in the invariant is caused by additional scatterers appearing within the region of Q-space being probed (for example growth of very small particles from below the low Q limit). Conversely, a decrease can then be ascribed to the

removal of these scatterers by dissolution of small particles above the high Q limit or growth of very large particles beyond the low Q limit.

2.3.3.2 : Experimental setup

Although SAXS can be performed in the laboratory, *in situ* measurements require the high flux of synchrotron radiation to provide rapid data accumulation. In modern setups the SAXS camera is combined with a WAXS camera allowing the measurement of particle size and shape to be compared with the onset of long-range crystalline Bragg planes (figure 2.14).

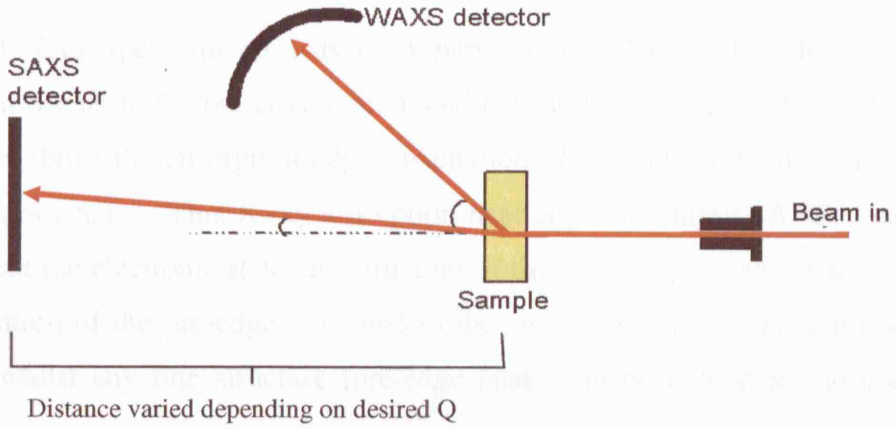

Figure 2.14: A schematic of a standard combined SAXS/WAXS experimental setup.

The WAXS detector is generally angular dispersive and, in the example of station 6.2 at the SRS, can cover an angle of 60° 2θ and record high quality diffraction data within seconds[30,31]. The small angle detector can be positioned at various distances from the sample in order to achieve the desired Q range. The analysis of the data recorded using this technique is described in chapter 5.

2.3.4 : X-ray absorption spectroscopy

X-ray absorption spectroscopy (XAS) requires no long range order and can be 'tuned' to target a specific element. It is therefore an ideal technique for studying samples containing a small number of atoms exchanged into the bulk. It is also a bulk technique and so all target atoms are sampled equally and the structural information is averaged.

2.3.4.1 : Theory

Lambert's law (equation 2.11) describes the attenuation of X-ray photons as they pass through a sample. It can be seen that if the materials thickness (x) remains constant, then the difference between the incident radiation (I_o) and the transmitted radiation (I) is dependant only on the absorption coefficient of the sample (μ)[32]. In a typical XAS experiment the incident radiation is slowly increased and the transmitted radiation measured, changes in the ratio $\ln(I_o/I)$ are then plotted.

$$I = I_o e^{-\mu x} \tag{2.11}$$

A typical XAS spectrum consists of 3 parts (figure 2.15). Initially, simple mass absorption occurs in the pre-edge region, and then in the 2nd region (from 50 eV below to 100 eV above the absorption edge), excitation of core electrons to bound or quasi-bound states occurs. This X-ray absorption near edge structure (XANES) can contain detail about the electronic state and structure of the adsorbing atoms. For example, the exact position of the pre-edge is related to the atoms oxidation state and coordination number, whilst any fine structure (pre-edge peak) can be related to the coordination geometry.

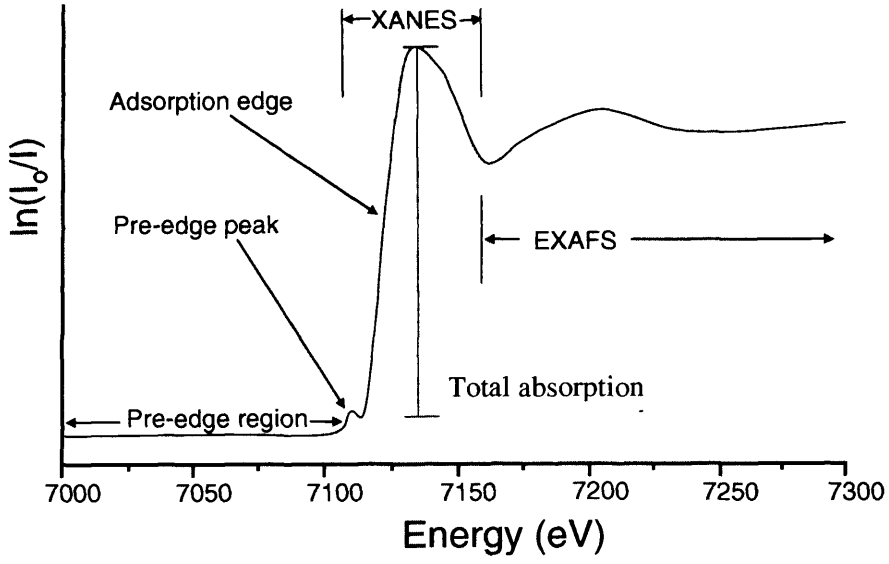

Figure 2.15: A typical K-edge XAS spectrum (iron edge) highlighting the three main regions: the pre-edge, XANES and EXAFS. Also highlighted are the pre-edge peak and the absorption edge (which is taken as approximately half the total absorption).

The final part of the spectrum extends from 100 eV above the absorption edge and contains the extended X-ray absorption fine structure (EXAFS). To understand the processes occurring in this region, the change in electronic structure at the absorption edge must first be understood.

From figure 2.15 it can be seen that as the energy of the incident radiation is increased, there is a point at which the absorption suddenly increases. The absorption edge is considered to be at approximately 50% of the total absorption of the sample, and at this point, the energy of the incoming radiation is identical to the energy required to eject an electron from the core of the target atom. Therefore, the electron is promoted to an excited state (or continuum) and the radiation is absorbed, rather than transmitted, resulting in a several fold increase in the absorption coefficient in equation 2.11. The type of absorption edge depends on which orbital the electron was excited from (K-edge for 1s orbitals, L_I for 2s, L_{II} for $2p_{1/2}$ etc).

When an electron is ejected from the target atom it propagates out from the atom as a wave, and as it moves out from the core it interacts with the neighbouring atoms, producing backscattered waves (figure 2.16).

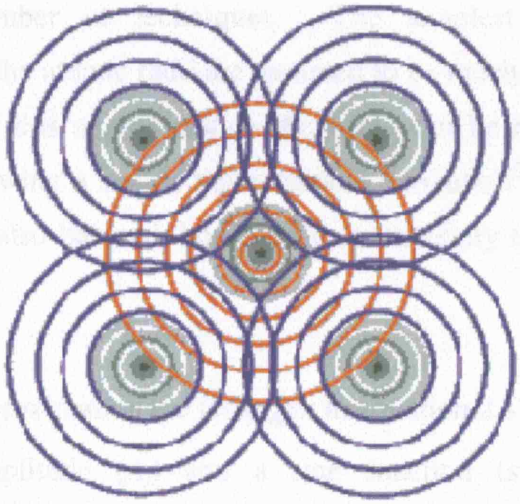

Figure 2.16: The interference between the outgoing (red) and backscattered (blue) electron waves with the excited atom in the centre surrounded by four neighbours.

The final state of the wave function then consists of a combination of the outgoing and backscattered waves and this will either be enhanced or dampened, depending on if the waves are in phase (constructive interference) or out of phase (destructive interference).

It is this interference, as a function of the distance between the absorber and scatterer, which gives rise to the sinusoidal oscillations seen in the EXAFS region of the spectrum. As the amount of interference is dependant on the type and position of scatterer, information regarding bond length, coordination number and disorder can be obtained by measuring these oscillations. Note that as the wave propagates out it can interfere not only with the 1st 'shell' of neighbouring atoms, but also additional shells further from the absorber, the EXAFS can therefore contain information on a number of shells of neighbours.

The oscillations are a modulation in the absorption coefficient of the system and so the total absorption (μ_{total}) can be defined as in equation 2.12, with μ_o representing the atomic background and χex representing the oscillatory part, describing the sum of all the interference patterns.

$$\mu_{total} = \mu_o [1 + \chi ex] \qquad \textbf{(2.12)}$$

From this point, it should be noted that further derivation of the EXAFS theory has been performed using a number of techniques. The simplest is the plane wave approximation, in which the atomic radii are assumed to be much smaller than the inter-atomic distances. Using this approximation the wave can be represented as a plane rather than a sphere, allowing a simple mathematical derivation[33]. The more complex curved wave theory can also be used, however; its complexity makes computation far more time consuming.

Using the plane wave approximation the term χex in equation 2.12 can be divided into a combination of the amplitude (A_j) and a sine function ($\sin\Phi_j$), describing the interference for the coordination shell of each atom (j) (equation 2.13).

$$\chi(k) = \sum_{j=1}^{Shells} A_j(k) \sin \Phi_j(k) \qquad \textbf{(2.13)}$$

These can then be broken down further, with the sine function being described by an inter-atomic distance (or phase delay) ($2kR_j$) and a phase shift ($\Phi_j(k)$) (equation 2.14). The phase delay can be thought of as the time taken for an electron to travel to the neighbouring atom and return, and the phase shift is caused by the kinetic energy of the electron changing as it speeds up and then slows again approaching both the neighbouring and absorber atom's nucleus.

$$\sin \Phi(k) = \sin\left[2kR_j - \Phi_j(k)\right] \qquad \textbf{(2.14)}$$

The amplitude term (from equation 2.13) then contains contributions from a number of factors, the most important for EXAFS analysis being the coordination number (N) of the atoms at a distance (R) and the disorder (Debye-Waller factor) (σ^2), which causes fluctuations in R due to thermal motion or structural disorder (equation 2.15).

$$A_j(k) = \frac{N_j}{kR_j^2} S_o^2 F_j(k) \mathrm{e}^{-2k^2\sigma_j^2} \mathrm{e}^{-2R_j/\lambda k} \qquad \textbf{(2.15)}$$

Other terms include the backscattering amplitude ($F_j(k)$), which is element specific and an amplitude reduction factor (S_o^2), representing many body effects such as central atom shake-up and shake-off (multiple excitation of 'other' passive electrons within the scatterer). The exponential term $2R_j/\lambda_j(k)$ represents the mean free path of the electron wave and is restricted by its lifetime and energy losses to competing EXAFS processes[32-34].

2.3.4.2 : Experimental setup

XAS can be recorded using a number of different experimental modes including dispersive, reflection, fluorescence and transmission. Transmission and fluorescence modes are the most widely utilised, and transmission data has been used in this thesis in all but one data set. A schematic of both types of setup is given in figure 2.17. In both cases a double crystal monochromater is used to tune the incoming radiation to the

desired energy. By moving slowly these can then slowly shift in energy to, and above the absorption edge being examined. By cutting the monochromator along different crystallographic planes (e.g. 111, 220 or 311) different regions of the electromagnetic spectrum can be accessed. The sample then passes through a pre-sample ion chamber, consisting of two parallel plates and an inert gas, the current between the plates is measured to give the incident beam intensity.

In a transmission experiment, the sample is held perpendicular to the beam and the radiation passes through the sample and the transmitted intensity is recorded. If the atom in the sample is of a low concentration then fluorescence detectors can be used to improve signal quality, since background absorption is reduced. In this mode the sample is placed at 45° to the beam and an array of fluorescence detectors record the fluoresced radiation.

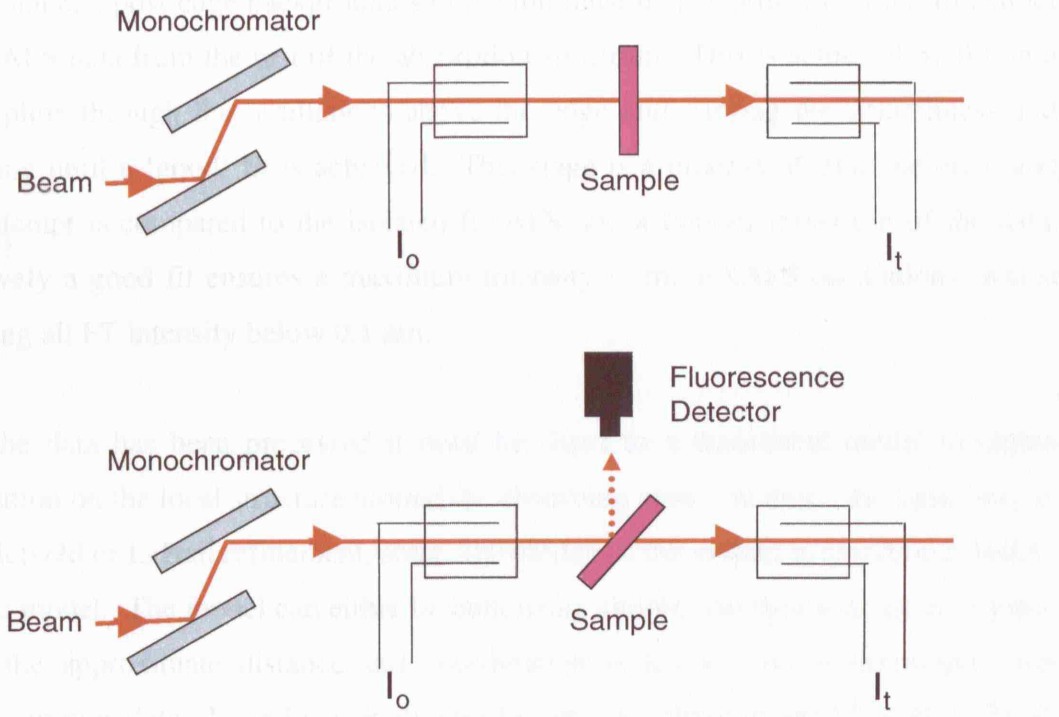

Figure 2.17: Typical EXAFS setups for transmission mode (top) and fluorescence mode (bottom). I_o and I_t represent the incident and transmission ion chambers respectively.

2.3.4.3 : Data analysis

In order to obtain information on the local environment of the adsorbing species raw EXAFS data requires a significant amount of possessing. In this work all analysis was carried out using the analysis suite of software available at Daresbury labs, including

EXCALIB for converting the RAW data files, EXSPLINE for background subtractions and EXCURV98 for analysis and fitting of the atomic shells.

Initially, any multiple data sets are summed to improve the sample to noise ratio and any 'glitches' in the data (caused by imperfections in the monochromator) are removed. Next, the pre-edge slope due to mass absorption and multiple scattering is removed by fitting a polynomial to the slope and extrapolating past the absorption edge. The spectra are then normalised by dividing by the edge step 50 eV above the edge, allowing comparisons of the XANES region. The edge position is then identified by either identifying the first inflection point in the total absorption or, if this is unidentifiable, by arbitrarily assigning it to be at 50% the height of the normalised edge (this can then be refined during fitting).

At this stage, a post-edge background subtraction must be performed in order to extract the EXAFS data from the rest of the absorption spectrum. This is achieved by fitting a cubic spline through the oscillations above the edge and varying the smoothness and weighting until a 'good' fit is achieved. This stage is a process of trial and error and each attempt is compared to the isolated EXAFS and a Fourier transform of the data. Effectively a good fit ensures a maximum intensity in the EXAFS oscillations, whilst removing all FT intensity below 0.1 nm.

Once the data has been processed it must be fitted to a theoretical model to obtain information on the local structure around the absorbing atom. In much the same way as with Rietveld or LeBail refinement, some knowledge of the system is required to build a realistic model. The model can either be built using simple absorber and scatterer pairs, where the approximate distance and coordination is known, or by derivation from crystallographic data. Initially, a single set of nearest neighbours (the 1st shell) is fitted, although a better fit and more detailed structural data can be found by considering additional shells (and the possibility of multiple scattering)[35]. Note that in this thesis only 1st shell fitting has been performed. Each shell of the inputted model is then refined using a least squares fitting procedure and factors such as the bond length (R), number of backscattered atoms (or coordination number) (N) and disorder (or Debye-Waller factor) (σ^2) can be refined. The R-factor gives an indication of the goodness of fit and values of about 20% can be considered good for a first shell fit[35].

2.4 : Computational techniques

2.4.1 : Basics

In this thesis, computational as well as experimental techniques have been used to identify trends and changes in AlPO systems. Two types have been used; one is a quantum mechanical (QM) approach, the other a molecular mechanical (MM) approach. In both cases the aim is to compute the potential energy surface of the system and to identify the lowest energy configurations.

To calculate the potential energy surface of a QM model it is necessary to attempt to solve the Schrödinger equation (equation 2.16):

$$\hat{H}\Psi=E\Psi \qquad \textbf{(2.16)}$$

Here Ψ is the wavefunction, which is dependant on the position and spin of all particles, E is the magnitude of the energy of the stationary state and $\hat{H}$ is the Hamiltonian operator. The total energy can be divided into contributions from the kinetic energy of the electrons (T_{elec}) and nuclei (T_{nucl}) and the potential energy from the electrostatic interactions between the nuclei and electrons (V_{ne}), the electrons themselves (V_{ee}) and an electron-electron exchange and correlation (V_{ex}) (equation 2.17).

$$\hat{H} = T_{elec} + T_{nucl} + V_{ne} + V_{ee} + V_{ex} \qquad \textbf{(2.17)}$$

Unfortunately, whilst the analytical solution to the Schrödinger equation can be found for one electron systems, for many electron systems (atomic and molecular) approximations are required. However, assuming the Born-Oppenheimer approximation (see below) modern QM methods are able to solve the equation to a sufficient level of approximation, although they are still relatively expensive computationally.

An alternative to QM calculation is molecular mechanics (MM) where the molecular interactions are based on empirical models of experimental data (force fields), which

have been previously determined for particular systems, making the method far cheaper computationally. However, as the calculations are based on these predetermined force fields, the accuracy of the results is determined by the quality of these force fields, and the method can only be used when adequate descriptions of the bonding in the model is available[36,37].

The basics of the two techniques are discussed below, with full in-depth explanations available in the sources listed within this text.

2.4.2 : Quantum mechanics

Computational QM methods work by attempting to solve the Schrödinger equation for nuclei and electrons to some level of approximation. As mentioned above this equation can only be solved exactly for one electron systems, therefore for molecules approximations are made. These often include the neglect of relativistic effects and the reduction of the many electron problem to effectively a one electron problem (i.e. the determination of the energy and movement of each electron in the potential field from the nuclei and sum of all other electrons).

2.4.2.1 : The Born-Oppenheimer approximation

The most important approximation is the Born-Oppenheimer approximation, which states, that because electrons move very rapidly compared to nuclei, the Schrödinger equation can be solved by assuming that the nuclei are stationary. The 'one-electron Hamiltonian in the Born-Oppenheimer' approximation effectively reduces the calculation of the energy of the Hamiltonian to just the kinetic and potential energy terms of the electrons alone[36] (i.e. T_{nuc} in equation 2.17 is effectively zero).

2.4.2.2 : Hartree-Fock and post Hartree-Fock Methods

The calculation of the electrostatic interactions and the exchange correlation effectively determine the type and quality of the *ab initio* QM method. Many methods are based on the Hartree-Fock (HF) approach in which a many (N) body wavefunction of the system can be approximated by a single Slater determinant[38]. This however means that the electron-electron correlation is not calculated explicitly. A number of post HF methods

have been developed to calculate the correlation, mainly by initially using the HF method and then adding the correlation, again however, this increase in complexity increases the computational cost of the measurements.

2.4.2.3 : Density functional theory

Another approach is the use of density functional theory (DFT), which allows calculations that include correlation effects, but is far less expensive compared to post-HF methods[39]. DFT achieves this by replacing the many-body electronic wavefunction with electron density. Therefore, rather than $3N$ variables (3 spatial parameters for each of the N electrons), only 3 variables are required to describe the electrons. A crucial feature of DFT methods is the use of the exchange and correlation functionals, which can be based on a local density approximation (LDA), the generalised gradient approximation (GGA) or another more complex method. There are currently many functionals used depending on the calculation, for example Perdew-Burke-Enzerhof (PBE) functional is generally used in solid-state systems, whilst the Becke, Lee, Yang and Parr functional (BLYP) is often used in molecular calculations[40]. In this thesis the DMOL^3 software[41,42], integrated into the Materials Studio suite of programs[43] has been used to perform DFT calculations.

2.4.2.4 : Modelling solvation

In order to model solvation, the localised interactions of water with the molecule being investigated needs to be modelled. However, modelling these interactions is computationally challenging. There are a number of methods for treating solvation[44], including surrounding the molecule with a large number of solvent molecules and performing a Monte-Carlo or molecular mechanics calculation. However, if the system is to be treated quantum mechanically this is prohibitively expensive.

Another method is to use a conductor-like screening description of the solute molecules (COSMO)[45,46]. This approach relies on the calculation of the dielectric screening charges and energies on a van der Waals-like molecular surface using the approximation of a conductor. This model has been incorporated into the DMOL^3 software and can be performed in combination with DFT calculations.

2.4.3 : Molecular mechanics

Unlike QM calculations, molecular mechanic (or interatomic potential) methods calculate the potential energy of a system using an energy expression based on the various interactions in the molecule (e.g. bond angles). The terms used in this energy expression may be derived empirically, or calculated from QM, for a series of typical molecules containing common features (e.g. functional groups). The method is classical with each atom often treated as a single particle with an assigned radius (typically van der Waals), polarisability and charge. Thus it can be considered as a 'ball and spring' model of a molecule[36,47].

The functional form of the potential energy is known as the force field, which divides the potential energy into individual energy terms (equation 2.18)

$$E_{eff} = E_{str} + E_{bend} + E_{tors} + E_{vdw} + E_{el} + E_{cross} \qquad \textbf{(2.18)}$$

Here the effective energy (E_{eff}) is a function of the energy to stretch a bond (E_{str}), bend around a central atom (E_{bend}), the torsional energy (E_{tors}) and the coupling between these energies (E_{cross}). Non-bonding terms such as the van der Waals (E_{vdw}) and electronic (E_{el}) energy are also included. Each part of the force field is modelled using different potentials depending on the need of the work. For example, bonding and angle terms can be modelled using a harmonic potential or a more accurate Morse potential. There are a number of different force fields available and popular ones include the polymer consistent (PCFF), condensed-phase optimisation (COMPASS) and the consistent-valence (CVFF) force fields. The CVFF force field in particular, has been used extensively and has been augmented to include parameters useful for silicates and aluminosilicates (CVFF_aug)[40]. Additionally, the consistent force field (CFF91_czeo) has also been developed specifically for modelling zeolite and AlPO materials[48,49]. In this thesis the Discover MM code, incorporated into Materials studio, has been used to perform MM minimisations using the CFF91_czeo force field.

2.4.3.1 : Monte Carlo docking

Monte Carlo procedures are used for the random searching of conformational space. For simulations of molecules the Metropolis method is generally used to give a

weighting based on the potential energies of the system resulting in a search that is not completely random, but based on a Boltzmann distribution of the conformations[36].

If the conformation of a particular molecule is being searched then the most flexible internal coordinates (e.g. dihedral angle and Cartesian coordinates) are varied and structures with a potential energy below a particular value are retained. The molecular docking procedure used in this thesis (chapter 3) employs a very crude Monte Carlo method, which varies the position of an already geometry optimised molecule (the organic) within a supercell of a zeolitic framework. If the molecule occupies a position that is in close contact with the framework, then the system has a high potential energy and the orientation is rejected and the procedure repeated. However, if the molecule is, for example, in the centre of a pore, then there is little close contact and the potential energy is low. If the potential energy is below a preset threshold, then the orientation of the organic molecule within the pore is retained. In this way a series of random interactions can determine the low energy region for the organic within the solid. Packing may be modelled by retaining molecules within the pore once an acceptable low energy site has been found and then continuing the procedure, allowing the pore to be packed to capacity.

2.4.4 : Geometry optimisation

Geometry optimisation (or minimization) is an iterative procedure used to find the minima on the potential energy surface of a molecule or group of molecules. Minimization results in a structural model with no strain and is the equilibrium geometry at zero Kelvin. It is used with both QM and MM calculations prior to further computational analysis[40].

Optimisation is a two step process: first the energy expression for the given configuration must be evaluated, and second, the conformation is adjusted to reduce the energy. This optimisation process is continued until a minimum on the potential energy surface is reached. This minimum is identified by comparing the energy gradient of the system with respect to the atomic coordinates for each iteration and waiting until changes in the gradient are below a pre-set limit.

It should be noted that local minima can sometimes be reached in which the geometry is apparently optimised but is not in its lowest energy form (figure 2.18). This local minimum can often be avoided by performing an initial rough optimisation to avoid these minima and then a fine optimisation to find the global minimum.

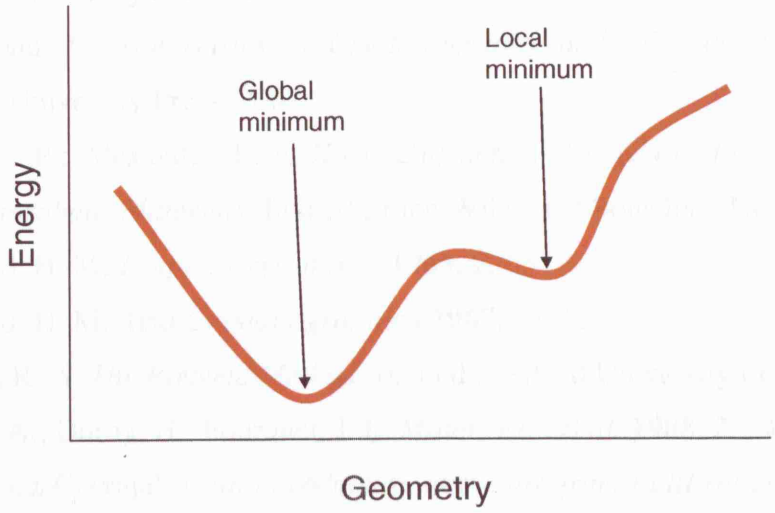

Figure 2.18: A representation of the potential energy surface of a system. The difference between a local minimum and the global minimum can be seen.

A number of different methods can be used to find the lowest energy configuration of a system. The steepest decent method relies on the direction of the downhill gradient to locate the minimum, and is extremely robust. However, it is also inefficient and slow (particularly towards the minimum). This is because each search for the direction to the minimum deviates from ideal and although successive searches attempt to correct for this, each search must be orthogonal to the last, therefore the path oscillates and over corrects for previous poor choices of direction[40].

The conjugate gradient method overcomes this by using an algorithm to produce a set of mutually conjugate directions such that each step continually refines towards the minimum, whilst the Newton-Raphson method uses the second derivative to create a matrix, which can be inverted and multiplied by the gradient, to give a vector that translates to the nearest minimum. Generally, the steepest decent method is used for the initial minimisation (10 – 100 steps) and then, when a minimum is approached, the conjugate gradient method (for large models such as zeolites) or the Newton-Raphson method is then used to obtain the minimised structure[40].

2.5 : References

(1) Giacovazzo, C.; Monaco, H. L.; Artioli, G.; Viterbo, D.; Ferraris, G.; Gilli, G.; Zanotti, G.; Catti, M. In *Fundamentals of Crystallography*; Giacovazzo, C., Ed.; Oxford University Press: 2002, p 168.

(2) Hammond, C. *The Basics of Crystallography and Diffraction*; Second ed.; Oxford University Press, 2002.

(3) Klug, H. P.; Alexander, L. E. *X-ray Diffraction Procedures for Polycrystalline and Amorphous Materials*; first ed.; John Wiley and Sons Inc.: New York, 1954.

(4) Rietveld, H. M. *J. Appl. Crystallogr.* **1969**, *2*, 65.

(5) Rietveld, H. M. *Acta Crystallographica* **1967**, *22*, 151.

(6) Young, R. A. *The Rietveld Method*; first ed.; Oxford University Press, 2002.

(7) Lebail, A.; Duroy, H.; Fourquet, J. L. *Mater. Res. Bull.* **1988**, *23*, 447.

(8) Rodriguez-Carvajal, J. *An introduction to the program FullProf 2000*; Published online with the FullProf suite of programs, 2001.

(9) Kellner, R.; Mermet, J.-M.; Otto, M.; Valcarcel, M.; Widmer, H. M. *Analytical chemistry*; second ed.; Wiley-VCH, 2004.

(10) Nafie, L. A. In *Handbook of Raman Spectroscopy*; Lewis, I. R., Edwards, H. G. M., Eds.; Marcel Dekker Inc.: 2001; Vol. 28, p 1.

(11) Horiba Jobin Yvon Ltd; http://www.jobinyvon.co.uk/ukdivisions/Raman/faq21.htm: 2006.

(12) Wittke, J. H.; Effects of electron bombardment: http://www4.nau.edu/microanalysis/Microprobe/Interact-Effects.html: 2006.

(13) Gunzler, H.; Wiliiams, A. *Handbook of Analytical techniques Volume II*; first ed.; Wiley-VCH: Weinheim, 2001.

(14) Marczewski, A. W.; A Practical Guide to isotherms of Adsorption on Heterogeneous surfaces; http://adsorption.org/awm/ads/: 2006.

(15) Sing, K. S. W.; Everett, D. H.; Haul, R. A. W.; Moscou, L.; Pierotti, R. A.; Rouquerol, J.; Siemieniewska, T. *Pure Appl. Chem.* **1985**, *57*, 603.

(16) Brunauer, S.; Emmett, P. H.; Teller, E. *J. Am. Chem. Soc.* **1938**, *60*, 309.

(17) Langmuir, I. *J. Am. Chem. Soc.* **1916**, *38*, 2221

(18) The John Hopkins University Dept of chemistry; http://www.jhu.edu/~chem/fairbr/derive.html: 2006.

(19) Atkins, P. W. *Physical Chemistry*; sixth ed.; Oxford University Press, 1998.

(20) Gunzler, H.; Wiliiams, A. *Handbook of Analytical techniques Volume I*; first ed.; Wiley-VCH: Weinheim, 2001.

(21) The Australian Synchrotron website; http://www.synchrotron.vic.gov.au: 2006.

(22) Duke, P. J. *Synchrotron radiation: Production and Properties*; Oxford University Press: Oxford, 2000.

(23) Catlow, C. R. A.; Sankar, G. In *Microporous Properties and Processes in Minerals*; Wright, K., Catlow, C. R. A., Eds.; Kluwer Academic: 1999, p 145.

(24) Clark, S. M. *Nucl. Instrum. Methods Phys. Res. Sect. A-Accel. Spectrom. Dect. Assoc. Equip.* **1996**, *381*, 161.

(25) Clark, S. M.; Nield, A.; Rathbone, T.; Flaherty, J.; Tang, C. C.; Evans, J. S. O.; Francis, R. J.; Ohare, D. *Nucl. Instrum. Meth. B* **1995**, *97*, 98.

(26) Barnes, P.; Jupe, A. C.; Colston, S. L.; Jacques, S. D.; Grant, A.; Rathbone, T.; Miller, M.; Clark, S. M.; Cernik, R. J. *Nucl. Instrum. Meth. B* **1998**, *134*, 310.

(27) Glatter, O.; Kratky, O. *Small Angle X-ray Scattering*; Academic Press: London, 1982.

(28) Guinier, A.; Fournet, G. *Small Angle Scattering of X-rays*; Chapman and Hall Ltd: London, 1955.

(29) Feigin, L. A.; Svergun, D. I. *Structure Analysis by Small angle X-ray and Neutron Scattering*; Plenum Press: New York, 1987.

(30) Tang, C. C.; Martin, C. M.; Laundy, D.; Thompson, S. P.; Diakun, G. P.; Cernik, R. J. *Nucl. Instrum. Methods Phys. Res. Sect. B-Beam Interact. Mater. Atoms* **2004**, *222*, 659.

(31) Cernik, R. J.; Barnes, P.; Bushnell-Wye, G.; Dent, A. J.; Diakun, G. P.; Flaherty, J. V.; Greaves, G. N.; Heeley, E. L.; Helsby, W.; Jacques, S. D. M.; Kay, J.; Rayment, T.; Ryan, A.; Tang, C. C.; Terrill, N. J. *J. Synchrot. Radiat.* **2004**, *11*, 163.

(32) Rehr, J. J.; Albers, R. C. *Rev. Mod. Phys.* **2000**, *72*, 621.

(33) Koningsberger, D. C.; Mojet, B. L.; van Dorssen, G. E.; Ramaker, D. E. *Top. Catal.* **2000**, *10*, 143.

(34) Teo, B. K. *EXAFS: Basic Principles and Data Analysis*; Springer-Verlag: Berlin, 1986.

(35) Mosselmans, F.; Harvey, I.; Fiddy, S.; Smith, A.; Lennie, A. *Basic EXAFS sample guide (from XAS for beginner's course, including manuals for a number of EXAFS programs)* Daresbury Labratories: Daresbury, 2005.

(36) Comba, P.; Hambley, T. W. *Molecular Modelling of Inorganic Compounds*; Second ed.; Wiley-VCH: Weinheim, 2001.

(37) Atkins, P.; Friedman, R. *Molecular Quantum Mechanics*; Fourth ed.; Oxford University Press: New York, 2005.

(38) Pilar, F. L. In *Elemental Quantum Chemistry*; Second ed.; McGraw-Hill Publishing Company: New York, 1990, p 269.

(39) Parr, R. G.; Yang, W. *Density-functional theory of atoms and molecules*; Oxford University Press: New York, 1989; Vol. 16.

(40) Accelrys *MS Modelling Getting Started, Release 3.2*; Accelrys Software Inc.: San Diego, 2005.

(41) Delley, B. *J. Chem. Phys.* **1990**, *92*, 508.

(42) Delley, B. *J. Chem. Phys.* **2000**, *113*, 7756.

(43) *Accelrys Software Inc, Materials Studio v3.1* **2005**.

(44) Tomasi, J.; Persico, M. *Chem. Rev.* **1994**, *94*, 2027.

(45) Klamt, A.; Jonas, V. *J. Chem. Phys.* **1996**, *105*, 9972.

(46) Klamt, A. *J. Phys. Chem.* **1995**, *99*, 2224.

(47) Katsunosuke, M. *Principles of Molecular Mechanics*; Wiley: New York, 1999.

(48) Hagler, A. T.; Lifson, S.; Dauber, P. *J. Am. Chem. Soc.* **1979**, *101*, 5122.

(49) Hill, J. R.; Sauer, J. *J. Phys. Chem.* **1994**, *98*, 1238.

Chapter 3

Understanding the formation of MeAPO-34 from initial species to unique metal-organic structure directing interactions

3.1 : Chapter overview

A number of metal substituted aluminophosphate 34 (MeAPO-34) systems have been prepared in a phase pure form using tetraethylammonium hydroxide (TEAOH) as the structure directing agent (SDA).

The synthesis of AlPO-34 (CHA topology) generally requires a metal framework substituent (or fluorine containing reaction medium) to be present in the synthesis gel, without it AlPO-5 (AFI topology) is formed. This seems to suggest that metal substitution has some form of structure directing properties giving rise to the formation of CHA over the AFI structure and two possibilities that may give rise to this direction have been considered. Firstly, as the AlPO-34 structure consists of a large number of 4-membered rings and it is considered possible that the metal substitution (or in some way HF) promotes the formation of 4 or fused 4-membered ring secondary building units (SBUs) allowing AlPO-34 to form. A series of quantum mechanical DFT calculations have therefore been devised to investigate the very early stages of growth. Secondly, as TEAOH can form both AlPO-5 and MeAPO-34 it is possible that the final structure is dependant on the exact conformation and/or position of the organic SDA. In order to investigate this, the interactions between the substituted metal atoms and the organic framework have been investigated. *Ex situ* synthesis was used to identify exactly which metals allow the most rapid formation of MeAPO-34 and *in situ* EDXRD was then used to investigate the effect of metal type on rate of formation. A series of *in situ* and *ex situ* Raman experiments were then performed to probe the behaviour of the SDA during the course of a reaction.

From these experiments the importance of both metal substitution and organic conformation will be demonstrated. An important cooperative role between the metal and the SDA, required in order to synthesis the chabazite AlPO-34 structure without the addition of fluorine is also demonstrated.

3.2 : Introduction

Chabazite is both a naturally occurring and synthetic zeolite[1-3] with a small pore 3-dimensional structure occupying the rhombohedral R-3m space with 4, 6 and 8-membered rings (figure 3.1)[4].

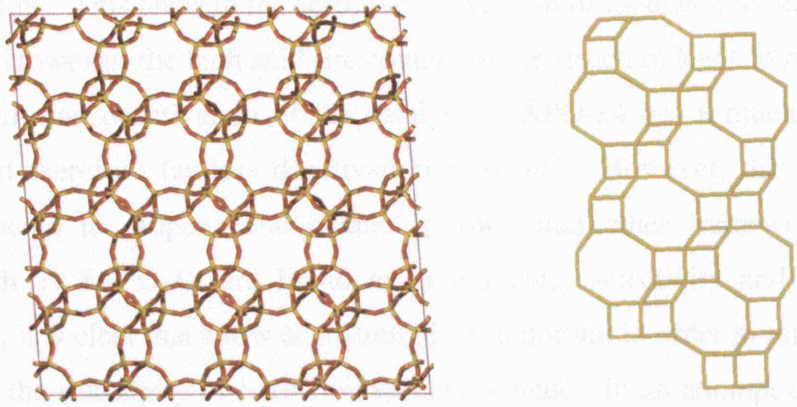

Figure 3.1: The structure of the AlPO-34 CHA topology showing the 8 membered ring apertures (left). By omitting the bridging oxygen atoms the number of 4 membered rings in the structure is clearly visible (right).

The aluminophosphate based form was first detailed by Lok *et al*[5] who found that by addition of substituted silicon, SAPO-34 could be synthesised from a gel usually known to produce AlPO-5. Ito[6] has described this structure (called ZYT-6 in the original paper) and found it to be almost structurally identical to the zeolitic form of chabazite but in a trigonal R3 space group. Significantly, it is found that in order to synthesise the pure end member of this form (i.e. AlPO-34) hydrofluoric acid is strictly necessary[7,8]. In this pure form the final crystalline structure remains a member of the chabazite topology but there are significant changes in the unit cell, giving rise to a P-1 triclinic space group and a more complex XRD pattern[8].

3.2.1 : Catalytic properties

Microporous aluminophosphates are known to possess intriguing physio-chemical and catalytic properties. In particular, when framework Al^{3+} or P^{5+} are partially replaced with metal ions, such as Co^{2+}, Ni^{2+}, Si^{4+} or Zn^{2+}, shape-selective catalysts are produced. For example, MAPO-18 selectively oxidises the terminal carbon atoms of linear alkanes such as *n*-hexane[9], whilst MAPO-36 is active for the cracking/conversion[10,11] of organic petroleum based products and adipic acid formation[12].

Over recent years the demand for olefinic products for the production of synthetic polymers and petrochemicals has increased rapidly, and the conversion of methanol to light alkenes such as ethene, propene and butene (the MTO process), has become increasingly important[13,14]. Due to its relatively small pores, only straight chain molecules are adsorbed/desorbed from the chabazite framework and the diffusion of aromatics is low. This leads to the selective conversion of methanol to olefins in the C_2 to C_4 range. However, the high acid site content of the structure leads to rapid coking of the framework and deactivation of the catalyst. SAPO-34 has a much reduced acid character and therefore far less deactivation is seen[15]. However, the selectivity for ethane compared to propene and butane is low[16] and other frameworks with low acidities such as SAPO-18 are found to give greater selectivity and reactivity[17,18]. Nevertheless, it is clear that a low acid strength is important in order to minimise coking and increase the selectivity of SAPO-34 towards ethane. In an attempt to improve the performance of SAPO-34 a number of transition metal-substituted frameworks were created. Nickel doped SAPO-34 was found to give the best selectivity for ethene[19,20] with almost 100 % conversion and 90 % selectivity occurring at a reaction temperature of 450°C, whilst the activity remained unchanged after 13 hours on stream. Ammonia temperature programmed desorption profiles of these catalysts confirms that as the nickel content increases, the number of strong and weak acid sites is reduced[21] and the selectivity for ethene increases, becoming particularly high for a Si/Ni ratio of 40 (figure 3.2).

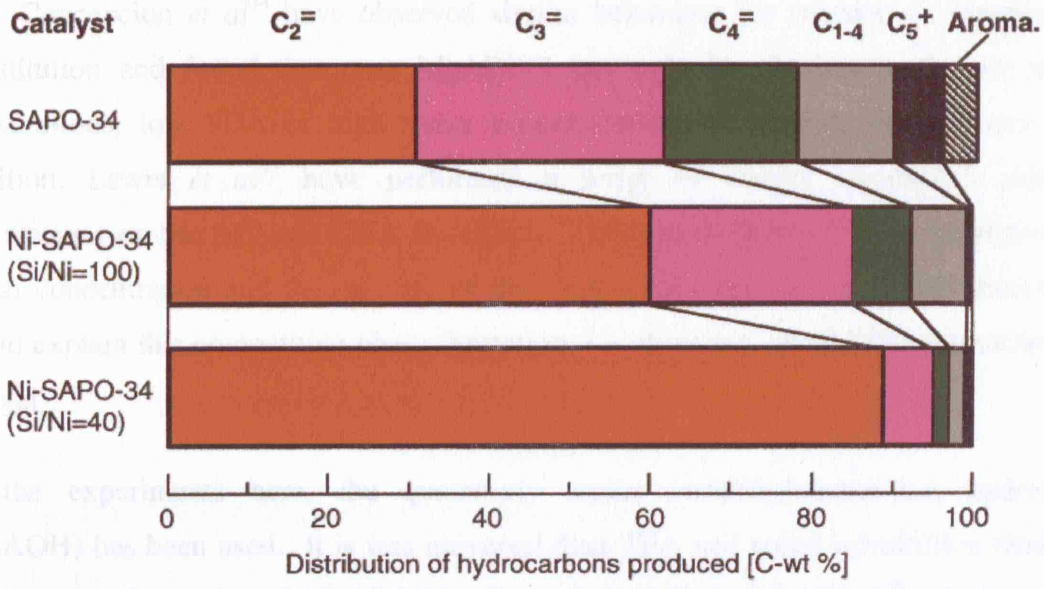

Figure 3.2: The selectivity of SAPO-34 and NiSAPO-34 for the MTO conversion. Modified from ref. 21.

The industrial potential of this process is clear, with a commercial production process being offered for licence by a Nors Hydro-UOP joint venture[22,23], and construction of a plant in Nigeria capable of producing 40,0000 metric tons of ethene and propene a year due for completion in 2006[24].

3.2.2 : Synthesis

Metal substituted and pure AlPO-34 can be synthesised using a variety of organic SDAs including piperidine[25], morpholine[7], triethanolamine[26], triethylamine and tetraethylammoniumhydroxide[27,28]. Synthesis using these SDAs performed in the absence of a substituted metal yields only AlPO-5 (as long as the temperature is high enough). The only known exception to this is when hydrofluoric acid is used in the reaction mixture in which case the triclinic form of AlPO-34 is formed[7,8]. When a substituted metal is introduced, the picture becomes more complex, with competition between the formation of MeAPO-34 and MeAPO-5 dependant on factors such as the type of SDA and metal concentration.

Triethylamine (TEA) is a particularly universal SDA and, depending on exact conditions, can yield either AlPO-5 or AlPO-34 (or a mixture) with metals including calcium, strontium, barium[29], manganese, chromium, vanadium, iron and titanium[28,30-32]. Uytterhoeven *et al*[33] have detailed this competition for cobalt substitution using TEA and found that increasing metal substitution increases the proportion of MeAPO-34. Concepcion *et al*[34] have observed similar behaviour for reaction of magnesium substitution and found that pure MgAPO-5 can only be obtained with low metal substitutions, low SDA or high water concentration and at high temperatures. In addition, Lewis *et al*[35] have performed a series of energy minimised packing calculations on the AFI and CHA structures. These have shown how a correlation of metal concentration and the packing of the TEA within the AFI and CHA structures could explain this competitive phase formation (i.e. there is a metal-SDA interaction in the gel).

In the experiments here, the quaternary amine tetraethylammonium hydroxide (TEAOH) has been used. It is less universal than TEA and metal substitution tends to result in the formation of MeAPO-34. Exceptions include MgAPO-5[34] which can be formed using TEAOH, although again only at very low substitution levels, and CoAPO-5 and MnAPO-5[27,28] which have also been synthesised, although not in a pure form,

suggesting the metal may not have entered the AlPO-5 framework. This suggestion has also been made by Beale[36] who has successfully synthesised pure CoAPO-5 (~4% substitution) but noted that EXAFS of calcined CoAPO-5 have unusual cobalt oxygen bond distances, indicating that some (or all) of the cobalt may be extra-framework.

At higher levels of substitution, MeAPO-5 is not observed and MeAPO-34 is obtained. Hill *et al*[37] has successfully synthesised highly substituted CoAPO-34 up to 0.4 mol fractions (resulting in ~30% substitution), whilst Tusar *et al*[38] has substituted 20% Zn into the framework of ZnAPO-34.

3.2.3 : Formation of AlPOs

From these previous experiments it can be seen that, as a general rule, formation of AlPO-34 it typified by high metal substitution levels, high template concentration and low preparation temperatures. In order to understand how these factors can affect the formation of aluminophosphates and control the final product, an understanding of the formation mechanisms and processes is necessary.

3.2.3.1 : Chains and building units

A large number of mechanisms for the formation of porous materials have been proposed by numerous authors, some of which were described in chapter 1. However, whilst a large amount of work has focused on the formation of zeolites[39,40], far less attention has been paid to the formation of aluminophosphates, despite the fact that similar and often even identical topologies can be achieved.

For a long time it has been known that polyphosphates tend to avoid branching due to the easy hydrolysis of PO_3^- branching points[41], and it is possible that aluminophosphate species may behave in a similar way. Early models to account for the final framework structure do include chain-like species such as double-crankshafts[42,43] and triple-crackshafts[44] that run parallel to the main channel system. However, these complex structures are unlikely to be stable in solution and there is no evidence for these structures participating in any formation mechanism[45].

Other chain-like species have been identified in solutions with increased amounts of phosphorus. For example, Kniep *et al*[46] have noted the formation of large crystals of $Al(H_2PO_4)_3$ chains by evaporation. Recently a number of chain and layer like

aluminophosphate have also been reported[47-51] and although the increased phosphorus levels leads to species not usually associated with the bulk of the microporous AlPO structure (such as terminal P=O and P-OH groups), these may be representative of species forming in microporous AlPO gels. Oliver *et al*[49] have also noted that a solution that produces these chain-like species can undergo a transformation to yield 2-dimensional sheets by simply increasing the reaction temperature and Wang *et al*[52] have demonstrated how 1-dimensional compounds can be converted to a 3-dimensional structure by addition of Ni to the structure.

Such evidence has led Oliver *et al*[45] to propose a formation model based on linear chain aluminophosphates. The parent chain for this mechanism is the 1-dimensional linear chain previously synthesised from a non-aqueous system[53] and consists of a meta-stable chain with corner-sharing Al_2P_2 four rings bridged at the Al centres. This parent chain then undergoes hydrolysis of the Al-O and P-O bonds followed by rapid rotation of the highly flexible chains. This brings Al-OH and P-OH groups close together and allows intra-chain condensation and the formation of edge sharing rings. These condensed chains then undergo further hydrolysis, rotation and condensation to form a variety of chains, layers and frameworks including AlPO-5, JDF-20 and VPI-5 (Figure 3.3).

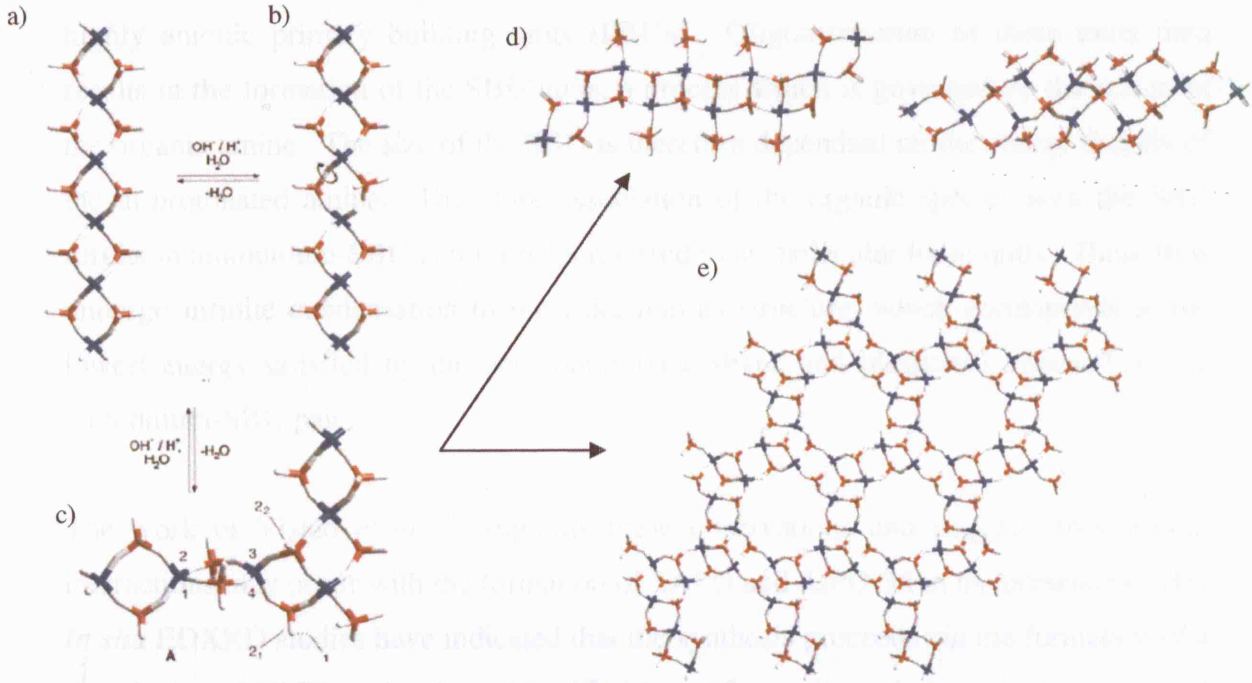

Figure 3.3: Part of the formation mechanism proposed by Oliver. Here the meta-stable parent chain (a) undergoes hydrolysis and rapid rotation (b) forming edge sharing rings (c). These then undergo further hydrolysis, rotation and condensation to form a variety of chains (d), frameworks including AlPO-5 (e). Modified from ref. 45.

Férey[54] has proposed an alternative scheme for AlPO formation based on SBUs similar to those observed by Barrer in zeolites[55]. It is founded on the observation that a number of recent *in situ* NMR studies on fluorinated AlPO species have shown that, unlike the species in Oliver's work[45], the aluminium is not tetrahedral. Of particular note is the work of Tauelle *et al*[56,57] who have indicated that aluminium exists as a 6-coordinate species in a fluorinated acidic solution, changing to 5-coordinated under neutral conditions. In $AlPO_4$-CJ2 fluro-aluminophosphate tetramer primary units (Al_2P_4) are formed and intramolecular nucleophillic addition occurs as crystallisation takes place. A similar situation is observed for the formation of large pore 3-dimensional gallophosphates from 1-dimensional galloflourophosphates under hydrothermal conditions[58,59]. Here a change in the gallium coordination from 6 to a mixture of 5 and 6 is observed[60] along with Al_3P_3 hexamer units. These pre-nucleation building units (PNBUs) are closely related to the SBUs that Férey has observed in the ULM-n series of materials[54]. These ULM materials can be entirely described from a few types of SBU, all with a formal charge of -2. These include the tetramer (Al_2P_2) and hexamer (Al_3P_3) units as well as octameric (Al_4P_4) units and a mechanism has been proposed which proceeds by the formation of these units in a series of steps[61].

In the proposed mechanism (figure 3.4), initial building units (IBUs) condense to give highly anionic primary building units (PBUs). Oligomerisation of these units then results in the formation of the SBU units, a process which is governed by the action of the organic amine. The size of the SBU is therefore dependant on the charge density of the di-protonated amine. The close association of the organic species with the SBU results in ammonium-SBU neutral pairs referred to as molecular basic units. These then undergo infinite condensation to form the porous structure, which corresponds to the lowest energy satisfied by the constraints (size shape and plasticity) imposed by the ammonium-SBU pair.

The work of Vistad *et al*[62,63] supports these observations and suggests that similar interactions may occur with the formation of SAPO and AlPO-34 in the presence of HF. *In situ* EDXRD studies have indicated that the synthesis proceeds *via* the formation of a pre-phase and NMR studies have identified 6 and 5-coordinated aluminium species and it is suggested that 4-membered rings form with coordinated fluorine. These species then form the layered prephase by simple stacking and condensation then occurs, resulting in the formation of triclinic AlPO-34 with fluorine bridges within the structure.

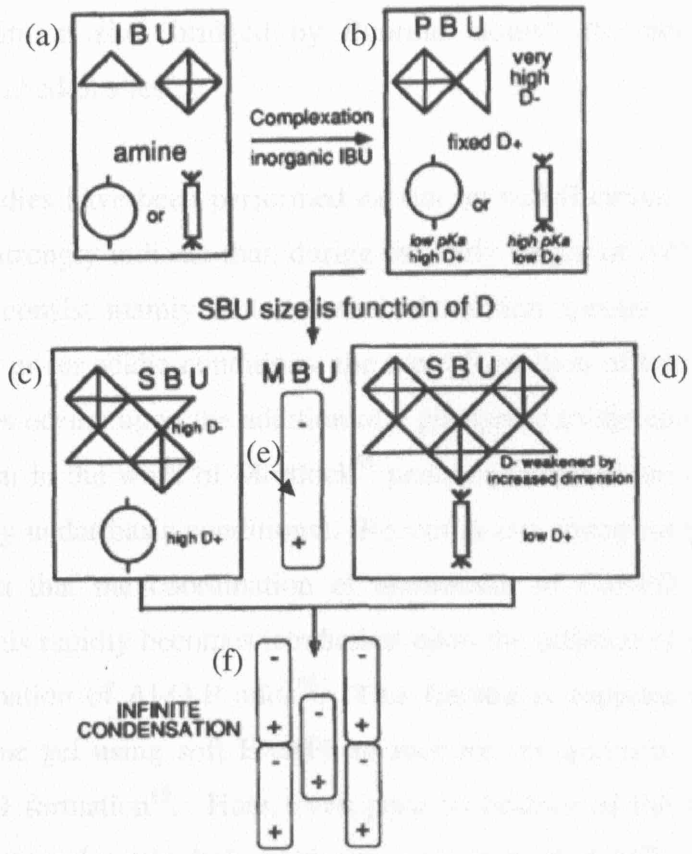

Figure 3.4: The formation of fluorinated AlPOs as proposed by Férey. The process involves the formation of primary building units (b) form initial building units (a). These then interact with the organic to form secondary building units (c and d) associated closely with the organic to form molecular basic units (e) which then condensate to form the final structure (f). Reproduced from ref. 61.

Clearly the formation of SBUs and ammonium-SBU neutral pairs has important implications for AlPO formation, as under this regime building units do not arrange around the template, but form depending on the MBU. However, it must be remembered that all of the experimental evidence for this mechanism is based on fluorinated liquid systems.

The vast majority of microporous AlPO systems are formed without the use of fluoride and in a gel-like medium, which would suggest that even if these SBU/MBU entities do exist they may not be forming in most circumstances. Indeed, it has already been noted that in the case of AlPO-34, fluoride is unique, allowing its formation in the absence of a substituted metal. Vistad *et al*[63] have also noted that without the presence of HF no pre-phase is observed and no AlPO-34 crystallisation occurs, which may be a consequence of an inability to form 6 or 5-coordinated species without fluorine, and this

is supported by the observation that, whilst the triclinic AlPO-34 structure contains octahedral aluminium sites bridged by fluorine atoms[8], the non-fluorinated form contains only tetrahedral sites[6].

A number of studies have been performed *ex situ* on non-fluorinated solution and gel systems and all strongly indicate that, during the early stages of AlPO formation, non-fluorinated gels consist mainly of tetrahedral aluminium species. These include the observation that, under acidic conditions, the rapid formation of tetrahedral aluminium phosphate species occurs upon the addition of a phosphate to the coordination sphere[64-67] (It is noted that in the work of Mortlock[65] penta-coordinated aluminium species are observed but only under basic conditions). Recent *in situ* spectroscopic Raman studies have also shown that the coordination of aluminium in CoAPO-5 gels is initially octahedral, but this rapidly becomes tetrahedral upon the addition of phosphoric acid to the gel and formation of Al-O-P units[68]. This finding is supported by a very recent study on the same gel using soft EXAFS to monitor the geometry of the aluminium throughout AlPO formation[69]. Here, even prior to heating of the gel the aluminium moves from a distorted octahedral coordination to tetrahedral Al^{3+} and this conversion then increases upon hydrothermal treatment.

From the work detailed above it would appear that the AlPO formation may proceed by two different mechanisms, dependant on the presence or absence of fluoride. In the presence of fluoride the formation of octahedral species occurs, which then form SBU or MBU like materials. However, in the absence of fluorine, all recent *in situ* experimental evidence suggests that only tetrahedral species are formed. Therefore, in these systems, growth occurs from tetrahedral species *via* either chains[45] or SBUs[55].

3.2.3.2 : Computational studies

A number of quantum mechanical studies have been used to examine the formation of microporous materials over the past decade. These studies have attempted to measure the free energies of formation of different silica clusters in both a vacuum and with a solvation model to account for the presence of water.

Pereira *et al*[70,71] have used these methods to examine the structures and energies of various neutral clusters thought to form from zeolite condensation processes. Density

functional theory (DFT) was used to calculate the structure of a large number of linear and branched clusters containing 3 to 5 silicon species as well as 5 and 6-member rings and branched rings. From these experiments it was noted that linear clusters appear to be energetically more stable than branched and cyclic structures and it is suggested that this may lead to the formation of amorphous silicates rather than the expected microporous phase. Note that full discussions of the quantum mechanical techniques used in this work are given in chapter 2.

Recently Mora-Fonz *et al*[72,73] have performed an extensive number of calculations using similar clusters, but also considering the effect of charged species on the formation of the system. From these calculations, a pH dependence for the polymerisation and formation of small rings is noted with cyclisation favoured by high pH conditions similar to those that would be found in a zeolitic synthesis. It was concluded that zeolite growth is more likely to occur by the condensation of small units and that large non-cyclic oligomeric species are unlikely to play a significant role in either nucleation or growth. As yet however, no similar calculations have been performed on aluminium and phosphorus clusters, most likely due to the more complex nature of these molecules and the non-uniform electrostatic field within such molecules.

3.2.3.3 : The conformation of the organic

The presence of an organic additive appears necessary for the crystallisation of most (Me)APO's[74,75]. However, the way in which the template achieves this microporosity remains unclear. The theories regarding this interaction are discussed in detail in chapter 1, but briefly Davis and Lobo[76] have attempted to rationalize the function of the template by proposing three possible roles: (i) Space filling, where packing occurs and is non-specific to a particular structure, (ii) structure direction, where the organic affects the nucleation process leading to specific structures from specific organics, and (iii) true templating, where enhanced guest-host interactions occur during crystalline ordering.

Various experiments have provided insight into how organics enable such microporous structures to form. For example, NMR has highlighted the importance of weak, non-covalent intermolecular forces in pre-crystalline phases during zeolite formation[77], whereas Raman spectroscopy has indicated the encapsulation of the organic in zeolitic pre-crystalline amorphous solids[78]. It should also be noted that pure AlPOs contain no

framework charge and therefore weak organic framework interactions are likely to dominate[79]. However, upon framework substitution a charge can be created (dependant on the charge of the substituted metal) which can be compensated by positive cations (in the case of zeolites) or the organic SDA. It is therefore possible that metal substitution may modify the interaction of the organic with the framework and can therefore have some 'structure directing' role.

As the size (e.g. organic chain length) and the conformation of the organic can alter the space filling ability of the molecule, these factors may also play a significant role in the formation of microporous materials. For example, Kubota *et al*[80] have observed that bulky rigid molecules with limited conformational variability result in a near unique formation of molecular sieves, whilst flexible molecules can give more than one molecular sieve. Paik *et al*[81] have also used combined NMR, Raman and modelling to show that the large organic Et_6-diquat-5 exists in three different conformations in the zeolites P1, SUZ-4 and ZSM-57. It is also shown that the type and concentration of alkali cations in the reaction mixture can affect the available conformations and therefore the synthesis product. Similar results are also seen for other diquaturnary ions in zeolites[82] and recently Gómez-Hortigüela *et al*[83] have used similar techniques to examine the formation of AlPO materials. These act in a similar manner to zeolites, with the amount of molecular flexibility providing an idea of the specificity of a molecule in directing a microporous (AlPO) structure.

TEAOH will be used in this series of experiments and as it is known to direct the formation of a number of microporous materials, it would therefore seem that, like the organics mentioned above, this molecule also has some degree of flexibility and can potentially occupy a number of conformations. Naudin *et al*[84] have demonstrated this, showing that TEAOH exists in two conformations; either all *trans* (tt.tt) or *trans-gauche* (tg.tg) (figure 3.5) in an aqueous solution. It was also demonstrated that the different conformations result in a variation in the Raman spectrum (table 3.1) and specifically the $\nu_s(C_4N)$ profile gives a good indication of the conformational state. Temperature dependence is also observed, with increasing temperature resulting in an increase in the amount of tg.tg conformer compared to tt.tt.

Importantly, measurements on the crystalline SAPO-34 phase indicate that only a single conformation of TEAOH exists within the pores[85]. This 'C_2' phase is closely related to

the tg.tg conformer seen in solution and seems to indicate that the TEAOH conformation may play an important role in specific phase formation.

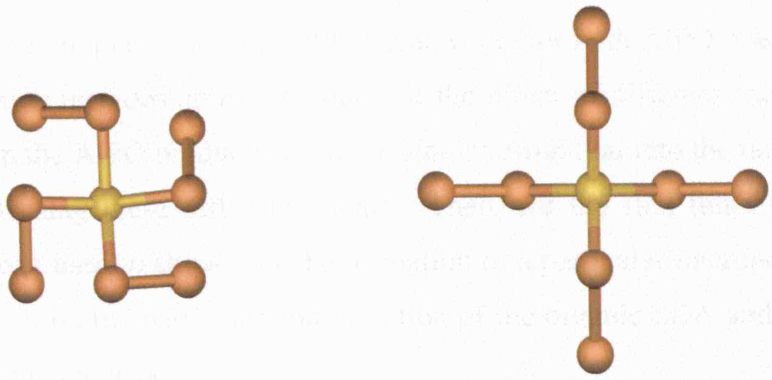

Figure 3.5: Idealised structures of the two solution state conformers of the TEA cation known as tg.tg (left) and tt.tt (right).

	δ(CNC)	$\nu_s(C_4N)$	$\nu_s(C_4N)r(CH_3)$
tt.tt	418	675	906
tg.tg	390,438	664.5	896

Table 3.1: The characteristic Raman shifts (cm^{-1}) of the two TEAOH cations in water according to Naudin *et al*[84].

3.2.4 : Aim of this work

MAPO-34 is one of the most successfully industrially utilised aluminophosphate porous materials to date. This is due to a number of factors including the ability to control the pore dimensions in the synthesis and the acidity of the framework through the introduction of metal substituents.

However, despite this success, the fundamentals of the formation processes of this (and similar) systems are still poorly understood. The aim of this work is to examine two important factors which may effect the formation of AlPO-34 and other microporous materials. Both the role of the substituted metal during the very early stages of the AlPO synthesis and the interaction of the organic with the framework through out the AlPO synthesis are examined.

The initial study is performed using computational quantum mechanics to measure small chain and ring condensation non-specific to AlPO-34. Therefore the results could also be relevant to all AlPO systems. The second part of the work has focused on the interaction of the template with the AlPO framework (for both AlPO-5 and MeAPO-34 formation), which includes an *ex situ* study of the effect of different framework metal substitutions on the AlPO products and an *in situ* investigation into the rate of formation of MeAPO-34 using these different metals. Then, for the first time, *in situ* Raman studies have been used to show how the formation of a particular microporous structure can be dependant on the particular conformation of the organic SDA and its interaction with the substituted metals.

By using these techniques, it will be shown how a greater understanding of the subtle and largely overlooked metal-framework-organic interactions can evolve our knowledge of the formation of microporous structures, advancing us towards the goal of rational design.

3.3 : Experimental

3.3.1 : Hydrothermal preparation of CoAPO-34 materials

The following chemicals and synthesis methods were used for the preparation of MAPO-34 (where M = transition metal) according to procedures previously described[1]

Gels were prepared to the following molar ratios:

$$1.5\ H_3PO_4 :\ 1\text{-}x\ Al(OH_3) :\ x\ M\ acetate :\ 0.8\ TEAOH :\ 26\ H_2O$$

Where x was varied between 0.025 and 0.3. In a typical experiment, 3.38 g of phosphoric acid (Sigma-Aldrich, 85 % wt) and 4.44 g of doubly distilled water were mixed in a Teflon Beaker with mechanical stirring. The desired amount of metal acetate (zinc acetate dihydrate, $(CH_3COO)_2Zn.2H_2O$ cobalt acetate tetrahydrate $(CH_3COO)_2Co.4H_2O$ or manganese acetate tetrahydrate, $(CH_3COO)_2Mn.4H_2O$ Sigma-Aldrich) was then added. Upon dissolution the corresponding amount of aluminium hydroxide was added slowly to the solution and then stirred until a homogenous gel was achieved (*ca.* 10 mins). Finally 6.56 g tetraethylammoniumhydroxide (TEAOH) (Sigma-Aldrich, 35 % wt.) was added drop wise to the gel. On addition of TEAOH solidification occurred and vigorous stirring by hand was required until the gel loosened. The solution was then stirred mechanically until a viscous homogenous gel was formed (*ca.* 15 mins). For the synthesis of AlPO-5 an identical synthesis procedure was used, but without adding the metal acetate(s) (i.e. x = 0). Note that initially a number of other metal substitutions were also attempted using metals with oxidation states other than two and the details of these reactions are given in the discussion.

3.3.2 : Characterisation techniques

Note that in chapters 3 to 6 of this thesis the techniques section details the exact instrument(s) and setups used for each technique in this chapter, a far more general discussion regarding the theory and the experimental setups is given in chapter 2.

3.3.2.1 : X-ray diffraction

XRD patterns of all the dried as-synthesised materials prepared in the laboratory were recorded using a Bruker D4 diffractometer in the Bragg-Brentano orientation using a rotating flat plate in order to reduce any preferred orientation effect. The X-rays were generated from a copper source emitting Cu $K_{\alpha 1}$ (1.540598 Å) with a secondary monochromator to remove any $K_{\alpha 2}$ and Cu K_{β} radiation. Comparative XRD samples relating the extent of crystallisation with time were recorded on a Siemens D8 with a Cu K_{α} source in a Debye-Sherrer geometry using a rotating capillary. The Fullprof suite of programs[86] was then used to perform LeBail fits on the XRDs with initial fitting parameters taken from literature sources.

3.3.2.2 : Scanning electron microscopy

Scanning electron microscopy (SEM) images were taken using a JOEL JSM-6301F scanning microprobe and energy dispersive X-ray analysis (EDX) was performed using a Hitachi EDX 5570 fitted with an Oxford Instruments INCA analysis suite for data processing.

3.3.2.3 : Extended X-ray absorption fine structure

EXAFS measurements were carried out at station 9.3 of the synchrotron radiation source (SRS) at the Daresbury laboratory, which operates at 2 GeV with typical currents of 150-250 mA. The station was equipped with a Si(220) double crystal monochromator and two ion chambers for measuring both incident and transmission beam intensities. A fluorescence detector was also mounted at a 45 degree angle above the sample holder to record reflected fluorescence data. Samples consisted of 40 mg laboratory prepared CoAPO's pressed into 13mm pellets and mounted for measurement using station based mounting equipment. The data were analysed using the analysis suite available from Daresbury laboratories, including EXCALIB for converting the raw data to energy vs. absorption coefficient, EXSPLINE for background subtraction and EXCURV98 for analysis of the resulting EXAFS data and fitting of the atomic shells.

3.3.2.4 : *In situ* energy dispersive X-ray diffraction

The crystallisation of these AlPO materials was monitored *in situ* using EDXRD. The advantages of this technique are discussed in chapter 2 and as this technique forms only a minor part of this work, the full details of the experimental set up and data analysis are given in chapter 3 - where they are used far more extensively.

Measurements were carried out at station 16.4 of the SRS using the three-element detector system at 4.18° for the middle detector (1.3° for the lower and 7.08° for the upper). Experiments were performed in modified stainless steel autoclaves with a PTFE liner and the gel mixture was introduced into an *in situ* oven preheated to the desired temperature, with measurements beginning 2 minutes after sample insertion, at a rate of 1 scan/minute.

3.3.2.5 : *In situ* and *ex situ* Raman spectroscopy

Raman spectra were recorded using a 532 nm laser operating at 60 mW with a Holoprobe Kaiser Optical spectrometer equipped with a holographic notch filter and CCD camera. A schematic of the *in situ* experimental set-up is given in figure 3.6.

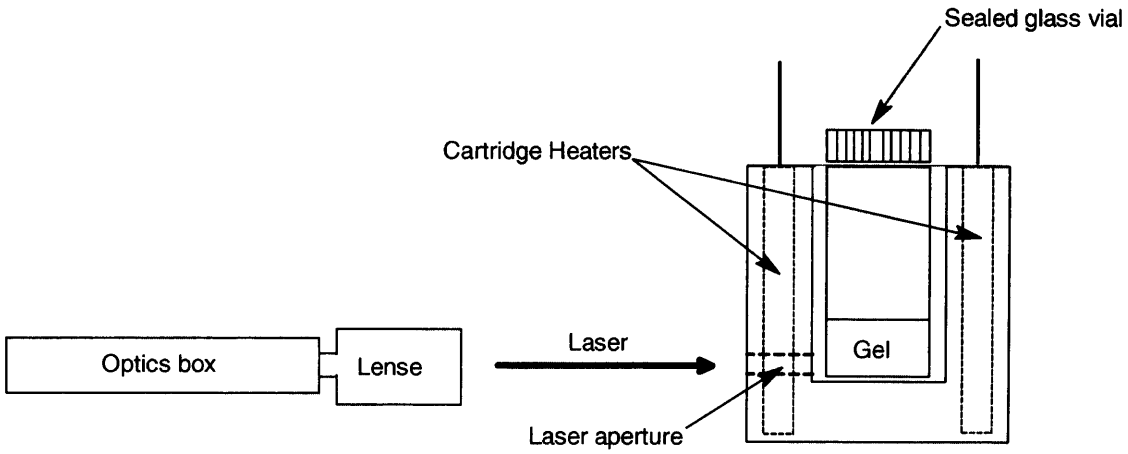

Figure 3.6: Schematic of the *in situ* Raman spectroscopy set up.

For *in situ* experiments the gel was heated in a sealed glass container inserted into a heating block with a small entrance hole to allow collection of the Raman data. Specifically the entrance hole was located at the bottom of the container in order to measure the crystalline product which tended to settle at the bottom. Data were

collected for 32 seconds every 10 minutes for samples reacted at 80 – 100°C and every 5 minutes for samples recorded at 120°C. *Ex situ* Raman data on the dried powders (which were first treated in 0.1 M NaOH solutions overnight in order to remove loosely-bound organics) were recorded in the same setup, although in order to reduce fluorescence, the samples were dampened slightly with distilled water. In order to improve the measurement statistics for the Raman signal, data were collected over a much longer time period of 500 seconds.

All data was recorded over a range of 300 – 4300 cm^{-1} and were collected using the HoloGRAMS software suite. In order to check the detector calibration and to maximize the intensity of the backscattered Raman signal, a sulfur reference sample was used.

All subsequent data analysis and band profiling were performed using GRAMS/AI spectroscopy software[87], initially a multipoint baseline subtraction over the region of interest (as detailed in the discussion) and peak profiling was then performed using the in-built Gaussian fitting routines in the software to accurately measure the band height of each conformer. In all cases the full width at half maximum (FWHM) was constrained in order to accurately simulate the peak shapes & positions.

In some circumstances band overlap occurred and became so significant that it was difficult to deconvolute the bands in the spectra sufficiently to set resonable starting parameters. In such circumstances, second derivative plots of the data were compared with simulated data in order to to establish resonable approximate initial fitting parameters.

3.3.3 : Computational techniques and methodology

Quantum mechanical computational calculations have been used to calculate the free energies of formation of a number of AlPO clusters, either with or without a substituted metal (in each case the substituted metal was zinc).

In all cases the initial geometry of the clusters used were those previously calculated by Mora-Fonz *et al*[72,73] for their series of works on pure silicate clusters and each molecule

had previously undergone simulated annealing in order to avoid local minima. These minimised silica structures were then converted to their AlPO counterparts by simple atom substitution and then re-optimised using DFT.

All calculations were performed using DMOL[3] version 3.0[88,89] using the BLYP functional and geometries were fully optimised to the minimum energy. In an attempt to consider the effects of water on the clusters the COSMO solvation approach was also introduced to the clusters, the effect of which is discussed below.

3.4 : Results and Discussion

As the computational results describe the very early stages of AlPO formation these have been discussed first. The formation of MeAPO-34 and AlPO-5 is then detailed, initially by *ex situ* techniques, for the examination of phase purity, and then by *in situ* (and also *ex situ*) Raman spectroscopy and *in situ* EDXRD. The results are then compared and discussed in the context of the role of the organic, as described above. Note that the raw data for all DMOL cluster energies can be found in appendix 1.

3.4.1 : DFT calculations

As described in the experimental section a number of clusters were modelled using DFT calculations performed using DMOL[3] and based on the silicate clusters used by Mora-Fonz *et al*[72,73]. In order to investigate whether the insertion of transition metals such as zinc directs the formation of 4-membered ring structures, clusters containing metal were also considered. Initially, all calculations were carried out in vacuo and then repeated using the COSMO model of solvation. As noted in the introduction, a tetrahedral geometry seems to predominate in the gels of non-fluorinated AlPO systems and therefore these initial experiments have been restricted to considering chains and units containing only this geometry.

3.4.1.1 : Un-substituted AlPO clusters

Initial observations of some of the minimised AlPO clusters (in vacuo) revealed a number of interesting features. First, it is noted that, when compared to silicon clusters, the arrangement of protons in the gas phase is distinctly different (figure 3.7). In the case of the silicates the most stable clusters feature internal hydrogen bonds around the entire cluster. However, for the AlPO clusters this is not the case, with H-bonds only forming between individual aluminium-phosphorus 'pairs'. It is also noted that in these systems the direction of the H-bond is also always from phosphorus proton to aluminium oxygen. This can be explained by simply considering the electronegativity of each atom in the clusters. In the pure silicate cluster there is no difference in electronegativity across all the Si-O bonds in the cluster and therefore the maximum number of bonds is achieved. However, in the AlPO clusters this is not the case and polar interactions are introduced. As phosphorus (Pauling scale = 2.19) is more electronegative compared to aluminium (1.61) and closer to the electronegativity of oxygen (3.44), the P-O bond is more covalent in nature than the Al-O bond. The

oxygen bonded to the aluminium is then more ionic and carries more charge, resulting in H-bonds always from phosphorus to aluminium and not the other way round.

The creation of these individual aluminium-phosphorus bonding pairs is interesting as it serves as an example as to the difference between AlPO clusters and the more simple silicon clusters. Indeed, whilst the silicon rings are a fully H-bonded cyclic system, the AlPO rings are not, and act as if they were still isolated dimeric species. Clearly this effect would be significantly reduced in solvated systems, and as it is present in each of the AlPO clusters it is unlikely to distort any observed trends. However, it is interesting to note as these differences serve to illustrate the increased complexity of AlPO clusters.

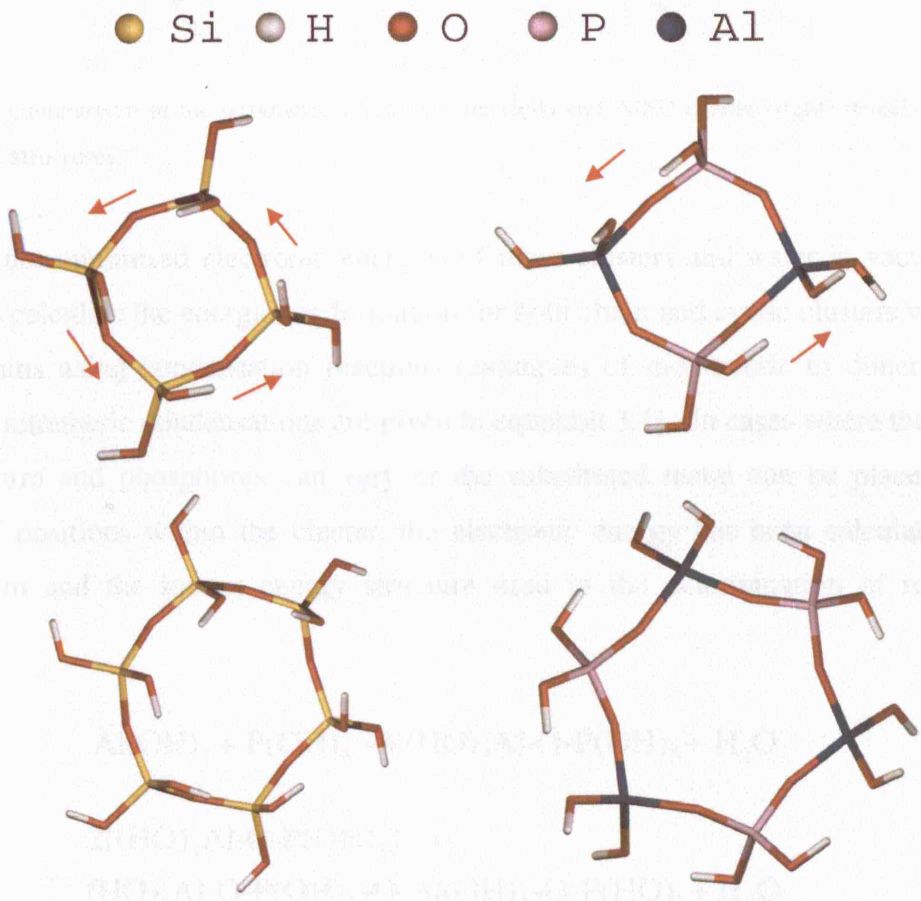

Figure 3.7: A comparison of the 4 (top) and 6 (bottom) membered ring clusters for silicates[72,73] (left) and AlPOs (right). The difference in the H-bonding is clear with the silicates being cyclic (highlighted by arrows) and the AlPOs only forming H-bond pairs.

Secondly, it is noted that in common with the silicate systems, the AlPO chain structures fold in on themselves, forming almost ring-like structures (figure 3.8). This

is interesting as it initially suggests that the AlPO clusters may follow the trends as described by Mora-Fonz *et al*[72,73].

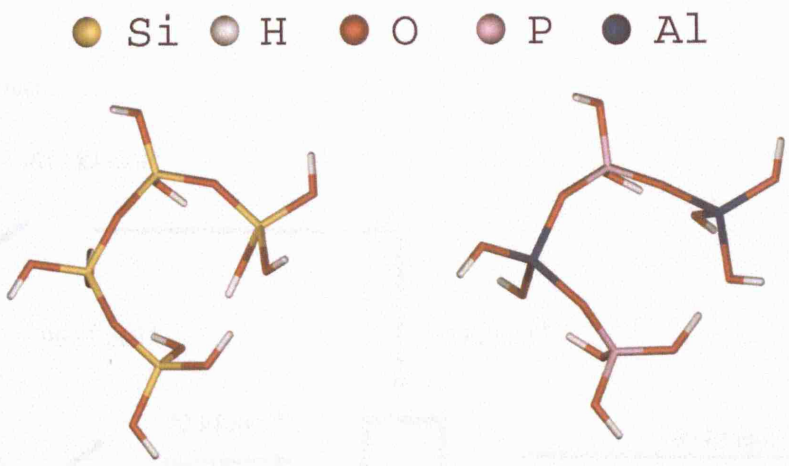

Figure 3.8: Comparison of the tetrameric silicon cluster (left) and AlPO cluster (right) reveals similar almost cyclic structures.

By taking the minimised electronic energies of these clusters and water in vacuo it is possible to calculate the energies of formation for both chain and cyclic clusters with up to 6 T atoms using condensation reactions (examples of monomeric to dimeric and dimeric to tetrameric condensations are given in equation 3.1). In cases where the order of aluminium and phosphorus can vary or the substituted metal can be placed in a number of positions within the cluster, the electronic energy has been calculated for each system and the lowest energy structure used in the determination of reaction energetics.

$$\mathrm{Al(OH)_4 + P(OH)_4 \rightarrow (HO)_3Al\text{-}O\text{-}P(OH)_3 + H_2O}$$

$$\mathrm{2[(HO)_3Al\text{-}O\text{-}P(OH)_3] \rightarrow}$$
$$\mathrm{(HO)_3Al\text{-}O\text{-}P(OH)_2\text{-}O\text{-}Al(OH)_2\text{-}O\text{-}P(HO)_3 + H_2O} \qquad \textbf{(3.1)}$$

For the non-metal substituted clusters (figure 3.9) it can be seen that the formation of dimers is very favourable with a very exothermic energy of formation (-612 kJ mol^{-1}). This suggests that, as observed experimentally[68, 69], this process will occur rapidly and at low temperatures and will result in a large number of dimers in the initial stages of formation. Conversely then, the number of monomeric species will be expected to be

very small, and therefore unlike the pure silicate condensation reactions, the addition of monomers to growing clusters is unlikely. This result also suggests that unlike silicate systems, species with an even number of T-sites will tend to dominate the formation process.

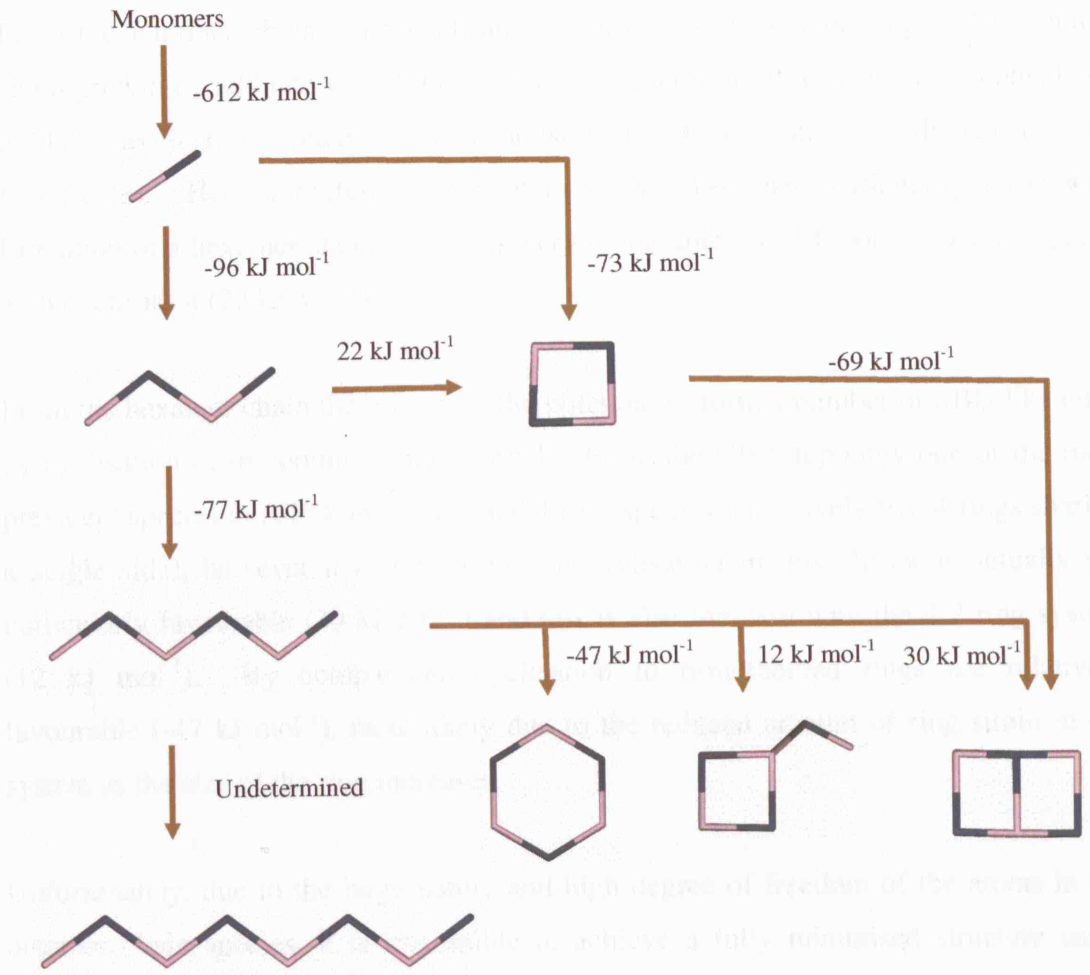

Figure 3.9: The formation energies of a number of different AlPO clusters. The structures represented are idealised with dark blue representing aluminium and light blue phosphorus. The energies of formation are calculated for the most stable form of the cluster from the condensation reaction of smaller clusters (i.e. releasing water).

The dimers can then undergo either a direct cyclisation to a closed 4-membered ring (a double condensation) or form a tetramer chain (a single condensation). The formation energies for these processes are similar at -73 kJ mol^{-1} and -96 kJ mol^{-1} respectively and suggest that whilst chain growth is preferred (by 23 kJ mol^{-1}), cyclisation is also possible. It is noted however, that although cyclisation is energetically possible, the alignment of two dimers in the right orientation to undergo a double condensation is

statistically far less likely to occur that a single condensation to form a chain. Given this fact and the very similar energies of each formation pathway it seems that chain growth would have to be considered the prime mode of formation species containing 4 T atoms.

From the tetramer chain, both cyclisation to give a 4-membered ring and continued chain growth by addition of a dimer are possible (addition of a monomer is considered unlikely as it has already been demonstrated that formation of dimers is very favourable). Here a preference for chain growth becomes particularly clear with formation of a hexamer chain remaining very favourable (-77 kJ mol^{-1}) when compared with cyclisation (22 kJ mol^{-1}).

From the hexamer chain there is again the potential to form a number of SBU like units by cyclisation or to continue chain growth. From the CHA topology one of the most prevalent species in AlPO-34 is the fused 4-ring species (effectively two 4-rings sharing a single side), however it can be seen that cyclisation to this cluster is actually not particularly favourable (30 kJ mol^{-1}) and this is also the case with the 4-2 ring system (12 kJ mol^{-1}). By comparison, cyclisation to 6-membered rings are relatively favourable (-47 kJ mol^{-1}), most likely due to the reduced amount of ring strain in the system as the size of the ring increases.

Unfortunately, due to the large nature and high degree of freedom of the atoms in the octamer chain species, it is impossible to achieve a fully minimised structure using reasonable lengths of computational time. Therefore, it is currently unknown if at this stage if cyclisation to a 6-ring is more or less favourable in comparison to the growth to octamer chains, although considering the trends seen with the shorter chains it would indicate that chain growth may be more likely.

It is interesting to note that once formed, the growth of a 4-ring species to a fused 4-ring will compete favourably with chain growth; suggestive of a route to the chabazite structure. However, as the formation of a 4-rings is unlikely (chain growth being the favoured pathway) and isolated fused 4-ring species is perhaps unlikely to play any role in the formation of these systems.

statistically far less likely to occur that a single condensation to form a chain. Given this fact and the very similar energies of each formation pathway it seems that chain growth would have to be considered the prime mode of formation species containing 4 T atoms.

From the tetramer chain, both cyclisation to give a 4-membered ring and continued chain growth by addition of a dimer are possible (addition of a monomer is considered unlikely as it has already been demonstrated that formation of dimers is very favourable). Here a preference for chain growth becomes particularly clear with formation of a hexamer chain remaining very favourable (-77 kJ mol^{-1}) when compared with cyclisation (22 kJ mol^{-1}).

From the hexamer chain there is again the potential to form a number of SBU like units by cyclisation or to continue chain growth. From the CHA topology one of the most prevalent species in AlPO-34 is the fused 4-ring species (effectively two 4-rings sharing a single side), however it can be seen that cyclisation to this cluster is actually not particularly favourable (30 kJ mol^{-1}) and this is also the case with the 4-2 ring system (12 kJ mol^{-1}). By comparison, cyclisation to 6-membered rings are relatively favourable (-47 kJ mol^{-1}), most likely due to the reduced amount of ring strain in the system as the size of the ring increases.

Unfortunately, due to the large nature and high degree of freedom of the atoms in the octamer chain species, it is impossible to achieve a fully minimised structure using reasonable lengths of computational time. Therefore, it is currently unknown if at this stage if cyclisation to a 6-ring is more or less favourable in comparison to the growth to octamer chains, although considering the trends seen with the shorter chains it would indicate that chain growth may be more likely.

It is interesting to note that once formed, the growth of a 4-ring species to a fused 4-ring will compete favourably with chain growth; suggestive of a route to the chabazite structure. However, as the formation of a 4-rings is unlikely (chain growth being the favoured pathway) and isolated fused 4-ring species is perhaps unlikely to play any role in the formation of these systems.

In summary these results indicate that for un-substituted AlPO clusters:

- In comparison to silicate species the formation of dimers is energetically favourable.
- Formation of a 4-ring from two dimers is comparatively favourable but statistically less likely to occur than chain growth.
- Cyclisation of both the tetramer and hexamer chains to form building units based on the 4-membered rings prevalent in AlPO-34 is not particularly viable, although cyclisation to 6-membered rings may be possible.
- Extended chain growth appears the most favoured polymerisation route.

3.4.1.2 : Clusters containing one or more substituted metal.

As discussed in the Introduction, it has been suggested that the introduction of a transition metal into the AlPO gel allows the preferential formation of AlPO-34 over AlPO-5 by making the formation of the 4-membered ring species seen in the chabazite structure more viable. Therefore, by inserting a single metal atom (in this case Zn – creating a negative charge on the cluster) into the AlPO clusters and calculating the new minimised electronic energies it is possible to investigate the effect of metal substitution. The species examined are identical to those for the un-substituted systems (but containing one zinc atom) and are represented in figure 3.10.

Clear, differences are seen when compared with the un-substituted systems. Most notably the formation of the dimers from the monomers (-1281 kJ mol^{-1}), tetramer chains from dimers (-152 kJ mol^{-1}) and hexamer chains from tetramers (-205 kJ mol^{-1}) all become significantly more favourable. This appears to indicate that metal substitution actually promotes chain growth rather than the formation of cyclic structures and certainly promotes polymerisation.

Indeed, this trend is reinforced by the result that, whilst metal substitution has made chain formation more likely, it has generally slightly decreased the probability of forming cyclic structures. For example, comparing the formation energies of a tetramer chain or 4-membered ring from two dimers, for the un-substituted system chain formation is more preferable by 23 kJ mol^{-1}, whilst for the substituted system this has

increased to 37 kJ mol^{-1}. Also the formation of a 4-ring from a tetramer becomes less favourable (35 kJ mol-1 compared to 22 kJ mol^{-1} in the un-substituted system) and a similar trend is observed for 6-ring and branched 4-ring formation hexamers. Only in the case of forming a fused 4-ring from a hexamer is there a decrease in relative formation energy (from 30 to 18 kJ mol^{-1}).

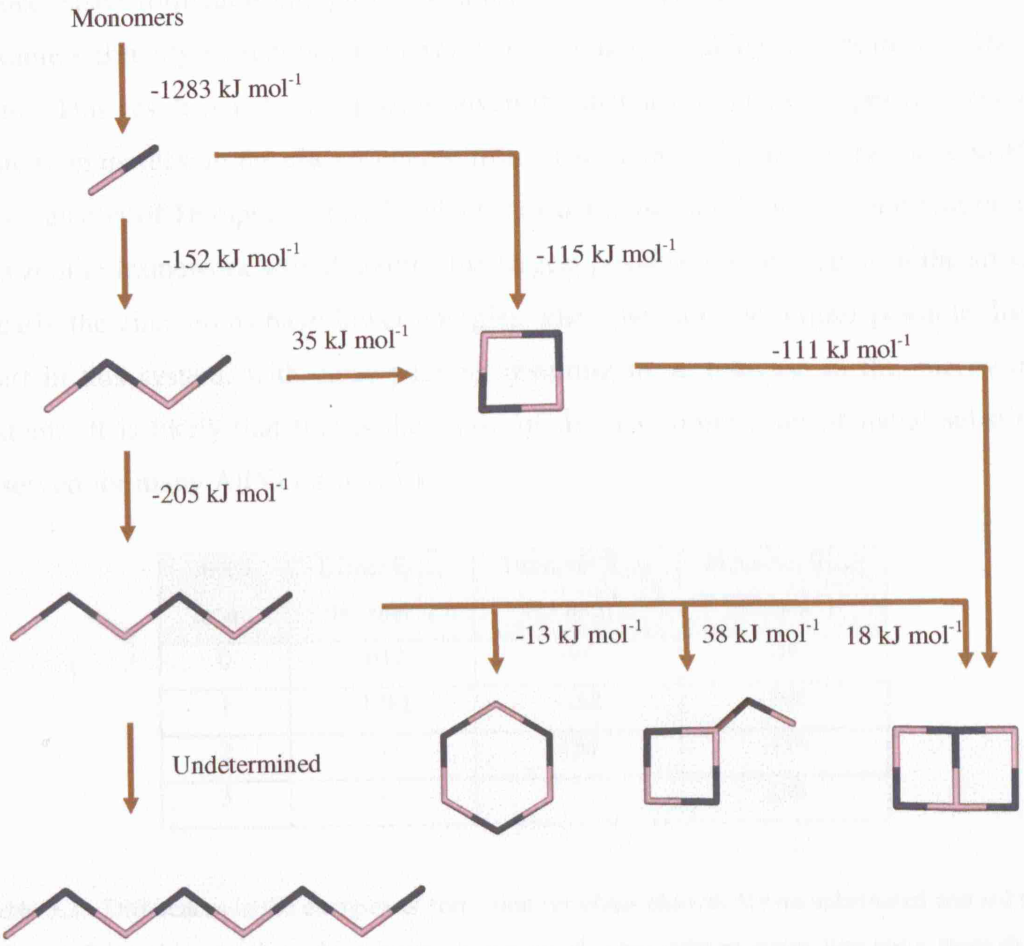

Figure 3.10: The formation energies of a number of different metal substituted AlPO clusters containing one zinc atom. The structures represented are idealised with dark blue representing aluminium or substituted zinc and light blue phosphorus. The energies of formation are calculated for the most stable form of the cluster from the condensation reaction of smaller clusters (i.e. releasing water).

It is also noted that, as with the un-substituted system, the formation of a fused 4-ring from a 4-ring and dimer has become more favourable (-69 to -111 kJ mol^{-1}). This is interesting as it suggests that, as in the case of pure AlPO, the formation of 4-membered rings can lead to the formation of fused 4-rings. Again however, the formation of 4-membered rings from dimers is not favourable (and actually slightly less favourable compared to the un-substituted system), and therefore the formation of fused 4-membered rings remains unlikely.

For clusters larger than a dimer it is theoretically possible to substitute more than a single metal atom into the structure. The formation energies for the tetramer and hexamer chains were therefore also determined with increasing metal substitution (i.e. a maximum of 2 for tetramers and 3 for hexamers). A comparison of these energies is given in table 3.2. It can be seen that although substitution of a single zinc atom results in decreased formation energies, substitution of two atoms for tetramers or three for hexamers actually increases the energies substantially, making the chains less likely to form. This result is not unsurprising given the increase in charge repulsion within the system on increasing the cluster charge from -1 to -2 or -3. This can then be considered an extension of Dempsey's rule[90], which has demonstrated how two aluminium atoms in a zeolite framework would assume the largest possible distance apart in the structure. Clearly the zinc atoms have lower energies when they are the largest possible distance apart in this system, with close packing resulting in an increase in the energy of the system. It is likely that this is the cause of the maximum limit of metal substitution observed for many AlPO frameworks.

metal atoms	Dimer E_{form} (kJ mol^{-1})	Tetramer E_{form} (kJ mol^{-1})	Hexamer E_{form} (kJ mol^{-1})
0	-612	-96	-76
1	-1281	-152	-205
2	-	154	-179
3	-	-	339

Table 3.2: Differences in the energies of formation for chain clusters for un-substituted and substituted systems. It can be seen that whilst inserting one metal atom induces chain formation more than one actually retards chain formation.

To summarise the results for the substituted AlPO clusters we see that in comparison to the un-substituted clusters:

- Formation of chain clusters becomes even more preferable compared to ring clusters
- Direct formation of a 4-ring from two dimers is now less favourable.
- Cyclisation of both the tetramer and hexamer chains generally becomes less favourable with increasing metal substitution.
- Inserting more than a single zinc atom retards chain formation

In order to improve the 'realism' of these calculations, the introduction of a model of solvation *via* a dialectric medium model (COSMO) was attempted on each of the clusters. However, in the majority of cases these minimisations failed to converge to minimised structures. The reason for this problem has not yet been identified although work is still ongoing to solve this issue. Despite this problem, the in vacuo energies presented in this work can be considered quantitatively comparable, as a comparison of the Gibbs free energy of silicate molecules in both a vacuum and solution calculated by Mora-Fonz *et al*[73] shows that although the actual magnitudes change significantly, the relative order is largely unaffected: A trend particularly apparent when the values are normalised for comparison, figure 3.11.

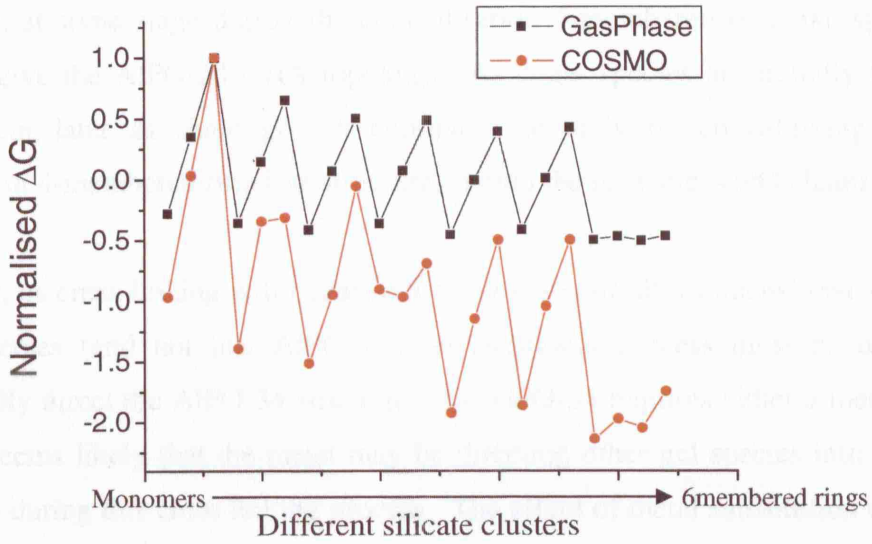

Figure 3.11: Comparison of the normalised gas phase and COSMO dielectric Gibbs free energies for a number of chain and cyclic silicate clusters taken from table 1 reference [73]. It can be seen that in almost all cases the trends remain the same. Note that the data plot includes all species from the primary reference starting with each monomer species and ending with the 6-membered rings.

These results were obtained using the knowledge and methodologies developed by Mora-Fonz *et al* for silicate systems, a process which has taken over three years to develop. Its implementation for the study of AlPO synthesis can therefore only be considered as exploratory. Many other clusters as well as protonated and deprotonated species need to be considered, and as such the results presented here should be considered preliminary findings.

Despite this however, there is clearly some strong qualitative evidence that, in contradiction to the original hypothesis, the insertion of a metal atom into forming

AlPO clusters results in the preferential formation of chain-like clusters rather than isolated ring systems. In silicate systems it has been shown that at high pH cyclic clusters form[72,73], however at more neutral values there is a preference for more chain like clusters[70,71]. Therefore, as AlPOs tend to form under acidic conditions (low pH), the formation of chains (rather than clusters), as observed in the calculations, is not unexpected and may well be occurring in AlPO gels.

As these results indicate chain rather than cluster formation in the initial gel, it would appear that the preferential formation of AlPO-34 over AlPO-5 is not due to metal substitution directing the formation of isolated 4 or fused 4-membered ring clusters. However, at some stage during the crystallisation 4-membered ring like species must form to give the AlPO-34 CHA topology. As chain species are initially formed this must occur later as chain growth continues; possibly by cross-linking of chains, resulting in 4-membered ring like structures within the growing AlPO chains.

However, as cross-linking will occur in the formation of all 3-dimensional AlPOs from chain species (and not just AlPO-34), an additional process must be occurring to specifically direct the AlPO-34 structure. As AlPO-34 requires either a metal or HF to form it seems likely that the metal may be directing other gel species into preferential locations during this cross linking process. The effect of metal substitution on other gel species is therefore examined using a number of experimental techniques detailed below.

Initially the synthesis of MeAPO-34 using a number of metals in different oxidation states is attempted. The results are discussed and then the phase purity of the successfully synthesised zinc, manganese and cobalt AlPO-34 and pure AlPO-5 structures used in the subsequent experiments are detailed. The *in situ* formation of MeAPO-34 is then examined using EDXRD and Raman spectroscopy is used to investigate the reaction using both *in situ* and *ex situ* techniques.

3.4.2 : Initial synthesis attempts

Initially a number of metal substitutions were attempted using various transition metals in differing oxidation states (table 3.3). In all cases the substitution level was 10% and the synthesis time 4 hours. As expected the AlPO-5 gel required a higher temperature

(140 °C) to form. Interestingly, it was also found that the synthesis temperature for the formation of MeAPO-34 was somewhat dependant on the metal type and that ZnAPO-34 could be formed at a lower temperature (80°C) compared to both cobalt and manganese (120°C).

From these experiments is it found that for metals in an oxidation state of (II) and for silicon (IV), pure MeAPO-34 is synthesised, except in the case of iron where an unidentified product is found (table 3.3). As expected a gel with no metal included results in AlPO-5. However, unexpectedly it was also possible to synthesise MeAPO-5 when metals with an oxidation state greater that (II) was used. For example, when manganese is used in the +2 oxidation state MeAPO-34 is formed, but when in the +3 state MeAPO-5 forms under the same conditions.

Metal (oxidation state)	Major product	Minor product / notes
NONE	AlPO-5	
Zn(II)	MeAPO-34	
Co(II)	MeAPO-34	
Mn(II)	MeAPO-34	
Mn(III)	MeAPO-5	unidentified impurity
V(III)	amorphous	AlPO-5 beginning to form
Fe(II)	unidentified	complex pattern – may contain some MeAPO-34
Fe(III)	MeAPO-5	unidentified impurity
Si(IV)	MeAPO-34	not performed – results from Marchese *et al*[7]

Table 3.3: The formation products from a gel containing different transition metals in varying oxidation states.

These results indicate that it is not just the availability of a metal ion which can be substituted into the framework that determines the preference for MeAPO-34 over MeAPO-5. The electronic state of the substituted metal is also essential for direction the structure, with metal (II) and silicon (IV) resulting in MeAPO-34. The introduction of metal (II) into the framework aluminium (III) sites and silicon (IV) for phosphorus (V) sites both result in a negative framework charge of -1 per substituted atom, whilst the introduction of a (III) metal does not induce a charge. It therefore seems that the induced framework charge may be partly responsible for direction of the MeAPO-34 structure. In the case of iron (II) the lack of MeAPO-34 formation can be explained by

considering the complex aqueous chemistry of iron[91], which results in the aerial oxidation of iron (II) to iron (III) under the mildly acidic reaction conditions.

3.4.3 : Characterisation of MeAPO-34 and AlPO-5

For the subsequent *in situ* and *ex situ* experiments, MeAPO-34 containing zinc, manganese and cobalt and pure AlPO-5 (resulting from the same gel) have been investigated at substitution levels varying between 0 and 30 molar percent. In order to check the purity of each system, LeBail fits were performed on MeAPO-34 at the maximum substitution level of 30% and on AlPO-5. The initial fitting parameters were taken from the measurements of Ito *et al*[6] for SAPO-34 at approximately 20% substitution. Figure 3.12 gives representative fits and table 3.4 details the unit cell parameters and refinement parameters for each system. It was noted that the ZnAPO-34 sample shows evidence of peak broadening, which can be attributed to the formation of smaller crystallite sizes in comparison to cobalt and manganese systems. Note that the diffraction pattern for the ZnAPO-34 system was recorded at a smaller step size (0.0073 2θ) compared to the other samples (0.01 2θ), and this difference in step size accounts for the difference in quality of the fitting parameters given below.

From the results we see that both MeAPO-34 and AlPO-5 have been successfully synthesised from the same gel (with and without substituted metal). The fitting parameters for each sample are good for each experimental set-up and indicate the unit cell has been successfully modelled (the fitting parameters for the Zn system are lower as it was recorded with a smaller step size). The synthesised MeAPO-34 compares very well with the SAPO-34 parameters previously recorded by Ito *et al*[6] with *a*, *b* and *c* as well as the unit cell volume around the same values.

It has been shown that the introduction of hetroatoms into microporous frameworks can be related to an increase in unit cell size[37,92-94]. As the SAPO-34 synthesised by Ito *et al* was 20% substituted, the similar unit cell volumes indicate a substitution of at least 20% may also have occurred in these MeAPO-34 systems. However, the substitution level may be higher than 20% as it has also been shown that increased substitution (particularly at high levels) is not always directly proportional to a unit cell expansion, with decreases even occurring in some circumstances[37,95]. The EDX data (see below) confirms this for ZnAPO-34, with a substitution of 29%.

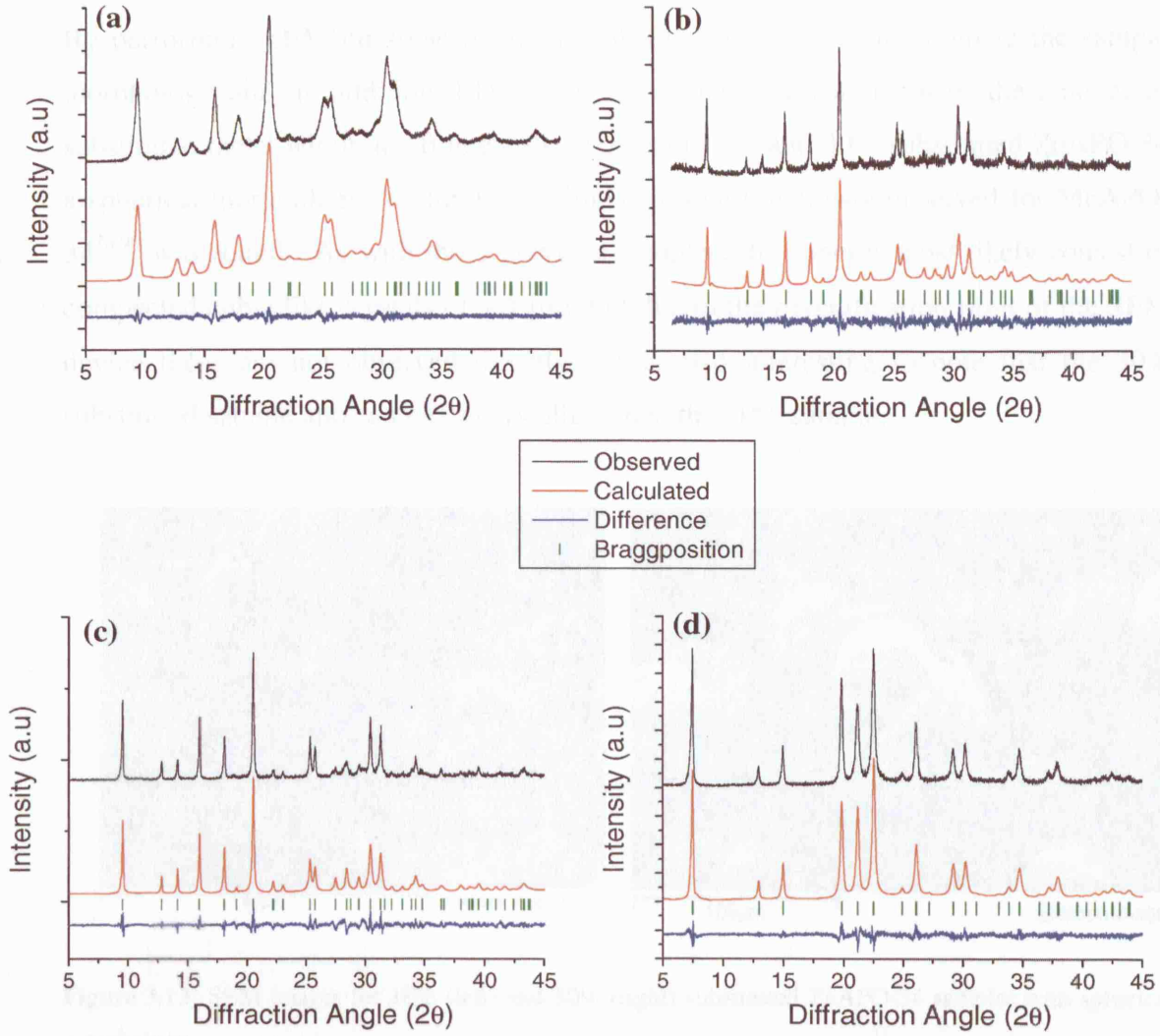

Figure 3.12: LeBail fits for ZnAPO-34 (a), CoAPO-34 (b) and MnAPO-34 (c) with 30% substitution and AlPO-5 (d) formed at higher temperatures.

Parameter	SAPO-34[6] (~20%)	ZnAPO-34 (~30%)	CoAPO-34 (~30%)	MnAPO-34 (~30%)	AlPO-5
Space group	R3	R3	R3	R3	P6cc
$a = b$ (Å)	13.781(1)	13.841(1)	13.823(2)	13.837(1)	13.660(1)
c (Å)	14.846(2)	14.833(2)	14.721(2)	14.717(1)	8.389(1)
Volume (Å^3)	2441.7(5)	2460.9(4)	2436.0(6)	2440.2(4)	1355.7(3)
R_p		3.87	12.5	8.39	10.5
R_{wp}		5.09	15.9	10.9	14.1
R_{exp}		3.81	13.19	9.73	11.05
DW-exp		1.9291	1.9041	1.9142	1.9142

Table 3.4: Final LeBail parameters for MeAPO-34 (compared with the work of Ito *et al*) and AlPO-5. The values are very similar indicating MeAPO-34 has been successfully synthesised. The number in brackets is the standard deviation of the last digit of a parameter. DW-exp is the Durbin-Watson statistic as described in 'The Rietveld Method (1st ed)', *R. A. Young*, Oxford University Press, 2002.

By performing SEM on some of the samples it was possible to compare the sample morphology and, in addition, EDX provides a direct measurement of the amount of substituted metal within the framework. For both 10% and 30% substituted ZnAPO-34 a spherical morphology (figure 3.13), similar to that previously observed for MeAPO-34[38,96] was found. As with these previous samples, the spheres most likely consist of compacted cubic like crystals of ~ 1 μm, but due to the magnification limit of the SEM device these are not observed directly. It is also interesting to note that the 30% substituted sample appears more crystalline than the 10% sample.

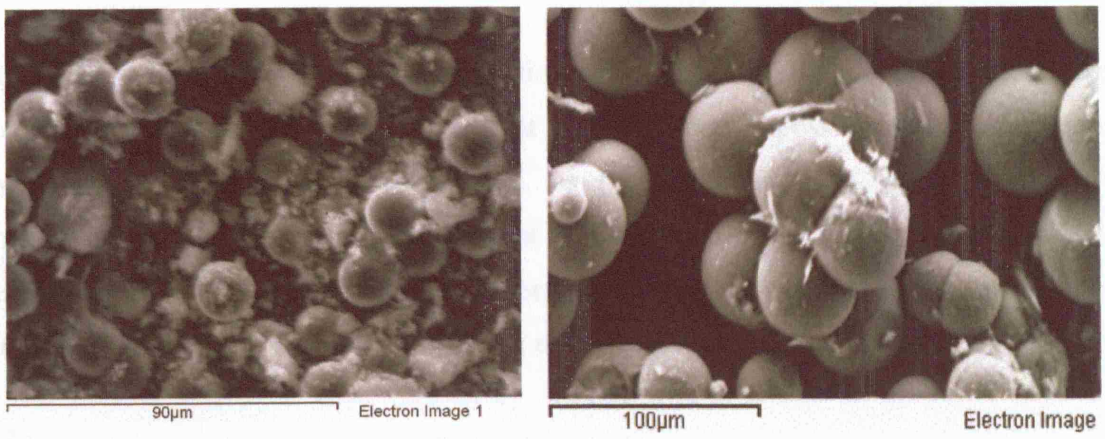

Figure 3.13: SEM images for 10% (left) and 30% (right) substituted ZnAPO-34 samples with spherical morphology.

The EDX measurements indicate metal substitution is occurring at the expected levels with substitution of 12 % and 29% determined for the 10% and 30% substituted systems respectively (this can be considered to be within the expected error for an un-polished EDX sample).

From this characterisation work two particularly important points are note worthy. The first is the fact that the zinc substituted system can form at a particularly low temperature compared to cobalt. Secondly, the formation of MeAPO-34 is facilitated specifically by the presence of a metal in the (II) oxidation state (or silicon (IV)) within the framework. These factors may both form part of the overall explanation as to why addition of a metal is required for the formation of MeAPO-34 rather than AlPO-5 and each is investigated in detail in the subsequent sections.

3.4.4 : The effect of metal type on rate of formation

As mentioned above, the insertion of zinc rather than cobalt or manganese allows the formation of MeAPO-34 at significantly lower temperatures. In order to further investigate this effect a series of *in situ* EDXRD experiments were carried out on both zinc and cobalt (10%) gels at a number of temperatures and the activation energies of the processes were calculated. Full details of the EDXRD experimental setup, measurements and analysis are given in chapter 4 where the technique is used more extensively.

From a direct comparison of the crystallisation curves (Figure 3.14) the difference in the rate of formation is clear. Indeed, except at 110 °C, it was impossible to compare each system at exactly the same temperature, as the formation of CoAPO-34 at low temperatures was very slow or did not occur in the time frame of the experiment, whilst the formation of ZnAPO-34 at high temperatures was very rapid resulting in too few data points on the growth curve to calculate the rate of formation.

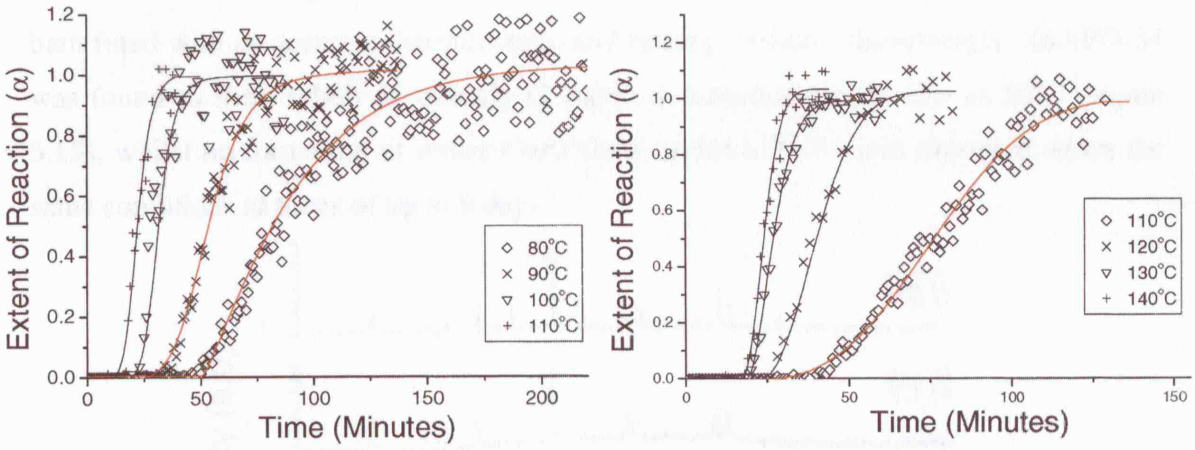

Figure 3.14: Growth curves for the formation of zinc (left) and cobalt (right) AlPO-34 at different temperatures. (Refer to chapter 4 for details)

At 110°C the induction times (time lapsed until appearance of crystalline material) are directly comparable (table 3.5) with zinc inducting after only 17 minutes compared to 37 minutes for the cobalt system. By adapting the kinetic model proposed by Avarami[97-99] and Erofe'ev[100] using the method detailed by Sharp and Hancock[101], it is possible to derive the rate constant (k) for each reaction (table 3.5). As expected, this is far higher for zinc (0.147 ± 0.01 min^{-1}) than cobalt (0.021 ± 0.002 min^{-1}) and a similar

trend is observed for the overall activation energy (E_a) each system. Using the well known Arrhenius expression, these were found to be 70 ± 5 kJ mol^{-1} for the zinc system and 83 ± 5 kJ mol^{-1} for the cobalt system.

Metal	Temp (°C)	Induction Time (mins)	k (min^{-1})	E_a (kJ mol^{-1})
Zinc	80	49	0.022	
	90	37	0.049	
	100	22	0.088	
	110	17	0.147	70
cobalt	110	37	0.021	
	120	24	0.053	
	130	19	0.100	
	140	17	0.141	83

Table 3.5: The induction times, rates of reaction (k) and induction energies (E_a) for zinc and cobalt substituted AlPO-34 formation. Note that percentage errors on these values are as given in chapter 4.

In order to investigate further the low temperature formation of 10% substituted ZnAPO-34, *ex situ* experiments were performed utilising polyurethane bottles and an oil bath fitted with an accurate thermocouple and heating system. Surprisingly, ZnAPO-34 was found to form relatively quickly (2 days) in temperatures as low as 50°C (figure 3.15), whilst no formation of either CoAPO-34 or MnAPO-34 was observed under the same conditions at times of up to 9 days.

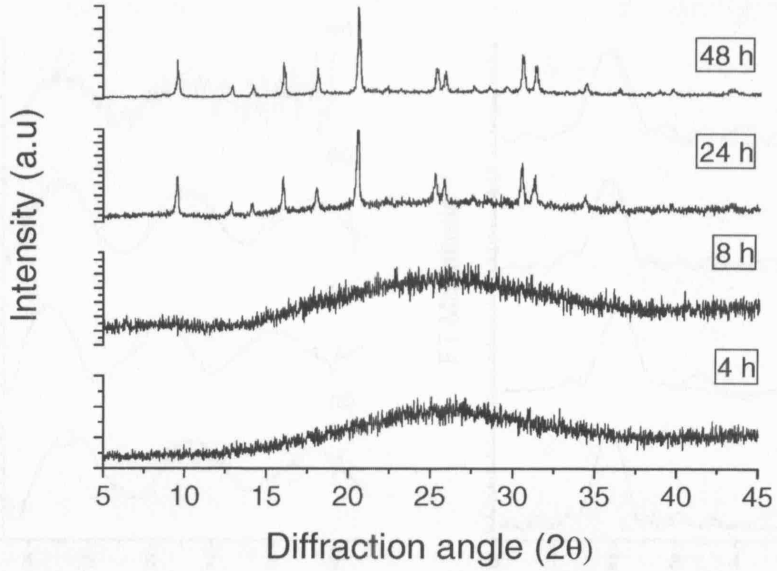

Figure 3.15: The formation of ZnAPO-34 at 50°C in an oil bath. Both CoAPO-34 and MnAPO-34 did not form after 10 days.

This is a very low temperature for the formation of a microporous AlPO system and supports the *in situ* work suggesting that either zinc has some enhancing role, significantly reducing the energy required to activate the system, or that cobalt causes some retardation in the rate of reaction. This result is interesting in the light of Walton *et al*[58] who have previously stated that the formation of AlPOs *via* a chain mechanism similar to that proposed by Oliver *et al*[45] is unlikely, as 'metastable 3-dimensional phosphates may crystallise at close to room temperature'. These results indicate that AlPOs can (under some circumstances) form at temperatures close to room temperature, and therefore the formation of AlPOs *via* such a mechanism must now be considered possible.

An understanding of the coordination chemistry of the substituted metals during the AlPO synthesis may give some indication as to the reason ZnAPO-34 formation is quicker than CoAPO-34 formation. XAS can give information on the local coordination environment of substituted metals and was performed on both pre-crystalline and as synthesised crystalline gels. The resulting zinc and cobalt K-edge EXAFS data and Fourier transforms are given in figure 3.16. Along with the experimental data (solid line), the results of a least squares fits using a primary single shell consisting of cobalt or zinc surround by oxygen atoms in a local average arrangement are shown (dotted line). From this plot it can be seen that a good fit can be obtained for each sample for the single shell.

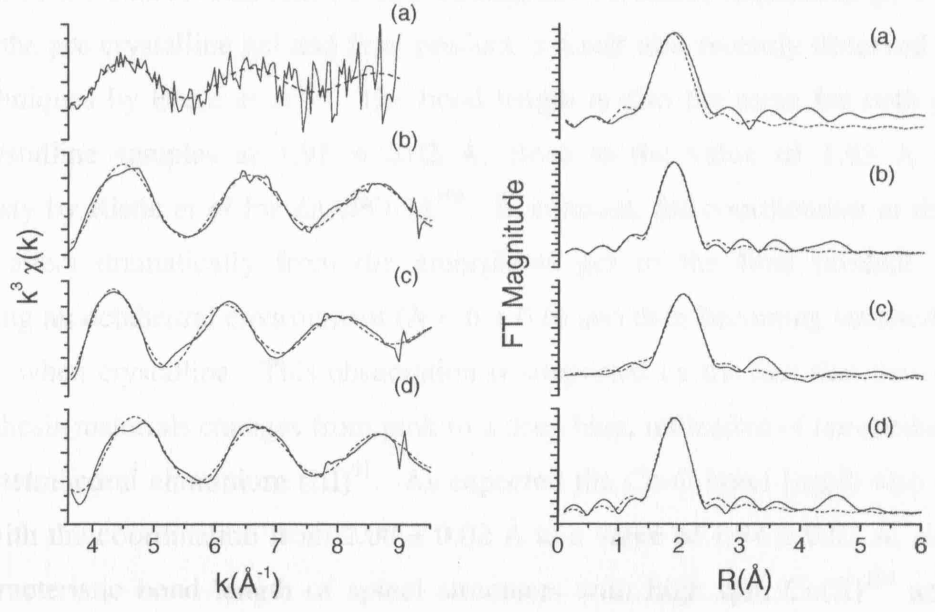

Figure 3.16: The EXAFS data (left) and corresponding Fourier transforms (right) for pre-crystalline ZnAPO (a), crystalline ZnAPO-34 (b) pre-crystalline CoAPO (c) and crystalline CoAPO-34 (d).

It is clear from figure 3.16 that the quality of the data for the ZnAPO pre-crystalline gel is much lower than for the other samples, which is due to the fact that these data were originally part of an *in situ* experimental attempt and therefore recorded using quick EXAFS (in fluorescence mode). This results in a far lower quality scan than the other samples recorded in normal EXAFS, however despite this loss of quality the data is sufficient to allow for a good fit of the first shell data.

The metal coordination (*N*), Metal oxygen bond distance, Debye-Waller factor (σ^2) and reliability 'R-factor' are given in table 3.6. As expected from the close overlap of the experimental and least squares simulations the R-factors are quite low (except in the case of ZnAPO gel which is explained above, and for the quality of data still reasonable) and indicate the correct model has been used.

Sample	***N***	**Me-O distance *R*(Å)**	**σ^2(Å^2)**	**R-factor (%)**
ZnAPO gel	4.1	1.910	0.014	69.32
ZnAPO-34	4.1	1.915	0.010	20.23
CoAPO gel	6.4	2.079	0.019	22.44
CoAPO-34	3.9	1.940	0.010	23.33

Table 3.6: The coordination number (*N*), cobalt oxygen bond distance, Deby-Waller factor (σ^2) and R-factor for each AlPO gel and crystalline material.

Analysis of the data reveals that the zinc coordination remains tetrahedral ($N = 4 \pm 0.4$) in both the pre crystalline gel and final product, a result also recently observed using *in situ* techniques by Beale *et al*[102]. The bond length is also the same for both pre- and post-crystalline samples at 1.91 ± 0.02 Å, close to the value of 1.93 Å reported previously by Ristic *et al* for ZnAPO-34[103]. In contrast, the coordination in the cobalt system alters dramatically from the amorphous gel to the final product, initially occupying an octahedral environment ($N = 6 \pm 0.6$) and then becoming tetrahedral ($N = 4 \pm 0.4$) when crystalline. This observation is supported by the fact that the colour of the synthesis materials changes from pink to a deep blue, indicative of tetrahedral cobalt (II) for tetrahedral aluminium (III)[91]. As expected the Co-O bond length also changes along with the coordination from 2.08 ± 0.02 Å to a value of 1.94 ± 0.02 Å, similar to the characteristic bond length of spinel structures with high spin Co(II)[104] and other CoAPO materials[105-107].

It is also noted that the Debye-Waller factors are far higher in the amorphous gels (0.014 and 0.019 ± 0.001 $Å^2$) than in the crystalline products (0.010 ± 0.001 $Å^2$). This is expected as there would be significant disorder around the metal environment in the amorphous materials but far less in the crystalline products.

These EXAFS results suggest that the difference in the rate of formation (and temperature requirement) for the ZnAPO and CoAPO systems can be at least partly attributed to the need to obtain a tetrahedral geometry to become inserted into the final AlPO framework. In the case of cobalt the initial geometry is octahedral and therefore a rearrangement and removal of some coordinating ligands is required before the metal is in a suitable geometry for successful inclusion in a crystalline framework. This rearrangement requires additional energy as reflected in the increased activation energy and slower rates of reaction seen for the cobalt system. The zinc substituted system does not require any rearrangement and therefore no additional energy is required for reordering. Therefore, the reaction has a lower activation energy and can take place at low temperatures and with increased rates of reaction. This requirement for rearrangement may also partly explain the fact that MeAPO-5 can be formed with TEAOH in the presence of low concentrations of cobalt but has never been observed in the case of zinc. These observations are explained in more detail after the interaction of the organic with the AlPO framework has been discussed below.

3.4.5 : The metal organic SDA interaction and conformation

3.4.5.1 : *In situ* Raman experiments

Whilst the experiments above can be used to understand the differences in the rate of formation between zinc and cobalt AlPO-34 systems, they still do not explain why the presence of a metal in the (II) oxidation state is required to form MeAPO-34 in preference over AlPO-5.

As discussed in the Introduction, the role of the organic is complex, with Davis and Lobo[76] suggesting three potential roles (space filling, structure directing, or true templating). Raman spectroscopy can be utilised to measure changes in the organic SDA throughout the formation process. Any changes in the SDA conformation may indicate interactions in the gel chemistry that may allow further characterisation of the role of the substituted metal and gel components in the preferential formation of

MeAPO-34 over AlPO-5, potentially leading to a greater understanding of the role of the organic.

A typical Raman spectrum is given in figure 3.17 and the majority of the bands are due to the TEAOH template and have been previously assigned[84]. The two possible template conformations give rise to bands in slightly different positions in the Raman spectrum. Unfortunately, due to bands of the TEAOH overlapping the bands from the other gel constituents (figure 3.17), it was not possible to follow the changes in the framework constituents during crystallisation. For example, the $\nu(C_4N)$ and $r(CH)_3$ bands for TEAOH both the tg.tg and tt.tt conformations at 892 and 902 cm^{-1} overlap a strong band at 896 cm^{-1} due to the $\nu(PO_3)$ of H_3PO_4. However, it has been previously shown that the intensity of the $\nu(C_4N)$ bands at 662 (tg.tg) and 672 cm^{-1} (tt.tt) give a quantitative indication of the amount of template in each orientation[84]. Fortunately these bands are not obscured or overlapped by bands due to other gel components and are therefore ideal to monitor any changes in the SDA as crystallisation takes place.

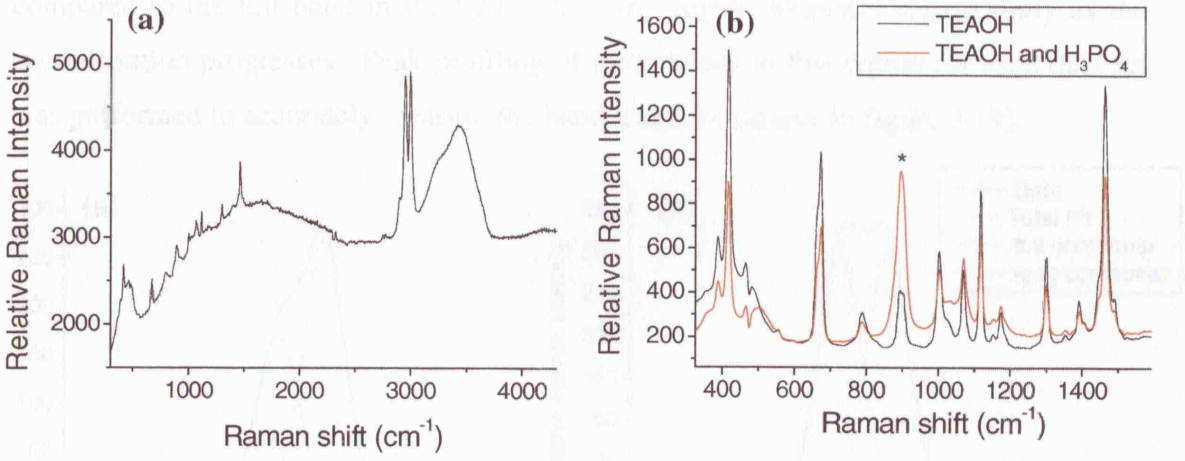

Figure 3.17: A total Raman spectrum for a ZnAPO-34 gel prior to heating (a) and a comparison of pure TEAOH and a TEAOH phosphoric acid mixture (b) the asterisk marks a phosphoric acid band masking two signals from the TEAOH.

In situ experiments were then used to monitor these bands for changes in the organic conformation throughout the entire course of the reaction, in both substituted and un-substituted gels. Time resolved stack plots for the 30% zinc substituted and un-substituted system over the $\nu(C_4N)$ band region are shown in figure 3.18. Critically, there are significant changes in the relative intensities of the bands for the 30% Zn^{2+} substituted gel during crystallisation. These changes are not seen in the un-substituted systems, which did not crystallise (note that at higher temperatures this gel will

crystallise to form AlPO-5, but due to temperature effects discussed below, *in situ* experiments on the formation of AlPO-5 were not possible).

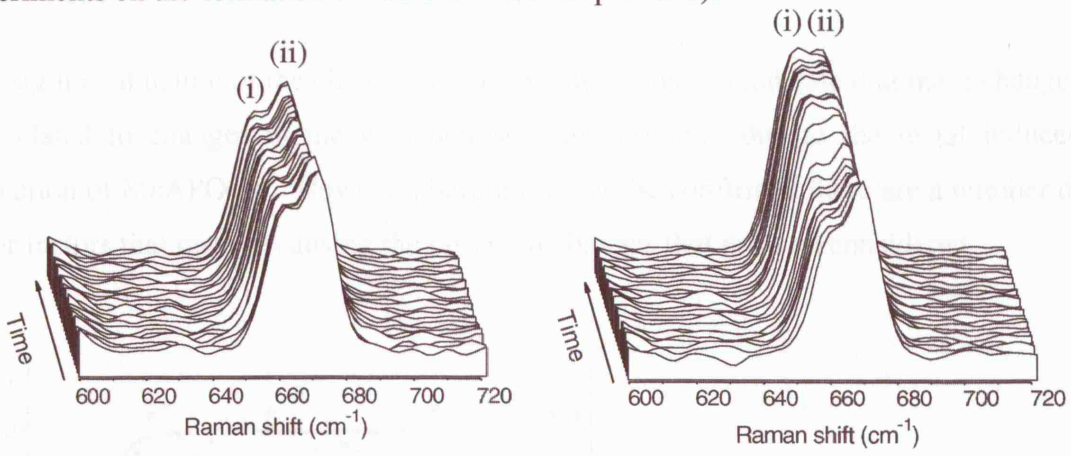

Figure 3.18: Time resolved Raman stack plots of the $\nu(C_4N)$ band region of an AlPO-5 gel (left) and ZnAPO-34 gel (right). An increase in the tg.tg conformation (i) compared to the tt.tt conformation (ii) is clearly seen for ZnAPO-34.

We see that for the metal substituted system, the relative intensity of the tg.tg band compared to the tt.tt band in the 620 – 720 cm^{-1} region increases significantly as the crystallisation progresses. Peak profiling of these bands in this region for each data set was performed to accurately measure the band height (example in figure 3.19).

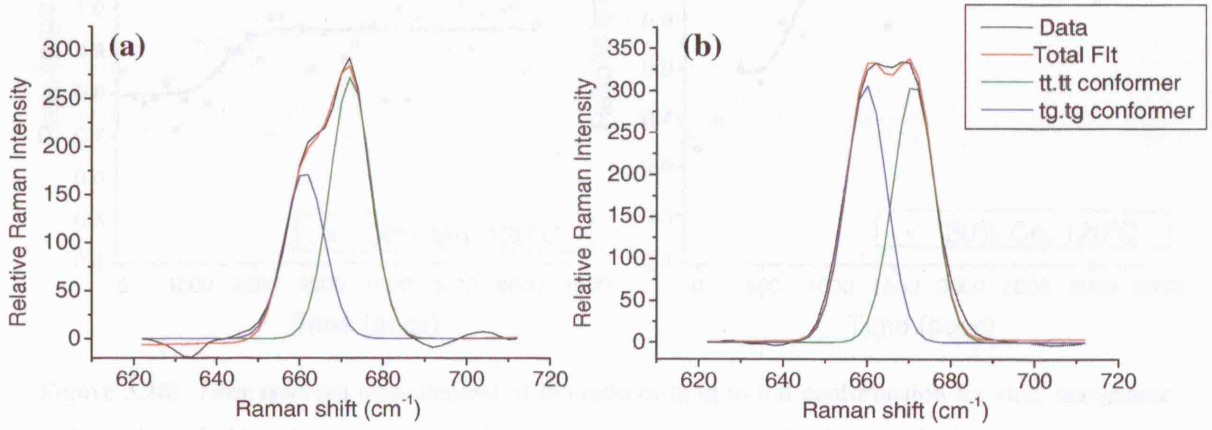

Figure 3.19: Example fits of the $\nu(C_4N)$ bands for both the tt.tt and tg.tg conformations, taken from the beginning (a) and end (b) of a 30% ZnAPO-34 experimental run.

By calculating the ratio of tg.tg to tt.tt and plotting these as a function of time (figure 3.20) we see that the SDA only changes conformation in the 30% metal substituted gels. In each case the growth is sigmoidal in nature and appears very similar in shape to the crystallisation curves seen for the growth of Bragg peaks. Experiments were also

performed using an identical experimental set up but with lower substitution levels; interestingly however no conformation changes were observed.

The sigmoidal nature of the change in ratios would appear to indicate that these changes are related to changes in the gel chemistry and possibly due to the metal induced formation of MeAPO-34. However, before this can be confirmed there are a number of other factors that may be causing the observed changes that must be considered.

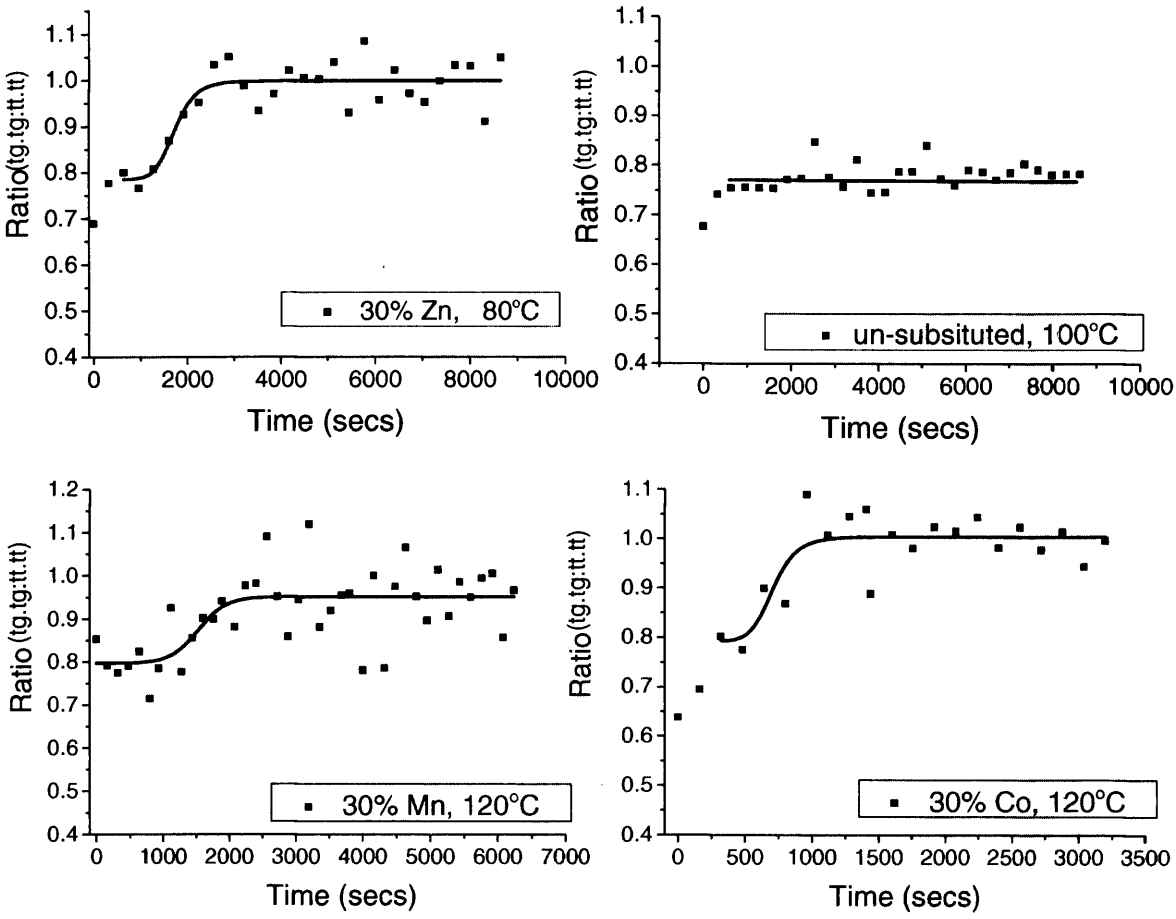

Figure 3.20: Time resolved measurement of the ratio of tg.tg to tt.tt conformation for zinc, manganese and cobalt APO-34 and a non-substituted gel; no changes are seen for the un-substituted system. Note that the lines are meant only as a guide to indicate the sigmoidal like nature of the curves.

The first consideration is the temperature dependence previously demonstrated by Naudin *et al*[84]. This leads to an increase in the relative amount of tg.tg conformer compared to tt.tt as temperature increases. It is therefore possible that the observed increase in tg.tg conformation in the ZnAPO-34 system could be a simple consequence of sample heating and not crystallisation. Therefore, in order to identify the extent of conformational exchange, Raman spectra for a TEAOH (35 % aqueous) solution was

recorded at room temperature and at a number of typical synthesis temperatures (figure 3.21, left). From these results it is observed that changes in the conformation ratio between 80 and 120°C are not of the extent seen in the gel during the crystallisation studies. However, at the temperature required for AlPO-5 formation (140°C) the changes would be substantial and therefore *in situ* experiments could not be performed at this temperature (as mentioned previously).

These results are confirmed by a closer examination of the initial stages of the ZnAPO-34 reaction which reveal that the temperature dependant stage of the conformation change is clearly separate from the sigmoidal changes. In a typical reaction (figure 3.21, right) as the sample vial heats up, the change in ratio due to temperature increase occurs (a) but stops once the experimental temperature is reached (b) and further changes are not seen until the formation of the crystalline framework begins (c).

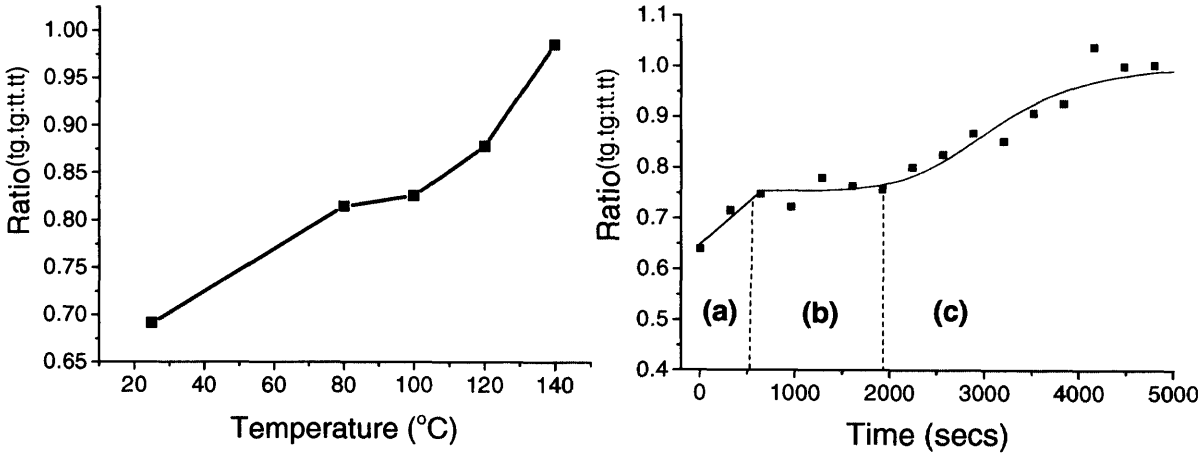

Figure 3.21: The effect of temperature on the relative ratios of the TEAOH conformer in solution (left) and in the gel crystallisation (right). The process of conformation change occurs early on in the reaction as the sample cell reaches the experimental temperature (80°C) (a) no further changes are then seen (b) until changes due to metal-framework interactions occur (c).

This experiment has shown that the observed changes are not simply due to temperature variations. However, as the changes appear to be directly related to the inclusion of a divalent metal in the gel system, it is possible that a simple metal-organic interaction unrelated to the crystallisation of MAPO-34 may be occurring. To investigate this possibility, TEAOH was added drop wise to a simple mixture of zinc acetate dissolved in water. Upon addition of TEAOH the solution became opaque, suggesting some form of interaction does occur. However, subsequent heating to 80°C of this solution (figure 3.22) show no changes in the ratio of conformers indicating that a direct metal-organic

interaction is not responsible for the conformation changes observed in the crystallization gel. Indeed, the final product from this reaction is crystalline zinc oxide, a product not observed during the formation of MeAPO-34.

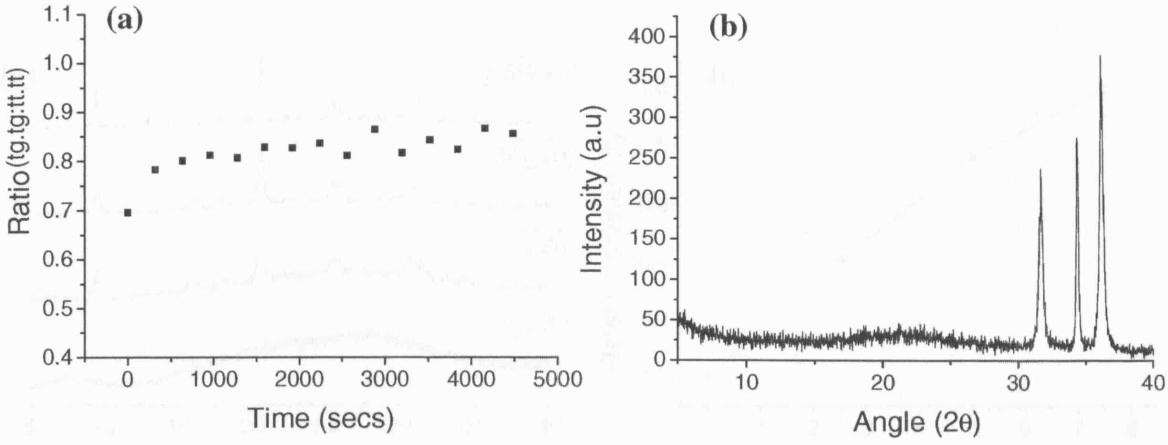

Figure 3.22: In situ Raman ratio measurements for a Zn acetate and TEAOH mix (a) indicating no change in the conformer ratio during reaction and an XRD of the final product formed from the reaction identified as ZnO (b).

One final consideration is the possibility that the substituted metal is acting purely as a nucleation point for the formation of MeAPO-34, which would imply that whilst some metal is necessary to begin the formation of the AlPO, it is not necessary for the conversion of the majority of the AlPO gel to AlPO-34. If this is the case, then the conformation changes observed due to increased metal insertion would most likely be unrelated to the crystallisation process.

To asses this possibility, a series of *ex situ* measurements were performed to measure the crystallinity of MeAPO-34 gels with low zinc components. Gels with substitution levels ranging from 0 to 7.5 % were heated for 24 hours at 80°C and the extent of crystallinity was assessed by measuring the area under the (1,0,0) diffraction peak (from a standard XRD pattern) using a Pseudo-Voigt function.

From these data (figure 3.23) it is clear that that the extent of crystallinity is related to the amount of zinc present in the synthesis mixture. If the substituted metal was acting purely as a nucleation centre then the amount of crystalline product would be dependant primarily on other factors, such as temperature and synthesis time, as 'pure' AlPO-34 growth occurs around the initial metal seed. The dependence of crystallinity on

substitution level is therefore strongly indicative that the metal is essential for the formation of MAPO-34, with growth occurring only when there are sufficient amounts in the gel to participate directly in the formation of the framework.

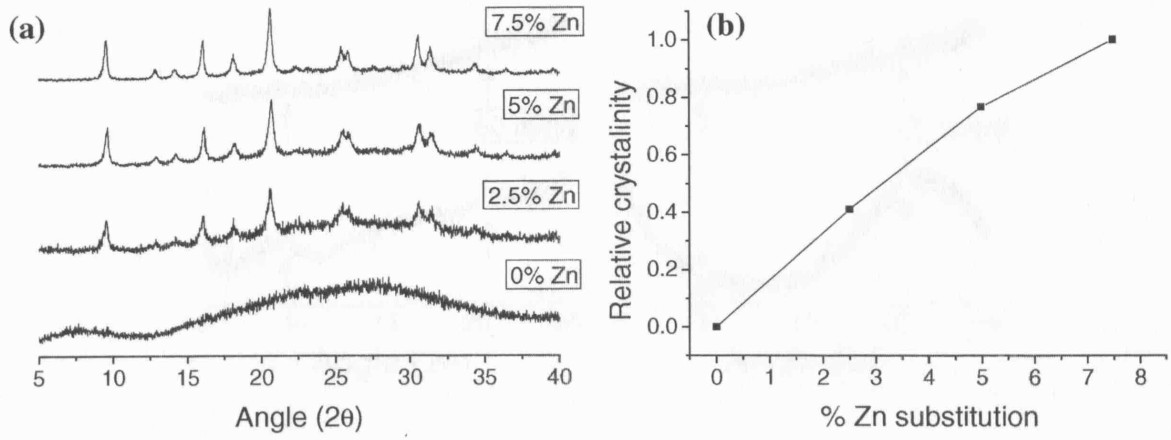

Figure 3.23: XRD patterns of low substitution level ZnAPO-34 samples (a) and the relative crystallinity of the (1,0,0) peak from each of these samples (b), demonstrating the direct relationship between substitution level and crystallinity.

All of the above experiments support the fact that the conformation changes measured in the substituted system are directly related to the formation of MeAPO-34 and that the metal is essential for crystallisation. The next step is to try and identify when these changes occur compared to the onset of AlPO crystallisation, which will indicate which process is actually being probed by these Raman measurements.

Thus a series of *ex situ* crystallisation measurements were performed on 30% ZnAPO-34, allowing the approximate point at which crystalline Bragg peaks begin to appear to be identified. In order to allow for direct comparison with the Raman data the experiments were performed at 80°C in the Raman heating furnace. The samples were tested by XRD at ten minute intervals and the plots between 20 and 70 minutes are shown in figure 3.24. The appearance of the two strongest Bragg reflections for MeAPO-34 (1,0,0) and the (2,0,-1 / 2,-1,0) are observed after 40 minutes and by 60 minutes the peaks are clearly visible.

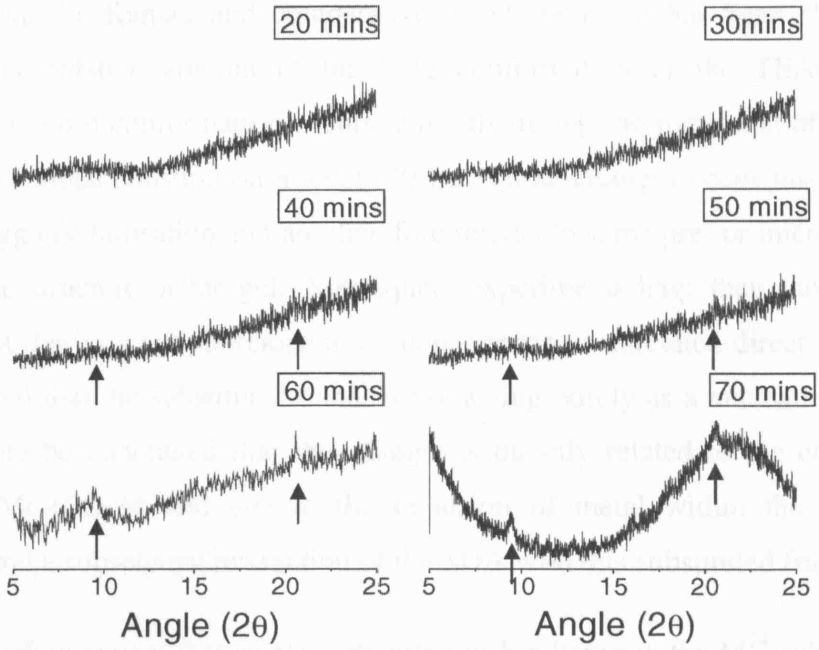

Figure 3.24: XRD patterns of ZnAPO-34 crystallisation at 10 minute intervals. Arrows indicate the onset of the strongest Bragg peaks (1,0,0) and the (2,0,-1 / 2,-1,0) which appear to form between 40 – 50 minutes.

The appearance of these Bragg reflections can be directly related to the changes in the Raman conformation ratios (figure 3.25). It can be seen that from this plot that the changes in Raman conformation take place after 1920 seconds (32 minutes), and are therefore occurring prior to the appearance of Bragg reflections. This indicates that the conformational changes coincide with the formation of a pre-phase, a metal-organic aggregate or even microcrystalline ZnAPO-34 which is undetectable by XRD.

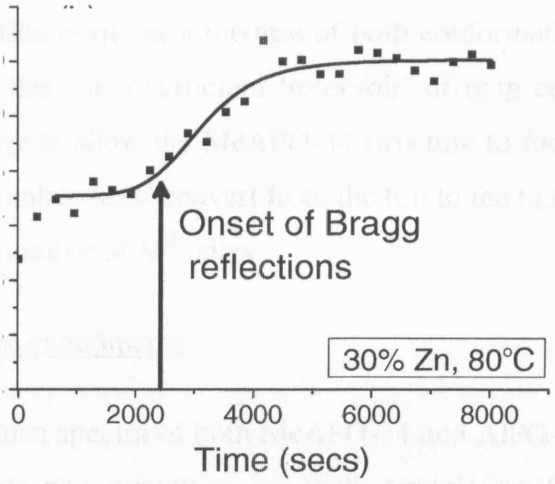

Figure 3.25: The combined *in situ* Raman and ex-situ XRD results for 30% ZnAPO-34, the arrow marks the onset of crystallization.

From these *in situ* Raman and comparative XRD studies it has been shown that a change in the relative amount of the tg.tg conformation of the TEAOH organic compared to the tt.tt conformation occurs, but only during the formation of MeAPO-34 at a very high metal substitution a level (30%). These changes occur just prior to the onset of Bragg crystallisation and are therefore related to some pre- or micro-crystalline change in the structure of the gel. Subsequent experiments have then shown that this change is not due to a simple temperature dependence or unrelated direct zinc-organic interaction and that the substituted metal is not acting purely as a nucleation centre. It must therefore be concluded that this change is directly related to the crystallisation process of MeAPO-34 and due to the inclusion of metal within the crystallising framework and a subsequent interaction of the SDA with this substituted framework.

It would therefore appear that an intimate relationship between the M^{2+} substituted into an Al^{3+} site of the microporous framework and the organic is occurring, which is critical for the formation of the MeAPO–34 structure. As changes are noted only for gels containing divalent metals it seems likely that the interaction is being induced by the resulting framework charge. This induced charge appears to cause one of the conformers (tg.tg) to locate at specific positions within the framework, and as suggested in the DFT calculations this may allow the formation of 4-membered ring like structures during the cross linking of AlPO chains. This specific tg.tg. SDA location therefore appears to be a necessary step to enable the MeAPO–34 framework to form.

It is noted that no changes in the *in situ* Raman data with gels containing $Zn^{2+} \leq 20$ % is observed, which can be rationalised by considering that, prior to reaction, the TEAOH SDA in aqueous solution exists as a mixture of both conformations. Therefore, at low metal concentrations, there is a sufficient 'reservoir' of tg.tg conformer already in the system at the beginning to allow the MeAPO-34 structure to form. However, at higher M^{2+} loadings some template must convert from the tt.tt to the tg.tg conformer in order to occupy the increased number of M^{2+} sites.

3.4.5.2 : *Ex situ* Raman experiments

By measuring the Raman spectra of both MeAPO-34 and AlPO-5 after synthesis it was possible to investigate the quantities of each organic conformation in the final crystalline structure. This procedure is particularly useful in the case of AlPO-5,

because, as previously noted, it was not possible to measure any changes *in situ* due to the higher temperature required.

Data were recorded for the initial gel, the final crystalline product (after filtration and washing in distilled water) and after an overnight treatment in alkaline solution for both ZnAPO-34 and AlPO-5. The treatment in alkaline solution was performed to remove any remaining loosely bound surface SDA organics, leaving only those trapped within the framework.

Example plots of the 620 – 720 cm^{-1} region for MeAPO-34 and AlPO-5 after alkaline treatment (figure 3.26) reveal that unlike the *in situ* experiments, significant overlap between the tt.tt and tg.tg bands now occurs. In the case of AlPO-5 it is possible to identify the tg.tg band as a shoulder on the main tt.tt band; however, for MeAPO-34 it almost appears as though only a single band is present. In both cases it was difficult to deconvolute the two bands sufficiently to set reasonable starting parameters for fitting. In such circumstances a second derivative plot of the data can be used to verify the number of bands present and approximate the relative intensities of each peak if more than one is present, allowing reasonable fitting parameters to be obtained.

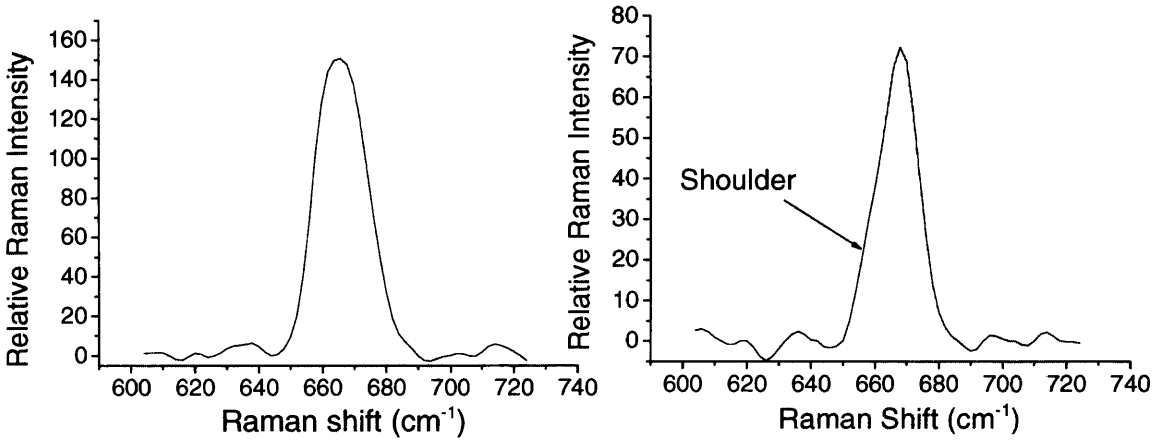

Figure 3.26: Plots of the 620 – 720 cm^{-1} region of the Raman spectrum for crystalline MeAPO-34 (left) and AlPO-5 (right) the overlap of the bands due to each conformer is clear and the shoulder representing part of the tg.tg band is marked.

The raw data and second derivative plot of crystalline MeAPO-34 are shown in figure 3.27. A comparison with simulated peaks containing one and two bands confirms that,

although the sample initially appears to consist of a single band centered at 667 cm^{-1}, it can be deconvoluted into two bands with the most intense being at a lower Raman shift.

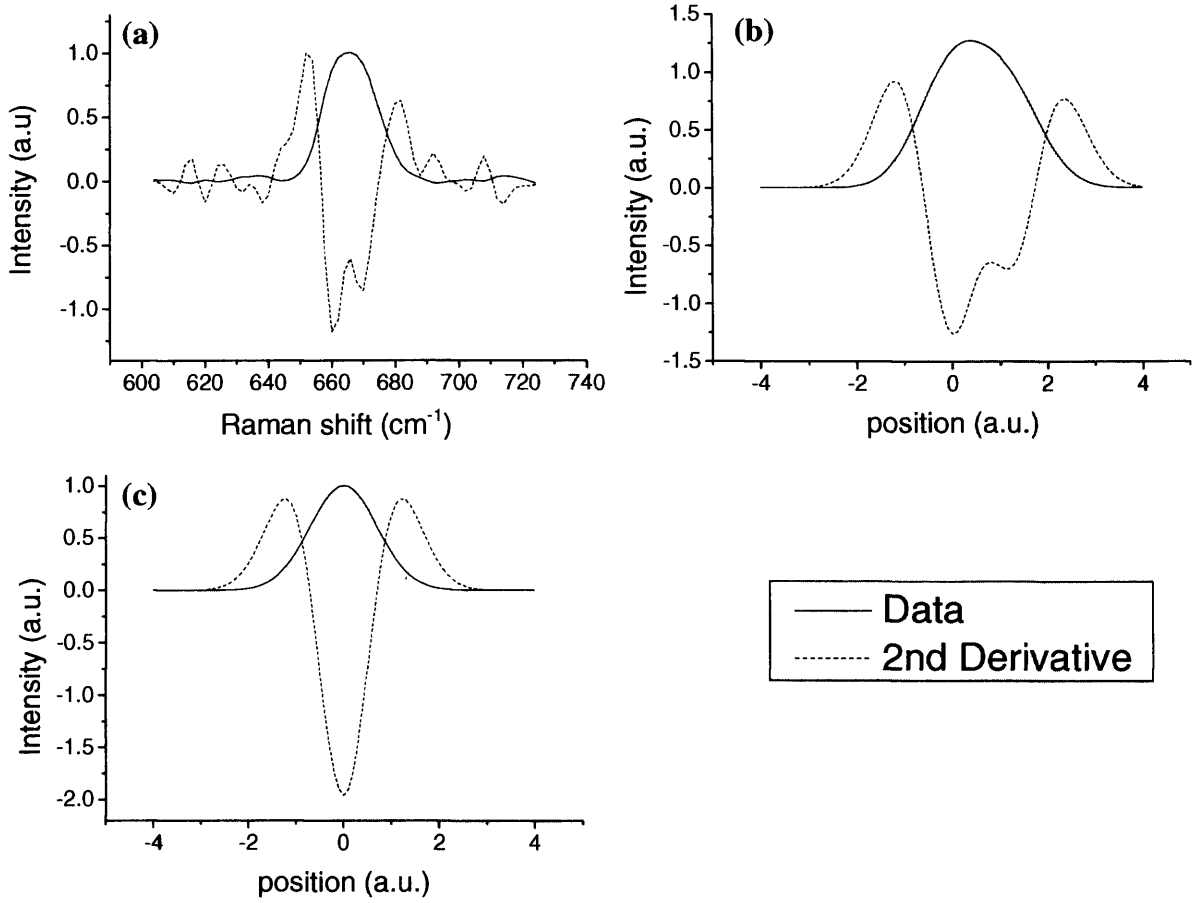

Figure 3.27: The raw data and second derivative plot (a) of crystalline ZnAPO-34 is compared with simulations of two bands (the more intense at a lower position) (b) and a single band (c). By comparison it is clear the sample is most closely related to simulation (b).

Using this method, good initial fitting parameters were obtained for both MeAPO-34 and AlPO-5, and the bands were successfully modeled (figure 3.28). This procedure was then used (when necessary) to fit the bands for each sample and calculate the conformer ratios (table 3.7). From these results it is found that a high proportion (ratio tg.tg:tt.tt = 1) of the tg.tg conformer is maintained in the framework of crystalline ZnAPO-34. Upon treatment, the relative amount of tt.tt conformer is reduced (1.2), indicating that it was loosely bound to the AlPO surfaces, and not in the framework cavities. This final ratio is significantly greater than in the initial gel (0.7), indicating a preference for the tg.tg conformation within the framework (as shown by the *in situ* experiments). The remaining tt.tt conformer in the final treated product is most likely due to random encapsulation during the formation of the ZnAPO-34 framework. Along with the *in situ* results this information indicates that both the location of the organic

caused by a metal substituted charge induction or the organic conformation (or indeed a combination of the two) are responsible for the formation of MeAPO-34.

Significantly, for the final AlPO-5 material, the opposite trend is seen, with a ratio of 0.8 in the final product and decreasing to 0.44 after treatment, indicating that the tt.tt conformer dominates the AlPO-5 cavities. This result is particularly interesting as no specific organic location caused by a metal substituted charge induction is occurring in this system. It therefore appears that, in this system, the organic conformation is the sole driving force for the formation of the AlPO-5 AFI topology.

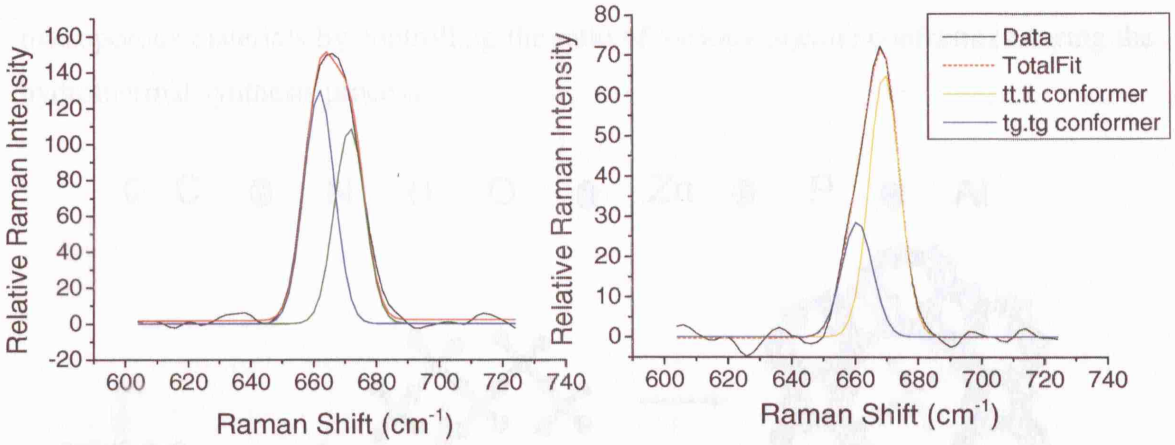

Figure 3.28: Final fits of the $\nu(C_4N)$ bands for the tt.tt and tg.tg conformations of crystalline treated 30% ZnAPO-34 (left) and AlPO-5 (right).

Sample	MeAPO-34	AlPO-5
Gel pre heating	0.77	0.74
Crystalline sample	1.03	0.82
Washed sample	1.20	0.44

Table 3.7: Ratios (tg.tg:tt.tt) of the MeAPO-34 and AlPO-5 samples measured *ex situ* before crystallisation, after crystallisation and after crystallisation and washing.

The *in situ* Raman measurements suggest a significant interaction between the organic species and the inorganic species in MeAPO-34. This indicates a 'true templating'[76] interaction occurring in MeAPO-34 synthesis, but this effect is caused not by the organic species but primarily by the substituted metal directing the position of the organic (and therefore changing its conformation). The organic is acting additionally as either a space filler or structure directing agent around which the final structure forms.

From the *ex situ* experiments it is noted that AlPO-5 forms primarily from the tt.tt conformer and MeAPO-34 from the tg.tg conformer. This then indicates the organic's role is somewhat more than space filling, but as both MeAPO-34 and AlPO-5 are known to form from other templates, it is difficult to class its role as specifically structure directing[76]. Clearly, classical theories about the role of the organic species tend to somewhat oversimplify its role, since there are complex metal-organic interactions which appear to favour the formation of one structure over another (figure 3.29)[108]. It is clear that a greater understanding of these effects will be necessary if a greater experimental control over hydrothermal synthesise of molecular sieves is to be realised. Indeed, it may become possible to synthesis many new (and pure) microporous materials by controlling the ratio of various organic conformers during the hydrothermal synthesis process.

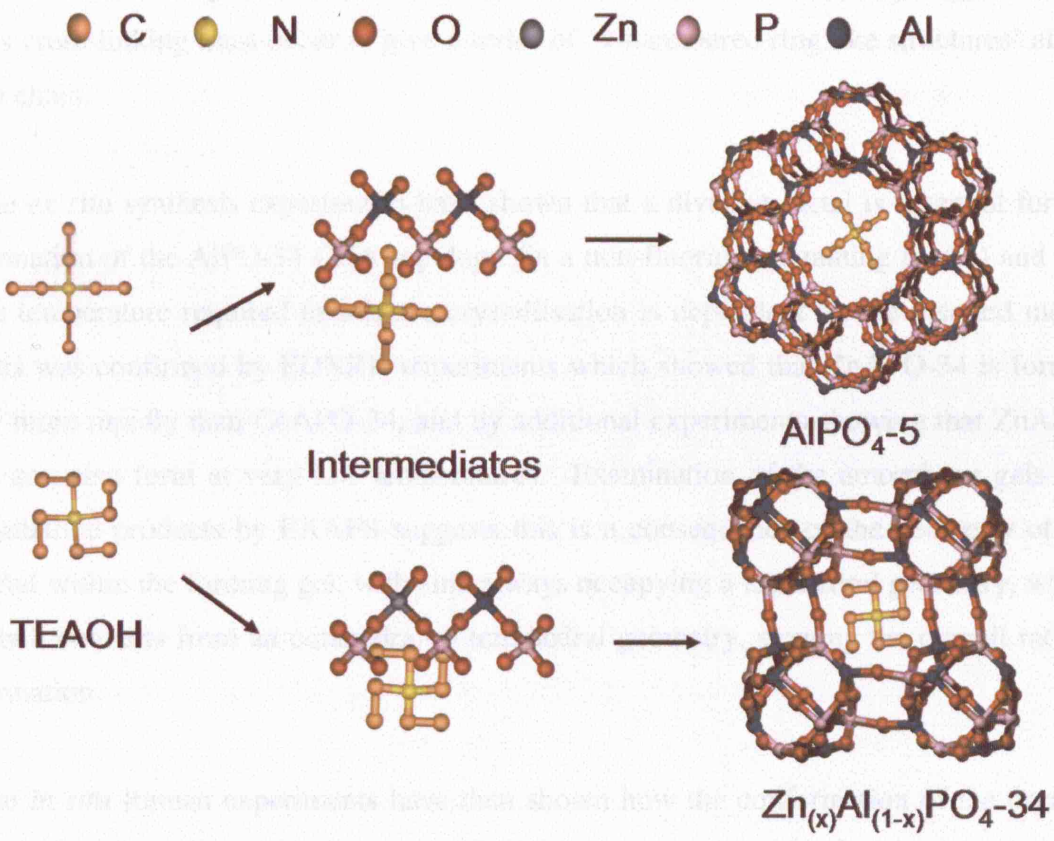

Figure 3.29: The proposed scheme representing the formation of MeAPO-34 and AlPO-5 from the similar gel compositions. The only difference in composition is the presence of a substituted metal in the (II) oxidation state for MeAPO-34 (in this case zinc). This leads to unique metal-organic interactions and a change in organic conformation resulting in the formation of ZnAPO-34. In AlPO-5 no metal-organic interaction is observed and the formation of the finals structure is governed by organic conformation alone. Note this image is adapted from ref.108 and ref. 109.

3.5 : Summary and conclusions

In this investigation, DFT calculations have been used to investigate the very early stages of AlPO formation. *Ex situ* crystallisation studies were then combined with EDXRD experiments to probe the rate of formation of MeAPO-34 with different substituted metals. Finally, *in situ* and *ex situ* Raman experiments have measured changes in the conformation of the TEAOH organic throughout a gel crystallisation.

Although still preliminary, the DFT results strongly suggest that, unlike the pure silicate systems, the early stages of AlPO formation is dominated by the formation of aluminophosphate chains and not isolated SBU-like units. It seems likely that as these chains grow they undergo self assembly to a degree and then cross link to give a three-dimensional microporous material. Indeed, for the AlPO-34 CHA topology, to form this cross-linking must occur to give a series of '4-membered ring like structures' along the chain.

The *ex situ* synthesis experiments have shown that a divalent metal is essential for the formation of the AlPO-34 CHA topology (in a non-fluoride containing media) and that the temperature required to achieve crystallisation is dependant on the inserted metal. This was confirmed by EDXRD experiments which showed that ZnAPO-34 is formed far more rapidly than CoAPO-34, and by additional experiments showing that ZnAPO-34 can also form at very low temperatures. Examination of the amorphous gels and crystalline products by EXAFS suggests this is a consequence of the geometry of the metal within the forming gel, with zinc always occupying a tetrahedral geometry, whilst cobalt converts from an octahedral to tetrahedral geometry, slowing the overall rate of formation.

The *in situ* Raman experiments have then shown how the conformation of the organic SDA is affected by the presence of divalent metal ions in forming framework, demonstrating unique metal-organic interactions which play a significant role in the formation of the MeAPO-34 structure. The *ex situ* Raman experiments have then shown how AlPO-5 is formed primarily from only a single organic conformer. As there was no metal-organic interaction in this system (no metal substitution) it was concluded that the conformation of the organic can also play a significant role, in this case determining the final framework topology adopted (i.e. ATS rather than CHA).

A mechanism which incorporates both these metal-organic interactions and the structure direction of the organic conformer has then been devised (figure 3.29).

In light of this increased understanding into the role of the metal and the organic it is possible to suggest why MeAPO-5 can be formed under some circumstances in the presence of TEAOH (as detailed in the introduction).

It has been noted that, generally, the formation of MeAPO-34 is typified by high metal and organic concentrations. If we consider a particularly low organic gel concentration, then the amount of organic available to interact with the charged metal framework becomes significantly reduced. According to the mechanism described above this would lead to reduced 'true templating' interactions between the metal and organic, allowing the formation of AlPO-5 to begin (if the temperature is sufficient). Lewis *et al*[35] have previously noted 'chabazitic AlPO cannot form as quickly as the corresponding AFI structure'. Therefore, it is then likely that once the formation of AlPO-5 begins, the conversion of the remaining amorphous gel to the same structure occurs, incorporating some substituted metal in either the framework or as extra framework atoms.

When considering the effect of substituted metal concentration and its influence on the formation of a particular structure, it is also important to note that even under the low metal concentrations that typically allow MeAPO-5 to form, ZnAPO-5 cannot be synthesised. In combination, these two facts suggest that both the geometry and the substitution level influence the final structure. From the EXAFS results it is known that cobalt requires a change in geometry in order to be incorporated in the framework (resulting in the slower rates seen by EDXRD). In circumstances where there is a very low concentration, almost all cobalt will be initially in the octahedral conformation and not incorporated in growing AlPO chains. Therefore, no metal-organic interaction occurs and AlPO-5 begins to form. However, if there is a high concentration of cobalt, some is likely to occupy a tetrahedral geometry quickly enough to form cooperative metal-organic interactions, resulting in the formation of CoAPO-34. Then, as the reaction continues, more cobalt is converted to a tetrahedral geometry, resulting in complete (if there is enough cobalt) conversion of the gel. In the case of a zinc gel, the metal is always in a tetrahedral geometry and therefore, even at low concentrations, metal-organic interactions occur and only MeAPO-34 can form (although pure AlPO-5

will form from the remaining gel once the zinc is exhausted and if the temperature is high enough).

The fact that other organics such as TPA can form MeAPO-5 under a broader range of conditions and with other metals compared to TEAOH may then be a consequence of different (possibly weaker) metal-organic interactions and / or the preferential adoption of one conformer over another better suited to the formation of the AlPO-5 structure.

3.6 : Future work

Whilst these results have considerably advanced the understanding of the formation of microporous materials, and in particular AlPOs, further work is required to fully understand the implications of this work.

The computational calculations have attempted to examine the earliest formation of species in an AlPO synthesis and appear to indicate that formation of chains rather than discrete SBUs occurs, particularly when a substituted metal is included in the cluster. However, as mentioned above these calculations are preliminary, therefore whilst they are indicative of a tendency towards chain formation, a number of more advance techniques need to be considered to confirm these findings. In particular it would be desirable to perform a complete set of calculations with the COSMO solvation model, which has currently proved problematic using the same conditions utilised by Mora-Fonz *et al*[72,73] for silicate clusters, suggesting the parameters need to be closely examined. It would also be desirable to examine larger chain clusters and examine how these can then cross-link to give '4-ring-like' structures within the chains.

The Raman experiments have demonstrated how a complex metal-organic interaction occurs when a charge is introduced into the forming AlPO framework. They have also demonstrated that AlPO formation can be controlled by this interaction or purely by the conformation of the organic. A necessary extension of this work would be to examine the formation of other microporous materials (such as zeolites) and see if it is possible to identify similar interactions and differences in organic conformation. If such interactions can be identified it would confirm that the mechanism represented above is more universal than just for the formation of AlPO materials and therefore a re-examination of the three roles of the organic template as described by Davis and Lobo[76] will have to be considered.

3.7 : References

(1) Smith, J. V.; Glasser, L. S. D.; Rinaldi, F. *Acta Crystallogr.* **1963**, *16*, 45.

(2) Smith, J. V. *Acta Crystallogr.* **1962**, *15*, 835.

(3) Dent, L. S.; Smith, J. V. *Nature* **1958**, *181*, 1794.

(4) Calligaris, M.; Nardin, G.; Randaccio, L. *Zeolites* **1983**, *3*, 205.

(5) Lok, B. M.; Messina, C. A.; Patton, R. L.; Gajek, R. T.; Cannan, T. R.; Flanigen, E. M. *J. Am. Chem. Soc.* **1984**, *106*, 6092.

(6) Ito, M.; Shimoyama, Y.; Saito, Y.; Tsurita, Y.; Otake, M. *Acta Crystallogr. Sect. C-Cryst. Struct. Commun.* **1985**, *41*, 1698.

(7) Marchese, L.; Frache, A.; Gianotti, E.; Martra, G.; Causa, M.; Coluccia, S. *Microporous Mesoporous Mat.* **1999**, *30*, 145.

(8) Harding, M. M.; Kariuki, B. M. *Acta Crystallogr. Sect. C-Cryst. Struct. Commun.* **1994**, *50*, 852.

(9) Thomas, J. M.; Raja, R.; Sankar, G.; Bell, R. G. *Accounts Chem. Res.* **2001**, *34*, 191.

(10) Wilson, S. T.; Flanigen, E. M. In *Zeolite Synthesis*; Occelli M, L., Robson H, E., Eds.; The American Chemical Society: 1989; Vol. 398, p 328.

(11) Akolekar, D. B. *J. Catal.* **1993**, *144*, 148.

(12) Sankar, G.; Raja, R.; Thomas, J. M. *Catal. Lett.* **1998**, *55*, 15.

(13) Stocker, M. *Microporous Mesoporous Mat.* **1999**, *29*, 3.

(14) Hartmann, M.; Kevan, L. *Chem. Rev.* **1999**, *99*, 635.

(15) Nawaz, S.; Kolboe, S.; Kvisle, S.; Lillerud, K. P.; Stocker, M.; Oren, H. M. In *Natural Gas Conversion*; Elsevier Science Amsterdam, 1991; Vol. 61, p 421.

(16) Inui, T.; Matsuda, H.; Okaniwa, H.; Miyamoto, A. *Appl. Catal.* **1990**, *58*, 155.

(17) Chen, J. S.; Wright, P. A.; Thomas, J. M.; Natarajan, S.; Marchese, L.; Bradley, S. M.; Sankar, G.; Catlow, C. R. A.; Gaiboyes, P. L.; Townsend, R. P.; Lok, C. M. *J. Phys. Chem.* **1994**, *98*, 10216.

(18) Chen, J. S.; Thomas, J. M.; Wright, P. A.; Townsend, R. P. *Catal. Lett.* **1994**, *28*, 241.

(19) Thomas, J. M.; Xu, Y.; Catlow, C. R. A.; Couves, J. W. *Chem. Mat.* **1991**, *3*, 667.

(20) Inui, T.; Phatanasri, S.; Matsuda, H. *J. Chem. Soc.-Chem. Commun.* **1990**, 205.

(21) Inui, T. In *Progress in Zeolite and Microporous Materials*; Chon, H., Ihm, S. K., Uh, Y. S., Eds.; Elsecier: Amsterdam, 1997, p 1441.

(22) Vora, B. V.; Marker, T. L.; Barger, P. T.; Nilsen, H. R.; Kvisle, S.; Fuglerud, T. In *Natural Gas Conversion IV*; Elsevier Amsterdam, 1997; Vol. 107, p 87.

(23) Barger, P. T.; Vora, B. V.; Pujado, P. R.; Chen, Q. J. In *Science and Technology in Catalysis 2002*; Kodansha Ltd: Tokyo, 2003; Vol. 145, p 109.

(24) Pastore, H. O.; Coluccia, S.; Marchese, L. *Ann. Rev. Mater. Res.* **2005**, *35*, 351.

(25) Dumitriu, E.; Azzouz, A.; Hulea, V.; Lutic, D.; Kessler, H. *Microporous Mater.* **1997**, *10*, 1.

(26) Gonzalez, G.; Pina, C.; Jacas, A.; Hernandez, M.; Leyva, A. *Microporous Mesoporous Mat.* **1998**, *25*, 103.

(27) Wilson, S. T.; Flanigen, E. M. *European Patent* **1985**, 0132708.

(28) Wilson, S. T.; Lok, B. M.; Flanigen, E. M. *US Patent* **1986**, 4567029.

(29) Saha, S. K.; Waghmode, S. B.; Maekawa, H.; Komura, K.; Kubota, Y.; Sugi, Y.; Oumi, Y.; Sano, T. *Microporous Mesoporous Mat.* **2005**, *81*, 289.

(30) Inoue, M.; Dhupatemiya, P.; Phatanasri, S.; Inui, T. *Microporous Mesoporous Mat.* **1999**, *28*, 19.

(31) Ahn, S.; Chon, H. *Microporous Mater.* **1997**, *8*, 113.

(32) Xu, Y.; Maddox, P. J.; Couves, J. W. *J. Chem. Soc.-Faraday Trans.* **1990**, *86*, 425.

(33) Uytterhoeven, M. G.; Schoonheydt, R. A. *Microporous Mater.* **1994**, *3*, 265.

(34) Concepcion, P.; Nieto, J. M. L.; Mifsud, A.; PerezPariente, J. *Zeolites* **1996**, *16*, 56.

(35) Lewis, D. W.; Catlow, C. R. A.; Thomas, J. M. *Chem. Mat.* **1996**, *8*, 1112.

(36) Beale, A. M. Unpublished results

(37) Hill, S. J.; Williams, C. D.; Duke, C. V. A. *Zeolites* **1996**, *17*, 291.

(38) Tusar, N. N.; Kaucic, V.; Geremia, S.; Vlaic, G. *Zeolites* **1995**, *15*, 708.

(39) Cundy, C. S.; Cox, P. A. *Chem. Rev.* **2003**, *103*, 663.

(40) Cundy, C. S.; Cox, P. A. *Microporous Mesoporous Mat.* **2005**, *82*, 1.

(41) Westman, A. E. R. In *Topics in Phosphorus Chemistry 9*; Griffith, E. J., Grayson, M., Eds.; Wiley: New York, 1977, p 247.

(42) Keller, E. B.; Meier, W. M.; Kirchner, R. M. *Solid State Ionics* **1990**, *43*, 93.

(43) Richardson, J. W.; Smith, J. V.; Pluth, J. J. *J. Phys. Chem.* **1990**, *94*, 3365.

(44) Li, H. X.; Davis, M. E.; Higgins, J. B.; Dessau, R. M. *J. Chem. Soc.-Chem. Commun.* **1993**, 403.

(45) Oliver, S.; Kuperman, A.; Ozin, G. A. *Angew. Chem.-Int. Edit.* **1998**, *37*, 47.

(46) Kniep, R.; Steffen, M. *Angew. Chem.-Int. Edit. Engl.* **1978**, *17*, 272.

(47) Wang Tieli; Yu Long; Pang Wenqin *J. Solid State Chem.* **1990**, *89*, 392.

(48) Jones, R. H.; Thomas, J. M.; Xu, R. R.; Huo, Q. S.; Cheetham, A. K.; Powell, A. V. *J. Chem. Soc.-Chem. Commun.* **1991**, 1266.

(49) Oliver, S.; Kuperman, A.; Lough, A.; Ozin, G. A. *Chem. Mat.* **1996**, *8*, 2391.

(50) Chippindale, A. M.; Powell, A. V.; Bull, L. M.; Jones, R. H.; Cheetham, A. K.; Thomas, J. M.; Xu, R. R. *J. Solid State Chem.* **1992**, *96*, 199.

(51) Kuperman, A.; Nadimi, S.; Oliver, S.; Ozin, G. A.; Garces, J. M.; Olken, M. M. *Nature* **1993**, *365*, 239.

(52) Wang, K. X.; Yu, J. H.; Li, C. J.; Xu, R. R. *Inorg. Chem.* **2003**, *42*, 4597.

(53) Jones, R. H.; Thomas, J. M.; Xu, R. R.; Huo, Q. S.; Xu, Y.; Cheetham, A. K.; Bieber, D. *J. Chem. Soc.-Chem. Commun.* **1990**, 1170.

(54) Ferey, G. *Chem. Mat.* **2001**, *13*, 3084.

(55) Barrer, R. M.; Baynham, F. W.; Meier, W. M. *J. Chem. Soc.* **1959**, 195.

(56) Taulelle, F.; Haouas, M.; Gerardin, C.; Estournes, C.; Loiseau, T.; Ferey, G. *Colloid Surf. A-Physicochem. Eng. Asp.* **1999**, *158*, 299.

(57) Haouas, M.; Gerardin, C.; Taulelle, F.; Estournes, C.; Loiseau, T.; Ferey, G. *J. Chim. Phys.-Chim. Biol.* **1998**, *95*, 302.

(58) Walton, R. I.; Millange, F.; Loiseau, T.; O'Hare, D.; Ferey, G. *Angew. Chem.-Int. Edit.* **2000**, *39*, 4552.

(59) Loiseau, T.; Walton, R. I.; Francis, R. J.; O'Hare, D.; Ferey, G. *J. Fluor. Chem.* **2000**, *101*, 181.

(60) Walton, R. I.; Millange, F.; O'Hare, D.; Paulet, C.; Loiseau, T.; Ferey, G. *Chem. Mat.* **2000**, *12*, 1977.

(61) Ferey, G. *J. Fluor. Chem.* **1995**, *72*, 187.

(62) Vistad, O. B.; Akporiaye, D. E.; Lillerud, K. P. *J. Phys. Chem. B* **2001**, *105*, 12437.

(63) Vistad, O. B.; Akporiaye, D. E.; Taulelle, F.; Lillerud, K. P. *Chem. Mat.* **2003**, *15*, 1639.

(64) Prasad, S.; Liu, S. B. *Microporous Mater.* **1995**, *4*, 391.

(65) Mortlock, R. F.; Bell, A. T.; Radke, C. J. *J. Phys. Chem.* **1993**, *97*, 775.

(66) Mortlock, R. F.; Bell, A. T.; Radke, C. J. *J. Phys. Chem.* **1993**, *97*, 767.

(67) He, H. Y.; Klinowski, J. *J. Phys. Chem.* **1994**, *98*, 1192.

(68) Grandjean, D.; Beale, A. M.; Petukhov, A. V.; Weckhuysen, B. M. *J. Am. Chem. Soc.* **2005**, *127*, 14454.

(69) Beale, A. M.; van der Eerden, A. M. J.; Grandjean, D.; Petukhov, A. V.; Smith, A. D.; Weckhuysen, B. M. *Chem. Commun.* **2006**, 4410.

(70) Pereira, J. C. G.; Catlow, C. R. A.; Price, G. D. *J. Phys. Chem. A* **1999**, *103*, 3252.

(71) Pereira, J. C. G.; Catlow, C. R. A.; Price, G. D. *J. Phys. Chem. A* **1999**, *103*, 3268.

(72) Mora-Fonz, M. J.; Catlow, C. R. A.; Lewis, D. W. In *Molecular Sieves: from Basic Research to Industrial Applications, Pts a and B*; Elsevier Science Bv: Amsterdam, 2005; Vol. 158, p 295.

(73) Mora-Fonz, M. J.; Callow, C. R. A.; Lewis, D. W. *Angew. Chem.-Int. Edit.* **2005**, *44*, 3082.

(74) Wilson, S. T.; Lok, B. M.; Messina, C. A.; Cannan, T. R.; Flanigen, E. M. *J. Am. Chem. Soc.* **1982**, *104*, 1146.

(75) Szostak, R. *Molecular Sieves*; second ed.; Blackie Academic, 1998.

(76) Davis, M. E.; Lobo, R. F. *Chem. Mat.* **1992**, *4*, 756.

(77) Burkett, S. L.; Davis, M. E. *J. Phys. Chem.* **1994**, *98*, 4647.

(78) Dutta, P. K.; Puri, M. *J. Phys. Chem.* **1987**, *91*, 4329.

(79) Francis, R. J.; O'Hare, D. *J. Chem. Soc.-Dalton Trans.* **1998**, 3133.

(80) Kubota, Y.; Helmkamp, M. M.; Zones, S. I.; Davis, M. E. *Microporous Mater.* **1996**, *6*, 213.

(81) Paik, W. C.; Shin, C. H.; Lee, J. M.; Ahn, B. J.; Hong, S. B. *J. Phys. Chem. B* **2001**, *105*, 9994.

(82) Han, B.; Lee, S. H.; Shin, C. H.; Cox, P. A.; Hong, S. B. *Chem. Mat.* **2005**, *17*, 477.

(83) Gomez-Hortiguela, L.; Perez-Pariente, J.; Cora, F.; Catlow, C. R. A.; Blasco, T. *J. Phys. Chem. B* **2005**, *109*, 21539.

(84) Naudin, C.; Bonhomme, F.; Bruneel, J. L.; Ducasse, L.; Grondin, J.; Lassegues, J. C.; Servant, L. *J. Raman Spectrosc.* **2000**, *31*, 979.

(85) Brand, H. V.; Curtiss, L. A.; Iton, L. E.; Trouw, F. R.; Brun, T. O. *J. Phys. Chem.* **1994**, *98*, 1293.

(86) Roisnel, T.; Rodriguez-Carvajal, J. In *Epdic 7: European Powder Diffraction, Pts 1 and 2*; Trans Tech Pub. Ltd: Zurich-Uetikon, 2001; Vol. 378, p 118.

(87) *Thermo Galactic GRAMS/AI.* **2001**, v7.00.

(88) Delley, B. *J. Chem. Phys.* **2000**, *113*, 7756.

(89) Delley, B. *J. Chem. Phys.* **1990**, *92*, 508.

(90) Dempsey, W.; Kuhl, G. H.; Olson, D. H. *J. Phys. Chem.* **1969**, *73*, 387.

(91) Cotton, F. A.; Wilkinson, G. *Advanced Inorganic Chemistry*; Fifth ed.; John Whiley and Sons Inc, 1988.

(92) Flanigen, E. M.; Grose, R. W. In *Advances in chemistry Series*; Van Bekkum, H., Flanigen, E. M., Jansen, J., C, Eds. Washington DC, 1971; Vol. 101, p 76.

(93) Dwyer, J.; Karim, K. *J. Chem. Soc.-Chem. Commun.* **1991**, 905.

(94) Dwyer, J.; Dewing, J.; Karim, K.; Holmes, A. J.; Ojo, A. F.; Garforth, A. A.; Rawlence, D. J. In *Proceedings of the International Symposium*; Jacobs, P. A., Jaeger, N. I., Kubelkova, L., Wichterlova, B., Eds.; Elsevier Amsterdam: Prague, 1991, p 1.

(95) Suzuki, K.; Kiyozumi, Y.; Shin, S.; Ueda, S. *Zeolites* **1985**, *5*, 11.

(96) Tuel, A.; Arcon, I.; Tusar, N. N.; Meden, A.; Kaucic, V. *Microporous Mater.* **1996**, *7*, 271.

(97) Avarami, M. *J. Chem. Phys.* **1939**, *7*, 1103.

(98) Avarami, M. *J. Chem. Phys.* **1940**, *8*, 212.

(99) Avarami, M. *J. Chem. Phys.* **1941**, *9*, 177.

(100) Erofe'ev, B. V. *Doklady academy of science URSS* **1946**, *52*, 511

(101) Hancock, J. H.; Sharp, J. D. *Journal of the American Ceramic Society* **1972**, *55*, 74.

(102) Beale, A. M.; van der Eerden, A. M. J.; Jacques, S. D. M.; Leynaud, O.; O'Brien, M. G.; Meneau, F.; Nikitenko, S.; Bras, W.; Weckhuysen, B. M. *J. Am. Chem. Soc.* **2006**, *128*, 12386

(103) Ristic, A.; Tusar, N. N.; Arcon, I.; Thibault-Starzyk, F.; Hanzel, D.; Czyzniewska, J.; Kaucic, V. *Microporous Mesoporous Mat.* **2002**, *56*, 303.

(104) Toriuma, K.; Ozima, M.; Akaoi, M.; Sato, Y. *Acta Crystallographica Section B* **1978**, *34*, 1093.

(105) Beale, A. M.; Sankar, G.; Catlow, C. R. A.; Anderson, P. A.; Green, T. L. *PCCP Phys. Chem. Chem. Phys.* **2005**, *7*, 1856.

(106) Barrett, P. A.; Sankar, G.; Catlow, C. R. A.; Thomas, J. M. *J. Phys. Chem.* **1996**, *100*, 8977.

(107) Moen, A.; Nicholson, D. G.; Ronning, M.; Lamble, G. M.; Lee, J. F.; Emerich, H. *J. Chem. Soc.-Faraday Trans.* **1997**, *93*, 4071.

(108) O'Brien, M. G.; Beale, A. M.; Catlow, C. R. A.; Weckhuysen, B. M. *J. Am. Chem. Soc.* **2006**, *128*, 11744.

(109) van Santen, R. A. *Nature* **2006**, *444*, 46

Chapter 4

The effect of organic structure directing agents on the formation and structure of aluminophosphate 36

4.1 : Chapter overview

The catalytically interesting cobalt substituted aluminophosphate-36 (CoAPO-36) has been prepared in a phase pure form using three different organic SDAs and a simple one step hydrothermal synthesis method developed previously in this laboratory[1]. An *in situ* study of the formation of these materials using time resolved energy dispersive X-ray diffraction (EDXRD) has revealed that the organic SDA component can significantly influence both induction times and rates of crystallisation of these materials. A crystallographic study of the materials also revealed that the exact crystal structure is altered depending on the SDA utilised. A measurement of the molecular dimensions and volume of the SDAs indicated that this alteration is related to the size of the organic molecule. Computational docking techniques were then used to demonstrate that the shape of the molecule is also important.

These two SDA properties give rise to two important crystal formation effects which have been labelled in the text as 'ordered' and 'forced' packing. Both occur as a result of the need to charge compensate for framework metal substitution and can significantly alter the rate of crystallisation of metal substituted porous materials.

4.2 : Introduction

AlPO-36 (ATS structural topology) is a large pore aluminophosphate type molecular sieve with no zeolitic analogue[2,3]. Its framework consists of 1-dimensional elliptical (6.5 x 7.5 Å) channels with 12-ring apertures and staggered annular side pockets (figure 4.1).[4]

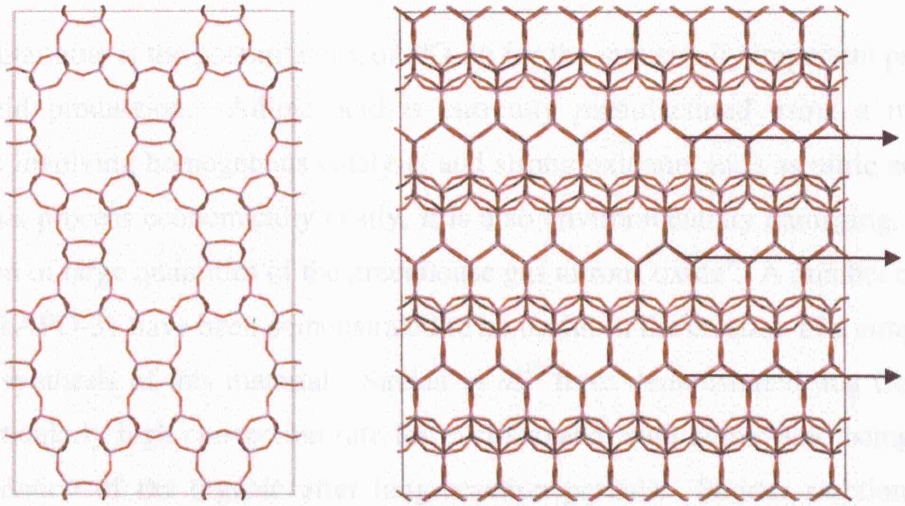

Figure 4.1: The structure of the AlPO-36 ATS topology, represented as super cells of the standard unit cell in order to display the 12-membered ring apertures clearly. These apertures are 1-dimensional running along the Z (or c) axis (indicated by arrows).

4.2.1 : Catalytic properties

The large pore nature of AlPO-36 gives rise to a high sorption capacity compared with smaller pored systems, such as AlPO-34 and 18. When combined with framework charge, induced by substitution of framework metals (for example the substitution of Al^{3+} by Zn^{2+}), a number of applications for this material become available.

Akolekar[5] has demonstrated that manganese substituted AlPO-36 (MAPO-36) has a high sorption capacity for nitrogen, water and *n*-hexane when compared with other large pore systems such as AlPO-5, which is believed to be due to the annular side pockets of the ATS structure. It was also demonstrated that the structure contains a very high number of strong Brønsted acid sites compared to the AlPO-5 structure. Wilson and Flanigen[6] have compared a variety of calcined metal substituted AlPOs for *n*-butane cracking and found that the structure type, metal type and metal framework content can

all affect catalytic activity. However, at comparable metal concentrations MAPO-36 was found to exhibit 'considerably greater activity than the corresponding 5 type'[6]. Later work by Akolekar[7] demonstrated that MAPO-36 also has a high catalytic activity and selection for aromatic formation in ethanol, cyclohexane, *n*-hexane and isooctane and a very high activity for toluene disproportionation. Raja *et al*[8] have also shown that manganese and cobalt substituted systems can convert a variety of alkenes into their corresponding epoxides and diols.

Of particular note is the potential of CoAPO-36 for the industrially important process of adipic acid production. Adipic acid is currently manufactured using a multi-step processes involving homogenous catalysts and strong oxidants such as nitric acid. Not only is this process economically costly, it is also environmentally damaging, with the production of large quantities of the greenhouse gas nitrous oxide[9]. A number of AlPOs such as FeAPO-31 have been demonstrated to be useful in the creation of a simple clean one-step synthesis of this material. Sankar *et al*[10] have demonstrated that CoAPO-36 has a particularly high conversion rate for cyclohexane, with adipic acid being formed upon oxidation of the organic after long reaction periods. Shorter reaction periods produce cyclohexanol and cyclohexanone. However, the products are then oxidised and converted to adipic acid during the later stages of the reaction. The reaction occurs with much greater activity compared to CoAPO-18, CoAPO-11 and Co-APO-5 (figure 4.2).

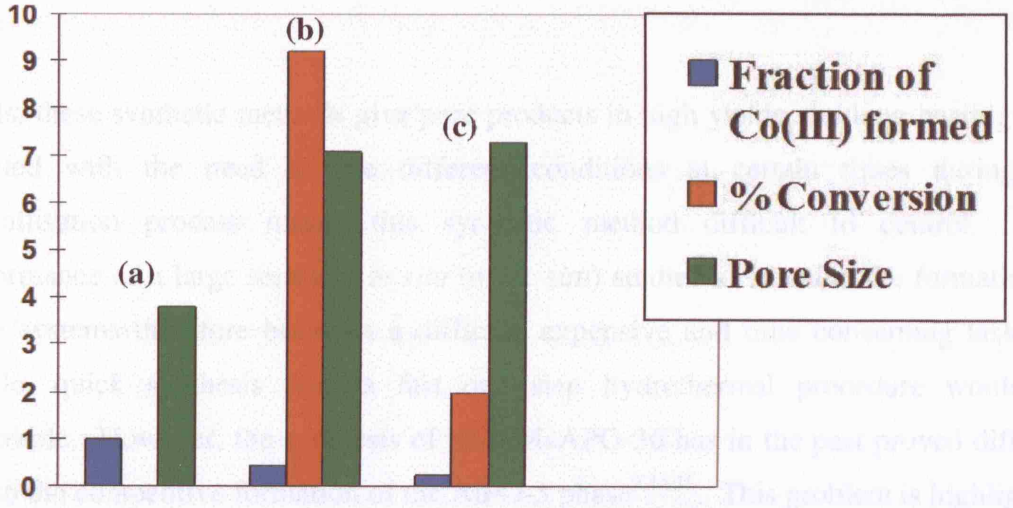

Figure 4.2: Bar chart representing the fraction of oxidised cobalt, pore dimension and catalytic activity of CoAPO-18 (a) CoAPO-36 (b) and CoAPO-5 (c), modified from ref. 10.

4.2.2 : Synthesis

AlPO-36 is generally synthesised following methods very similar to those originally adopted by Flanigen *et al*[11] for the MAPO member of the AlPO-36 family. Some slight modifications, such as changing the metal source type, aging and order of addition are often employed depending on the exact nature of the work in question.

In all cases tripropylamine (TPA) is used as the SDA. A typical synthesis involves the mixing of a phosphorus source (e.g. phosphoric acid) in water, into which a metal salt (e.g. cobalt, manganese or zinc acetate) is then dissolved, either prior to, or after the addition of an aluminium source (e.g. aluminium hydroxide or aluminium isoperoxide). The SDA is then added and the gel mixed until homogenous. Some aging of the gel is often employed, with heating under hydrothermal conditions forming the final crystalline product.

A typically example is given by Macando *et al*[12] and uses a gel with the composition:

$$1.0P_2O_5: (1\text{-}yAl_2O_3): 2yMgO: rPr_3N: 40H_2O: 4yHOAc$$

The gel requires two hydrothermal treatments, one at 100°C for an initial period of 50 hours, followed by a further 48 hours at 150 °C. Zahedi-Niaki *et al*[13] have demonstrated it is possible to synthesise the pure end member (AlPO-36) using an almost identical gel composition, although once again the synthesis required a long two-stage hydrothermal stage.

Whilst these synthetic methods give pure products in high yields, the long heating time coupled with the need to use different conditions at certain times during the crystallisation process makes this synthetic method difficult to control. The performance of a large series of *in situ* (or *ex situ*) studies to examine the formation of these systems therefore becomes a difficult, expensive and time consuming task. A simple, quick synthesis with a fast one step hydrothermal procedure would be preferable. However, the synthesis of pure MeAPO-36 has in the past proved difficult due to the competitive formation of the AlPO-5 phase[5,14,15]. This problem is highlighted by an extensive study on pure AlPO-36 and MAPO-36 in which it was observed that AlPO-5 always co-crystallised with AlPO-36. Increasing the manganese substitution level did achieve pure MAPO-36, but only with very specific ageing, crystallisation and aluminium sources[16].

Recently advances in this laboratory have demonstrated that, with careful selection of the right synthesis materials and conditions, it is possible to synthesise phase pure CoAPO-36 using TPA as the SDA, in a simple single-step processes at a constant temperature with short synthesis times[1]. Additionally, CoAPO-36 was synthesised using two novel SDAs: *n,n*-diisopropylisobutylamine (DPBA) and *n*-ethyldicyclohexylamine (ECHA). These advances therefore offer a unique opportunity to study the kinetics of crystallisation of AlPO-36 using *in situ* methods and examine the effect of different SDAs on this process.

4.2.3 : Aim of this work

Despite the catalytic potential mentioned above, industrial scale usage of aluminophosphates remains restricted to a few examples (e.g. AlPO-34 for the MTO process), which is due to a variety of factors, including problems with metal leaching[17] and deactivation of the micropores due to the production of large organics or coking[18]. A large number of studies have focused on the catalytic activity of these systems and the variety of synthesis routes, using different substituted metals, SDAs, aluminium sources etc. However, very little work has focused directly on how certain factors can effect the formation of these materials. A greater understanding of this formation process and the underlying kinetics would allow the development of lower cost synthesis methods for the existing AlPO frameworks. It could also lead to the development of new frameworks capable of performing current catalytic reactions with greater efficiency and the development of new catalytic processes.

In particular, the aim of this work is to synthesise CoAPO-36 using different SDAs and investigate the largely overlooked effect of SDA type on its formation kinetics and crystalline properties. By using *in situ* EDXRD, in combination with computational and crystallographic methods, it will be demonstrated how a greater understanding into the formation of molecular sieves can be developed. This is a method that may be applied to any molecular sieve system in order to identify cheaper lower cost synthesis routes to these important materials and the development of new materials.

4.3 : Experimental

4.3.1 : Hydrothermal preparation of CoAPO-36 materials

The CoAPO-36 phases were prepared in the laboratory by hydrothermal treatment using the following procedure. 1.0 molar equivalents of 85% orthophosphoric acid and 10 molar equivalents of water were mixed with mechanical stirring. 0.1 molar equivalents of cobalt acetate tetrahydrate was then added slowly to the solution with continual stirring. Upon dissolution, 0.9 molar equivalents of aluminium hydroxide were slowly added to the solution and stirred vigorously until a homogenous gel was achieved (c.a. 5 - 10 mins). Finally, the desired SDA was added to the gel, initially drop-wise until solidification occurred and then rapidly with vigorous stirring by hand. After 5 minutes the gel returned to a more liquid state and was stirred mechanically for 1 hour, until a viscous homogenous gel was obtained. Gels were then placed in Teflon lined hydrothermal bombs (autoclaves) and heated for the required amount of time (see table 4.1). Post synthesis products were filtered, washed with distilled water and dried at 100°C. *In situ* experiments were prepared in an identical manner but the gels were added to specially machined autoclaves for EDXRD studies, detailed below. Note some slight variation in the molar quantities for the synthesis of the TPA sample was necessary in order to ensure a completely pure product was obtained.

AlPO synthesised	$Al(OH)_3$	H_3PO_4	M(acetate)	SDA	H_2O	Synthesis temp (°C)	Synthesis time (h)
CoAlPO-36 (TPA)	0.9	1.0	0.1	0.9	10	160 ± 5	20
CoAlPO-36 (ECHA)	0.9	1.0	0.1	0.8	10	160 ± 5	15
CoAlPO-36 (DPBA)	0.9	1.0	0.1	0.8	10	160 ± 5	6

Table 4.1: Molar quantities of reagents and synthesis conditions of CoAlPO-36 using the three structure directing agents.

4.3.2 : Characterisation techniques

4.3.2.1 : X-ray diffraction

XRD patterns of all samples were recorded using the Bruker D4 diffractometer as described in detail in chapter 3. The Fullprof suite of programs[19] was used to perform LeBail fits on the XRDs and initial fitting parameters were based on those given previously by Smith *et al*[20], calculated from a combination of diffraction techniques.

4.3.2.2 : Scanning electron microscopy

The JOEL JSM-6301F scanning microprobe was used for SEM, and the Hitachi EDX 5570 for EDX analysis, as described in chapter 3.

4.3.2.3 : Extended X-ray absorption fine structure

As in chapter 3, EXAFS measurements were carried out at station 9.3 of the SRS and used a Si(220) double crystal monochromator in transmission mode only. Samples consisted of 40 mg laboratory prepared CoAPO's pressed into 13mm pellets and mounted for measurement using station based mounting equipment. The data were then analysed using the analysis suite available from Daresbury laboratories.

4.3.2.4 : *In situ* energy dispersive X-ray diffraction

The crystallisation of these AlPO materials was monitored *in situ* using EDXRD. As discussed in chapter 2, EDXRD is of a particular advantage in the study of these systems as the highly collimated, high flux white beam allows rapid data collection and the use of real sample environments such as stainless steel autoclaves[21]. Measurements were carried out at station 16.4 of the SRS. The station was set-up using the 3-element detector system detailed in figure 4.3 and as described previously for the studies of microporous materials[22,23]. For these experiments, the centre of the detector array was held at a fixed 2θ angle of 4.18°, setting the lower and upper detectors at fixed angles of 1.3° and 7.08° respectively. Experiments were performed using stainless steel autoclaves with a PTFE liner (~ 40 ml sample capacity) specifically designed with the bottom half of the shell machined in order to reduce the thickness of the walls and

maximise the radiation flux passing through the sample[24,25]. In a typical experiment an autoclave containing the appropriate gel mixture was introduced into an *in situ* oven preheated to the desired temperature. The time between introduction of the sample to heat and the beginning of measurements was 2 minutes and a data collection time of 1min/scan was used for all experiments.

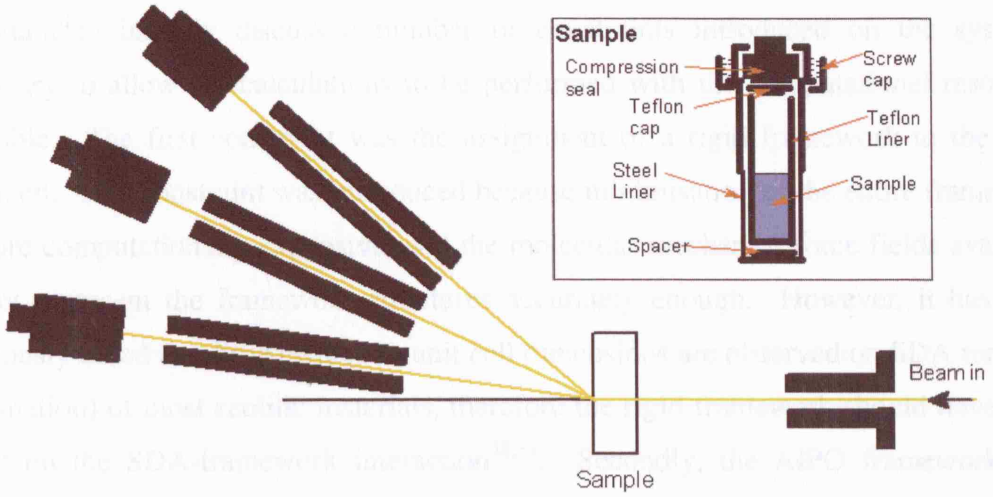

Figure 4.3: Schematic of the three element detector used on station 16.4 at the SRS. The beam passes through pre sample collimators, the sample cell and post sample collimators before striking the energy discriminating detectors. The sample cell (inset) consists of a specially machined PTFE lined autoclave.

The raw data files were smoothed, calibrated and output in standard 2 column ASCII format using the XRD explorer software program available on station 16.4[26]. All further conversions of data to appropriate formats were performed using in-house developed macros. Peak areas were integrated using the Gaussian curve fitting routine available in the XFIT peak profiling software[27] available from the Collaborative Computer Project 14 (CCP14) software libraries.

4.3.3 : Computational techniques and methodology

The molecular mechanics (MM) calculations performed in this chapter are similar in methodology to those previously applied to the study of template-zeolite interactions.[28-30] SDA molecules were built in Materials Studio[31] and their optimised geometries were calculated using the Discover code[32] (see chapter 2 for a description on molecular mechanics and geometry optimisation). These minimised SDA molecules were then inserted into a (1 1 4) supercell consisting of 4 crystallographic unit cells of the ATS

framework as defined by Smith *et al*[20] using either a Monte Carlo based docking procedure or manual insertion based on orientation considerations.

4.3.3.1 : Constraints

The details of the computational procedures are discussed below. However, it is important to initially discuss a number of constraints introduced on the systems, necessary to allow the calculations to be performed with the computational resources available. The first constraint was the assignment of a rigid framework to the ATS supercell. This constraint was introduced because minimisation of the entire framework is more computationally expensive, and the molecular mechanics force fields available cannot represent the framework structures accurately enough. However, it has been previously noted that little change in unit cell dimensions are observed on SDA removal (calcination) of most zeolitic materials, therefore the rigid framework should have little effect on the SDA-framework interaction[28,33]. Secondly, the AlPO framework was treated as purely siliceous. This can be considered a reasonable approximation because $2Si^{4+} \equiv Al^{3+} + P^{5+}$ due to strict metal alternation in AlPO frameworks, and because framework oxygen is believed to be the dominating source of non-bonding interactions with the system[33]. Moreover, this approximation also allows the use of more reliable force fields. The third limitation was the omission of electrostatics. Although this is clearly a simplifying assumption, the use of a siliceous network means the SDA is subject to a largely uniform electrostatic field and therefore columbic interactions are expected to have a comparatively small effect on the calculated structure. Indeed, Lewis *et al*[28] have demonstrated that although the inclusion of electrostatics results in a significant numerical difference in the calculated energies, the overall trends remain the same. This observation is further supported by previous computational studies that indicate little similarity between the electrostatic characteristics of different SDA molecules that form the same framework, with size and shape dominating[34,35]. Finally, substituted cobalt was omitted from the framework, as there is a lack of suitable potential parameters and more importantly, any knowledge of the location of these atoms in the framework. This is generally considered an acceptable approximation since although these long range electrostatic forces determine the relative framework SDA concentration due to the need for electroneutrality, they do not greatly influence the magnitude of the template/host geometry or binding energy, as van der Waals interactions predominate[36].

Despite the use of these constraints, this methodology has been previously used successfully to study the SDA-framework interaction and has been shown to reproduce the experimental SDA geometries[28,30], therefore providing a useful correlation between these interactions and crystallisation times in other microporous systems[29]. In the context of this work, these calculations have been used to compare the effect of organic shape and orientation within the framework of a model structure. The results should represent a reasonable indication as to any effect these properties have on the overall energy of the system, and therefore be indicative of any effect these properties have on the formation kinetics of the AlPO.

4.3.3.2 : Monte Carlo docking procedure

The first procedure attempted in this work utilised a Monte Carlo docking method[37] (figure 4.4), placing the minimised SDAs in random orientations into the ATS framework cavity. Orientations in which the molecules were found to have an energy lower than a pre-determined threshold energy were recorded, whilst the others were discarded.

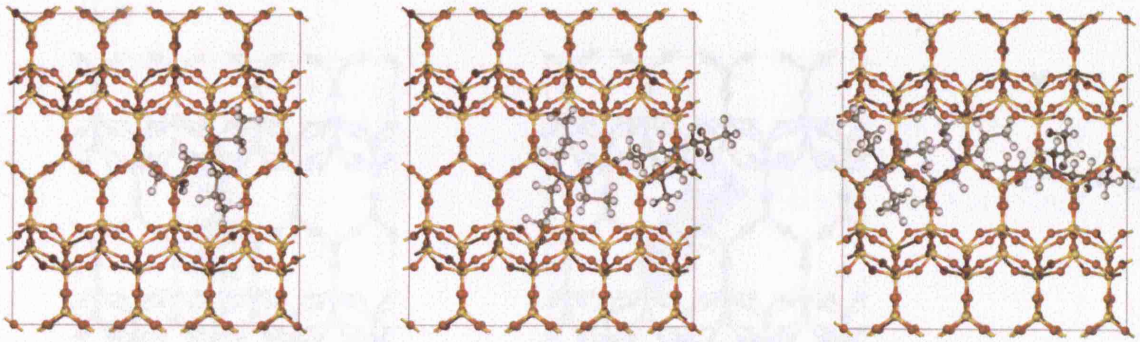

Figure 4.4: Examples of one, two and three molecules located in the ATS framework using the Monte Carlo docking procedure.

When more than one SDA per supercell was required, a sequential packing routine was employed, as described in chapter 2. All frameworks with acceptable energies were then minimised using the Discover MM code[32].

4.3.3.3 : Manual orientation procedure

The relatively small and rigid nature of the SDA molecules and the small pore space of the ATS framework limits considerably the number of likely SDA orientations within the structure. It was therefore possible to attempt SDA minimisation based on five orientations of each SDA, taking into account most possibilities. Each SDA molecule was inserted into the pore either parallel to the YZ, YX or ZX orientation or at 45° between two of the planes, YX(45)ZX and YZ(45)ZX (figure 4.5). Additional molecules were then inserted in identical orientations to create packing with the channel. All supercells were then minimised using the Discover MM code[32].

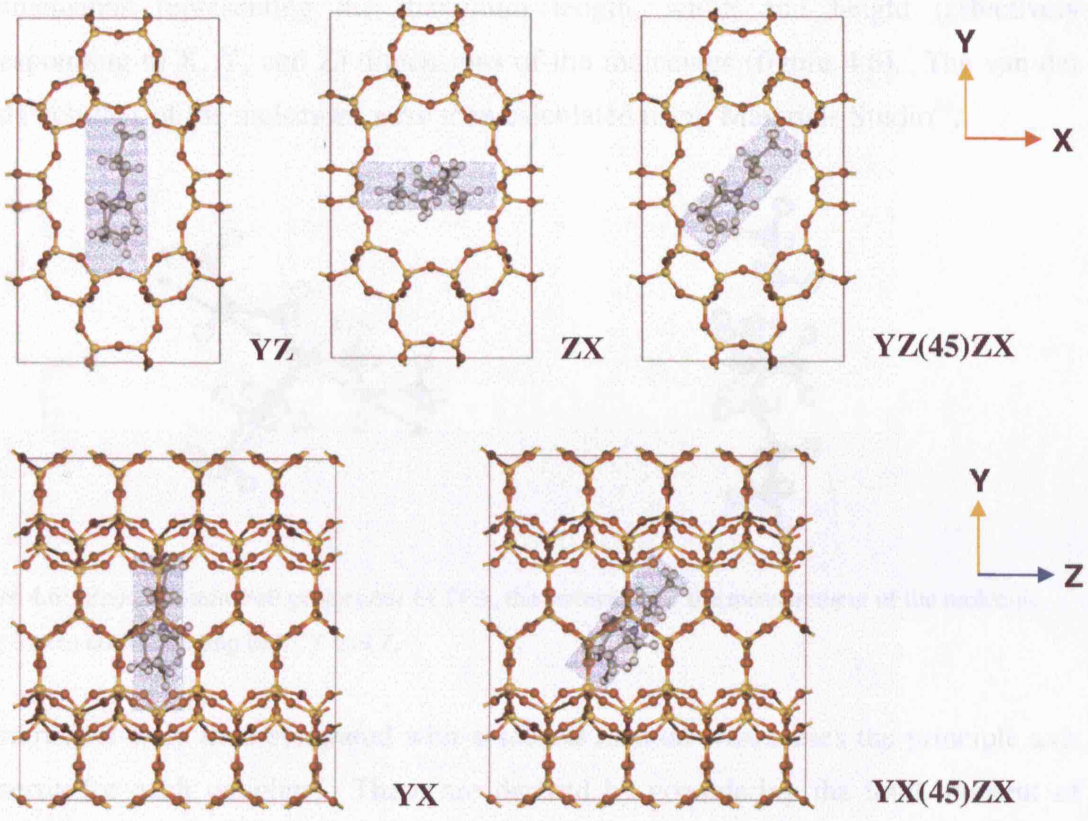

Figure 4.5: The manually assigned orientations for the insertion of TPA into the ATS framework. The use of five orientations allows sampling of most possibly SDA orientations within the structure.

4.3.3.4 : Data analysis

As noted above, and in chapter 2, all structures generated from both the Monte Carlo and orientational procedures were energy minimised using the Discover MM code[32] using the *ab initio* derived force field cff91_czeo, with parameters as detailed by Hagler *et al*[38] and Hill and Sauer[39]. All comparative energies are quoted as the interaction

energy (E_{inter}) as defined in equation 4.1. E_{host} is the total energy of the framework/SDA combination and E_{free} is the energy of an isolated gas-phase template molecule.

$$E_{inter} = E_{host} - E_{free} \quad \textbf{(4.1)}$$

4.3.3.5 : Molecular size measurements

Two methods were utilised for measuring the size and shape of the molecules. In the first method the extremities of the energy minimised SDA molecules were measured in 3 dimensions representing the maximum length, width and height (effectively corresponding to X, Y, and Z) dimensions of the molecules (figure 4.6). The van der Waals volumes of the molecules were then calculated using Materials Studio[31].

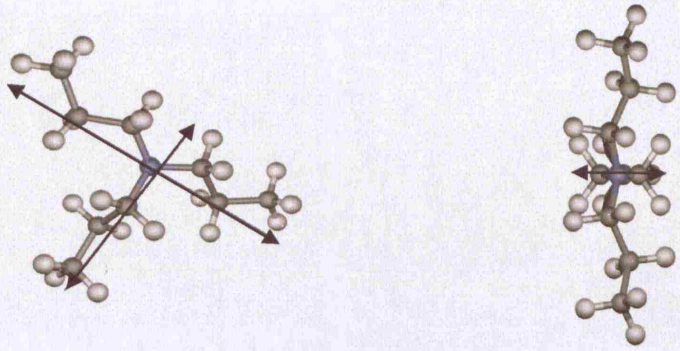

Figure 4.6: Energy minimised projections of TPA, the arrows show the measurement of the molecule along 3 axes corresponding to X, Y and Z.

These results were then compared with a second method which uses the principle axis of inertia for each template. These are derived by considering the total moment of inertia of a polyatomic molecule (equation 4.2).

$$I = \sum_i m_i r_i^2 \quad \textbf{(4.2)}$$

Here, the mass m of each atom i is multiplied by the square of its distance from the rotational axis through the centre of mass of the molecule, with r_i being the perpendicular distance of the atom from the axis of rotation[40].

The principle axis *RX*, *RY* and *RZ* are then inversely proportionally to the corresponding orthogonal moments *IX*, *IY* and *IZ* and are scaled to describe an inertial ellipsoid around the molecule (figure 4.7). Boyett *et al*[34,35] have previously demonstrated that this provides a quantitative description of the structure of organic SDAs, and both methods allow for good comparison between each organic SDA.

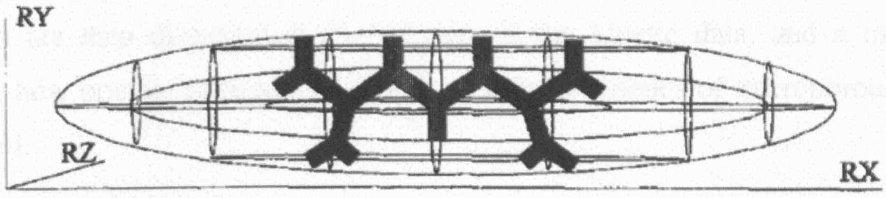

Figure 4.7: The inertial ellipsoid formed around a typical organic SDA molecule. Reproduced from ref. 34.

4.4 : Results and discussion

Initially, samples were synthesised *ex situ* and subjected to a number of techniques to check for phase purity and complete metal substitution and these are initially discussed. The *in situ* EDXRD technique is then detailed and the results of the kinetic studies described. The results of the crystallographic, molecular size and shape and docking calculation are then discussed in the context of the kinetic data, and a mechanism describing how organic packing can influence growth kinetics of microporous systems is described.

4.4.1 : *Ex situ* characterisation

Prior to performing any *in situ* experiments it was important to determine if the CoAPO-36 synthesis methods produced phase pure, well substituted materials for each SDA. The dried filtered laboratory synthesised products were subjected to analysis by XRD and found to be consistent with the AlPO-36 ATS structural framework[20]. Figure 4.8 gives representative XRD patterns for each sample. Some deviation from the standard ATS peak positions are noted, and are believed to be due to SDA effects on the framework and are discussed in detail below.

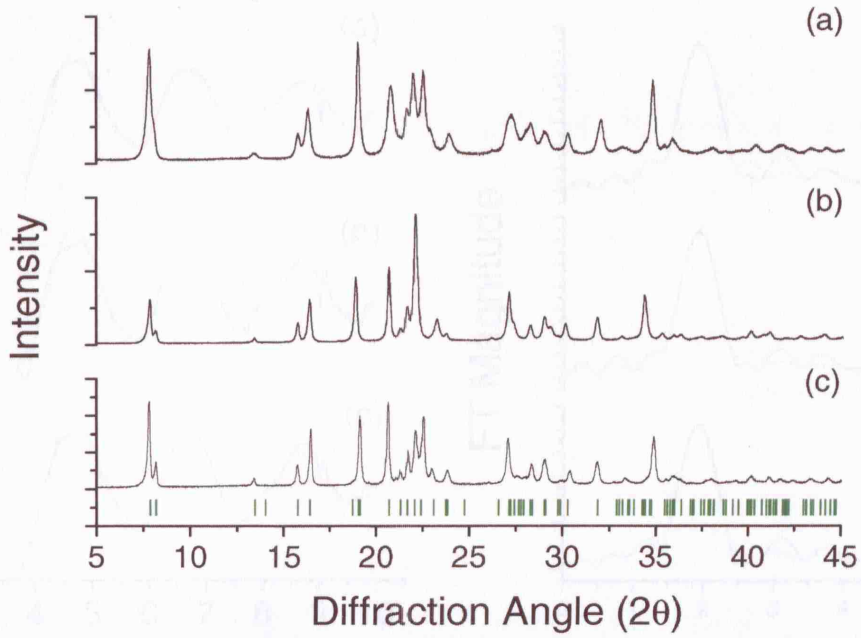

Figure 4.8: XRD patterns of the as synthesised CoAPO-36 materials synthesised using TPA (a), ECHA (b) and DPBA (c). The tick marks represent the peak positions of standard ATS[20], slight deviations from these are observed due to template effects which will be discussed below.

The deep blue colour of the samples suggested the successful framework substitution of tetrahedral cobalt (II) for tetrahedral aluminium (III)[41]. Further evidence of cobalt incorporation was obtained from EDX and EXAFS data. Analysis of the atomic percentages obtained from EDX indicate that 10.9%, 10.8% and 11% of the aluminium sites are substituted for cobalt in the TPA, ECHA and DPBA samples respectively. Which is within the error range for such un-polished microcrystallite samples measured using this technique.

In order to further understand the coordination of the cobalt within the actual AlPO structure, XAS measurements were performed on the as-prepared samples. This technique gives the local average bond length and coordination number for the cobalt.

The resulting EXAFS data (left) and the associated real space Fourier transforms (right) for each sample can be seen in Figure 4.9. The solid line represents the experimental data, while the dotted line represents the calculated EXAFS and Fourier transforms for a primary single shell consisting of a cobalt atom surround by oxygen atoms in a local average arrangement. There is quite good overlap between the experimental and calculated data, suggesting a good model has been used to represent the material, a fact supported by the low standard errors for the results (table 4.2).

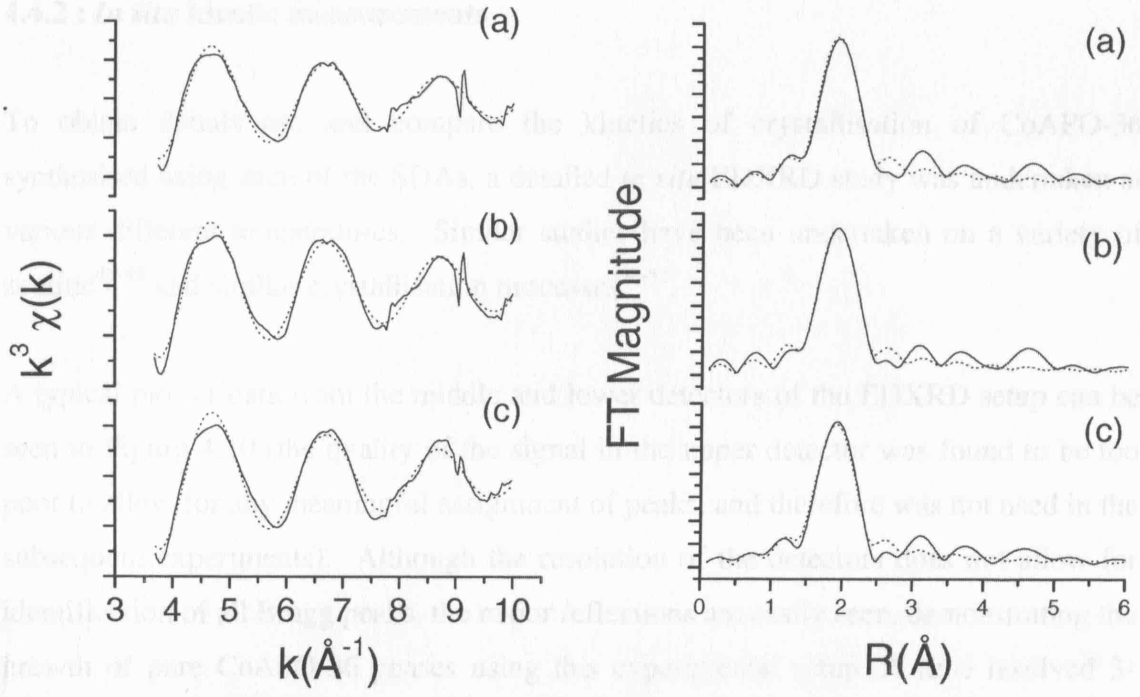

Figure 4.9: Cobalt data EXAFS curves (left) and there corresponding real space Fourier transforms (right) for TPA (a), ECHA (b) and DPBA (c).

Sample	*N*	Me-O distance *R*(Å)	σ^2(Å^2)	R-factor (%)
CoAlPO-36 (TPA)	3.7	1.939	0.011	22.01
CoAlPO-36 (ECHA)	4.1	1.938	0.011	21.80
CoAlPO-36 (DPBA)	3.9	1.939	0.013	21.63

Table 4.2: Resulting coordination number (*N*), cobalt-oxygen distances (*R*), Debye-Waller factors (σ^2) and R factors for each as prepared CoAPO-36 sample obtained from the EXAFS fits shown in figure 4.3.

Analysis of the data revealed that cobalt is surrounded by four oxygen nearest neighbours ($N = 4 \pm 0.4$) at an average distance of 1.94 ± 0.02 Å, which is consistent with Co-O bond distances for both the well characterised Spinel structure, $CoAl_2O_4$ (in which high spin Co(II), occupying mainly the A-site, is known to predominate[42]) and other similar cobalt substituted AlPO-n materials[43-45]. These results demonstrate that the cobalt atoms have been successfully substituted into aluminium tetrahedral sites and that there is little or no octahedral cobalt species in the system. The Debye-Waller factors are also similar to each other ($\sigma^2 = 0.012 \pm 0.001$ Å^2), suggesting there is no significant static disorder around the cobalt environments.

4.4.2 : *In situ* kinetic measurements

To obtain details on, and compare the kinetics of crystallisation of CoAPO-36 synthesised using each of the SDAs, a detailed *in situ* EDXRD study was undertaken at various different temperatures. Similar studies have been undertaken on a variety of zeolitic[46-49] and similar crystallisation processes[50-52].

A typical plot of data from the middle and lower detectors of the EDXRD setup can be seen in Figure 4.10 (the quality of the signal in the upper detector was found to be too poor to allow for any meaningful assignment of peaks, and therefore was not used in the subsequent experiments). Although the resolution of the detectors does not allow for identification of all Bragg peaks, the major reflections are easily seen, demonstrating the growth of pure CoAPO-36 phases using this experimental setup. A time resolved 3-dimensional stack plot of the middle detector data shows the appearance of these reflections after an initial induction/nucleation period and then subsequent growth.

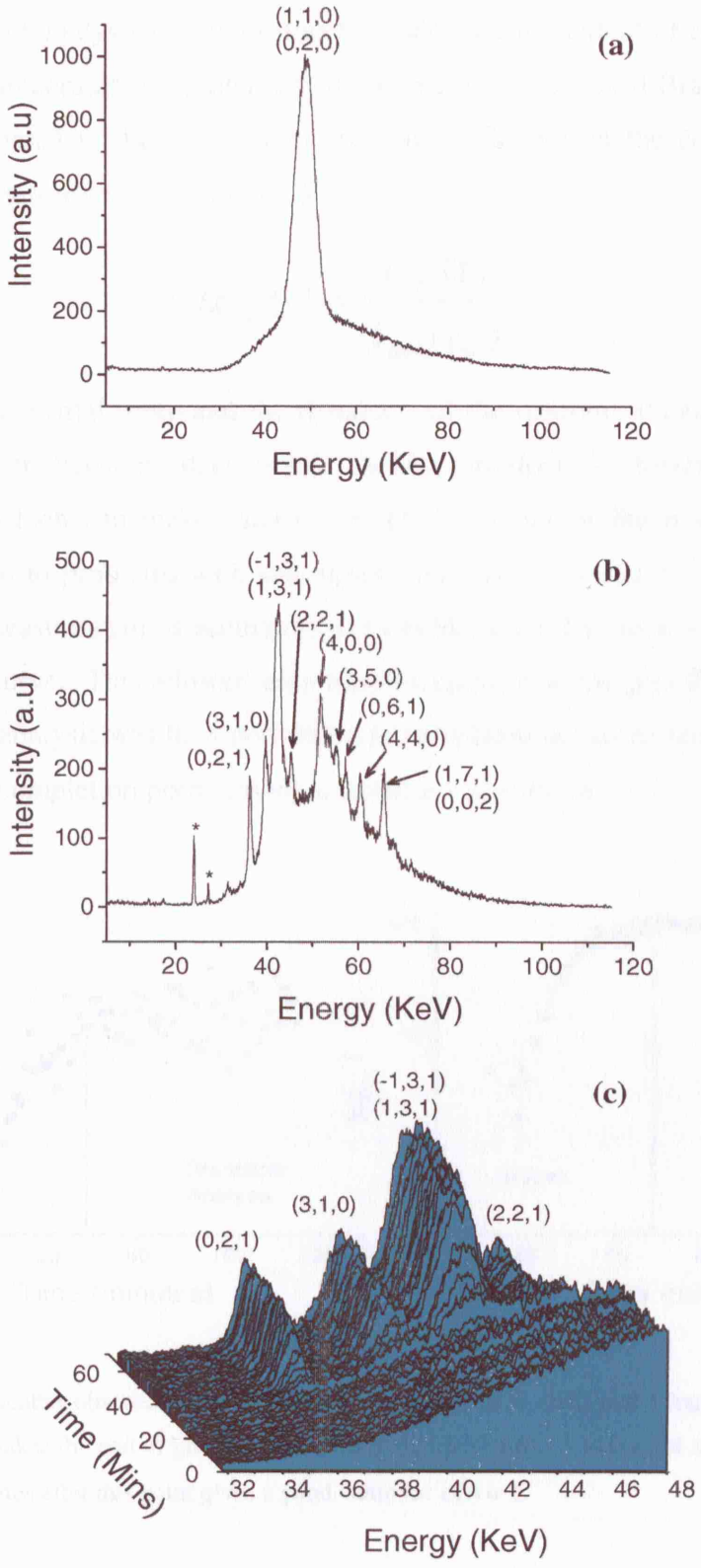

Figure 4.10: Typical plots of data from the middle (a) and lower detectors (b) of the EDXRD set-up after a data acquisition time of 1 minute. The (*h,k,l*) values of the major Bragg reflections are labelled. Peaks labelled (*) are due to florescence and are consistent throughout all experiments. A stack plot resulting from the accumulation of many 1 minute scans (c) demonstrates the growth of these reflections as a function of time.

For all subsequent analysis it is convenient to calculate the extent of reaction (α_{hkl}) by considering the integrated peak intensity of a particular normalised Bragg reflection I_{hkl} at time (t) compared to the intensity of the same reflection at the completion of the reaction (t_∞), as described in equation 4.3.

$$\alpha_{hkl}(t) = \frac{\mathrm{I_{hkl}}(t)}{\mathrm{I_{hkl}}(t_\infty)} \qquad (4.3)$$

Due to the experimental setup and the dynamics of the reaction, it can be seen (figure 4.11) that scatter between data points occurs, particularly towards the end of crystallisation, which can make calculating the end point of the reaction ($\alpha(t) = 1$) difficult and lead to problems with subsequent analysis. In order to calculate the end point for each measurement as accurately as possible, a log I vs time graph was plotted for the growth curve. This allowed easy identification of when growth was completed and a statistical analysis was then performed to calculated the mean intensity of all data points after this completion point, giving a suitable value for $\alpha(t) = 1$.

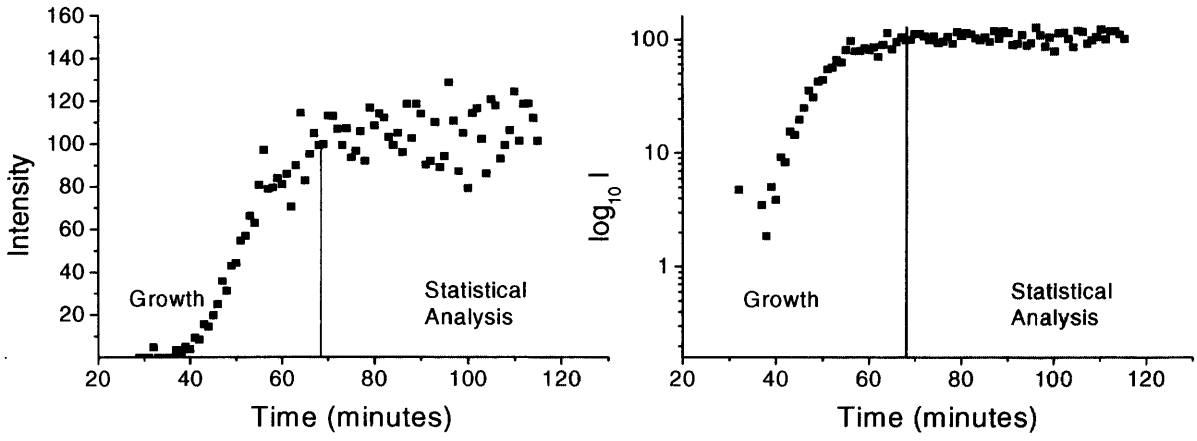

Figure 4.11: The scatter observed during the formation of AlPO-36 (left) and a logarithmic plot of the same data, which makes the end of growth more clearly visible (right). A statistical analysis of the mean values of all intensities after this point gives a good value for $\alpha(t) = 1$.

In order to assess the validity of profiling a single peak for these *in situ* studies, the area of a number of peaks from a single experimental run were compared (figure 4.12). It is apparent that despite slight differences, the growth curves are generally super-imposable over the duration of the experiment, indicating that there is little preference for crystal growth on any of these particular crystallographic planes, and therefore all should be

representative of the growth mechanism occurring. For subsequent analysis the (0, 2, 1) reflection was measured as its distance from other reflections allows a simple Gaussian peak fitting procedure to be employed.

It is noted that there are some minor differences, particularly at the beginning of crystallisation, which are due to an increased error in peak area measurement caused by the reduction in the signal to detector noise ratio during the early stages of the experiment.

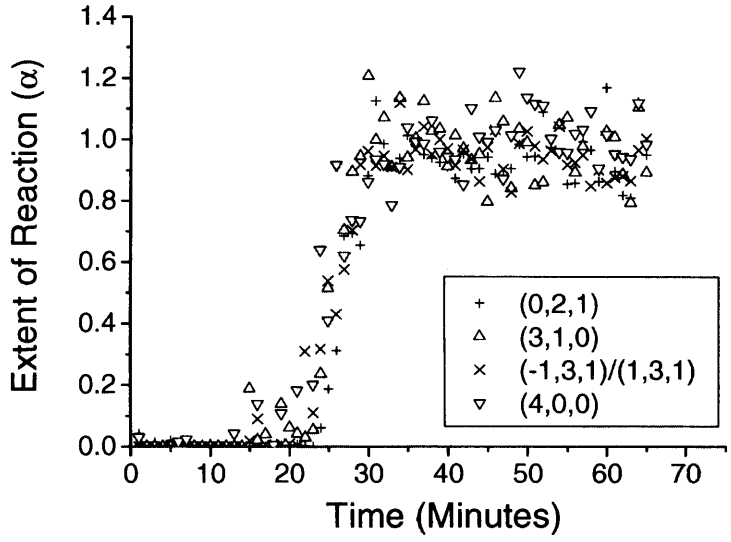

Figure 4.12: Peak profiles for CoAPO-36 (ECHA) at 150°C for a number of Bragg reflections. The curves are super imposable within the error for the technique indicating no preference for crystal growth on any particular crystallographic plane.

In order to estimate the error on all calculated values using these procedures, the calculations on each data set were performed considering the statistically determined value of $\alpha(t) = 1$ and also at the maximum and minimum deviation from this value. Using this method the percentage errors are 8% on the exponent (n) and the rate of reaction (k) and 7 % on the activation energy (E_a).

The fitting procedure detailed above was performed on each subsequent data set. Experiments were performed using each of the SDAs over a range of temperatures. Figure 4.13 displays results for the crystallisation of CoAPO-36 (TPA) at different temperatures (top) and crystallisation using different SDAs at the same temperature (bottom).

An increase in temperature leads to an expected reduction in the induction period as the energy available in the system to overcome reaction barriers is greater. An increase in the rate of crystallisation is also observed, due to the increased kinetic motion of the molecules making contact more frequent. More interesting however, is the fact that the type of SDA also appears to have a substantial effect on both the induction time and crystallisation rate of CoAPO-36. Using DPBA gives rise to a substantially reduced induction time and increased rate of reaction, compared to both TPA and ECHA, whilst the reaction using TPA proceeds after a longer induction period and at a much slower rate than both the other SDAs.

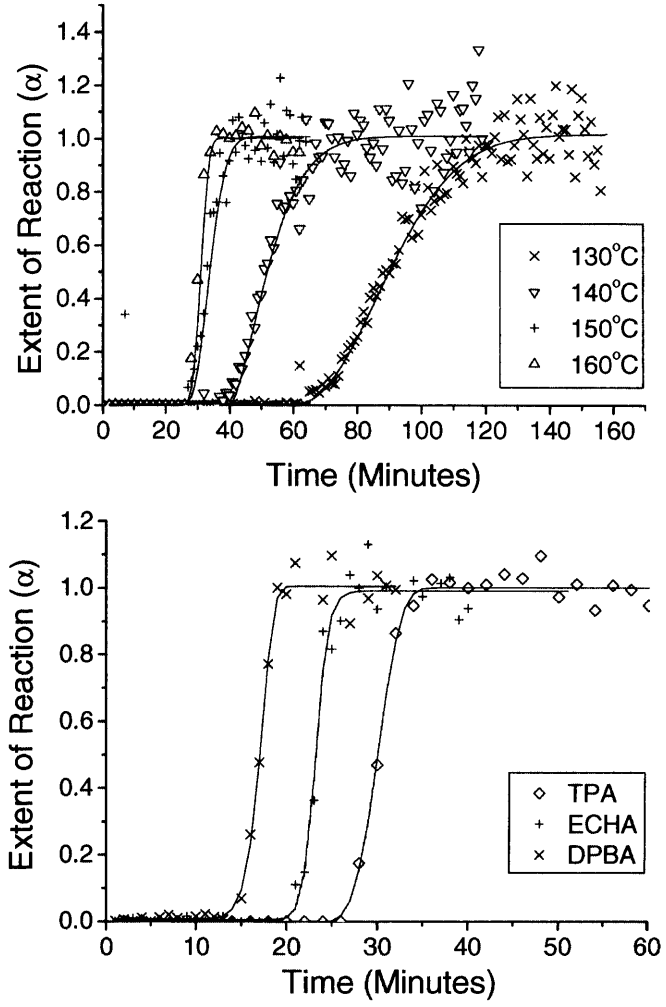

Figure 4.13: The crystallisation curves of CoAPO-36 (TPA) at varying temperatures (top) clearly demonstrate the expected reduction in induction time and increased reaction rate upon increasing temperature, whilst the crystallisation curves of CoAPO-36 using each SDA at 160°C (bottom) demonstrates the unexpectedly pronounced effect of changing the organic on these variables.

In order to investigate these SDA-mediated changes in more detail, a systematic study was undertaken to obtain kinetic information on these reactions. Growth curves were recorded at a number of temperatures and the kinetic model proposed by Avarami[53-55] and Erofe'ev[56] was utilised for analysis. This model separates the overall course of the reaction in separate stages of nucleation and growth. It is the most widely used model for analysing a variety of solid state processes such as phase transformations[57] as well as crystallisations in zeolitic[46-49] and other reactions[50,58]. The general form of the equation is given in equation 4.4, where α is the extent of the reaction and k represents the rate constant for the reaction. The exponent n is known to be related to the mechanism of both nucleation and growth. Hulbert[59] has analysed a number of ideal reaction mechanisms and demonstrated that n contains information on the dimensionality of growth of the crystallisation process, with typical values ranging from $n = 0.5 - 4$.

$$\alpha = 1 - \exp^{(-kt)^n} \qquad \textbf{(4.4)}$$

It is important to note that rate constants calculated using this expression and any derived values, such as activation energies, are useful only for direct comparison with similar reactions and should not be considered as independently meaningful. However, while a number of other more complex exponential functions have been derived, the Avarami-Erofe'ev expression still allows for simple comparisons of similar reactions under slightly differing conditions.[60]

The most straightforward way to extract information from the Avarami-Erofe'ev equation is by performing a Sharp-Hancock[61] analysis of the data. By rearrangement and taking a double logarithm of equation 4.4 we derive equation 4.5, the Sharp-Hancock equation .

$$\ln[-\ln(1-\alpha)] = n\ln(t) + n\ln k \qquad \textbf{(4.5)}$$

A plot of ln[-ln(1-α)] vs. ln(t) should then yield a straight line giving both n from the gradient of the slope and k from the x-axis intercept. Generally, this analysis is performed when the extent of reaction has values of $0.15 < \alpha < 0.8$, as deviations during

the very early and late parts of crystallisation can effect the results[50, 62]. The resulting Sharp-Hancock plots for each CoAPO-36 system are given in figure 4.14, and the derived rates of reaction (k) and Avarami exponents (n) are given in table 4.3.

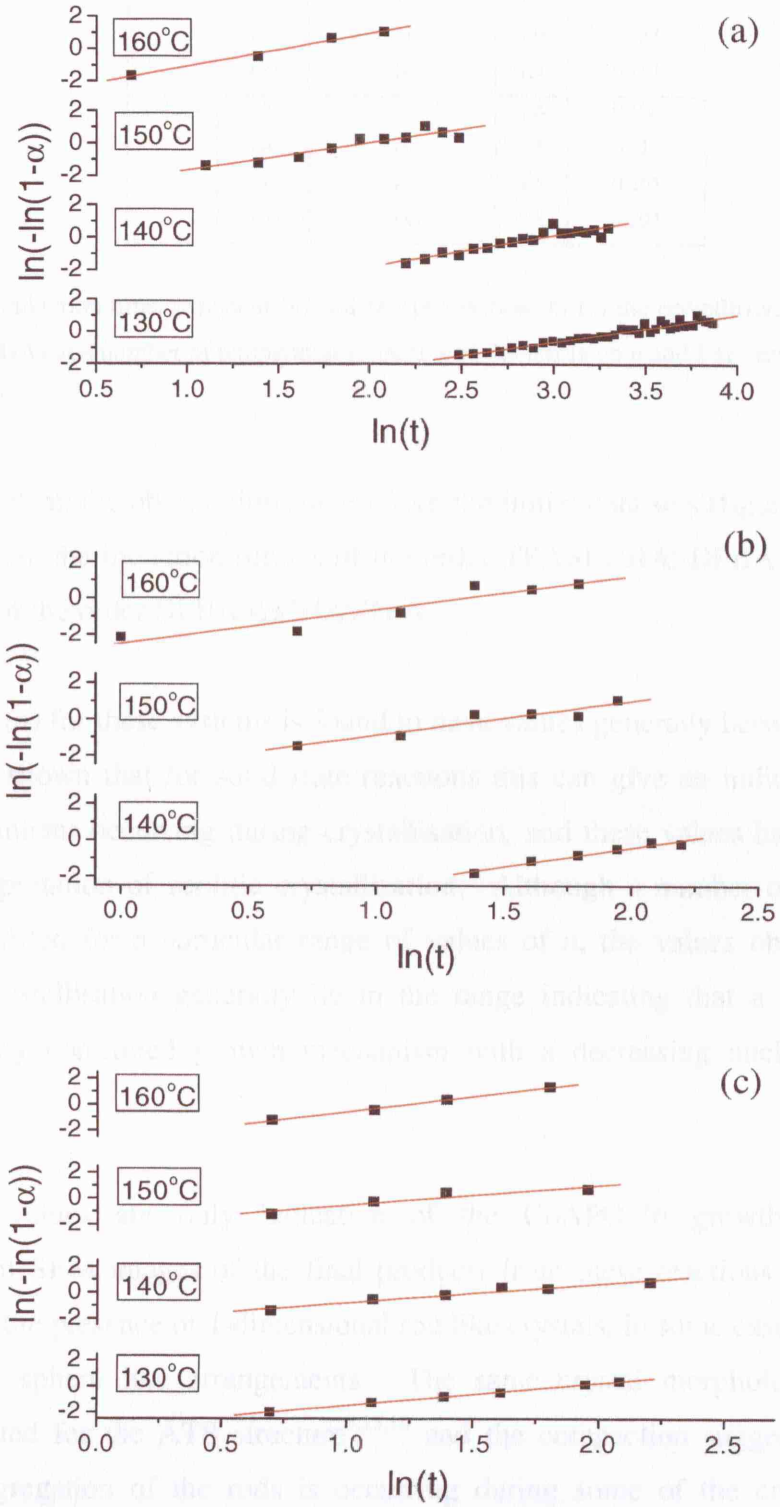

Figure 4.14: Sharp-Hancock plots derived from the crystallisation of CoAPO-36 using the SDAs TPA (a), ECHA (b) and DPBA (c).

SDA	Temp (°C)	Induction Time (mins)	n	k (min^{-1})
TPA	130	65	1.7	0.034
	140	36	1.9	0.054
	150	27	1.7	0.137
	160	26	2.0	0.217
ECHA	140	32	2.1	0.112
	150	23	1.9	0.233
	160	20	1.9	0.263
DPBA	130	27	1.8	0.158
	140	22	1.5	0.215
	150	16	1.5	0.265
	160	14	2.4	0.293

Table 4.3: The induction time, exponent (n) and rate of reaction (k) for the crystallisation of CoAPO-36 using different SDAs at a number of temperatures. Note that the errors on n and k are estimated to be 8%, as detailed above.

The results confirm the observations taken from the initial data sets (figure 4.13), and at each temperature the induction time is of the order TPA>ECHA>DPBA while the rate of reaction is of the order DPBA>ECHA>TPA.

The exponent (n) for these systems is found to have values generally between 1.5 and 2. Hulbert[59] has shown that for solid state reactions this can give an indication into the growth mechanisms occurring during crystallisation, and these values have often been used for interpretation of zeolitic crystallisation. Although a number of mechanisms can often be fitted for a particular range of values of n, the values obtained for the CoAPO-36 crystallisation generally lie in the range indicating that a 1-dimensional phase boundary controlled growth mechanism with a decreasing nucleation rate is occurring.

While these values are only indicative of the CoAPO-36 growth mechanism, examination of SEM images of the final products from these reactions (figure 4.15), clearly shows the presence of 1-dimensional rod like crystals, in some cases packed into 3-dimensional sphere like arrangements. The same crystal morphology has been previously noted for the ATS structure[5,13,16] and the compaction suggests that some secondary aggregation of the rods is occurring during some of the crystallisations. Hulbert's range for this type of 3-dimensional growth is n = 1.5 – 2.5, and may explain

why for a number of experiments (in particular DPBA at 160°C) n has values slightly greater than 2.

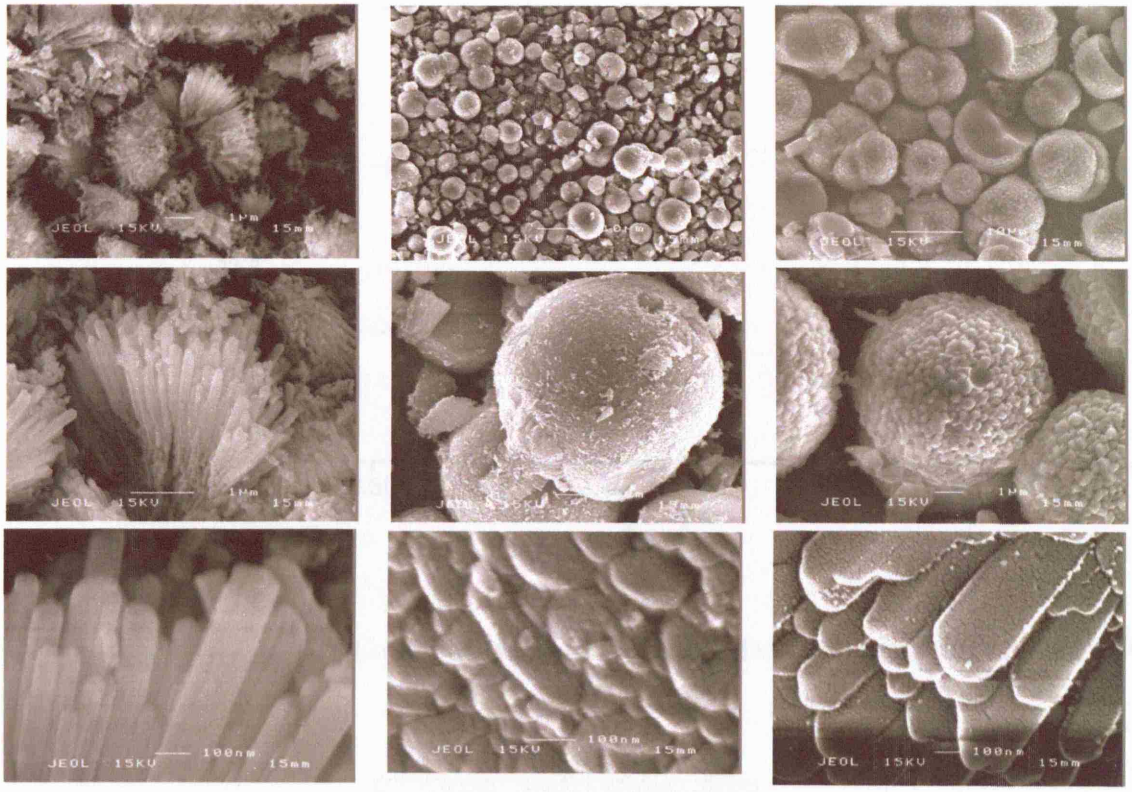

Figure 4.15: SEM images of CoAPO-36 synthesised using the SDAs TPA (left), ECHA (middle) and DPBA (right). The spherical nature of the ECHA and DPBA particles can be clearly seen, whilst the rod like structure of crystallisations is also clearly evident.

From the Arrhenius expression (equation 4.6) it is possible to use the rate of reaction to derive the activation energy (E_a) for each system by plotting ln(k) against 1/T.

$$k = A\exp^{(-E_a/RT)} \qquad \textbf{(4.6)}$$

The resulting Arrhenius plots are shown in figure 4.16, while table 4.4 contains the derived activation energies. Again, whilst we must remember that these activation energies can be used only as a comparison between similar systems, these values are similar to those previously reported for other hydrothermal synthesis[46,47,63,64] and support the results from the Sharp-Hancock analysis. DPBA has the lowest apparent activation energy (30 ± 2 kJ mol^{-1}), while ECHA's value is twice as high (64.0 ± 5 kJ mol^{-1}). TPA has by far the highest apparent activation energy (93 ± 7 kJ mol^{-1}), being approximately 3 times higher than that of DPBA.

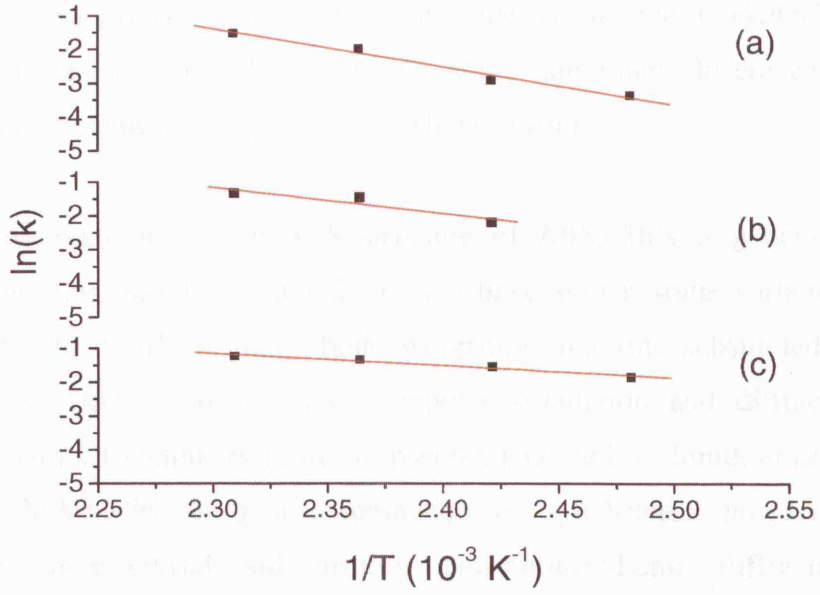

Figure 4.16: Arrhenius plots of CoAPO-36 synthesised using the SDAs DPBA (a), ECHA (b) and TPA (c).

SDA	E_a (kJmol^{-1})
TPA	93
ECHA	64
DPBA	30

Table 4.4: Apparent activation energies (E_a) derived from Arrhenius plots of CoAPO-36 crystallisation using each SDA. Percentage error is estimated to be 7%.

The important points to summarise from this *in situ* section of the work are that the SDA used in the synthesis of CoAPO-36 affects both the induction time and rate of reaction of the crystallisation, as is evident from the rates of reaction derived from the Sharp-Hancock plots and from the derived activation energies. In order to begin to understand what is causing this pronounced effect, a detailed diffraction study has been performed on samples synthesised using each SDA.

4.4.3 : Crystallographic studies

A close examination of X-ray diffraction patterns for the CoAPO-36 structure, synthesised using different SDAs, reveals some important differences in the as synthesised samples space groups and unit cell parameters.

While the space group for the ATS structure of AlPO-36's is generally given as Cmcm[65] (table 4.5), metal substituted systems have shown some variation from this structure. Wright *et al*[4] examined both manganese and zinc substituted ATS and a combination of electron microscopy, computer simulation and diffraction gave a triclinic cell with C1 symmetry (close to pseudomonoclinic). Smith *et al*[20] solved the structure of MAPO-36 using a combination of synchrotron powder diffraction, Weissenberg single crystal and electron and Guinier-Lenné diffraction using a monoclinic C2/c space group. In both cases the variation away from the Cmcm symmetry results in a change in one or more of the unit cell parameter angles from 90°, which reduces the symmetry of the system and leads to a splitting of the (1 3 1) and (1 3 -1) peaks in the X-ray diffraction pattern. Both Wright *et al*[4] and Smith *et al*[20] have observed this splitting and Smith *et al*[20] have demonstrated it to be temperature dependant, with the peaks merging above 773K. The monoclinic symmetry of the structure is therefore described as a result of a 'crinkling of the framework at room temperature'[20].

	IZA database[65]	Wright *et al*[4]	Smith *et al*[20]
Space group	Cmcm	C1	C2/c
a (Å)	13.164	13.46	13.1483(4)
b (Å)	21.584	22.17	21.5771(7)
c (Å)	5.257	5.29	5.1639(2)
α (°)	90	90.16	90
β (°)	90	92.01	91.84(2)
γ (°)	90	89.95	90

Table 4.5: Comparative table of space groups and unit cell parameters for the ATS framework.

In the work of both Wright *et al*[4] and Smith *et al*[20], measurements were performed on calcined samples with the template molecules removed from the framework. For the present work, the effect of the template on the framework was examined, and therefore

no calcination of the sample was initially performed. By simple visual examination of each XRD pattern (figure 4.8), clear differences in the pattern of CoAPO-36 synthesised using ECHA compared to TPA and DPBA can be seen. A closer examination of the patterns in the range 20 – 25° 2θ (figure 4.17) reveals that in the case of both DPBA and TPA the (1 3 1) and (1 3 -1) peaks are non-equivalent. As discussed above, this is a strong indication that these two samples exist in the low symmetry C2/c space group. For the ECHA sample this is not the case and the peaks are coalesced, suggesting this sample exists in the higher symmetry Cmcm space group.

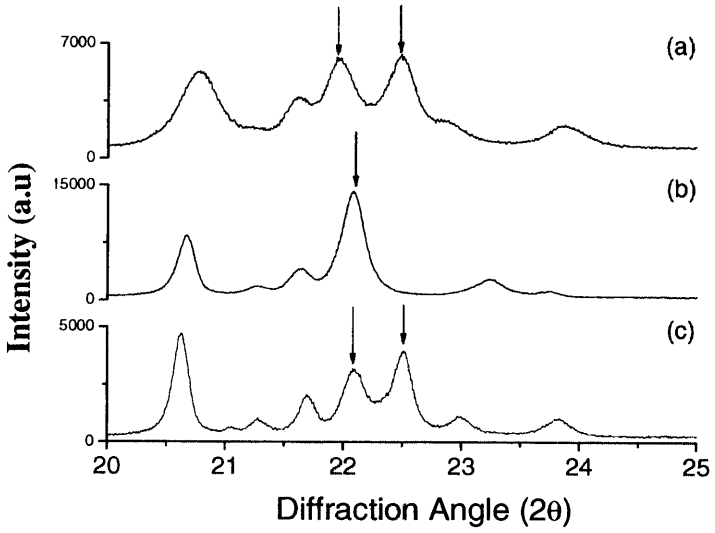

Figure 4.17: Close ups of CoAPO-36 synthesised with TPA (a), ECHA (b) and DPBA (c). The arrows mark the (1 3 1) and (1 3 -1) peaks, in the case of ECHA only a single peak is present.

A change in symmetry is also indicated by normalising each XRD pattern to the (1 1 0) peak and comparing the intensities of the (1 3 1) and (-1 3 1) peaks for each system. For the ECHA system, the single (1 3 1) normalised peak intensity is very high at over 288 counts, whilst for the TPA and DPBA systems, the (1 3 1) and (-1 3 1) peak intensities are far lower (79 and 82 counts in TPA and 67 and 83 counts in DPBA). Smith *et al*[20] have previously demonstrated that, in calcined samples the intensity of the coalesced peak in the Cmcm space group is very high compared to that of the split peaks in the C2/c space group. Therefore the high intensity of the peak in the ECHA sample indicates that it is in the higher symmetry space group. It is noted that in Smiths work the sum of the (1 3 1) and (-1 3 1) peaks in the C2/c systems total the intensity of the single (1 3 1) peak in the Cmcm system sample. This is clearly not the case in these systems with the total intensity being only 160 and 150 counts in TPA and ECHA respectively. This may be a consequence of the un-calcined nature of the materials in this work or possibly some preferred orientation effect.

To confirm this change in symmetry and measure other changes in the unit cell parameters, it was necessary to perform LeBail fits on the uncalcined patterns for each structure. Initially, cell parameters from the C2/c space group were used for each sample to allow for a direct comparison between the derived cell parameters. Figure 4.18 displays the fits for each of the systems, while table 4.6 describes the final minimised parameters for each system. In each case the fits are good with reliability factors reasonable for a LeBail fit of unit cell parameters from a powder diffraction pattern.

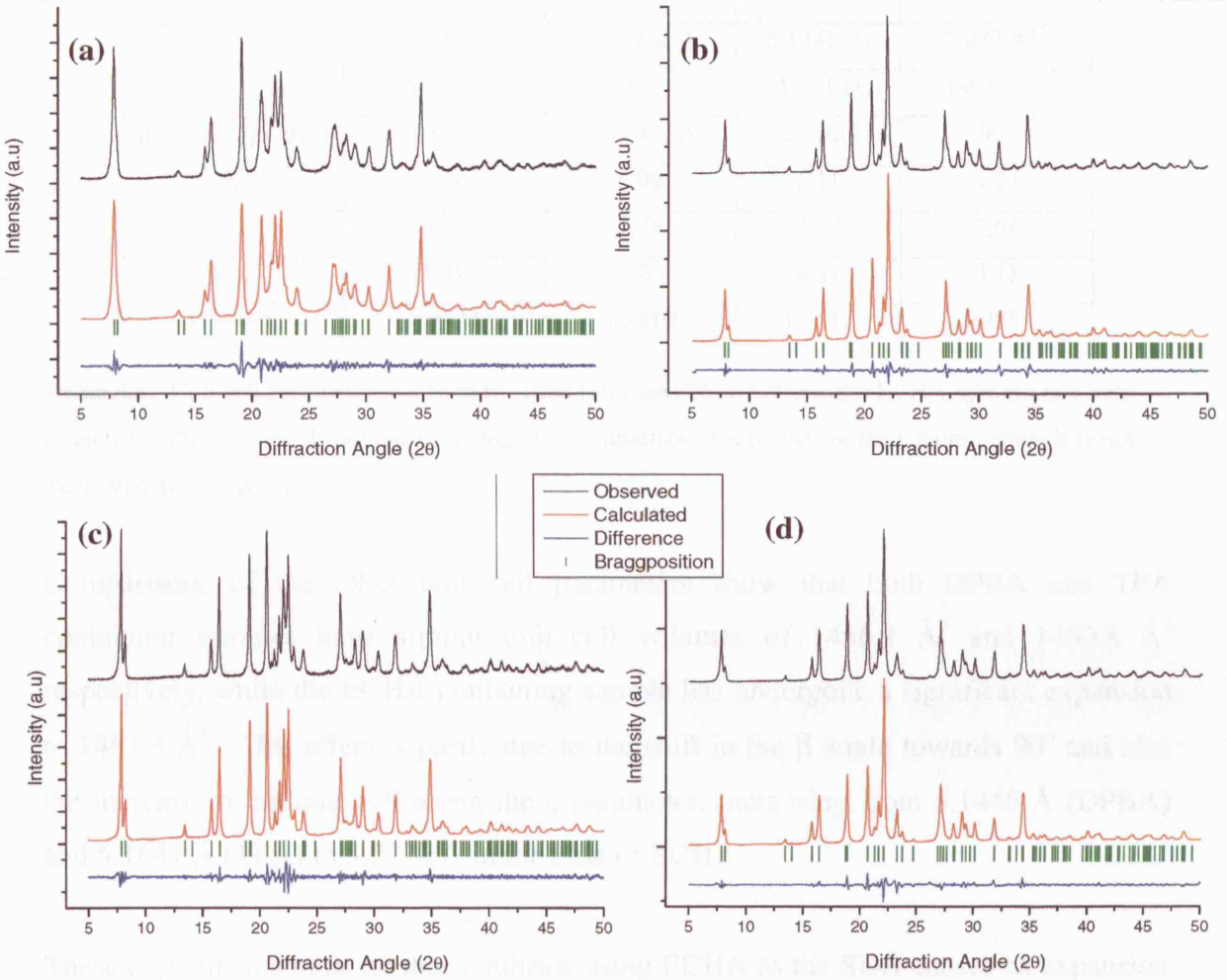

Figure 4.18: LeBail fits for **un-calcined** CoAPO-36 synthesised using TPA (a), ECHA (b) and DPBA (c) fitted using the C2/c space group and the ECHA system fitted with the Cmcm space group (d).

The results confirm the initial observations, with both DPBA and TPA having a β angle with significant deviation from 90° at 92.176° and 92.848° respectively, again indicating the space group to be C2/c. For ECHA the β angle is almost 90° (90.141°), indicating that this system is much closer to the higher symmetry Cmcm space group. By repeating the fit for the ECHA sample specifically within the Cmcm space group, the reliability factors for the fit were decreased (e.g. R_p decreased by 4.2% and R_{wp} by

2.2%). The DW-exp factor does increase (moving away from the ideal of 2)[66,67]. However, all other reliability factors improved and a visual inspection of the difference plots clearly indicates a slightly improved fit. Therefore, these results confirm that Cmcm is indeed the correct space group for the ECHA system.

Parameter	TPA	ECHA	DPBA	ECHA
Space group	C2/c	C2/c	C2/c	Cmcm
a (Å)	13.0875(7)	13.1473(5)	13.1733(5)	13.1779(7)
b (Å)	21.638 (1)	21.605(1)	21.501(1)	21.632(1)
c (Å)	5.1647(2)	5.2148(5)	5.1445(2)	5.2279(3)
Volume ($Å^3$)	1460.8(1)	1481.2 (1)	1456.1 (1)	1491.3(1)
β (°) ($\alpha = \gamma = 90°$)	92.848(6)	90.141(5)	92.176(4)	90*
R_p	4.90	5.98	6.11	5.73
R_{wp}	6.62	7.78	7.92	7.61
R_{exp}	2.91	3.20	4.41	3.11
DW-exp	1.9421	1.9419	1.9413	1.9254

Table 4.6: Unit cell parameters for each **un-calcined** CoAPO-36 system, the ECHA systems has been fitted using the C2/c and Cmcm space groups for comparison. *note that for the Cmcm system β is not calculated as ($\alpha = \beta = \gamma = 90°$)

Comparisons of the other unit cell parameters show that both DPBA and TPA containing samples have similar unit cell volumes of 1456.1 $Å^3$ and 1460.8 $Å^3$ respectively, while the ECHA containing sample has undergone a significant expansion to 1491.3 $Å^3$. This effect is partly due to the shift in the β angle towards 90° and also the increase in the unit cell along the c parameter, increasing from 5.1445 Å (DPBA) and 5.1647 Å (TPA) to 5.2279 Å in the case of ECHA.

These experiments indicate that synthesis using ECHA as the SDA causes an expansion of the ATS unit cell and a distortion away from the 'crinkled' lower symmetry C2/c space group, whilst synthesis using both TPA and DPBA does not cause such an expansion.

The above suggestion is supported by considering what happens upon removal of the ECHA organic species by calcination of the sample. The XRD of this sample (figure 4.19) shows there is a relatively large loss in the quality of the pattern, which is probably due to a partial collapse of the framework as the organic species is removed.

However, despite this degradation it was possible to note important changes in the system. An initial examination of the post-calcined sample appeared to indicate that its symmetry was identical to the pre-calcined sample, with the (1 3 1) and (1 3 -1) peaks apparently coalesced. However, upon closer examination it was noted that the peak in the calcined sample has a much lower intensity than expected for the Cmcm system and when compared to the pre-calcined sample. From the earlier results and previous works[4,20] this would seem to indicate that in fact the system does not remain in the Cmcm symmetry upon calcination.

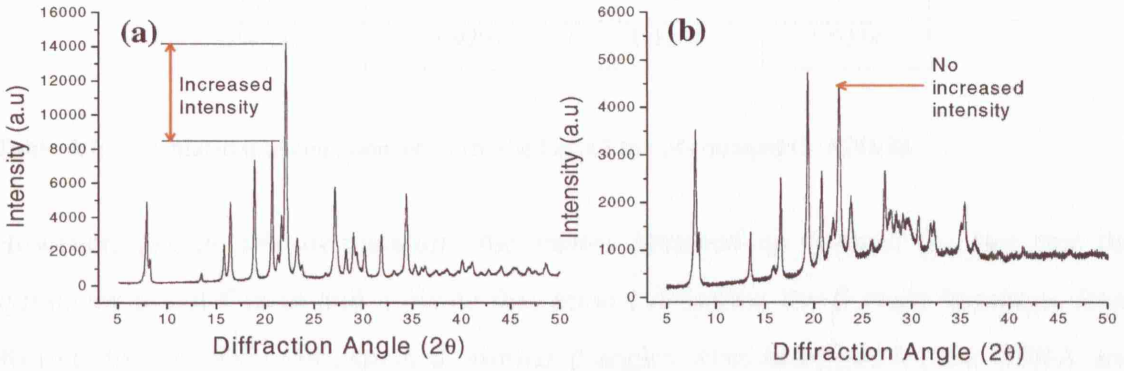

Figure 4.19: XRDs of ECHA pre-calcination (a) and post-calcination (b), the substantial increase in intensity caused by (1 3 1)/(1 3 -1) peak coalescence is only seen in the pre-calcined sample.

By performing a LeBail fit using identical procedures to the pre-calcination ECHA sample it was possible to confirm that this is indeed the case. As expected, the degradation of the pattern leads to a considerably lower quality final fit (figure 4.20), with the reliability factors higher compared to the pre-calcination sample (table 4.7).

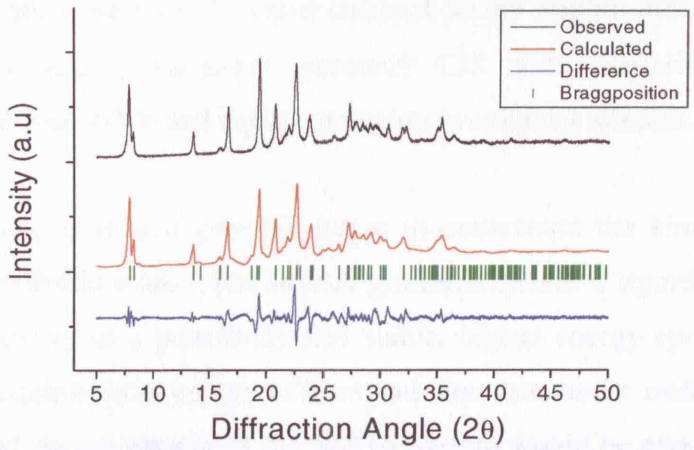

Figure 4.20: LeBail fit for the **calcined** ECHA sample. The quality of the fit is lower due to the degradation in sample quality.

Parameter	TPA	ECHA	DPBA
Space group	C2/c	C2/c	C2/c
a (Å)	13.167(3)	13.127(3)	13.109(2)
b (Å)	21.507 (4)	21.421(5)	21.356(3)
c (Å)	5.159 (1)	5.158(1)	5.164(1)
Volume ($Å^3$)	1458.9(5)	1448.2(5)	1442.6(5)
β (°) (α, γ = 90°)	93.01(2)	93.10(2)	93.68(3)
R_p	6.15	8.53	7.60
R_{wp}	8.41	12.3	10.7
R_{exp}	3.25	3.2	3.16
DW-exp	1.9291	1.9294	1.9314

Table 4.7: Calculated unit cell parameters for the LeBail fits of **calcined** CoAPO-34.

However, despite this degradation, the values obtained do support the fact that the symmetry is not Cmcm and indicate that upon calcination the β angle increases from 90.141° to over 93°. As expected, similar β angles were observed for the DPBA and TPA samples after calcination (table 4.7), therefore the framework does appear to be acting in a manner similar to that noted by Smith *et al*[20], with a 'crinkling' of the framework occurring upon removal of the SDA from the framework channel.

In summary, these crystallographic studies have indicated that ECHA synthesised samples occupy a higher symmetry space group compared to TPA and DPBA samples. This higher symmetry is achieved by an expansion along the c axis of the unit cell and a shift of the β angle towards 90°. Upon calcination the sample moves away from this higher symmetry state to the lower symmetry C2/c state, indicating that the higher symmetry state is less stable and higher in energy in calcined samples.

From these results, it is now possible begin to understand the kinetics of formation detailed in the EDXRD work. The ECHA synthesis causes a significant expansion of the unit cell resulting in a potentially less stable, higher energy system. This higher energy system requires more energy to form and therefore, under isothermal conditions, the induction and crystal growth of the ECHA system would be expected to be slower than the other systems. From the EDXRD results we see that for the DPBA and ECHA systems this is the case, with the activation energy for the formation of the ECHA materials greater by about 30 $kJmol^{-1}$. However, the activation energy for the TPA

system is unusually high, being 60 $kJmol^{-1}$ greater than non-expanded DPBA. Indeed, it is so high that TPA actually shows slower induction and growth than ECHA. As the crystallographic studies have shown that the TPA templated system does not exist in the higher symmetry state, another process must be affecting the rate of crystallisation of this particular system.

4.4.4 : Computational studies

4.4.4.1 : Molecular size measurements

From the EDXRD studies, there is clearly some difference between ECHA, TPA and DPBA as-synthesised systems. The crystallographic studies have shown that ECHA causes an expansion of the unit cell. However, they do not reveal the reason why ECHA causes this expansion whilst the other organics do not. The studies have also shown no significant crystallographic differences between the TPA and DPBA systems, and therefore the differences in the growth kinetics cannot be explained from these results alone. A measurement of the size and shape of the SDAs may prove useful in explaining the expansion of the unit cell with ECHA, and reveal differences between DPBA and TPA, which do not affect the overall symmetry, but may effect crystalline growth.

As discussed in the experimental section, to allow for a good comparison, two methods were used for measuring the size and shape of the molecules. The results from the maximum dimensions and principal axis measurements are given in table 4.8, and while the values differ, they both follow similar trends.

	Max. Dimensions measurements				Principle axis measurements			
SDA	X(Å)	Y(Å)	Z(Å)	VdW vol. ($Å^3$)	RX(Å)	RY(Å)	RZ(Å)	mol. Vol. ($Å^3$)
TPA	9.226	6.436	2.817	175.94	5.096	4.573	2.545	134.265
ECHA	9.509	7.410	5.488	239.71	11.177	3.953	3.351	183.426
DPBA	6.061	6.920	4.834	193.57	6.498	3.227	3.099	145.749

Table 4.8: Size and volume measurements for each SDA molecule using the maximum dimensions and principle axis measurements.

It is immediately apparent from these measurements that ECHA occupies a much larger volume compared to both DPBA and TPA. If we then consider the same number of each different SDA molecule packed into a given volume of the framework, ECHA will occupy the largest volume. Therefore, an expansion of the unit cell might occur in an attempt to reduce the higher energy of this system. What is still not clear however, is why ECHA packs to an extent whereby an expanded higher energy system results, rather than packing to a lesser extent giving a more stable system.

From these measurements a second interesting feature was also noted. Significantly, TPA has a smaller total volume than DPBA indicating, that perhaps contradicting the EDXRD results, the induction and rate of crystallisation would be expected to be faster than DPBA. It is noted, however, that that TPA is the only molecule to be exceptionally short across one (the Z) dimension. It can therefore be considered relatively planar, with a small cross section in comparison to the other molecules, which are more spherical. This fact suggests that the packing of TPA into the forming AlPO framework may be subject to considerably more orientation effects than the more 'rounded' SDAs. In order to identify if this difference could possibly cause the slow crystallisation rate witnessed for TPA a series of docking experiments were devised.

4.4.4.2 : Docking simulations

To measure if inserting the more planar TPA molecule into the framework has any effect when compared with the more spherical ECHA and DPBA molecules, the interaction energies of the system at different packing levels was measured. Due to the constraints mentioned in the experimental section these experiments cannot completely describe the CoAPO-36 system. However, they are adequate to describe the interaction between an increasing number of SDA molecules in a model section of the framework. The relative interaction energies of the systems can then be calculated and the optimum SDA packing level for each system (and other trends) may be noted. It is particularly important to note that cobalt was not modelled explicitly in these model systems, the significance of which is described below.

The aim of these simulations was to compare the interactions of each SDA at different packing levels within an identical environment. Therefore, each experiment was performed using identical unit cell parameters taken for the ATS structure, as derived by

Smith *et al*[20]. All experiments were then performed as described in the experimental section and chapter 2, using the Discover code[32] and the CFF91_czeo[38,39] force field. Initially, the Monte Carlo docking approach is discussed, followed by the manual orientation approach, and the results will then be put into context. Note that the raw data for all docking calculations are given in appendix 2.

The average minimum energies calculated for each SDA using the Monte Carlo docking method are shown in figure 4.21 (average based on the 5 lowest energies). No successful simulations could be completed for more than three SDAs per supercell, and in the case of ECHA a maximum of only two SDAs per supercell, which is expected as ECHA is shown above to occupy a larger volume that the other SDA molecules. Clearly, although the docking method works well for systems with a low SDA content, the random nature of the software's packing method causes problems at higher SDA concentrations. The packing problem at higher SDA concentrations can be understood by the fact that the random probability of packing more than three molecules in the supercell is very low. Indeed, attempts to pack more SDAs into the channel failed, even after one hundred thousand iterations. However, despite this limitation, a trend towards more stable interaction energies with increased packing is clearly visible, suggesting that the insertion of more SDAs into the framework may still be energetically viable.

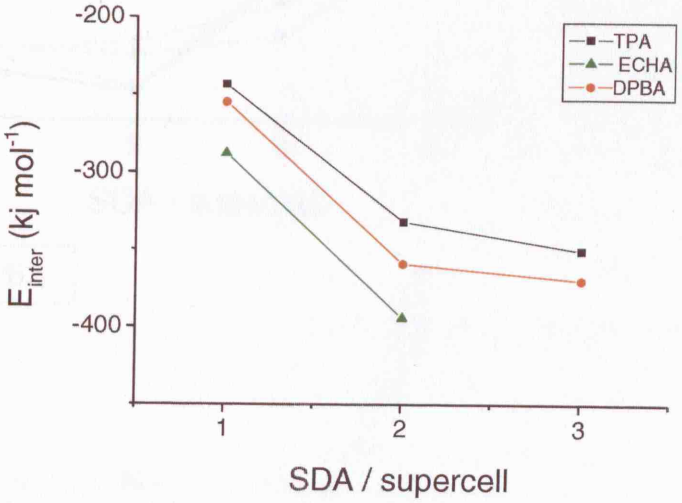

Figure 4.21: The average interaction energies for Monte Carlo simulations with up to three SDAs per supercell.

By using orientation considerations to manually pack the templates into the framework it was possible to investigate the interaction energies at higher packing levels. The interaction energies for each SDA, with up to four SDAs per supercell, in each of the

five previously described orientations are given in figure 4.22. In each case the packing level up to 4 templates per supercell is shown. More dense packing was attempted, but in all cases resulted in very high energy systems and was therefore considered unrealistic.

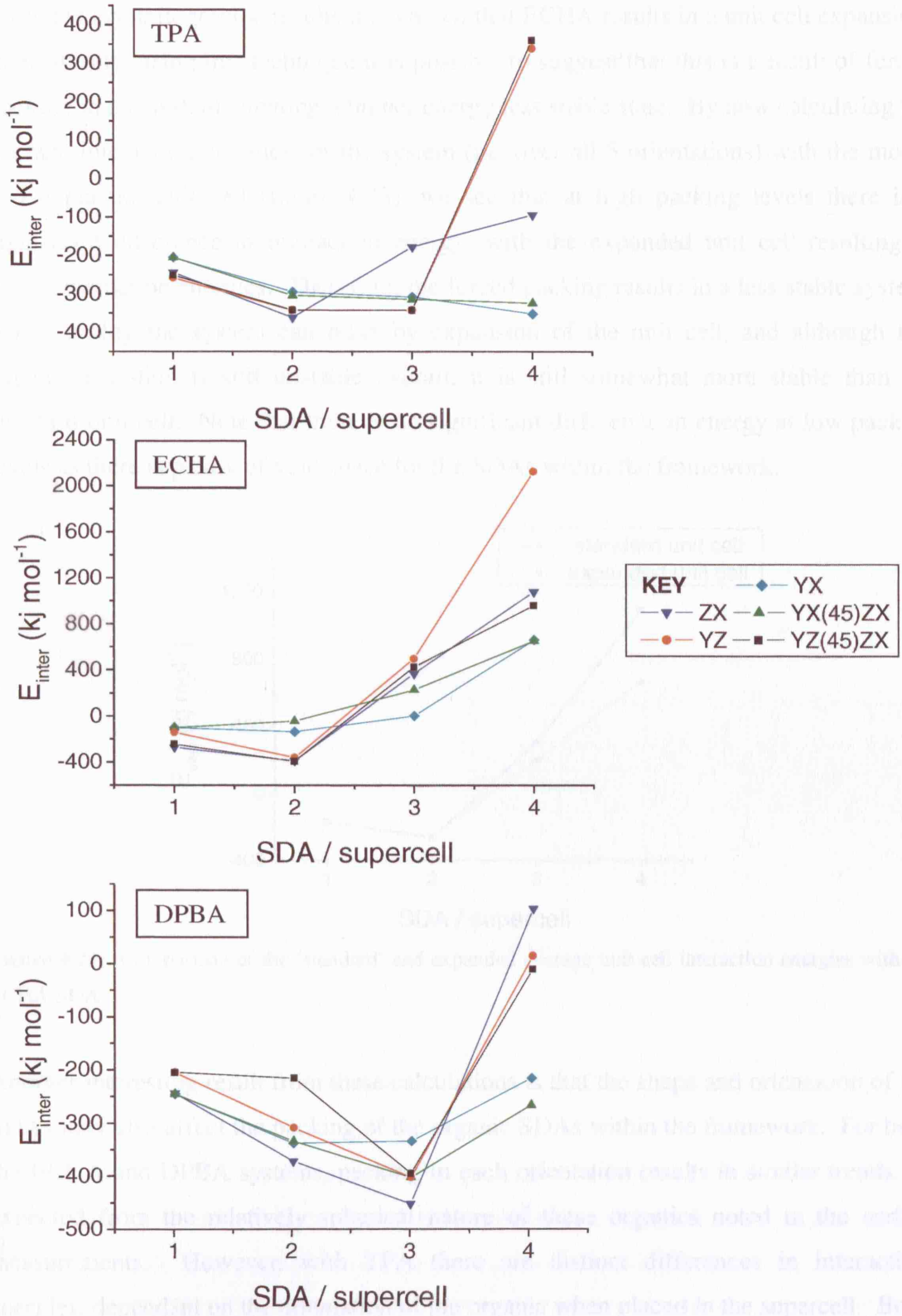

Figure 4.22: The interaction energies for TPA, ECHA and DPBA for each SDA orientation.

From these results the effect of the larger molecular volume of ECHA is once again confirmed. The smaller DPBA molecules easily pack up to 3 SDAs per supercell but the larger ECHA molecules can achieve only 2 SDAs per supercell.

From the crystallographic results it is known that ECHA results in a unit cell expansion. Interestingly, using this technique it is possible to suggest that this is a result of forced packing in the system, creating a higher energy less stable state. By now calculating the average interaction energies for the system (i.e. over all 5 orientations) with the model and expanded unit cell (figure 4.23), we see that at high packing levels there is a significant difference in interaction energy, with the expanded unit cell resulting in lower interaction energies. Therefore, the forced packing results in a less stable system, but in reality the system can relax by expansion of the unit cell, and although this expanded system is still unstable overall, it is still somewhat more stable than the standard unit cell. Note that there is no significant difference in energy at low packing levels as there is plenty of void space for the SDAs within the framework.

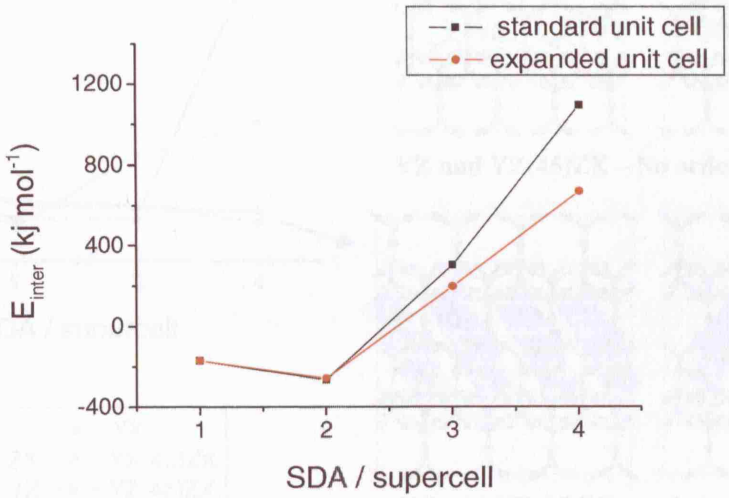

Figure 4.23: Comparison of the 'standard' and expanded average unit cell interaction energies with the ECHA SDA.

Another interesting result from these calculations is that the shape and orientation of the SDAs may also affect the packing of the organic SDAs within the framework. For both the ECHA and DPBA systems, packing in each orientation results in similar trends, as expected from the relatively spherical nature of these organics noted in the earlier measurements. However, with TPA there are distinct differences in interaction energies, dependant on the orientation of the organic when placed in the supercell. Both the YX and YX(45)ZX orientations give rise to significantly enhanced packing allowing

up to 4 SDAs per supercell, while the YZ and YZ(45)ZX orientations are highly unfavourable at this packing level, with the system being unstable after 3 SDAs per supercell. The ZX orientation is even less favourable achieving a packing of only 2 SDAs per supercell. Note that packing of up to 4 SDAs per supercell (equivalent to 1 SDA/unit cell) for the TPA template is not unexpected as Wilson *et al*[68] have previously demonstrated this level of TPA packing can occur in AlPO-5, which has very similar pore sizes to AlPO-36 (it was not possible to compare ECHA and DPBA as these have not been previously used as SDAs for these materials).

A closer examination of the final minimised structures (figure 4.24) confirms that the ability to pack up to 4 SDAs per supercell whilst retaining low interaction energy is a function of the SDA orientation in the framework.

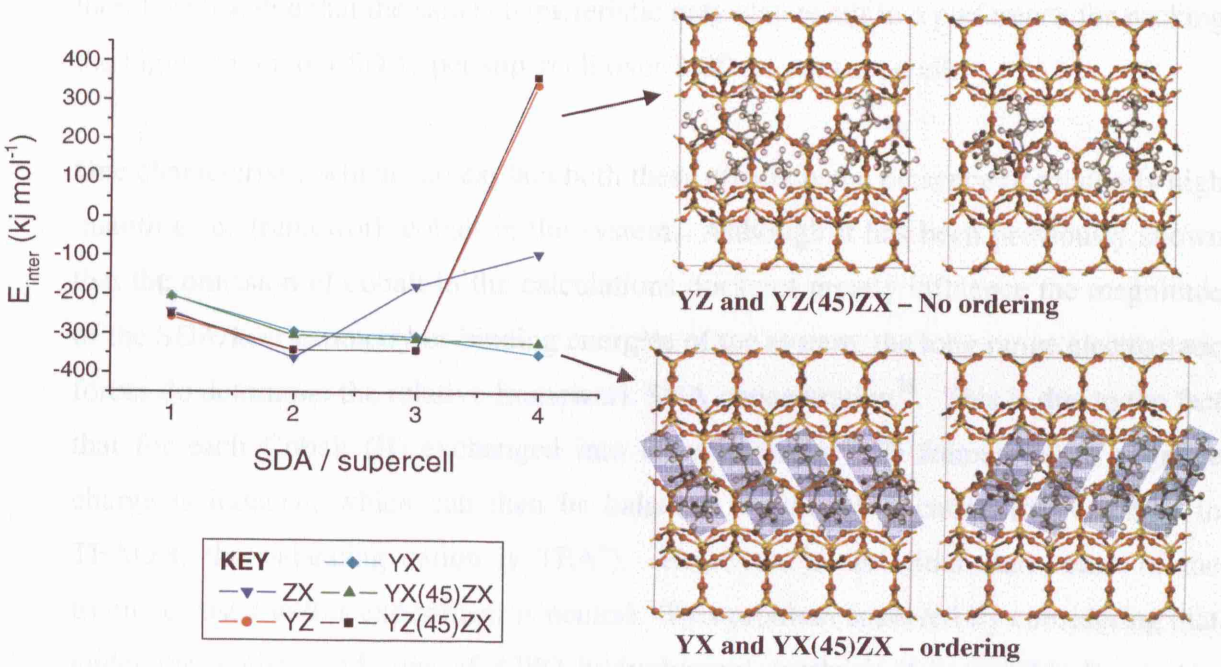

Figure 4.24: The Packing of TPA into the framework is dependant on the ordering of the molecule with its narrow cross section pointing along the channel. In this orientation packing of 4 SDA per super cell is achieved.

The minimised structures for the most energetically favourable packing shows that the SDA is highly ordered along the length of the channel, with the narrow (z) cross section located along the channel of the framework. In the less energetically favourable cases there is no particular ordering, suggesting that it is the planar nature of the TPA molecule giving rise to these orientation effects.

It is possible that the formation of these highly ordered systems will result in slow induction times and rates of growth as specific reorientation of the organic into the growing framework is required. The calculated interaction energies suggest that it is possibly to achieve these highly ordered states, which may offer an explanation as to why the rate of crystallisation of the TPA sample is unusually slow when compared to DPBA. However, it is still not yet clear as to why either ECHA undergoes forced packing to levels creating less stable systems, which require unit cell expansion, or why TPA may pack preferably in the highly ordered 4 SDAs per supercell orientation when the less ordered 3 SDA orientations are of similar energy.

It is already clear from the crystallographic results that some separate characteristic of the system is resulting in more ECHA is being forced into the AlPO-36 framework than indicated by the docking calculations and space filling considerations alone. It is therefore feasible that the same characteristic may also result in a preference for packing the highly ordered 4 SDAs per supercell over 3 SDAs per supercell.

One characteristic which can explain both these effects is the presence of relatively high quantities of framework cobalt in the system. Although it has been previously shown that the omission of cobalt in the calculations does not greatly influence the magnitude of the SDA/host geometry or binding energies of the system, the long range electrostatic forces do determine the relative framework SDA concentration[36]. This is due to the fact that for each Cobalt (II) exchanged into the aluminium (III) framework, a negative charge is induced, which can then be balanced by the SDA cation (for example in TEAOH, the balancing cation is TEA^+). However, in its initial state, each of the triamines used in this experiment is neutral. This problem is solved by considering that under the acidic conditions of AlPO hydrothermal synthesis it is possible for proton transfer to occur (equation 4.7)[69], which results in a protonated organic and a positive charge capable of compensating for cobalt substitution.

$$NR_3 + H_3O^+ \rightleftharpoons NR_3H^+ + H_2O \qquad \textbf{(4.7)}$$

Size measurements on these protonated forms of the SDAs confirm that the exchange of a proton on the organic for the available lone pair does not increase the size of the organics or significantly increase their van der Waals volume (which increases by between 0.6 and 1.3%). Therefore, the results and trends detailed above remain

unaffected and can now be explained using the charge balancing abilities of these protonated species.

From the EDAX results, about 11% of Al has been substituted for Co in these systems. Therefore by calculation, 5.3 aluminium T sites per supercell will contain cobalt. Although the actual positions of the cobalt within the framework are unknown and some might occupy inaccessible parts of the framework, it is now possible to understand the preference for increased SDAs per supercell.

For ECHA the maximum packing level from space filling considerations alone is only 2 SDAs per supercell, which leaves a large charge imbalance within the framework. Therefore, additional SDAs are 'forced' into the supercell in an attempt to balance the framework charge, resulting in the change in unit cell parameters seen in the crystallographic results and the slow rate of reaction.

For TPA, the maximum packing level from the space filling considerations is 3 or 4 SDAs per supercell, which requires no forced packing. The packing of 3 SDAs per supercell can result from either ordered or less ordered orientations. However, given the need for electro-neutrality of the framework, it seems likely that packing of 4 SDAs per supercell will occur resulting in a greater balance of charge. As this packing can only result from a highly ordered SDA orientation, the rate of crystallisation then becomes retarded as each SDA has to be reoriented from the gel for the framework to grow.

In the case of DPBA packing of up to 3 SDAs per supercell is easily achieved. In comparison to ECHA the charge on the framework is then relatively well balanced and therefore little forced packing will occur. Additionally, the packing of the SDA within the system is not particularly ordered, (as the SDA is spherical) and so little reorientation of the SDA from the gel into the growing framework is also required.

It must also be noted that whilst these packing calculations are indicative of the amount of SDA available for charge balancing, they clearly do not fully model the experimental systems as they are not electro-neutral. Therefore, some additional charge balance must be being supplied by other cations such as acidic protons.

4.5 : Summary and conclusions

In this series of experiments, a complementary combination of experimental and computational techniques have been used to demonstrate how metal substitution and SDA type can have substantial influence over the formation kinetics and final crystalline structure of CoAPO-36.

Two important factors have been identified as affecting the rate of formation of CoAPO36:

1. The ability of the SDA to pack in an ordered fashion.
2. The need for forced packing of the SDA (and resulting in an expansion of the unit cell)

Both factors are influenced strongly by the need for charge compensation caused by the insertion of cobalt into the AlPO framework. In the case of the ordered packing, greater charge compensation can be achieved, whilst forced packing occurs when the charge balance requirement is not significantly satisfied.

Forced packing results in an expanded unit cell and in systems with higher energies and therefore retards the crystallisation rate. Ordered packing requires significant reorientation of the template, a process which is suggested will also retard the crystallisation. The EDXRD results suggest that that ordered packing causes a significant retardation, whilst forced packing also results in some retardation, but to a lesser extent (figure 4.25).

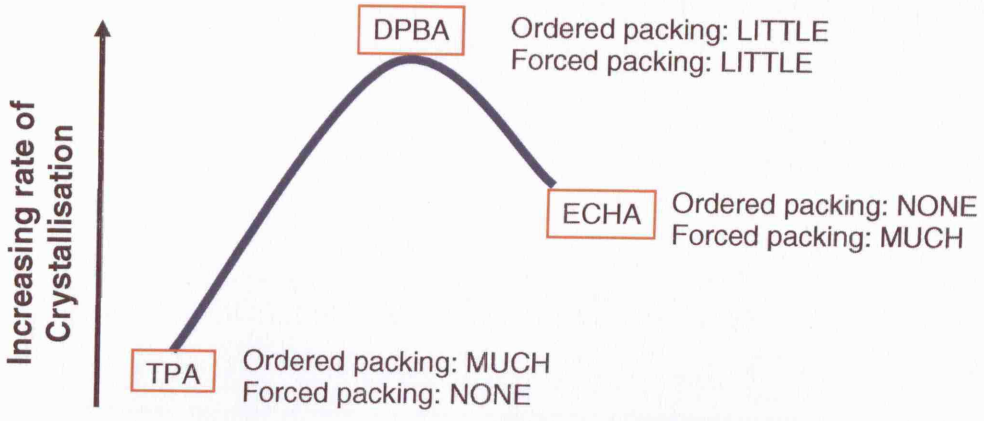

Figure 4.25: Representation of the factors affecting the rate of formation of the CoAPO-36 system.

As described above, DPBA is found to have the fastest rate as it represents a balance between the two extremes of TPA and ECHA. It is relatively well charge balanced and therefore little forced packing is required and the spherical volume results in little ordered packing.

This series of experiments has shown how a use of experimental and computational techniques in a complementary fashion can reveal new insights into the crystallisation of porous materials. It has been demonstrated that neither experiential techniques nor computational techniques alone can fully predict the reaction kinetics of AlPO-36. In addition it has been shown, that although the use of relatively cheap computationally techniques cannot fully model the system, they can offer insight into organic framework interactions, which cannot always be achieved from experimental work alone.

It is suggested that further use of these complementary techniques may reveal more insights into the understanding of the complex interactions occurring between porous frameworks and the organic SDA. These experiments will then aid in the development of faster, more cost effective formation routes for the synthesis of porous materials, with both current and novel structures.

4.6 : Future work

A number of techniques would help evolve the understanding of the CoAPO-36 system and help confirm the theories presented in this work.

From an experimental stand point, the use of synchrotron powder diffraction or synchrotron single crystal diffraction would be particularly useful. These techniques would give very high quality diffraction patterns and enable the positions of the cobalt and possibly the SDA within the framework to be accurately mapped. TGA analysis would also be particularly useful as it should allow the measurement of the different template concentrations within the AlPO framework (i.e. 2 – 3 SDA/supercell for DPBA and ECHA and 4 SDA/supercell for TPA) confirming the packing calculations. It would also be useful to investigate increased cobalt loading in the system and see if this results in further expansion of the unit cell and measure the kinetics of other metal substituted systems (e.g. zinc or manganese) synthesised with the same SDAs, as similar trends should be seen.

From a computational stand point, the code used in these calculations was constrained in a number of ways. Therefore, the use of more advanced methods and force fields with more flexible codes, such as GULP, would improve the calculations and allow the framework to be modelled more accurately. It may then be possible to predict the relaxation of the framework around the organic molecules and how the positioning of cobalt and other substituted metals in the framework may affect the unit cell parameters. Additionally it would be useful to investigate ways of entirely charge balancing the framework, perhaps by modelling protons as well as SDA molecules within the system.

4.7 : References

(1) Sanchez-Sanchez, M.; Sankar, G. In *Recent Advances in the Science and Technology of Zeolites and Related Materials, Pts a - c*; Elsevier Science Amsterdam, 2004; Vol. 154, p 1021.

(2) Wilson, S. T.; Lok, B. M.; Flanigen, E. M. *US Patent* **1983**, 4310440.

(3) Wilson, S. T.; Lok, B. M.; Messina, C. A.; Cannan, T. R.; Flanigen, E. M. *J. Am. Chem. Soc.* **1982**, *104*, 1146.

(4) Wright, P. A.; Natarajan, S.; Thomas, J. M.; Bell, R. G.; Gaiboyes, P. L.; Jones, R. H.; Chen, J. S. *Angew. Chem.-Int. Edit. Engl.* **1992**, *31*, 1472.

(5) Akolekar, D. B. *J. Catal.* **1993**, *143*, 227.

(6) Wilson, S. T.; Flanigen, E. M. In *Zeolite Synthesis*; Occelli M, L., Robson H, E., Eds.; The American Chemical Society: 1989; Vol. 398, p 328.

(7) Akolekar, D. B. *J. Catal.* **1993**, *144*, 148.

(8) Raja, R.; Sankar, G.; Thomas, J. M. *Chem. Commun.* **1999**, 829.

(9) Thomas, J. M.; Raja, R.; Sankar, G.; Johnson, B. F. G.; Lewis, D. W. *Chem.-Eur. J.* **2001**, *7*, 2973.

(10) Sankar, G.; Raja, R.; Thomas, J. M. *Catal. Lett.* **1998**, *55*, 15.

(11) Flanigen, E. M.; Lok, B. M.; Patton, R. L.; Wilson, S. T. In *7th International zeolite Conference*; Murakami, Y., Ijima, A., Ward, J. W., Eds.; Tokyo and Elsevier Amsterdam: Tokyo, 1986, p 103

(12) Machado, M. D. S.; Perez-Pariente, J.; Sastre, E.; Cardoso, D.; Giotto, M. V.; Garcia-Fierro, J. L.; Fornes, V. *J. Catal.* **2002**, *205*, 299.

(13) Zahedi-Niaki, M. H.; Xu, G. Y.; Meyer, H.; Fyfe, C. A.; Kaliaguine, S. *Microporous Mesoporous Mat.* **1999**, *32*, 241.

(14) Flanigen, E. M.; Lok, B. M.; Patton, R. L.; Wilson, S. T. *Pure Appl. Chem.* **1986**, *58*, 1351.

(15) Nakashiro, K.; Ono, Y. *J. Chem. Soc.-Faraday Trans.* **1991**, *87*, 3309.

(16) Machado, M. D.; Cardoso, D.; Perez-Pariente, J.; Sastre, E. *Chem. Mat.* **1999**, *11*, 3238.

(17) Sheldon, R. A.; Wallau, M.; Arends, I.; Schuchardt, U. *Accounts Chem. Res.* **1998**, *31*, 485.

(18) Haanepen, M. J.; ElemansMehring, A. M.; vanHooff, J. H. C. *Appl. Catal. A-Gen.* **1997**, *152*, 203.

(19) Roisnel, T.; Rodriguez-Carvajal, J. In *Epdic 7: European Powder Diffraction, Pts 1 and 2*; Trans Tech publications Ltd: Zurich-Uetikon, 2001; Vol. 378, p 118.

(20) Smith, J. V.; Pluth, J. J.; Andries, K. J. *Zeolites* **1993**, *13*, 166.

(21) Catlow, C. R. A.; Sankar, G. In *Microporous Properties and Processes in Minerals*; Wright, K., Catlow, C. R. A., Eds.; Kluwer Academic: 1999, p 145.

(22) Barnes, P.; Jupe, A. C.; Colston, S. L.; Jacques, S. D.; Grant, A.; Rathbone, T.; Miller, M.; Clark, S. M.; Cernik, R. J. *Nucl. Instrum. Meth. B* **1998**, *134*, 310.

(23) Muncaster, G.; Davies, A. T.; Sankar, G.; Catlow, C. R. A.; Thomas, J. M.; Colston, S. L.; Barnes, P.; Walton, R. I.; O'Hare, D. *PCCP Phys. Chem. Chem. Phys.* **2000**, *2*, 3523.

(24) Clark, S. M.; Nield, A.; Rathbone, T.; Flaherty, J.; Tang, C. C.; Evans, J. S. O.; Francis, R. J.; Ohare, D. *Nucl. Instrum. Meth. B* **1995**, *97*, 98.

(25) Evans, J. S. O.; Francis, R. J.; Ohare, D.; Price, S. J.; Clark, S. M.; Flaherty, J.; Gordon, J.; Nield, A.; Tang, C. C. *Rev. Sci. Instrum.* **1995**, *66*, 2442.

(26) Thompson, S. P. *XRD Explorer v 1.2* **2001**.

(27) Coelho, A. A.; Cheary, R. W. *X-ray Line Profile Fitting Program (XFIT) v0.07.002* **1997**.

(28) Lewis, D. W.; Freeman, C. M.; Catlow, C. R. A. *J. Phys. Chem.* **1995**, *99*, 11194.

(29) Harris, T. V.; Zones, S. I. In *Zeolites and Related Microporous Materials: State of the Art 1994*; Elsevier Science: Amsterdam, 1994; Vol. 84, p 29.

(30) Bell, R. G.; Lewis, D. W.; Voigt, P.; Freeman, C. M.; Thomas, J. M.; Catlow, C. R. A. In *Zeolites and Related Microporous Materials: State of the Art 1994*; Elsevier Science: Amsterdam, 1994; Vol. 84, p 2075.

(31) *Accelrys Software Inc, Materials Studio v3.1* **2005**.

(32) *Accelrys Software Inc, Discover v2.9* **2005**.

(33) Lewis, D. W.; Catlow, C. R. A.; Thomas, J. M. *Chem. Mat.* **1996**, *8*, 1112.

(34) Boyett, R. E.; Stevens, A. P.; Ford, M. G.; Cox, P. A. *Zeolites* **1996**, *17*, 508.

(35) Boyett, R. E.; Stevens, A. P.; Ford, M. G.; Cox, P. A. In *Progress in Zeolite and Microporous Materials, Pts a-c*; Elsevier Science: Amsterdam, 1997; Vol. 105, p 117.

(36) Martens, J. A.; Mertens, M.; Grobet, P. J.; Jacobs, P. A. In *Innovations in Zeolite Materials Chemistry*; Grobet, P. J., Mortier, W. J., Vansant, E. F., Shulz-Ekloff, G., Eds.; Elsevier: Amsterdam, 1988; Vol. 37, p 9797.

(37) Freeman, C. M.; Catlow, C. R. A.; Thomas, J. M.; Brode, S. *Chem. Phys. Lett.* **1991**, *186*, 137.

(38) Hagler, A. T.; Lifson, S.; Dauber, P. *J. Am. Chem. Soc.* **1979**, *101*, 5122.

(39) Hill, J. R.; Sauer, J. *J. Phys. Chem.* **1994**, *98*, 1238.

(40) Atkins, P. W. *Physical Chemistry*; sixth ed.; Oxford University Press, 1998.

(41) Cotton, F. A.; Wilkinson, G. *Advanced Inorganic Chemistry*; Fifth ed.; John Whiley and Sons Inc, 1988.

(42) Toriuma, K.; Ozima, M.; Akaoi, M.; Sato, Y. *Acta Crystallographica Section B* **1978**, *34*, 1093.

(43) Beale, A. M.; Sankar, G.; Catlow, C. R. A.; Anderson, P. A.; Green, T. L. *PCCP Phys. Chem. Chem. Phys.* **2005**, *7*, 1856.

(44) Barrett, P. A.; Sankar, G.; Catlow, C. R. A.; Thomas, J. M. *J. Phys. Chem.* **1996**, *100*, 8977.

(45) Moen, A.; Nicholson, D. G.; Ronning, M.; Lamble, G. M.; Lee, J. F.; Emerich, H. *J. Chem. Soc.-Faraday Trans.* **1997**, *93*, 4071.

(46) Christensen, A. N.; Jensen, T. R.; Norby, P.; Hanson, J. C. *Chem. Mat.* **1998**, *10*, 1688.

(47) Davies, A. T.; Sankar, G.; Catlow, C. R. A.; Clark, S. M. *J. Phys. Chem. B* **1997**, *101*, 10115.

(48) Norby, P.; Christensen, A. N.; Hanson, J. C. *Inorg. Chem.* **1999**, *38*, 1216.

(49) Walton, R. I.; Millange, F.; O'Hare, D.; Davies, A. T.; Sankar, G.; Catlow, C. R. A. *J. Phys. Chem. B* **2001**, *105*, 83.

(50) Beale, A. M.; Sankar, G. *Chem. Mat.* **2003**, *15*, 146.

(51) Loh, J. S. C.; Fogg, A. M.; Watling, H. R.; Parkinson, G. M.; O'Hare, D. *PCCP Phys. Chem. Chem. Phys.* **2000**, *2*, 3597.

(52) Evans, J. S. O.; Price, S. J.; Wong, H. V.; O'Hare, D. *Journal of the American Chemical Society* **1998**, *120*, 10837.

(53) Avarami, M. *J. Chem. Phys.* **1939**, *7*, 1103.

(54) Avarami, M. *J. Chem. Phys.* **1940**, *8*, 212.

(55) Avarami, M. *J. Chem. Phys.* **1941**, *9*, 177.

(56) Erofe'ev, B. V. *Doklady academy of science URSS* **1946**, *52*, 511

(57) Sheridan, A. K.; Anwar, J. *Chem. Mat.* **1996**, *8*, 1042.

(58) Wilkinson, A. P.; Speck, J. S.; Cheetham, A. K.; Natarajan, S.; Thomas, J. M. *Chem. Mat.* **1994**, *6*, 750.

(59) Hulbert, S. F. *Journal of the British Ceramic Society* **1969**, *6*, 11.

(60) Thompson, R. W.; Dyer, A. *Zeolites* **1985**, *5*, 292.

(61) Hancock, J. H.; Sharp, J. D. *Journal of the American Ceramic Society* **1972**, *55*, 74.

(62) Fogg, A. M.; Price, S. J.; Francis, R. J.; O'Brien, S.; O'Hare, D. *J. Mater. Chem.* **2000**, *10*, 2355.

(63) Gualtieri, A.; Norby, P.; Artioli, G.; Hanson, J. *Microporous Mater.* **1997**, *9*, 189.

(64) Gualtieri, A.; Norby, P.; Artioli, G.; Hanson, J. *Phys. Chem. Miner.* **1997**, *24*, 191.

(65) Baerlocher, C.; McCusker, L. B.; Database of Zeolite Structures: http://www.iza-structure.org/databases/: 2005.

(66) Hill, R. J.; Flack, H. D. *J. Appl. Crystallogr.* **1987**, *20*, 356.

(67) Young, R. A. In *The Reitveld Method*; Young, R. A., Ed.; Oxford University Press: 1993, p 1.

(68) Wilson, S. T.; Lok, B. M.; Messina, C. A.; Cannan, T. R.; Flanigen, E. M. In *Intrazeolite Chemistry*; Stucky, G. D., Ed.; American Chemical Society: Washington, 1983; Vol. 218, p 79.

(69) Clayden, J.; Greeves, N.; Warren, S.; Wothers, P. *Organic Chemistry*; First ed.; Oxford University press, 2001.

Chapter 5

A combined SAXS/WAXS study into the formation of pure and metal substituted zeolite-A

5.1 : Chapter overview

Clear solution syntheses of zeolites can be considered as a model for the formation of zeolites and other porous materials from gels. Such clear solution syntheses are studied here by combined small angle X-ray scattering (SAXS) and wide angle X-ray scattering (WAXS) to monitor the formation of nano-sized particles, from the early stages of nucleation through to crystallisation. Furthermore, for the first time, germanium doped zeolite-A has been synthesised from a clear solution and the method is found to increase the size of these nano sized particulates and the rate of formation of crystalline product.

A mechanism is proposed for the nucleation and growth of crystals from this system, similar to that proposed for other zeolite systems. From this mechanism a number of processes have been identified that lead to the eventual growth of the crystalline product. It has been found that inclusion of germanium not only affects the overall rate of formation, but significantly changes the balance of these processes within the system, resulting in changes in amount of intergrowth in the final crystalline product.

5.2 : Introduction

Zeolite-A, together with zeolite-X was one of the first synthetic zeolites to be successfully prepared. Developed by Robert Milton of the Linde division of the Union Carbide corporation in the 1950's[1,2], zeolite-A has the general structural formula:

$$[Na_{12}(Al_{12}Si_{12}O_{48}).27H_2O]$$

The strict alternation of silicon and aluminium atoms gives rise to the maximum Si/Al ratio of 1 (in accordance to Lowenstein's rule) leading to the highest possible framework charge, and therefore the maximum number of Na^+ counter-balancing ions. Structurally, zeolite-A has the 3-dimensional topology LTA (Figure 5.1), comprising of 4, 6 and 8-membered rings to form a series of large β-cages linked by double four rings (4-4)[3]. This large open framework and high counter ion content have made zeolite-A particularly suitable as an ion exchanger for water softening applications. Identified commercially as one of the Linde molecular sieves (LMS), zeolite-A became one of the first zeolites to be synthesised and exploited on a commercial scale[4]. Its use has become increasingly important as the introduction of tighter environmental rules have restricted the use of damaging chemicals such as sodium tripolyphosphates. Zeolite-A is therefore one of the most commercially utilised molecular sieves[5].

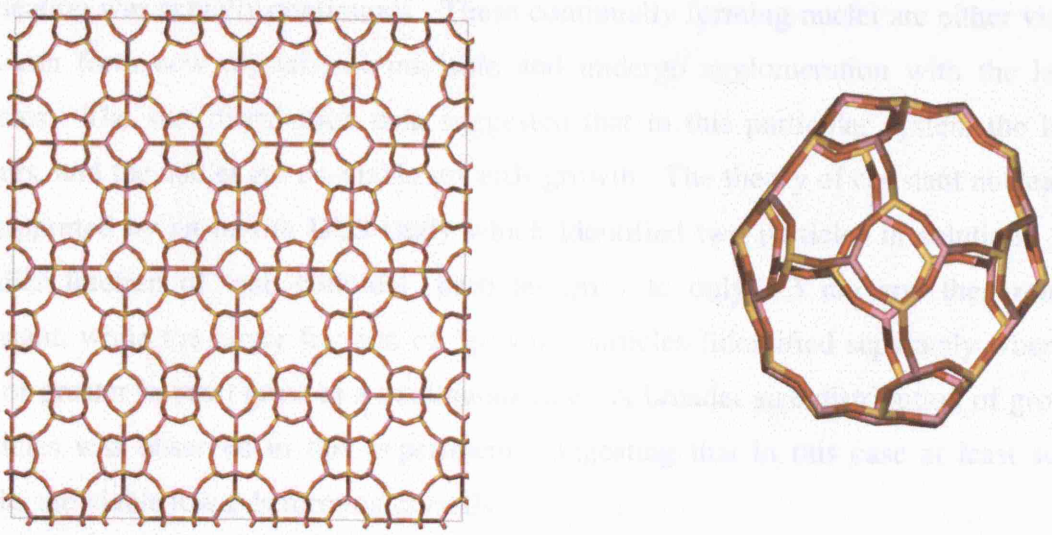

Figure 5.1: The structure of zeolite-A (LTA) (left) consists of individual sodalite (β) cages (right) interconnected by double four rings. It contains 4, 6 and 8 member rings and can be comprised of 4, 4-2, 6-2, 4-4 and 8 secondary building units.

5.2.1 : Nucleation and growth from clear solutions

As mentioned earlier, an understanding of the nucleation and growth of molecular sieve materials is essential if rational design of new commercially important products is to be achieved. Numerous studies on a variety of zeolites (as detailed in chapter 1) have lead to a variety of proposed nucleation and growth mechanisms.

In this chapter, we will focus particularly on zeolite-A formed from clear solutions. This system is particularly useful in the study of early nucleation as the dilute nature of the solution allows the use of a number of techniques which are unable to probe the thicker gel counterparts. Here, we examine the previous work on the formation mechanisms of both zeolite-A and other zeolites from clear solutions, in order to gain insight into the work performed in this chapter.

5.2.1.1 : Light scattering experiments

The early stages of silicalite (the aluminium free end member of ZSM-5[6]) growth have been probed using a variety of techniques, including optical microscopy, dynamic light scattering (DLS) and quasi-elastic light scattering (QELS)[7-9]. Twomey *et al*[10] observed a very narrow particle size distribution of crystals, indicating that nucleation was apparently quasi-instantaneous, ceasing shortly after growth begins. However, removal of the crystallites from the solution caused growth to restart, thus it was concluded that nucleation was actually continuous. These continually forming nuclei are either viable, and can form new crystals, or unviable and undergo agglomeration with the larger species. The size distribution data suggested that in this particular system the latter occurs, and the nuclei are un-viable towards growth. The theory of constant nucleation is supported by an *in situ* DLS study which identified two particles in solution. The smaller fraction of 'sub colloidal' particles grew to only 3.3 nm and then remain constant, while the larger fraction of 'growth' particles (identified separately when 10 nm or greater in size) grow at a continuous rate. A broader size distribution of growth particles was observed in this experiment, suggesting that in this case at least some nuclei are viable towards forming crystals[11].

Similar techniques have been used by a number of groups to study the formation of zeolite-A. Prolonged aging at room temperature was shown to increase crystallite yield and indicates a constant formation of nuclei which can undergo agglomeration. Some

small (1 nm) particulates were persistent during the reaction and may be similar to the constantly forming nuclei in silicalite. It was also noted in this work that the amorphous gel suspends and isolates the crystallites until near the end of the reaction[12,13]. This suspension of crystallites within amorphous particles was later identified visually by Mintova *et al*[14]. Using very slow room temperature synthesis techniques and TEM it was possibly identify small (5 – 10 nm) spherical particles (figure 5.2) prior to template addition. Upon addition of the template, rapid (c.a. 5 mins) formation of 40 – 80 nm was observed, indicating that a change in the electrolyte solution or a chemical reaction can cause initial aggregation. Small 10 – 30 nm crystallites were then observed embedded in the amorphous aggregates, growing to about 40 -80 nm over 7 days. When heated the crystal size increased rapidly to 200 – 400 nm, while the total mass of crystals remained unchanged, suggesting that the smaller zeolite-A particles are, like the nuclei discussed above, unviable. They therefore act only as a nutrient source, supplying material to less soluble larger crystals, which grow in a similar fashion to Oswald ripening. The same group have also used similar studies to reveal a broadly similar mechanism for both zeolite-Y[15] and silicalite[16] phases.

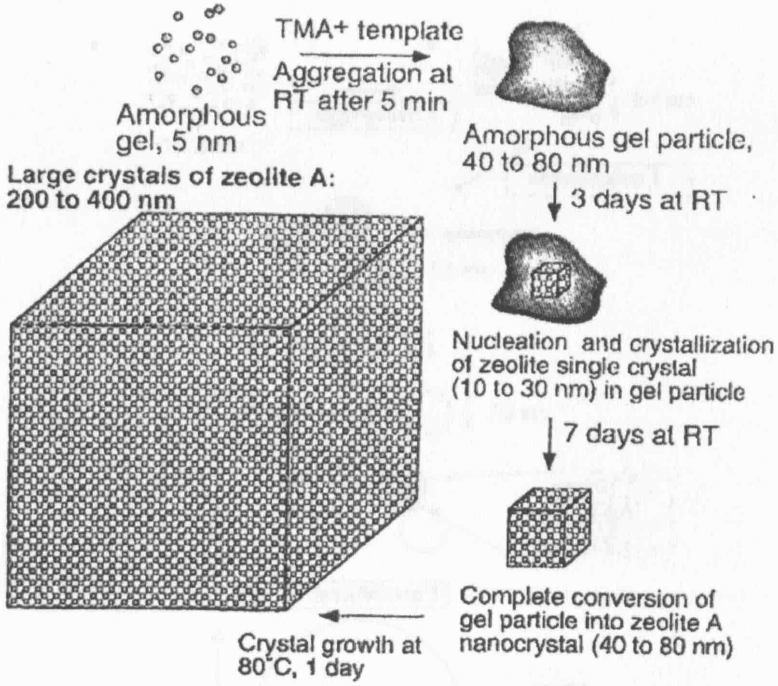

Figure 5.2: The growth mechanism of zeolite-A as proposed by Mintova *et al*. Amorphous 5nm particles undergo aggregation to form larger 40 – 80 nm amorphous gels, crystallites then grow from these particles forming large crystals after heating. Reproduced from ref. 14.

5.2.1.2 : Small angle scattering techniques

SAXS is another powerful technique for investigating the formation of nano-sized particles, and unlike DLS, is less subject to limitations due to multiple size distributions and high concentrations of larger particles. It has been used in combination with a number of other experimental and computational techniques to identify mechanistic details of the formation of zeolites.

Measurement of silicalite formation using fractal analysis[17,18] of SAXS has indicated the rapid formation of small (<3.2 nm) clusters, which may be similar in nature to those observed by Burkett and Davis[19], and would appear consistent with the nuclei identified in the light scattering work detailed above. These clusters then form primary 'fractal' aggregates 6.4 nm in size (Figure 5.3) which undergo densification to 7.2 nm amorphous aggregates. A secondary fractal aggregation then occurs, resulting in structures similar to those seen on a smaller scale in the initial densification (and therefore the term fractal aggregate). These then undergo a second densification step resulting in crystalline materials, although the mechanism for the final re-orientation of the amorphous particle to crystalline material remains unclear.

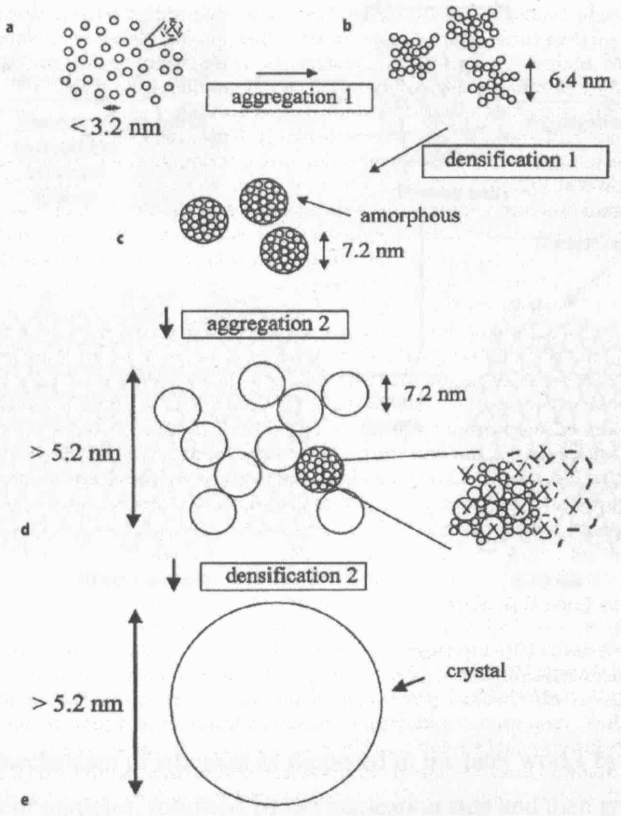

Figure 5.3: The proposed nucleation and growth mechanism of Dokter *et al*, consisting of a number of aggregation and densification steps. Reproduced from ref. 18.

Later work by de Moor *et al*[20,21] suggested that the nucleation and growth process is dominated by small primary units (~2.8nm) and larger aggregates (~10nm). At low alkalinities both species were shown to form. However, at higher alkalinities only the primary units were observed, indicating nucleation was occurring directly from solution, which suggests that a gel phase is not indispensable for crystallisation. However, the aggregates, acting as a gel phase, do play an active role in the nucleation process, enhancing the nucleation rate. Later experiments investigated the slow rate of crystallisation in highly alkaline systems and it was demonstrated that this could be accounted for by considering the very low number of aggregates. It was considered that the aggregation of 10 – 15 nm sized particles is an essential step in the formation of viable crystals[22,23], and a mechanism suggested (figure 5.4) whereby aggregation of primary units into 5-10 nm particles occurs, followed by nucleation of small crystals and growth by transport of primary particles to the growing surface[24].

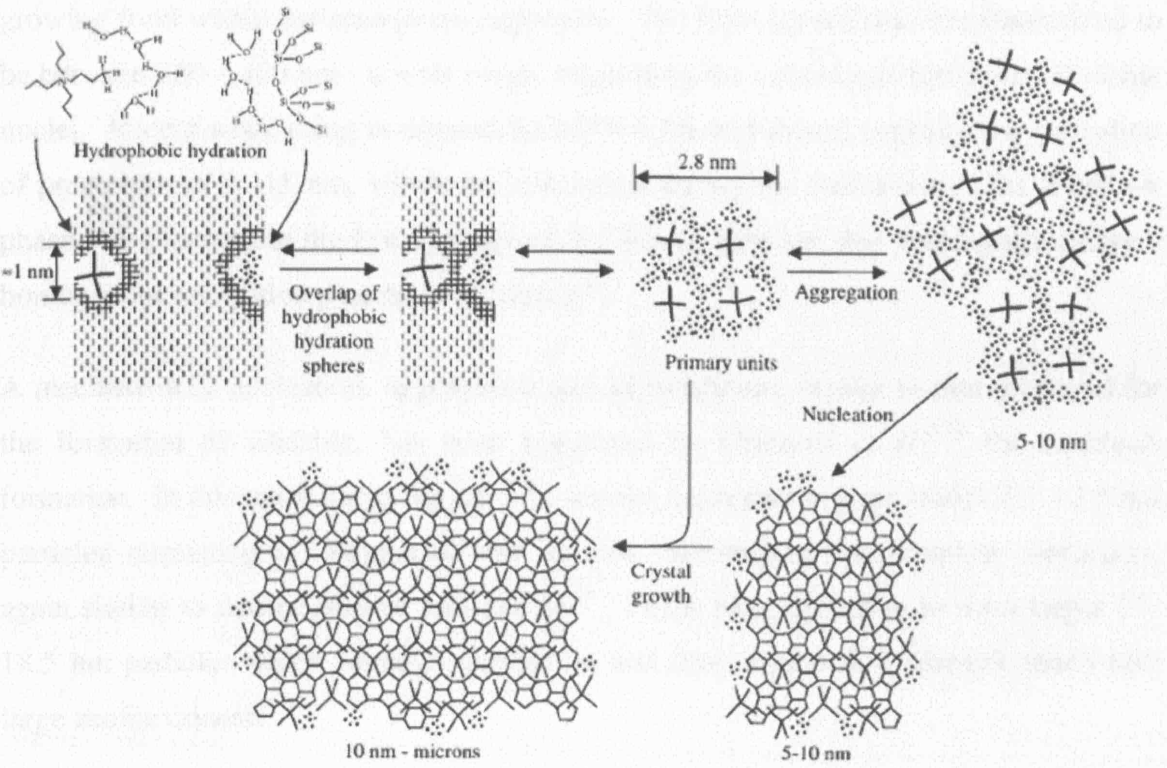

Figure 5.4: The growth mechanism of silicalite as proposed in the later works by de Moor *et al*. Growth consists of agglomeration of particles, followed by the nucleation step and then growth from the transport of primary particles. Reproduced from ref. 24.

While less attention has been directed toward SAXS investigations of zeolite-A, a number of studies have been performed. Some similarities to the silicalite synthesis are noted, whilst distinct variations in mechanisms occur, apparently dependant on the exact synthesis technique used.

Combined SAXS and light scattering techniques performed on a non-templated system indicated precursor 8 nm species which undergo an 'intermediate' stage before the growth of zeolite A beyond 80 nm[25]. However, significant differences are noted as synthesis conditions are varied. For example, a template mediated synthesis yielded 2.2 nm particles which grew to 4.4 nm before the onset of crystallisation, while in colloidal systems the particles grew from 10.2 to 12.1 nm before crystalisation[26]. Another investigation using a non-templated 'opaque' synthesis detailed the presence of large 40 – 100 nm non-uniform gel aggregates in the initial solution[27]. No change in morphology was observed, even when traces of crystalline product where observed, which suggests a mechanism similar to that outlined by Mintova[14], with the crystallites growing from within the amorphous aggregate. The final crystal size was determined to be between 300 – 400 nm - a wide range, suggesting the continuous formation of viable nuclei. Recent work using combined SAXS/WAXS techniques suggests the formation of precursors of 5 -15 nm, which are consumed during the formation of the zeolite-A phase. Oscillations in the low Q range of the SAXS data are also noted and indicate a homogenous nucleation process is occurring[28].

A mechanism of nucleation, aggregation and densification, similar to that proposed for the formation of silicalite, has been suggested by Grizzetti *et al*[29,30] for zeolite-A formation. In this mechanism (figure 5.5) species aggregate to form initial 2.3 – 2.5 nm particles consisting of aluminosilicate species surrounding the template molecules, again similar to that of Burkett and Davies[19]. These then aggregate to form larger 17-18.5 nm particles which undergo nucleation and then compaction (densification) into large zeolite crystals.

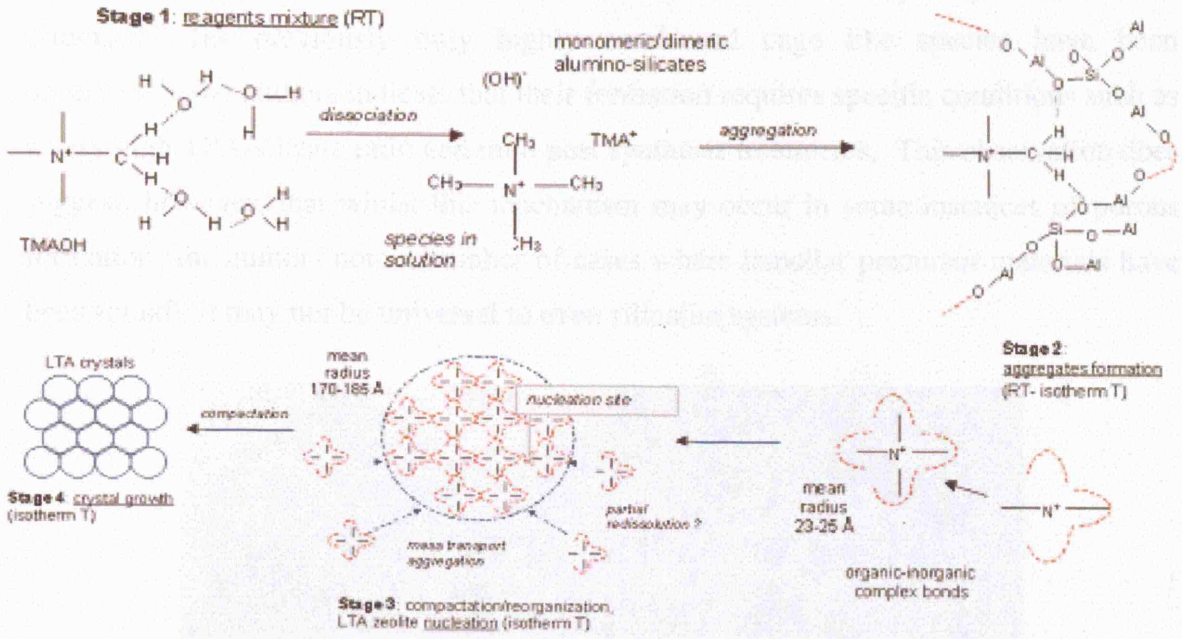

Figure 5.5: The mechanism of formation of zeolite-A as proposed by Grizzetti *et al*, consisting of aggregation and compaction stages. Modified from ref. 29.

Recently, some work has focused on the formation of well ordered entities which then 'click' together to form the zeolite structure. For example, Kirschhock *et al*[31] has used SAXS in combination with techniques such as TEM and NMR to examine the formation of silicalite from a mixture of TPA and tetraethylsilicate (TEOS) solution. The identification of tile-like features within the zeolite crystals and small oligomer building units has lead to the proposal of 'nanoslabs', formed from open organic-silicalite precursors. It was suggested that these may be fundamental in the growth of zeolitic materials, with their formation proceeding as in figure 5.6. Here TPA molecules are initially located at the interface between the organosilicate and aqueous phases. The silicalites then polymerise around the organic species, forming open silicalite molecules, apparently similar in nature to the SBUs as originally proposed by Barrer[32] (species 1 -3). These precursors (species 4) can then link together to form rows of three (species 5), which the click together to form partial or complete nanoslabs (species 6 and 7). The exact distribution of these partial or complete nano slabs was found to be dependant on a number of experimental variables. The formation of the final silicalite crystals (10) then proceeds by fusion of the particles into tablets (8) and then intermediate sized slabs (9). It has been suggested that the nanoslab species may be equivalent to the primary particles seen in previous work[10, 19, 20] and these may also

belong to the nanoslab family[33]. Whilst the formation of these open species has been criticised[34] (as previously only highly condensed cage like species have been observed[35]), the authors indicate that their formation requires specific conditions such as a very high TPA/silicate ratio and mild post synthesis treatments. This observation does suggest, however, that whilst this mechanism may occur in some instances of porous formation (the authors note a number of cases where lamellar precursor materials have been found), it may not be universal to even silicalite systems.

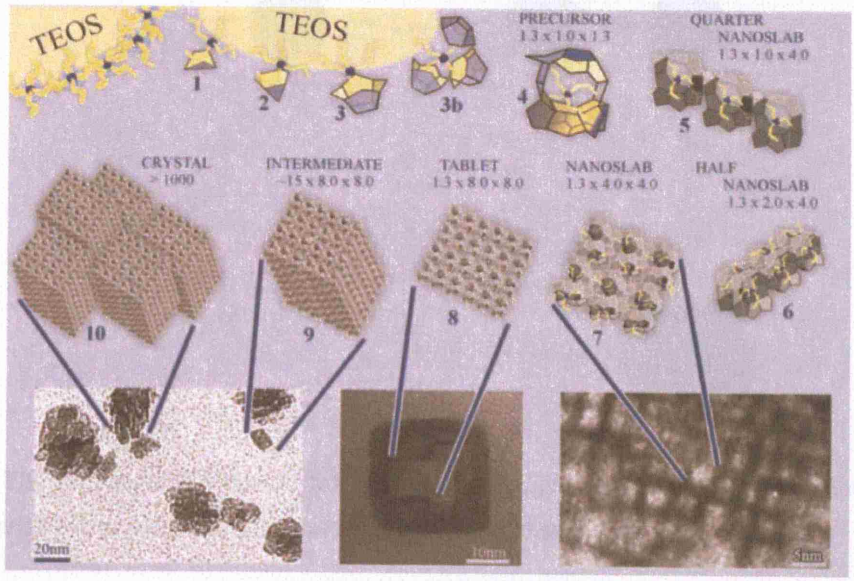

Figure 5.6: The formation of nanoslabs from open silicalite precursors. Reproduced from ref. 31.

SAXS and SANS measurements by Fedeyko *et al*[36] on the reaction of silicalite with tetraalkylaamonium hydroxides (TAA), have indicated that the amorphous silica exists as a core-shell arrangement with an amorphous silica centre and TAA mainly present on the surface. Modelling of nano-particle growth of silica solutions gave results in good agreement with this core-shell model. Spontaneous formation of metastable particles consisting of a core-shell arrangement was observed, with nucleation and growth then continuing by a process similar to Ostwald ripening, ending once the layer of organic cations is formed[37]. Davis *et al*[38] have used this model to propose a growth mechanism for the formation of silicatlite with TPA (figure 5.7). Importantly, they note that there is no evidence for the nanoslabs described by Kircshhock *et al*[31]. SAXS measurements of silicalite solutions at room temperature show only a single size distribution of particles up to 245 days, thought to be silicalite precursor nanoparticles. At 245 days a second distribution, believed to be due to forming crystals, is observed. The lack of any other size distributions has lead to the novel proposal that growth proceeds by an evolving

population of silica nanoparticles, which whilst homogenous in size and shape, exhibit a functional diversity towards aggregation. Precursor nanoparticles (a) consisting of the core shell arrangement have a high rate of dissolution and/or colloidal stability and do not contribute to aggregate growth. These then evolve through *m* intermediates (B_1 to B_m) each of which exhibit lower rates of dissolution and/or colloidal stability, and are increasingly similar to zeolite particles. These intermediates can then contribute to crystal growth by attachment to the nuclei or growing crystals (C_1 to C_n).

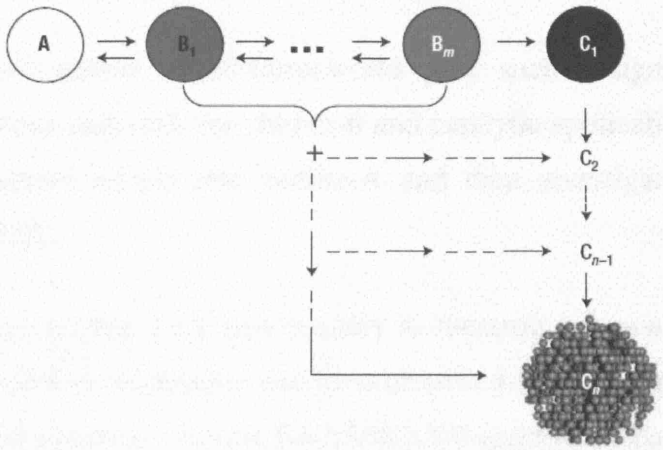

Figure 5.7: The formation of silicalite from particles homogenous in size and shape, but differing in functional diversity as proposed by Davis *et al.* Reproduced from ref. 38.

It is clear from this brief review that the formation of zeolitic materials is complex: small variations in synthesis mixture and conditions appear to dramatically change the type of pre-crystalline material present in the solution. It is also evident that the mechanism by which one zeolite forms may not be entirely comparable with another. However, although the details of each mechanism may differ, there are distinct similarities. In all cases a clear solution synthesis involves some form of particles (e.g. colloids / nanoslabs) undergoing aggregation/densification/attachment and growth by a number processes, but the exact details of these particles and processes are dependant on the synthesis. Effectively there are two modes of growth, either constant or instantaneous nucleation. The former results in a wide size distribution in the forming crystals, whilst the latter leads to a single or very narrow size distribution. However, narrow size distributions can result from constantly forming nuclei if, at any stage of the reaction the forming nuclei, aggregates or crystals are unstable and undergo dissolution or agglomeration. In this case they then act only as nutrients for the growth of the more stable larger species. With fractal aggregation constantly forming nuclei can also result

in similar sized crystals as each forming particle undergoes a series of densification and aggregation steps to form the final crystal structure.

5.2.2 : Aim of this work

A large amount of data that has been collected on the nucleation and growth of a number of zeolitic systems synthesised from clear solutions. However, work has yet to focus on the effect of metal substitution of these systems.

Considering that substituted metal frameworks play such a significant role in the development of porous materials for chemical and catalytic applications, it was decided to attempt to substitute metals into zeolite-A and then investigate how this effects nucleation and growth.

In particular, the aim of this work was initially to measure an un-substituted zeolite-A system, devise a probable mechanism and then observe how this is affected or modified by metal substituted systems. *In situ* SAXS/WAXS techniques have been utilised as this allowed us to monitor the formation processes from beginning to end, with the SAXS measurements probing the development of pre-crystalline amorphous entities while the WAXS probes the growth of crystalline regions.

5.3 : Experimental

5.3.1 : Hydrothermal preparation of germanium substituted zeolite-A

Pure and substituted germanium zeolite-A phases were prepared in the laboratory by hydrothermal treatment using a method similar to Mintova *et al*[39] but using tetramethylammonium silicate solution, to allow clear solutions to be easily achieved. The overall ratio of components for a pure gel is given as:

$$11.25SiO_2 : 1.95Al_2O_3 : 14.5(TMA)_2O : 0.75Na_2O : 770H_2O$$

As germanium is substituted for silicon in to the zeolite-A framework, its addition to the solution results in a decrease in the molar ratio of silicon added, the ratio of the system components then becomes:

$$(11.25\text{-}y)\ SiO_2 : y\ GeO_2 : 1.95Al_2O_3 : 14.5(TMA)_2O : 0.75Na_2O : 770H_2O$$

where y is the ratio of germanium substitution

In a typical synthesis, to the required quantity of 16.9 % tetramethylsilicate solution (Aldrich), the corresponding molar equivalent of germanium oxide powder was slowly added whilst agitating the mixing vessel and the mixture was stirred (*c.a.* 10 -15 mins). Upon dissolution of the powder, 25 % tetramethylammonium hydroxide (TMAOH), water and 10M sodium hydroxide solution was added to the mixture. The solution was then aged (*c.a.* 15 mins) and then finally aluminium isoperoxide was added to the solution with stirring. The opaque solution was left to stand with occasional agitation for 2 hours during which time a clear solution was achieved. The solution was then filtered through 2 μm Whattman syringe filters prior to treatment by hydrothermal methods.

Note, that exact molar quantities for each synthesis reagent are not quoted as these all vary depending on the substitution of germanium. For example, increased germanium oxide requires less TMA-Si solution to be used, resulting in less water and TMA in the system, which must be accounted for by increased addition of other reagents. Other substitution experiments were attempted based on this system, using a variety of other

metal oxides and acetates, details of which are given in the Results and Discussion section.

5.3.2 : Characterisation techniques

5.3.2.1 : X-ray diffraction

XRD patterns were recorded using a Bruker D4 diffractometer in the Bragg-Brentano orientation as described in chapter 3. High quality diffraction patterns were also recorded using a Bruker D8 diffractometer in the Debye-Sherer orientation using a copper source identical to the D4, with samples loaded into 5 mm quartz capillaries.

The Fullproff suite of programs[40] was used to perform LeBail fits on the XRD patterns and initial fitting parameters were based on data obtained from the Checkcell unit cell estimation software and previously derived parameters given by Gramlich *et al*[41] and Pluth *et al*[42]

5.3.2.2 : Scanning electron microscopy

Scanning electron microscopy (SEM) images and energy dispersive X-ray analysis (EDX) were performed as described in chapter 3.

5.3.2.3 : Extended X-ray absorption fine structure

As in chapter 3, EXAFS measurements were carried out at station 9.3 of the SRS and used a Si(220) double crystal monochromator in transmission mode only and data was then analysed using the analysis suite available from Daresbury laboratories.

5.3.2.4 : *in situ* small angle / wide angle X-ray scattering

The nucleation and growth of these materials was monitored *in situ* using combined SAXS/WAXS techniques. As discussed in chapter 2, SAXS/WAXS is particularly good at probing the size evolution of amorphous particulates prior to crystallisation. Measurements were carried out at station 6.2 of the SRS. The station was set-up as described in chapter 2 using a 3 metre camera. The wavelength of the X-rays was tuned

to 1.400 Å (8.856 KeV) for the germanium substituted materials and 1.127 Å (11.000 Kev) for the un-substituted zeolite-A.

Samples were inserted into a specially designed hydrothermal cell (detailed below) and place into a heating block mounted to the SAXS/WAXS sample stage and pre-set at the desired temperature. All measurements were started 2 minutes after the insertion of the sample. The resulting SAXS data was calibrated for beam decay, normalised, background subtracted and converted to ASCII format using the OTOKO[43] software suite. Subsequent channel calibration and area fits were performed using Origin Pro 7. The WAXS data was converted to ASCII format using the OTOKO program and subsequent peak area analysis was performed using XFIT[44].

Calibration of the small angle detector was performed using the periodic standard wet rat tail collagen (d = 670 Å). The calibration procedure requires the measurement of the collagen sample at the set camera length, resulting in a plot of the pattern vs. channel number (figure 5.8). From the plot the peaks for each reflection are clearly visible and the strongest useful signals corresponding to the 3rd (d = 223.33 Å), 5th (d = 134 Å) and 9th (d = 74.44 Å) reflections are used. Note that the 1st reflection is not used because it is very close to the edge of the observable range and therefore its centre can not be measured accurately.

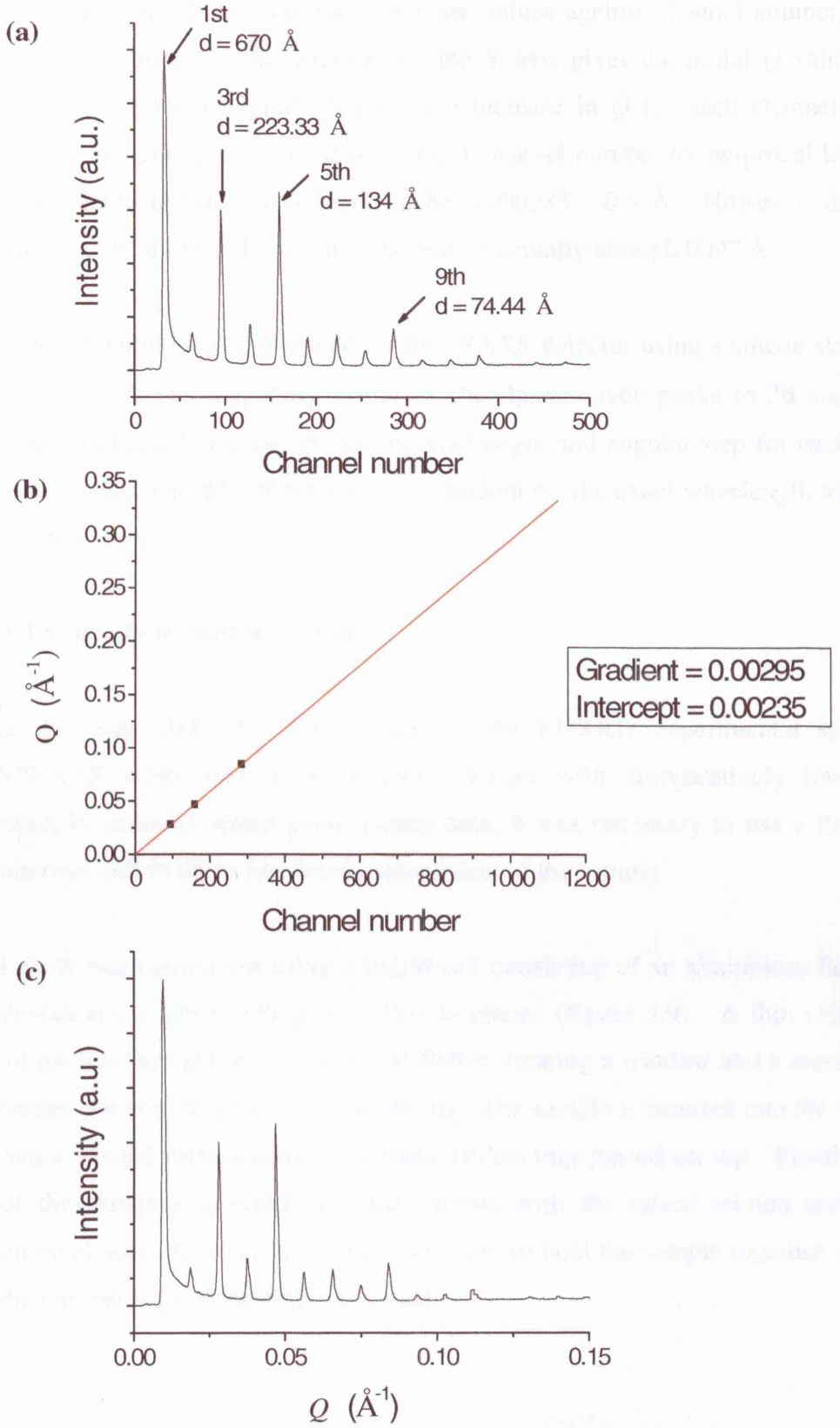

Figure 5.8: Calibration of the SAXS detector using wet rat tail collagen. The 3rd, 5th and 9th peaks in the pattern are picked (a) and their calculated Q values are plotted against channel number (b). From the gradient and intercept of a linear fit the scale for the whole scanned range can be determined(c)

By now converting the known *d*-spacings to the reciprocal space unit $Q = 2\pi/d$ (see chapter 2 for more details) and plotting these values against channel number, a linear correlation is achieved. The intercept on the Y axis gives the initial Q value for the detector range, while the gradient gives the increase in Q for each channel number, allowing the full conversion of the scale from channel number to reciprocal length. At 3m the available Q range was found to be 0.000235 - 0.3 Å. However, due to the position of the beam stop the useful minimum is actually about 0.0097 Å.

A similar calibration was performed for the WAXS detector using a silicon standard by converting the known *d*-spacing values of the characteristic peaks to 2θ and plotting these against channel number, giving the start angle and angular step for each channel for this detector. The effective range is dependant on the exact wavelength used in the experiment.

5.3.3 : The *in situ* hydrothermal cell

Unlike the very high flux white beam of the EDXRD experimental setups, the SAXS/WAXS setup uses monochromatic X-rays with comparatively low energy. Therefore, in order to obtain good quality data, it was necessary to use a thin walled hydrothermal cell to allow maximum penetration of the sample.

Initial work was carried out using a liquid cell consisting of an aluminium flange with an indentation on which a ring of Teflon is placed (figure 5.9). A thin (100micron) sheet of mica is then placed on top of the Teflon creating a window and a second spacer then creates the void in which the sample sits. The sample is inserted into the void drop wise and a second mica window and third Teflon ring placed on top. Finally the top half of the flange is pressed onto the sample with the raised section creating the hydrothermal seal. A metal bracket is then used to hold the sample together, clamping onto the tapered edge of the body of the cell.

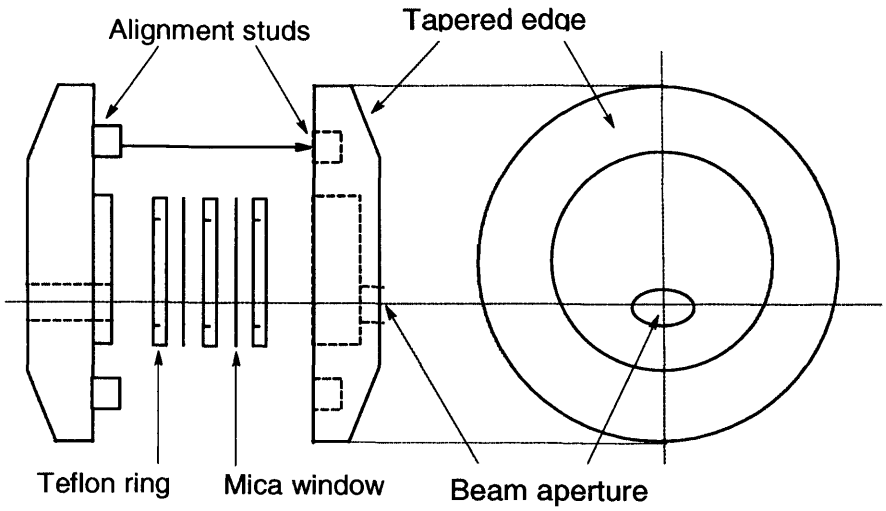

Figure 5.9: A schematic of the original compression hydrothermal cell consisting of a series of mica windows and Teflon rings compressed into an aluminium flange.

This cell has been successfully employed in monitoring the formation of bismuth molybdate by combined EXAFS/XRD.[45] It has also been successfully employed for studying the formation of zeolite-A from clear solutions.[28] However, during these experiments, it proved difficult to load the very fluid clear solution samples with reliability and leakage occurred, particularly at hydrothermal temperatures. Therefore a modified cell was developed for use with more fluid systems.

The modified cell was designed at the Royal Institution[46] after several modifications and utilised a screw thread in the centre of a brass base (figure 5.10). The cell pieces (bottom) are loaded into the base unit (top left) in order from left to right. The bottom Teflon ring and mica window are inserted into a lip on the bottom of the sample holder, which is then screwed into the base unit, creating a sealed bottom part of the cell which can be easily loaded with fluid samples without leakage.

The top mica window and Teflon ring are then placed over the sample, followed by the aluminium retainer, designed to prevent excessive bowing of the mica window during hydrothermal treatment. The top aluminium retainer is then screwed into the base sealing the top half of the cell and creating a complete hydrothermal unit. Small grub screws on the side of the base unit are then tightened stopping the cell pieces coming loose due to expansion and contraction of the cell. The equipment used to tighten the cell (top right) has a window locator bar which is inserted into the beam window of the

retainer during tightening to keep it in the correct position. This cell was found to be easy to load and capable of performing hydrothermal synthesis with fluid samples up to 130°C.

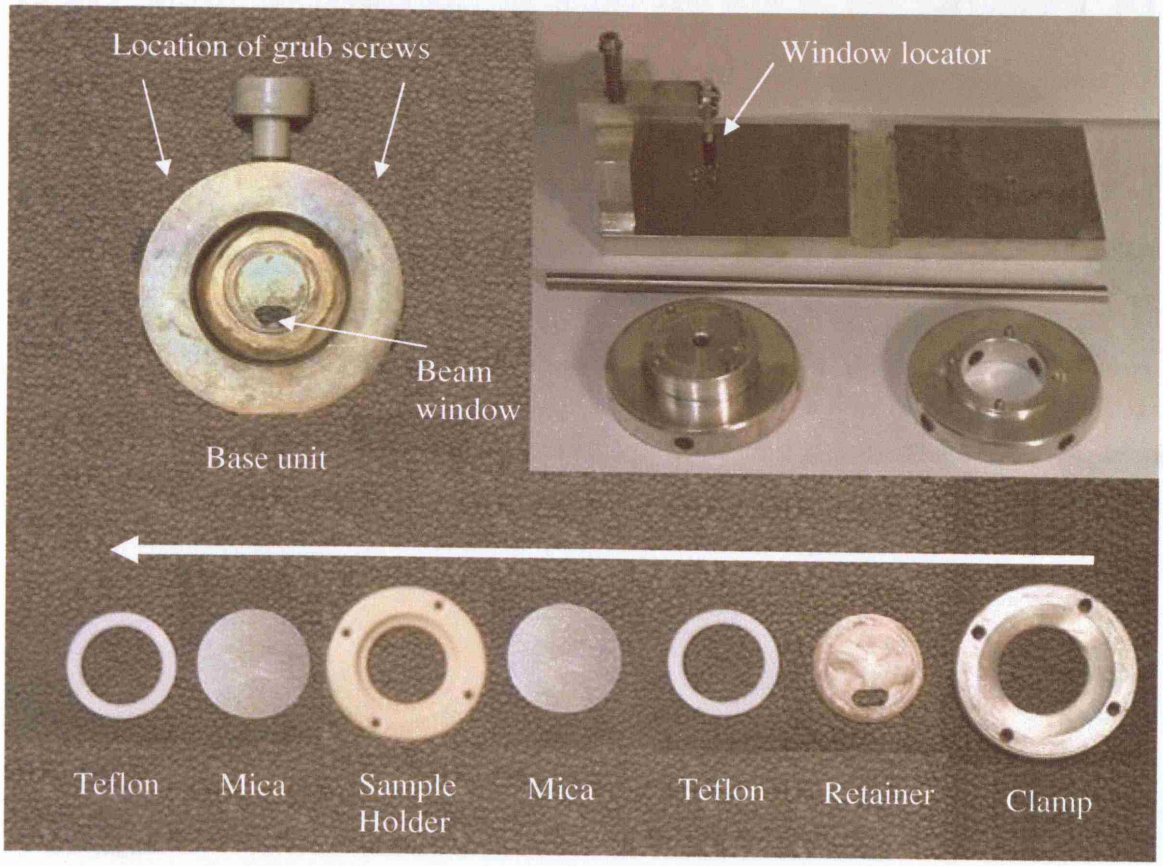

Figure 5.10: The modified hydrothermal cell used for the experiments performed in this chapter. The ability to seal the bottom half of the cell by screwing the sample holder into the base unit made the loading of the cell easy, with leakage occurring only rarely.

The sample cell is then inserted into a spring loaded brass sample heater (figure 5.11), located on the SAXS/WAXS sample stage. Cartridge heaters connected to a Eurotherm control unit and 'K' type thermocouple feed back system are used to heat the unit. Upon completion of the experiment the sample cell can be cooled and the top retainer and clamp removed.

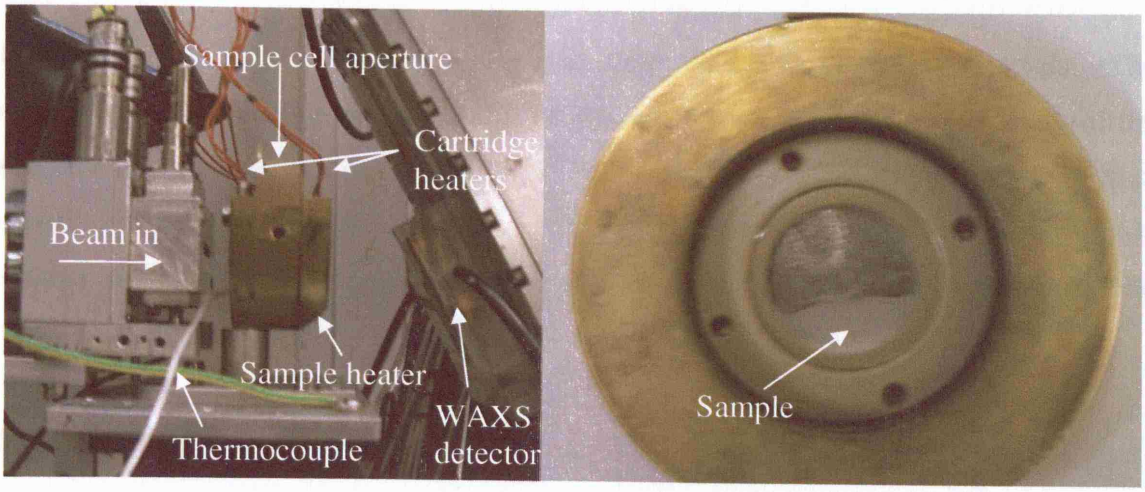

Figure 5.11: The sample heater mounted to the SAXS/WAXS sample stage (left) and the sample in the hydrothermal cell post synthesis, demonstrating the hydrothermal conditions created in the sample holder.

5.4 : Results and Discussion

Initially, syntheses were attempted *ex situ* using a number of different metals. The results of these tests are discussed first, followed by details of the phase purity of the successfully synthesised Ge-zeolite-A. The *in situ* SAXS/WAXS technique is then described and the results from both the SAXS and WAXS detectors for a un-substituted system are described. A scheme is proposed for this system and compared with variations caused by metal substitution.

5.4.1 : Initial synthesis attempts

Whilst only the successful synthesis method for pure and germanium substituted zeolite-A was discussed in the experimental section, a number of other metal substitutions were also attempted (table 5.1).

The synthesis conditions were varied from the exact procedure described for Ge-zeolite-A to try and accommodate insertion of metals for framework aluminium and obtain clear solutions. For example, cobalt acetate was not directly soluble into a solution of tetramethylammomium silicate, therefore it was dissolved in water initially and then mixed with the remaining synthesis components, allowing a clear blue solution to be achieved.

Metal salt/oxide	Note	clear sol?	zeolite ?	metal sub?
Co acetate	Co added to TMA silicate	NO	-	-
Co acetate	Co initially dissolved in water	YES	NO	NO
Fe acetate		YES	NO	NO
Fe nitrate		NO	-	-
Zn acetate		NO	YES	NO
Zn oxide		YES	YES	NO
Ga nitrate		NO	-	-
Ge oxide		YES	YES	YES*

Table 5.1: A list of metal substituted zeolite-A syntheses attempted using a number of metal salts and oxides. Only in the case of germanium oxide was this successfully achieved. *see section 5.4.2.

In a number of cases, no clear solution of the synthesis components could be achieved, which is believed to be due to two factors. First, this clear solution synthesis has relatively high concentrations of silicon, but not as high as in gel systems. Therefore, at the very high initial pH conditions, monomeric species are present, but the addition of the acidic acetates or nitrates decreases the pH towards the instability region, where solids are known to precipitate[4,47]. Second, a number of metal solution species are known complex to form hydroxides that precipitate from solution. For example, iron tends to form the highly insoluble rust-red colloidal ferric hydroxide above pH 4[48].

For cobalt and iron acetate, coloured clear solutions were achieved. However, during synthesis the remaining solutions remained deeply coloured, indicating little or no metal substitution had taken place, and XRD of the final materials revealed only amorphous products. Only in the cases of germanium and zinc was a clear solution achieved and Zeolite-A successfully synthesised. However, in both zinc cases framework substitution of the metal did not occur. For the ZnO synthesis an examination of the XRD pattern revealed (figure 5.12), that although zeolite-A had formed, the zinc was present as the starting material (crystalline ZnO) and had not been incorporated into the framework. Again this is most likely due to the fact that ZnO is known to form under alkaline hydrothermal conditions[49,50], and indeed these conditions are commonly used for zinc oxide production[51,52]. Therefore, incorporation of zinc into the growing zeolite framework is difficult.

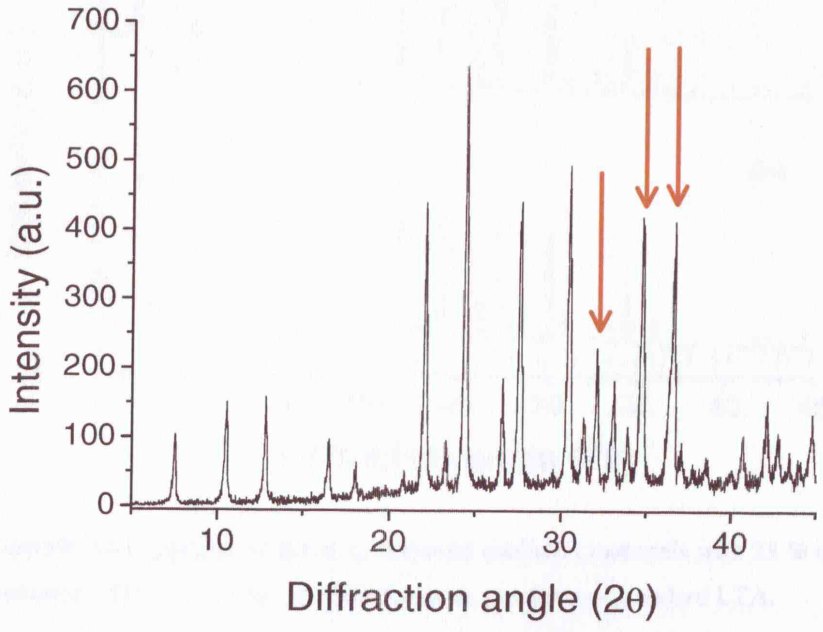

Figure 5.12: The zeolite-A synthesised using zinc oxide, zeolite-A has clearly been formed, however the zinc oxide can be identified clearly in the XRD (arrows), indicating no zinc incorporation has occurred.

For the Zn acetate synthesis XRD of the sample revealed no zinc acetate or oxide species mixed with the zeolite. However, an EDX measurement on the sample revealed no zinc signals in the sample, indicating that, once again, zinc had not been retained in the framework and has been washed out of the final product.

It is clear from these initial experiments why little or no clear solution work has been previously reported on metal substituted systems. Obtaining a clear solution and framework substitution is a difficult task requiring a balance between metals in a form that can yield a clear solution and that can easily substitute into the framework. Perhaps unsurprisingly germanium, which is known to easily substitute for silicon, was the only successful substitution. The details of the characterisation of this system are given below.

5.4.2 : *Ex situ* characterisation of Ge-Zeolite-A

Zeolite-A was successfully synthesised from clear solution containing germanium at a number of substitution levels. The dried filtered laboratory synthesised products were subjected to analysis by XRD (figure 5.13) and were found to be consistent with the LTA structural framework[53].

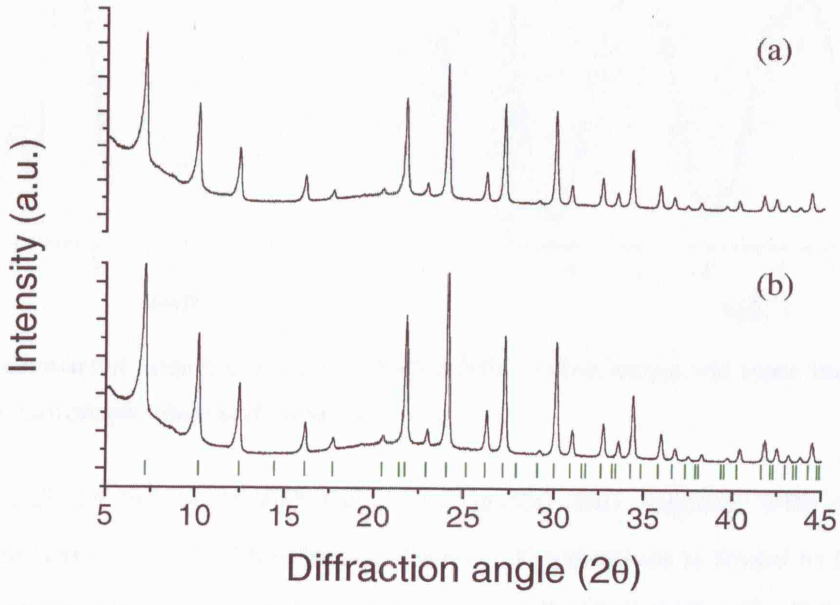

Figure 5.13: Example XRD patterns of the as synthesised zeolite-A materials with 23 % (a), and 0 % (b) germanium substitution. The tick marks represent the peak positions of standard LTA.

Unlike the zinc oxide containing synthesis no germanium oxide peaks are seen in the final XRD, indicating that substitution into the zeolite has probably occurred. Also noted is a slight deviation of the diffraction peaks from the standard LTA framework, particularly at higher substitution levels, indicative of framework substitution, resulting in a small change in the unit cell dimensions and local structure.

The presence of germanium within the sample can be confirmed by both EDX and EXAFS techniques. EDX measurements on the samples give substitutions of 8.0 %, 12.9 % and 25.5 % for the 5 %, 10% and 23% substituted samples respectively, these values are slightly higher than expected from the molar ratios but are within the error for this technique for unpolished samples, and do demonstrate the presence of germanium in the sample with increasing substitution. EXAFS measurements were performed on the final crystalline product and the EXAFS (left) and real space Fourier transform (right) curves for the 10% sample are shown in figure 5.14. The solid line represents the experimental data while the dotted line represents the calculated EXAFS and Fourier transforms for a primary single shell consisting of a germanium atom surround by oxygen atoms in a local average arrangement.

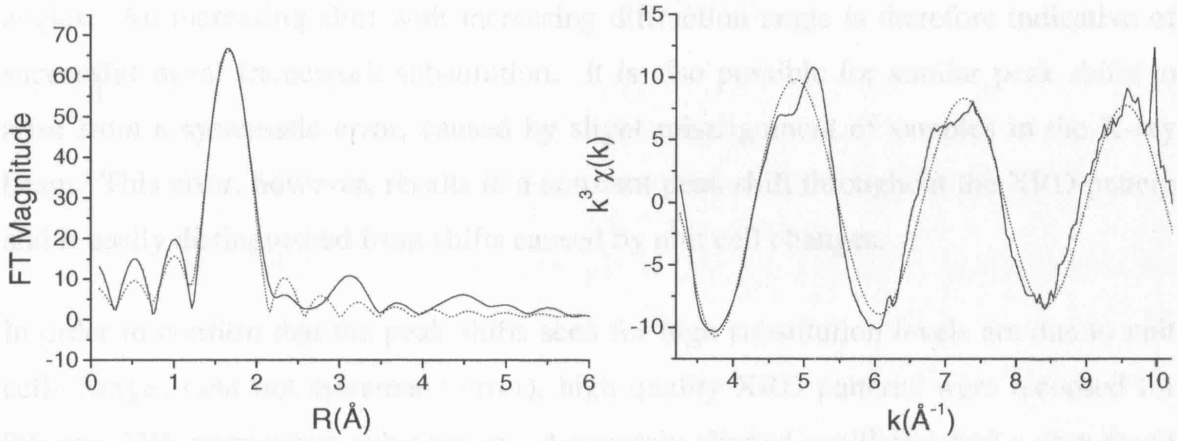

Figure 5.14: Germanium edge EXAFS curve (left) and the corresponding real space Fourier transform (right) for 10% germanium substituted zeolite-A.

The close match of the calculated and experimental data, together with the R factor, (table 5.2) confirms a good fit has been achieved. Germanium is found to be present in the sample, occupying a tetrahedral geometry ($N = 3.7 \pm 0.4$) with a Ge-O bond distance of 1.719 ± 0.02 Å, similar to germanium substitution in other zeolitic systems[54]. This technique demonstrates the presence of germanium in the sample bonded to oxygen as would be expected if present in the framework, however it is still possible that the

germanium may be extra framework, which could result in very similar bonding and coordination.

Sample	*N*	Ge-O distance *R*(Å)	σ^2(Å^2)	R-factor (%)
10% Ge-zeolite-A	3.7	1.719	0.010	22.71

Table 5.2: The resulting coordination number (*N*), germanium-oxygen distances (*R*), Debye-Waller factors (σ^2) and R factors for as prepared 10% substituted germanium zeolite-A.

However, as mentioned above, a slight shift in peak positions was noted for high substitution level samples. It has been previously demonstrated that incorporation of a large hetroatom into the framework of a zeolite[55-57] or other microporous material[58] can cause changes in unit cell parameters, resulting in a peak shift towards lower angles. A close examination of the XRD peak positions should therefore reveal if framework substitution has been successful. As crystal planes at smaller *d*-spacings are closer together, they are more sensitive to changes and any shift is more apparent at higher angles. An increasing shift with increasing diffraction angle is therefore indicative of successful metal framework substitution. It is also possible for similar peak shifts to arise from a systematic error, caused by slight misalignment of samples in the X-ray beam. This error, however, results in a constant peak shift throughout the XRD pattern and is easily distinguished from shifts caused by unit cell changes.

In order to confirm that the peak shifts seen for high substitution levels are due to unit cell changes (and not systematic error), high quality XRD patterns were recorded for 0% and 23% germanium substitution. Accurately aligned capillaries and a very small step size (0.007°) were used, allowing the peak positions to be located with high accuracy. An overlay of the two patterns (figure 5.15) reveals that at low angles the peaks almost coincide (Δ 2θ = 0.022°). However, as the angle increases the difference becomes more substantial, with the germanium substituted system shifting to lower angles. Between 30° and 40° 2θ the difference becomes 0.124° while at 70° 2θ it has increased to 0.277°, confirming that an increase in unit cell parameter and not a systematic error is causing the shift.

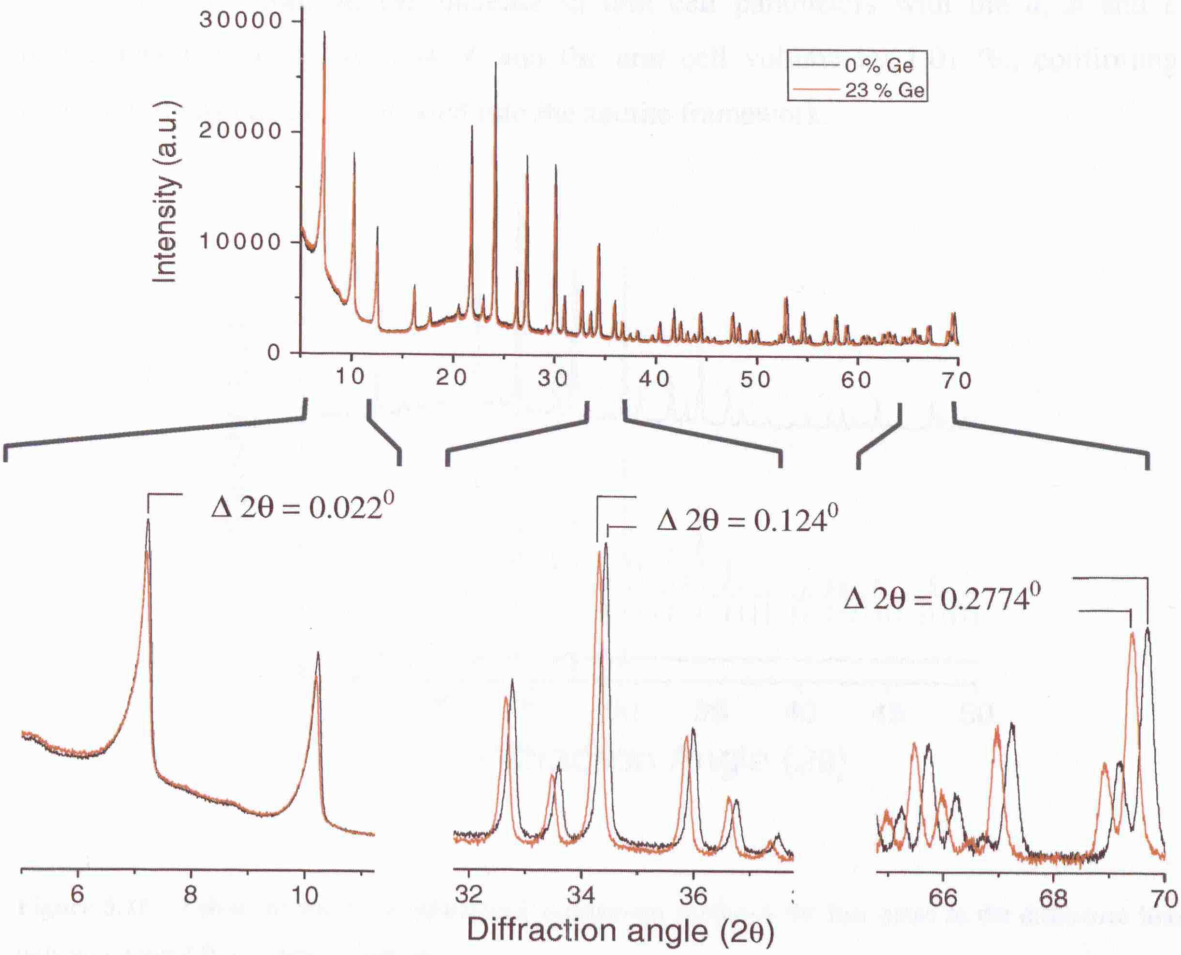

Figure 5.15: Overlay of un-substituted and 23% zeolite-A. The full scan is displayed top, demonstrating both syntheses produced the desired compounds. Expansions of the plot (bottom left to right) demonstrates how the difference in peak positions increases as the diffraction angle increases.

From these high quality scans it was possible to perform LeBail fits and calculate the unit cell parameters for the substituted and non-substituted samples. The fit for 23% substitution is displayed (figure 5.16) and the unit cell parameters and reliability factors for both systems are given in table 5.3. Note that due to the Debye-Sherrer orientation of the XRD setup, excessive Lorentzian components are seen in peaks at low angles. This component is very difficult to model satisfactorily using the LeBail fitting software and therefore peaks below 13° were excluded. This exclusion has very little effect on the overall unit cell parameters because, as mentioned previously, the peaks at higher diffraction angle are far more sensitive to expansion of the unit cell. The initial unit cell parameters were derived from the Checkcell peak positioning software, and symmetry was set as previously reported[41,42]. It can be seen from the difference plot and the reliability parameters given in the table that a good fit was achieved.

The LeBail fits confirm the increase in unit cell parameters with the *a*, *b* and *c* parameters increasing by 0.34 % and the unit cell volume by 1.01 %., confirming germanium has been incorporated into the zeolite framework.

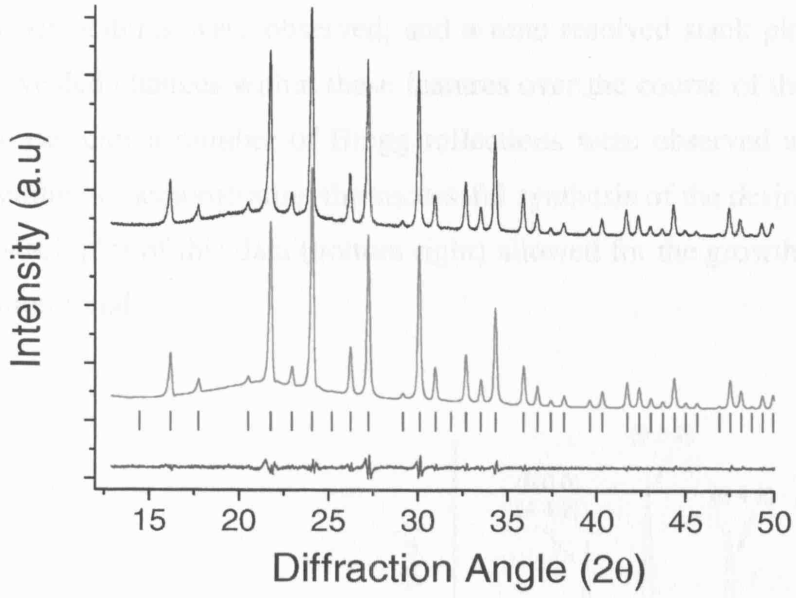

Figure 5.16: LeBail fit for 23 % substituted germanium zeolite-A the low noise in the difference line indicates a good fit has been achieved.

Sample	Space group	$a = b = c$ (Å)	Volume (Å^3)	R_p	R_{wp}	R_{exp}	DW_{exp}
0 % Ge	Fm -3c	12.2005(1)	1816.080(3)	2.75	3.76	2.08	1.9346
23 % Ge	Fm -3c	12.2418(1)	1834.59(3)	2.80	3.73	2.16	1.9420

Table 5.3: Unit cell parameters and reliability factors for the fitting of non-substituted and 23% substituted Ge-zeolite-A.

5.4.3 : *In situ* SAXS/WAXS experiments

The nucleation and growth of pure and substituted zeolite-A was measured using *in situ* combined SAXS/WAXS. To allow identification of the nucleation and crystal growth processes occurring in these zeolite systems, the un-substituted zeolite-A was initially examined. This system was then compared with zeolites substituted with increasing amounts of germanium to examine any effect on the mechanism caused by metal framework substitution.

5.4.3.1 : Analysis of un-substituted zeolite-A formation

A typical data set from the SAXS (top left) and WAXS (top right) detectors used in the experimental set-up can be seen in Figure 5.17. In the small angle camera, a number of broad and sharper features were observed, and a time resolved stack plot of this data (bottom left) revealed changes within these features over the course of the reaction. In the wide angle detector a number of Bragg reflections were observed and have been identified as zeolite-A, demonstrating the successful synthesis of the desired product. A time resolved stack plot of this data (bottom right) allowed for the growth of the zeolite crystals to be monitored.

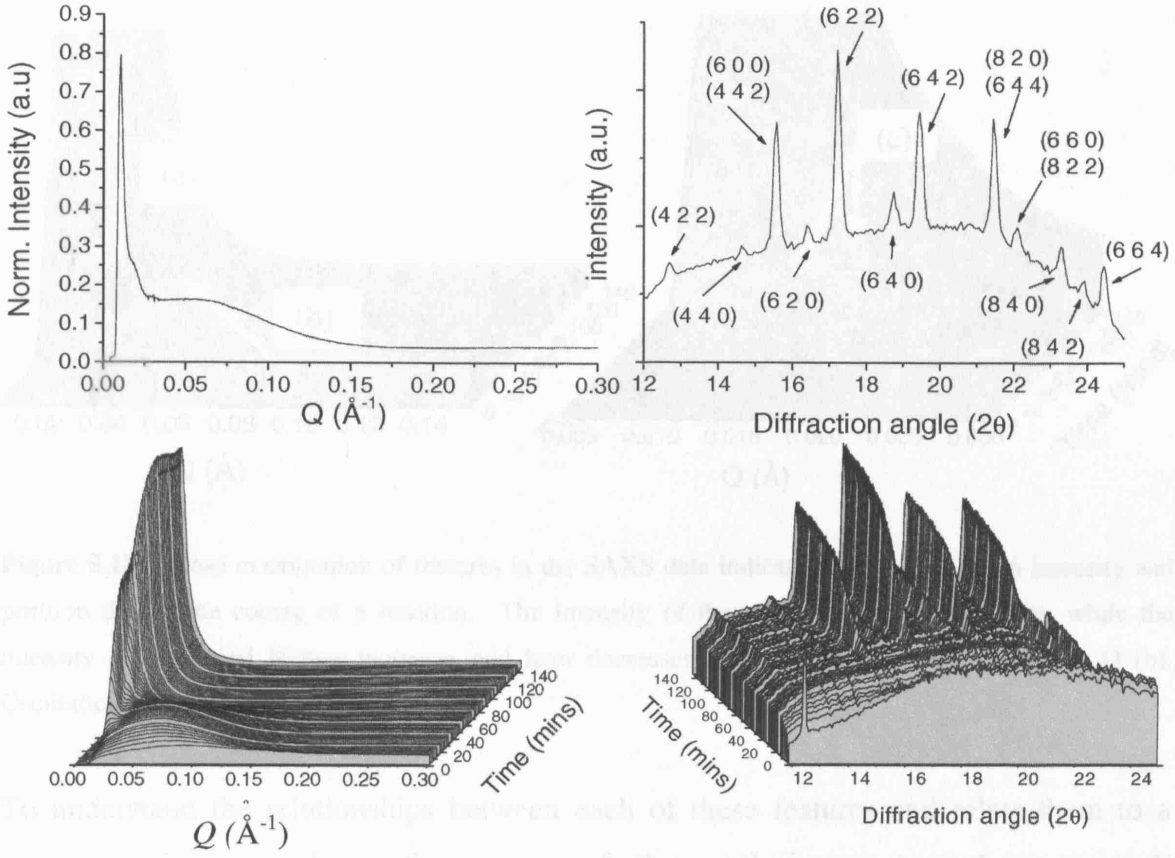

Figure 5.17: Single data sets from the SAXS and WAXS detectors after 50 minutes (top left and right respectively), and full data sets from the experimental run demonstrating the evolution during the growth process (bottom).

A closer examination of the time resolved SAXS data (figure 5.18) identified a broad feature continuing in the Q range from 0 to approximately 0.15 Å^{-1}, as well as a sharp feature at lower Q (0.02 Å^{-1}). These may be similar to the aggregates and crystallites seen in the work by Dokter and de Moor[22-24]. However, it is noted that no 'primary

units' are observed in this system. The broad nature of the aggregate feature would also appear to indicate constant nucleation is occurring in this system[10,11]. During the course of the reaction, the intensity of the broad 'aggregate' feature initially increases in intensity, but, upon the appearance of the 'crystallite' feature, the intensity drops. The maximum intensity of the 'aggregate' feature also appears to shift towards lower Q during the earlier stages of the reaction, indicating an increase in average aggregate size is occurring during the nucleation stage of the reaction. Very close examination of the 'crystallite' feature appearing towards Q = 0 reveals oscillations, suggesting a homogenous nucleation process may be occurring[28]. It is also clear that the oscillations in the feature move towards, and beyond the edge of the detector range, indicating an increase in size during the course of the reaction.

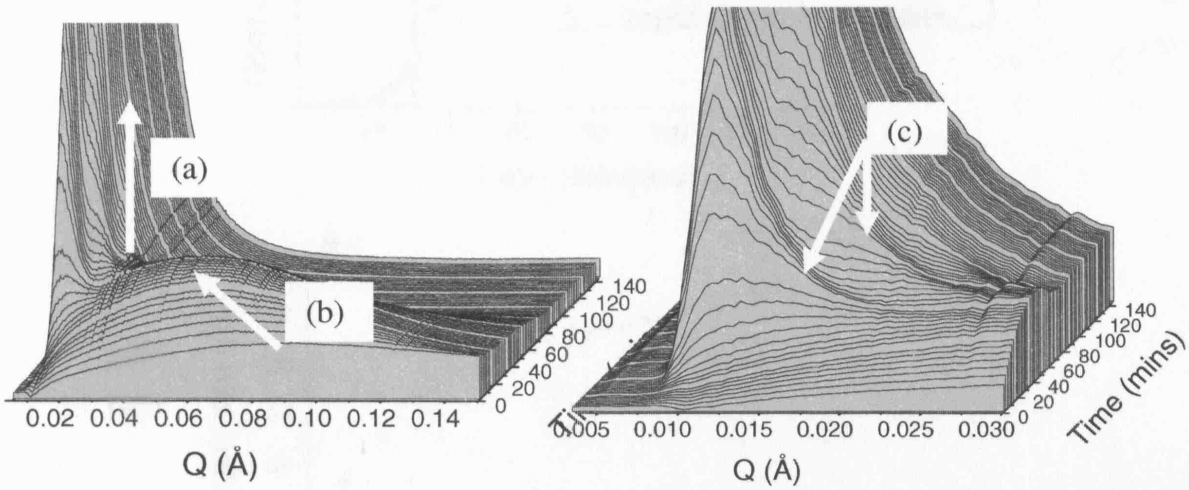

Figure 5.18: Close examination of features in the SAXS data indicate distinct changes in intensity and position during the course of a reaction. The intensity of the sharp feature (a) increases, while the intensity of the broad feature increases and later decreases while its position shifts to lower Q (b). Oscillations are also noted at low Q (c).

To understand the relationships between each of these features and relate them to a general nucleation and growth processes, further analysis was carried out on each feature at each time frame.

Initially, measurement of the intensity of both features was performed throughout the course of the reaction. The intensity at the maximum point of the broad feature (at 0 – 0.15 $Å^{-1}$) was measured. However, due to the oscillations in the sharp ('crystallite') feature and its relatively close proximity to the beam stop, the intensity of this feature was measured using only a single point analysis as close to Q = 0 as possible. From

these measurements (figure 5.19), the initial observations are confirmed, the intensity of the aggregate peak initially increases very rapidly, and then as the crystallite peak begins to appear its growth first slows and then decreases. This characteristic would appear to indicate the rapid formation of WAXS amorphous aggregate entities, which are then consumed into growing crystallites.

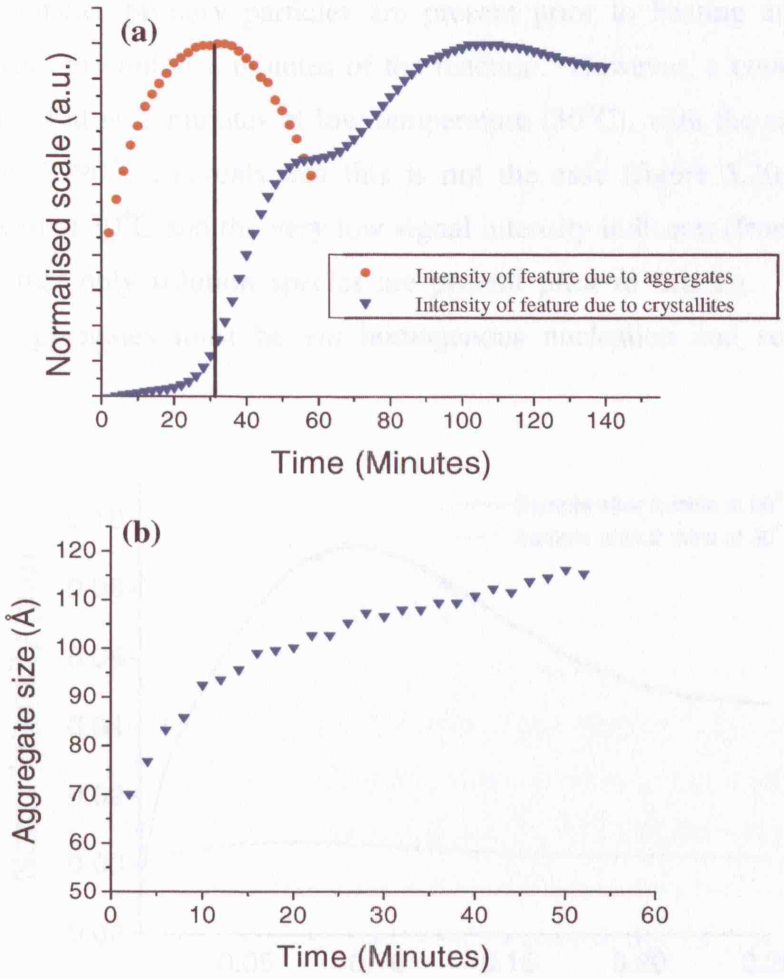

Figure 5.19: A comparison of the intensities of the aggregate band and SAXS crystallite peak (a) shows that the maximum aggregate intensity occurs as the formation of crystallites begins (black line). From the maximum aggregate intensities position on the q axis it was also possible to calculate the average aggregate size (b).

By measuring the position of the broad aggregates maximum intensity the average aggregate size was calculated. The aggregates already measured 70 Å after 2 minutes of heating and the size increases rapidly during the early stages of the experiment. As crystallite peaks began to appear, the growth slows, with a maximum size of about 116

Å reached at the point where it becomes impossible to distinguish the aggregate feature from the crystallite signals. As no smaller particles are noted during the reaction it would appear that either agglomeration and / or direct transport of solution species to the growing aggregates are now occurring.

As the aggregates already measure 70 Å after the first 2 minutes of the reaction, it is possible that smaller primary particles are present prior to heating and are rapidly consumed during the initial 2 minutes of the reaction. However, a comparison of the sample measured after 2 minutes at low temperature (30°C), with the sample inserted into the hot cell (90°C), reveals that this is not the case (figure 5.20). Almost no features are seen at 30°C and the very low signal intensity indicates (from the invariant – see below) that only solution species are present prior to heating. Therefore, the formation of aggregates must be *via* homogenous nucleation and solution species growth.

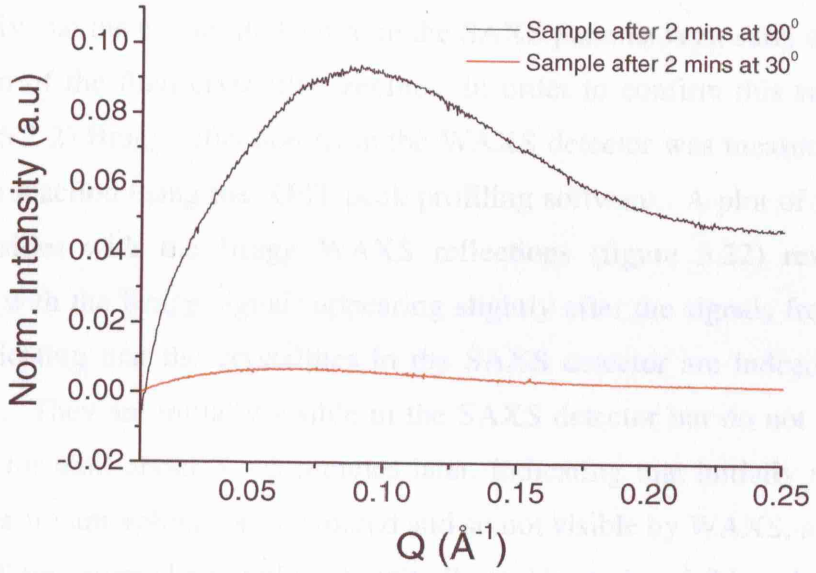

Figure 5.20: Comparison of a sample after 2 minutes heating at 30°c and at 90°c, the lack of features and signal intensity at the lower temperature indicates only solution species are present at prior to heating.

The crystallite growth occurs very close to the beam stop (i.e. Q approaches 0 Å), with the position of the initial oscillation indicating a size of about 400 Å, increasing towards the beam stop where the maximum measurable size of 600 Å is reached. It is noted that growth is likely to continue as the signal moves beyond the limit of the detector, and this is confirmed by SEM imaging. Images recorded on samples synthesised using identical synthesis procedures[28] give crystallite sizes between 500 and 1000 Å after 2

hours, while images of these samples taken after 4 hours show an increase to between 1000 and 5000 Å in size (figure 5.21).

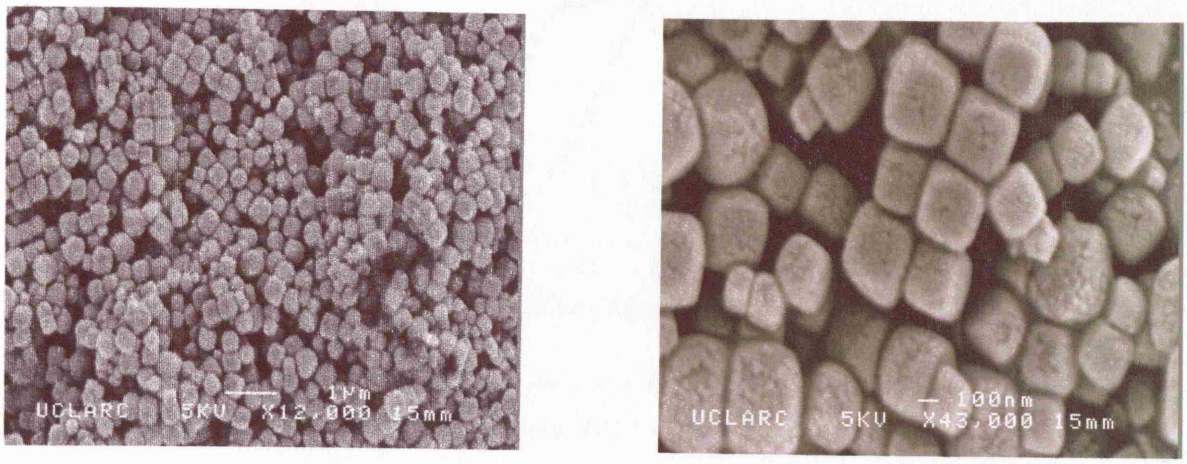

Figure 5.21: SEM images of un-substituted zeolite-A after 4 hours synthesis at 90°C. Sizes range from approximately 1000 – 5000 Å.

It seems likely that the crystallite feature in the SAXS patterns is an early observation of the formation of the final crystalline zeolite. In order to confirm this suggestion, the area of the (6 2 2) Bragg reflection from the WAXS detector was measured during the course of the reaction using the XFIT peak profiling software. A plot of the crystallite SAXS intensities with the Bragg WAXS reflections (figure 5.22) reveals a close relationship, with the Bragg signals appearing slightly after the signals from the SAXS detector, indicating that the crystallites in the SAXS detector are indeed the forming final product. They are initially visible in the SAXS detector but do not appear in the WAXS detector until about 3 – 5 minutes later, indicating that initially most of these large particles are amorphous or disordered and so not visible by WAXS, and/or that the population of any ordered crystallites is initially to low to be visible. As the reaction proceeds, more ordered crystalline material becomes visible. Therefore, the amorphous/disordered particles are being converted by some mechanism to crystalline material, with well defined Bragg planes observable by WAXS.

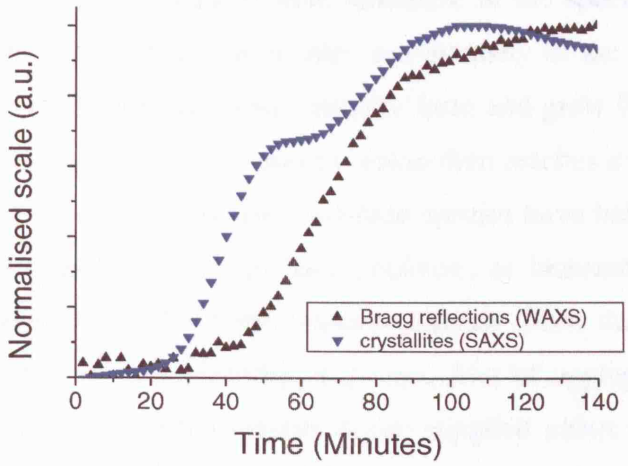

Figure 5.22: Comparison of the 'crystallite' peak area in the SAXS detector and appearance of Bragg reflections (intensity) in the WAXS detector, indicating a close relationship.

As noted above, the appearance of aggregates in the system is a very rapid process, apparently occurring *via* a homogenous nucleation and a solution species transport growth mechanism. Using the invariant equation described in chapter 2[59] it is possible to estimate the total volume of scattering material (i.e. species large enough to be within the limits of SAXS detector range) throughout the synthesis process. A comparison of this invariant volume with the aggregate intensity, aggregate size and Bragg peak area (all normalised to the same scale) shows that the volume increases rapidly during the initial few minutes of the experiment, reaching a maximum just prior to the aggregate intensity. No further increase then occurs, but the volume begins to decrease as crystallisation (appearance of Bragg peaks) occurs (figure 5.23).

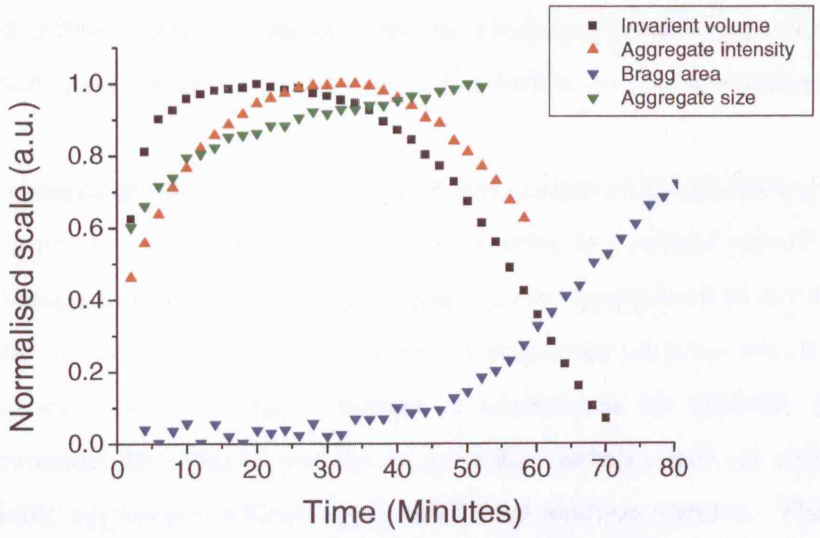

Figure 5.23: Comparison of the normalised invariant, aggregate intensity, aggregate size and Bragg area. Note that only the initial part of the Bragg growth is shown for clarity.

The sudden increase in the invariant volume (increase in the species being measured) coincides with the most rapid increase in size and intensity of the aggregate particles, supporting the observation that aggregates initially form and grow from the transport of homogenous solution species. The invariant volume then reaches a maximum just prior to the aggregate intensity, indicating most solution species have been consumed by the aggregates. However, as the aggregate size continues to increase (at a slower rate), continued growth must occur by some process directly from the aggregates. It is possible that this growth occurs by either agglomeration of aggregates or by solution species transport, with the solution species being supplied either directly from those remaining in solution, or *via* the dissolution of small less viable aggregates. Additionally, as no further increase in invariant volume occurs, crystallite growth must also occur by one or both of these processes. These growing crystals then eventually reach sizes larger than the detector range, resulting in the final decrease in invariant volume.

For formation of amorphous aggregates, growth *via* both agglomeration and dissolution and solution species transport appears to be viable. However, as SEM imaging (figure 5.21) shows little evidence of crystal intergrowth and irregularities, it appears that crystal growth must be occurring primarily by dissolution and solution species transport and not agglomeration. This is because any agglomeration of amorphous particles onto a crystalline surface or the agglomeration of two crystalline particles would be expected to result in substantial amounts of crystal intergrowth and irregularities, and this is clearly not the case. This finding therefore suggests that, in the un-substituted system, dissolution and solution species transport are the primary crystallite growth processes, with the transport rapid enough in the liquid clear solutions to lead to regular crystals.

From the experiments discussed and analysis of the combined SAXS/WAXS data, it is now possible to propose a mechanism for the nucleation and crystal growth of zeolite-A, synthesised using this procedure. The mechanism is summarised in figure 5.24 and proceeds *via* the initial homogenous nucleation of aggregate particles which then grow by three processes: (a) The agglomeration of amorphous (or globally disordered) particles (b) transport of solution species to growing surfaces and (c) dissolution of smaller less viable aggregates which supply additional solution species. The relatively broad range of final crystallite sizes suggests that all stages the processes are dynamic,

with the formation of crystallites and growth/dissolution of aggregates constantly occurring.

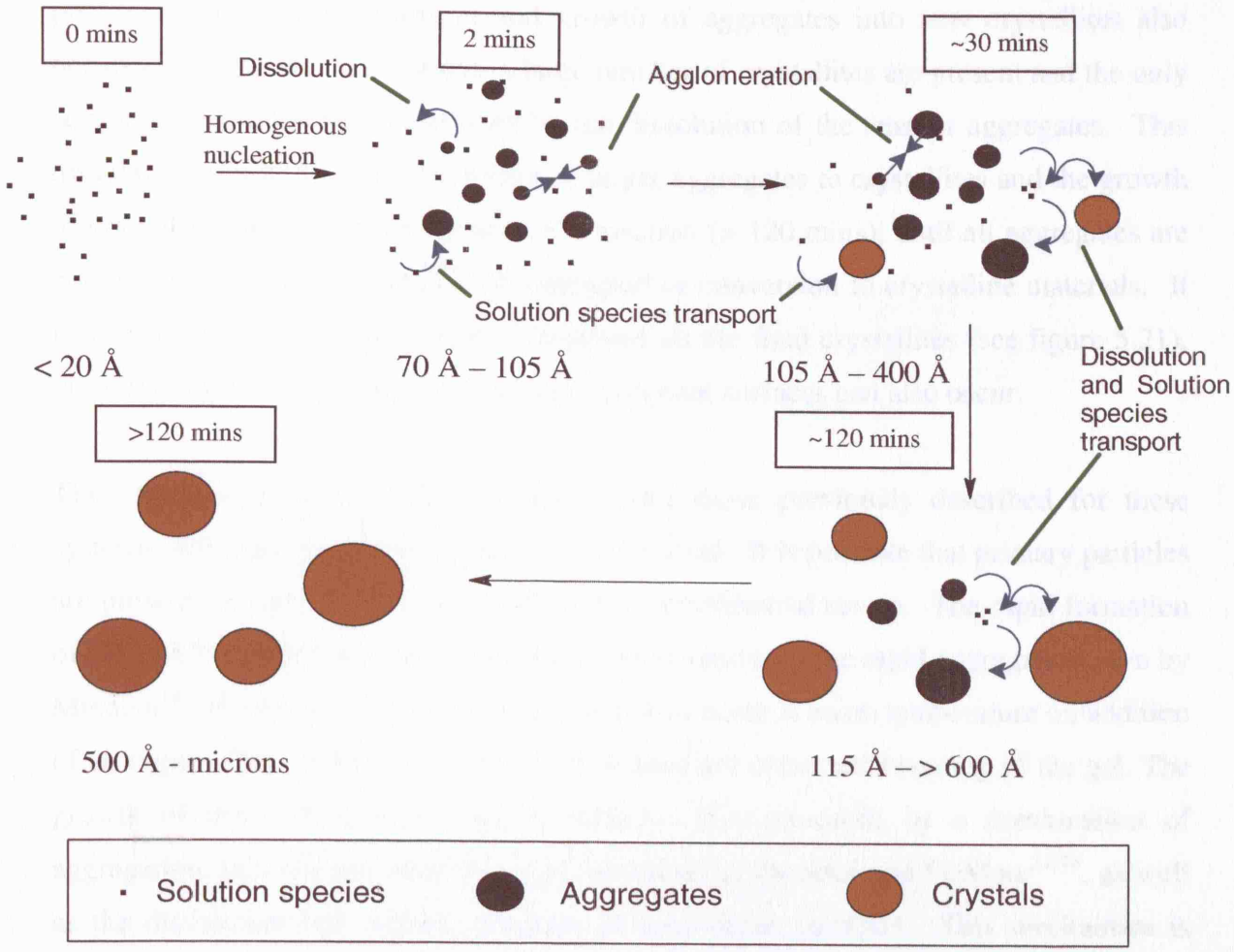

Figure 5.24: The proposed mechanism for the formation of zeolite-A by clear solution synthesis. Formation of crystals occurs by homogenous nucleation and then a process of continued solution species transport, agglomeration and dissolution of aggregates. Crystallites form when aggregates reach a critical size and continue to grow by solution species transport.

Prior to heating, only solution species are present in the sample. Rapid homogenous nucleation and growth by solution species transport then occurs within 2 minutes of introduction of the sample to the heated cell, in a manner similar to previous zeolite synthesis. During the early stages of the reaction (2 - 30 mins) these WAXS amorphous/disordered aggregates then increase in size by both solution species transport and agglomeration, with the dissolution of less viable aggregates also occurring. This process continues until a critical size is achieved by some aggregates (~30 mins) and conversion by an as yet unknown mechanism to crystallites occurs.

Growth of these crystallites then proceeds mainly by solution species transport to the growing crystal surface (resulting in little intergrowth), from either the few remaining solution species or dissolution and solution transport. A stated above, this is a dynamic process with the agglomeration and growth of aggregates into new crystallites also occurring. After 40 -120 minutes a large number of crystallites are present and the only solution species are being provided by the dissolution of the smaller aggregates. This dissolution of smaller and conversion of larger aggregates to crystallites and the growth of crystallites then continues later in the reaction (> 120 mins), until all aggregates are consumed, by either dissolution and transport or conversion to crystalline materials. It is also noted that as some pitting is observed on the final crystallites (see figure 5.21), therefore some dissolution of species on the crystal surfaces can also occur.

This mechanism is generally consistent with those previously described for these systems, although no primary particles are observed. It is possible that primary particles are present, but below 20 Å size limit of the experimental set-up. The rapid formation of the WAXS amorphous particles on heating is similar to the rapid aggregation seen by Mintova[14]. However, in that case it was found to occur at room temperature on addition of an organic base, whilst in this reaction it does not occur until heating of the gel. The growth of these WAXS amorphous particles then proceeds by a combination of aggregation, in a manner similar to that described by Dockter and DeMoor[22-24], as well as the dissolution and surface transport of less viable particles. This mechanism is similar to that described in Twomey *et al*[10], but the broader size distribution of crystals indicates that, as in the work of Schoeman[11], the nuclei are more viable. It was noted above that there is some surface detail on the formed crystals. As this is approximately the same size as the nanoslabs seen by Kirschhock *et al*[31,33] it is possible to interpret these not as pitting, but as evidence of nanoslabs. However, this detail is not present on all the crystals, particularly in the germanium substituted systems (see below), therefore it is unlikely to be due to the presence of nanoslabs.

5.4.3.2 : The effect of germanium substitution on the formation of zeolite-A

By performing identical experiments to those above on germanium substituted systems, it was possibly to assess the effect of metal substitution on the proposed mechanism.
An initial observation of the data from a 23% substituted synthesis (figure 5.25) revealed very similar features to the un-substituted synthesis. In the SAXS detector

both the broad amorphous aggregate feature and the sharper crystallite feature are observed.

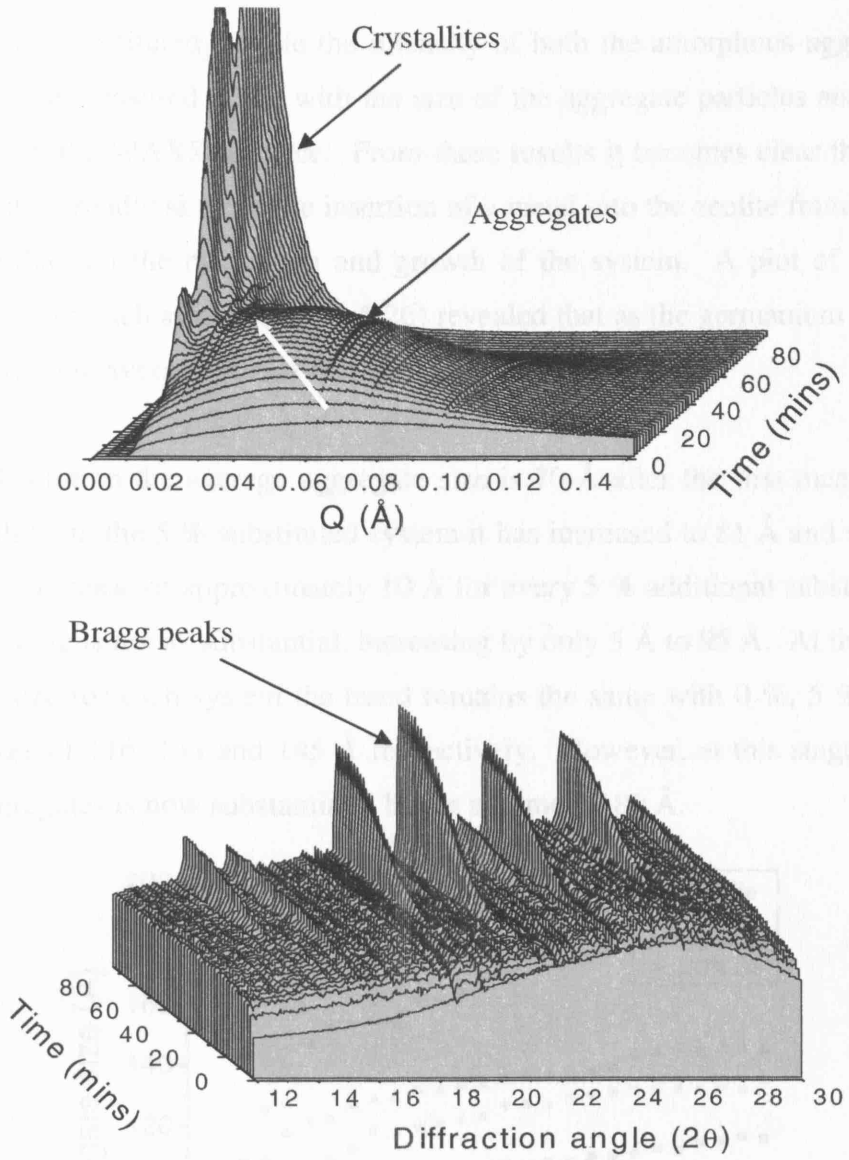

Figure 5.25: Time resolved SAXS (top) and WAXS (bottom) plots of 23% germanium substituted zeolite-A during formation, demonstrating features similar to those observed in the un-substituted systems. Note the Bragg peaks in the WAXS detector differ in position as this sample was recorded at 1.127 Å.

These features also change in a similar manner with the aggregate feature, initially increasing in intensity and then decreasing as the crystallite peak appears. The shift of the aggregate peak towards lower Q as the reaction take place is also observed and the formation of Bragg peaks for zeolite-A are also seen. It would appear therefore, that the

mechanism of formation of the substituted system is broadly similar to the un-substituted system.

As with the un-substituted sample the intensity of both the amorphous aggregates and crystallites were measured along with the size of the aggregate particles and growth of Bragg peaks in the WAXS detector. From these results it becomes clear that although the features are broadly similar, the insertion of a metal into the zeolite framework has a significant effect on the nucleation and growth of the system. A plot of the average aggregate size for each system (figure 5.26) revealed that as the germanium substitution level increases, the average size of the aggregates increases.

With no substitution the average aggregate size is 70 Å after the first measurement (2 minutes), whilst in the 5 % substituted system it has increased to 81 Å and with 10 % it is 89.5 Å, an increase of approximately 10 Å for every 5 % additional substitution. For 23% the increase is not as substantial, increasing by only 5 Å to 95 Å. At the maximum measurable size for each system the trend remains the same with 0 %, 5 %, and 10 % reaching sizes of 116, 135 and 145 Å respectively. However, at this stage the size of the 23% aggregates is now substantially larger at almost 180 Å.

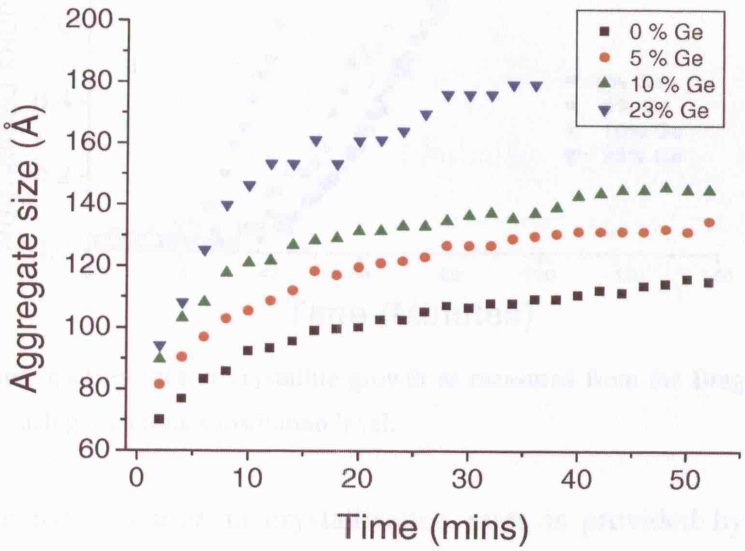

Figure 5.26: The average size of the amorphous aggregates at different substitution levels throughout an experiment.

These results show that addition of germanium to the reaction solution allows the formation and growth of significantly larger aggregates. A feasible explanation for this effect is that the larger germanium atoms contained in the solution species act as

nucleation points and stabilisers, allowing aggregates to form earlier and grow more rapidly, resulting in larger species.

A more rapid growth in aggregate size would be also expected to result in the more rapid onset of crystallisation as the critical size described in the proposed mechanism will be achieved more quickly. Measurement of the Bragg peak growth in the WAXS detector demonstrates that this is indeed the case (figure 5.27).

The 23% substituted system begins to crystallise after just 24 minutes compared to about 38 minutes for the 10% substituted system and about 42 minutes for the 5% and 0% systems. It is noted that it is not possible to differentiate the crystallisation profiles of the 0% substituted and 5 % substituted, possibly due to slight deviations in the synthesis conditions shifting the curve slightly. However, this does not occur with the other systems, and in particular a significant change is seen for the 23% substituted system; the change in the rate of crystallisation therefore appears real.

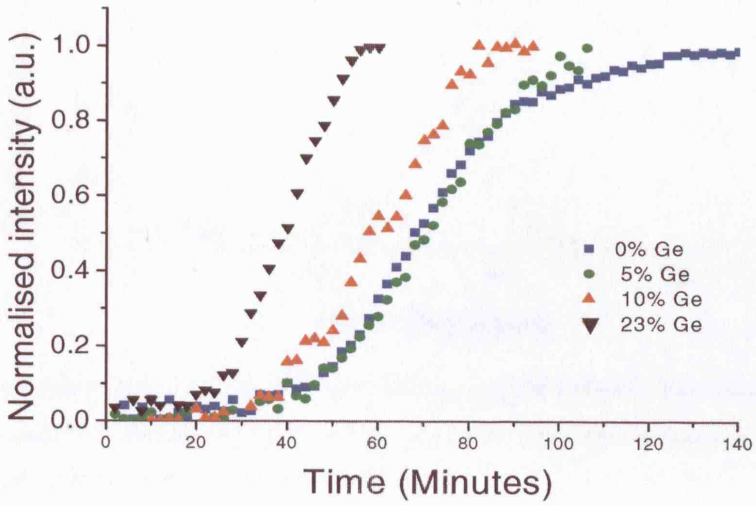

Figure 5.27: A time resolved plot of crystallite growth as measured from the Bragg reflections in the WAXS detector for each germanium substitution level.

Further evidence for a change in crystallisation rates is provided by comparing the invariant, aggregate intensity and Bragg crystallisation of the 23% and un-substituted systems (figure 5.28). The behaviour of each feature is identical, with the invariant rapidly rising and reaching a maximum slightly prior to the maximum aggregate intensity, both the intensity and invariant then drop as crystallites begin to form. The only difference between the systems is the rate at which each of these processes occurs,

demonstrating that the fundamental mechanisms of systems are the same, but the processes occur more rapidly in the substituted systems.

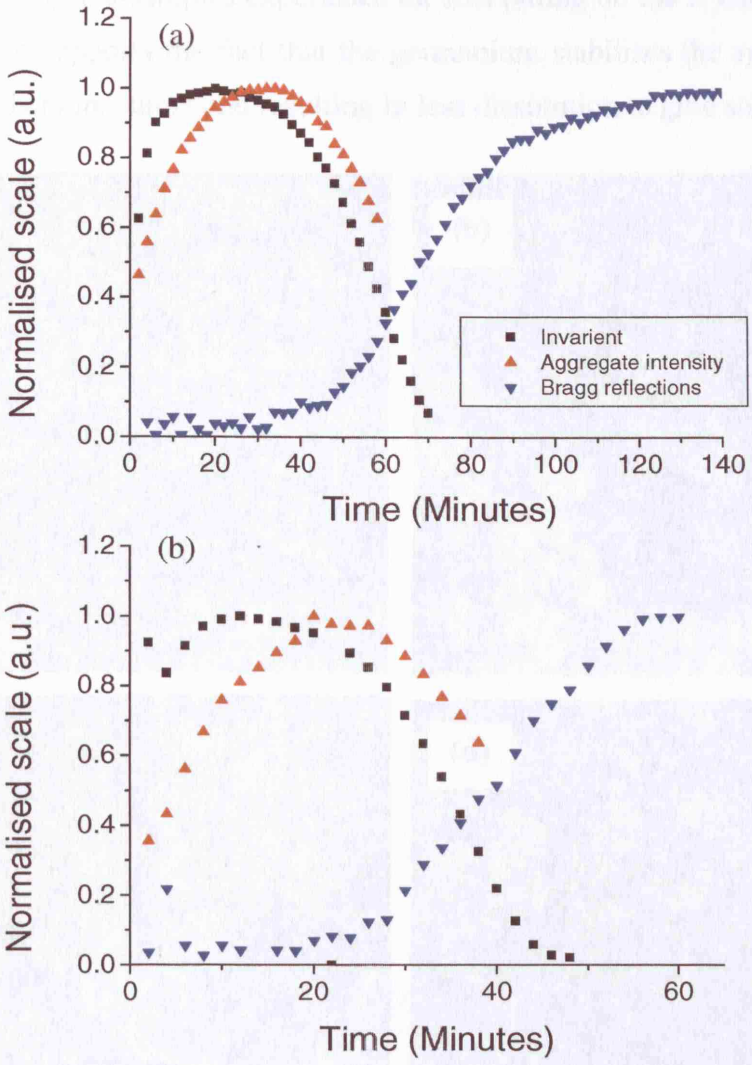

Figure 5.28: Comparison of the normalised invariant, aggregate intensity and Bragg reflections for the un-substituted (a) and 23% substituted systems (b). It can be seen that the evolution of these feature is almost identical and only the rate of change is different.

Considering these results in the context of the mechanism proposed in figure 5.24, we can see that germanium substitution favours larger stable aggregates. Therefore, there are fewer small unviable aggregates in the solution and dissolution of these larger species will be less favourable. This could lead to a shift away from solution species transport towards agglomeration as the main process of aggregate and crystal growth. As mentioned previously, agglomeration on to a growing crystal would be more likely to yield intergrowths of crystals, a shift towards agglomeration would therefore yield more crystal intergrowth in the final product. A comparison of SEM images supports this idea, with the un-substituted system containing mainly single crystals and the

germanium substituted systems having a significant amount of intergrowth (figure 5.29). From a close examination of the SEM images it is also apparent that the germanium substituted samples experience far less pitting on the crystal surface. Again this observation supports the fact that the germanium stabilises the system making the forming crystals more stable and resulting in less dissolution to give solution species.

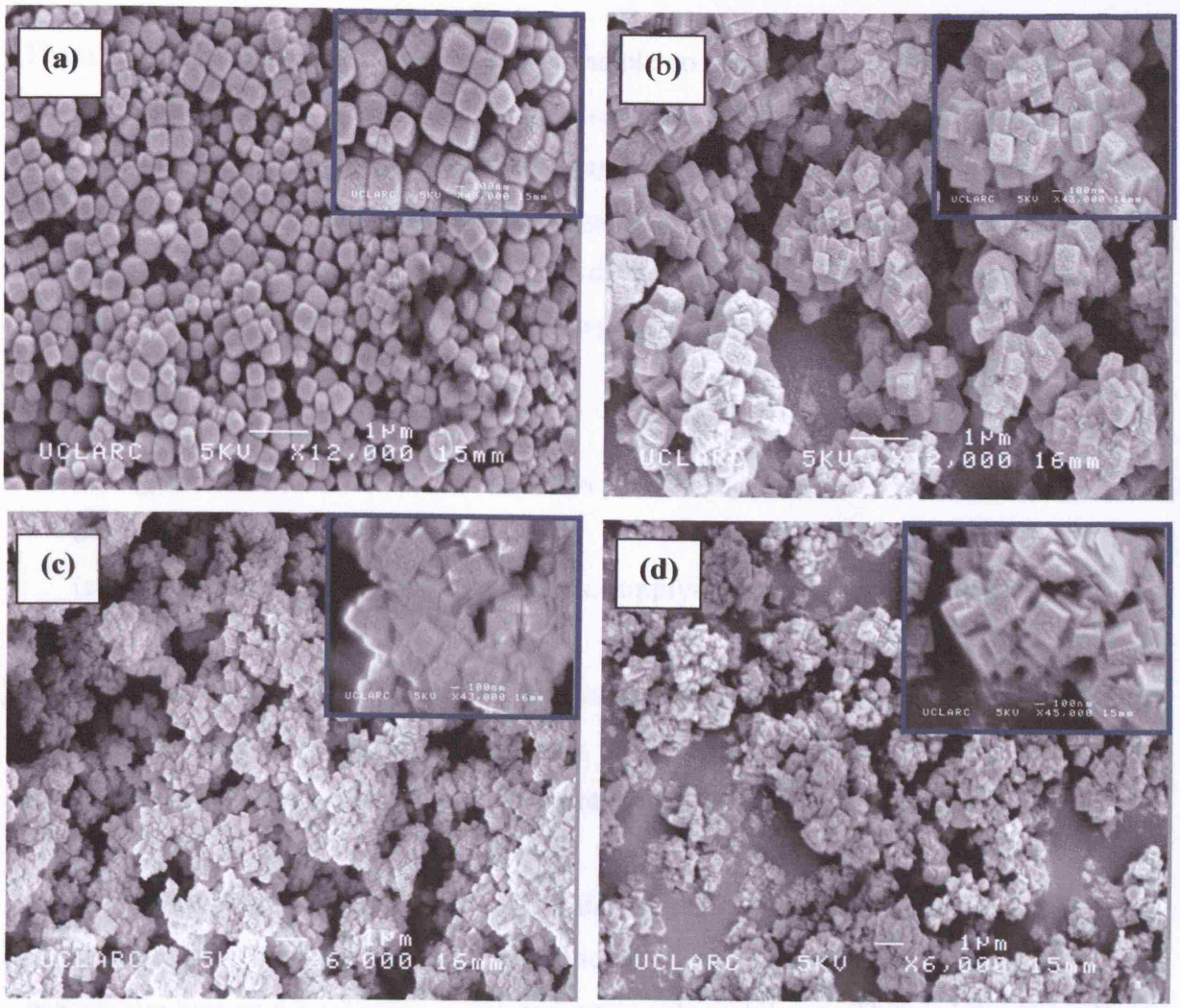

Figure 5.29: SEM images for (a) un-substituted, (b) 5% substituted, (c) 10% substituted and (d) 23% substituted zeolite-A after 4 hours at 90°C. Images were taken at the 1 micron and 100 nm scale (boxed). The increase in intergrowth between the substituted and un-substituted systems can clearly be seen.

It is therefore apparent that, although the general mechanisms for the un-substituted and substituted systems are the same, the addition of germanium does change the balance of processes by which growth occurs. In the un-substitution system solution species transport is dominant, particularly in the crystal growth stage, whilst germanium substitution causes stabilisation of larger aggregates making agglomeration more preferable, resulting in more crystal intergrowth.

5.5 : Summary and conclusions

In this series of experiments, germanium has been successfully incorporated into a clear solution zeolite-A synthesis for the first time, and combined SAXS/WAXS experiments have then been performed on both these and un-substituted systems.

From the un-substituted system it was possible to measure the entire nucleation and growth of the system. Analysis of the data revealed amorphous aggregate particles with a broad size distribution are formed through a homogenous nucleation and solution species transport mechanism. These aggregates then grow until a critical size is reached and crystallisation occurs. Crystal growth then continues until all aggregates are consumed. The formation mechanism was shown to be dynamic and dependant on three processes:

(a) agglomeration of WAXS amorphous particles
(b) Solution species transport
(c) Dissolution of less viable aggregates, supplying more solution species

In the un-substituted system both agglomeration and transport are viable for aggregate formation. However, for crystallite growth, solution species transport is expected to be more favourable as almost no crystallite intergrowth is seen in the final products.

Germanium substitution causes the size of the aggregates and the rate of their formation to significantly increase, along with the rate of crystallisation, indicating that germanium acts as a nucleation point and aggregate stabiliser. This stabilisation effect leads to a decrease in aggregate dissolution and a corresponding decrease in solution species transport. Agglomeration therefore becomes the dominating process in these systems, resulting in more crystal intergrowth in the final product.

It has been demonstrated that zeolite-A formation from this clear solution synthesis proceeds in a similar manner to those described previously. More importantly, insertion of germanium has demonstrated that, whilst the overall mechanism of formation can remain the same, changes in the balance of the components can result in significantly different final products. A greater understanding of how changes in synthesis composition and environmental variables can affect processes occurring within the

synthesis mechanism may lead to greater control of the formation mechanism as a whole, allowing a more rational approach to be used in the synthesis of microporous materials.

5.6 : Future work

Whilst a general mechanism for the formation of zeolite-A has been described, and the effect of metal substitution detailed, the exact process by which the aggregate particles convert into crystalline materials remains unknown. TEM techniques may prove useful in visualising this mechanism in a manner similar to that of Mintova[14], and DLS studies may also prove useful.

Other experiments which may prove useful include the study of temperature variations, allowing the calculation of activation energies at each substitution level and giving a direct comparison of how the changing of the mechanistic processes can effect the growth of the system. Also investigating the effect of concentration of solution species within the mother liquor may be useful, as this could also affect the mechanistic processes and would result in yields more comparable to the full gel counterparts.

5.7 : References

(1) Milton, R. M. US Patent, 1959, p 2882243.

(2) Milton, R. M. US Patent, 1959, p 2882244.

(3) Baerlocher, C.; Meier, W. M.; Olson, D. H. *Atlas of Zeolite Framework Types*; Fifth ed.; Elsevier, 2001.

(4) Szostak, R. *Molecular Sieves*; second ed.; Blackie Academic, 1998.

(5) Fawer, M.; Postlethwait, D.; Klüppel, H. *International Journal of Life Cycle Assessment* **1998**, *3*, 71.

(6) Flanigen, E. M.; Bennett, J. M.; Grose, R. W.; Cohen, J. P.; Patton, R. L.; Kirchner, R. M. *Nature* **1978**, *271*, 512.

(7) Schoeman, B. J.; Sterte, J.; Otterstedt, J. E. *Zeolites* **1994**, *14*, 208.

(8) Schoeman, B. J.; Sterte, J.; Otterstedt, J. E. *Zeolites* **1994**, *14*, 568.

(9) Persson, A. E.; Schoeman, B. J.; Sterte, J.; Ottesstedt, J. E. *Zeolites* **1994**, *14*, 557.

(10) Twomey, T. A. M.; Mackay, M.; Kuipers, H.; Thompson, R. W. *Zeolites* **1994**, *14*, 162.

(11) Schoeman, B. J. *Zeolites* **1997**, *18*, 97.

(12) Gora, L.; Streletzky, K.; Thompson, R. W.; Phillies, G. D. J. *Zeolites* **1997**, *18*, 119.

(13) Gora, L.; Thompson, R. W. *Zeolites* **1995**, *15*, 526.

(14) Mintova, S.; Olson, N. H.; Valtchev, V.; Bein, T. *Science* **1999**, *283*, 958.

(15) Mintova, S.; Olson, N. H.; Bein, T. *Angew. Chem.-Int. Edit.* **1999**, *38*, 3201.

(16) Mintova, S.; Olson, N. H.; Senker, J.; Bein, T. *Angew. Chem.-Int. Edit.* **2002**, *41*, 2558.

(17) Dokter, W. H., TU Eindhoven, 1994.

(18) Dokter, W. H.; Vangarderen, H. F.; Beelen, T. P. M.; Vansanten, R. A.; Bras, W. *Angew. Chem.-Int. Edit. Engl.* **1995**, *34*, 73.

(19) Burkett, S. L.; Davis, M. E. *J. Phys. Chem.* **1994**, *98*, 4647.

(20) de Moor, P.; Beelen, T. P. M.; vanSanten, R. A. *Microporous Mater.* **1997**, *9*, 117.

(21) de Moor, P.; Beelen, T. P. M.; Komanschek, B. U.; van Santen, R. A. *Microporous Mesoporous Mat.* **1998**, *21*, 263.

(22) de Moor, P.; Beelen, T. P. M.; van Santen, R. A. *J. Phys. Chem. B* **1999**, *103*, 1639.

(23) de Moor, P.; Beelen, T. P. M.; van Santen, R. A.; Beck, L. W.; Davis, M. E. *J. Phys. Chem. B* **2000**, *104*, 7600.

(24) de Moor, P.; Beelen, T. P. M.; Komanschek, B. U.; Beck, L. W.; Wagner, P.; Davis, M. E.; van Santen, R. A. *Chem.-Eur. J.* **1999**, *5*, 2083.

(25) Singh, P. S.; Dowling, T. L.; Watson, J. N.; White, J. W. *PCCP Phys. Chem. Chem. Phys.* **1999**, *1*, 4125.

(26) Singh, P. S.; White, J. W. *PCCP Phys. Chem. Chem. Phys.* **1999**, *1*, 4131.

(27) Smaihi, M.; Barida, O.; Valtchev, V. *Eur. J. Inorg. Chem.* **2003**, 4370.

(28) Fan, W.; O'Brien, M.; Ogura, M.; Sanchez-Sanchez, M.; Martin, C.; Meneau, F.; Kurumada, K.; Sankar, G.; Okubo, T. *PCCP Phys. Chem. Chem. Phys.* **2006**, *8*, 1335.

(29) Grizzetti, R.; Artioli, G. *Microporous Mesoporous Mat.* **2002**, *54*, 105.

(30) Grizzetti, R.; Artioli, G.; Gemmi, M.; Carsughi, F.; Riello, P. In *Recent Advances in the Science and Technology of Zeolites and Related Materials, Pts a - c*; Elsevier Science: Amsterdam, 2004; Vol. 154, p 355.

(31) Kirschhock, C. E. A.; Kremer, S. P. B.; Vermant, J.; Van Tendeloo, G.; Jacobs, P. A.; Martens, J. A. *Chem.-Eur. J.* **2005**, *11*, 4306.

(32) Barrer, R. M.; Baynham, F. W.; Meier, W. M. *J. Chem. Soc.* **1959**, 195.

(33) Kirschhock, C. E. A.; Buschmann, V.; Kremer, S.; Ravishankar, R.; Houssin, C. J. Y.; Mojet, B. L.; van Santen, R. A.; Grobet, P. J.; Jacobs, P. A.; Martens, J. A. *Angew. Chem.-Int. Edit.* **2001**, *40*, 2637.

(34) Knight, C. T. G.; Kinrade, S. D. *J. Phys. Chem. B* **2002**, *106*, 3329.

(35) Knight, C. T. G. *Zeolites* **1990**, *10*, 140.

(36) Fedeyko, J. M.; Rimer, J. D.; Lobo, R. F.; Vlachos, D. G. *J. Phys. Chem. B* **2004**, *108*, 12271.

(37) Jorge, M.; Auerbach, S. M.; Monson, P. A. *J. Am. Chem. Soc.* **2005**, *127*, 14388.

(38) Davis, T. M.; Drews, T. O.; Ramanan, H.; He, C.; Dong, J. S.; Schnablegger, H.; Katsoulakis, M. A.; Kokkoli, E.; McCormick, A. V.; Penn, R. L.; Tsapatsis, M. *Nat. Mater.* **2006**, *5*, 400.

(39) Mintova, S.; Fieres, B.; Bein, T. In *Impact of Zeolites and Other Porous Materials on the New Technologies at the Beginning of the New Millennium, Pts a and b*; Elsevier Science: Amsterdam, 2002; Vol. 142, p 223.

(40) Roisnel, T.; Rodriguez-Carvajal, J. In *Epdic 7: European Powder Diffraction, Pts 1 and 2*; Trans Tech publications Ltd: Zurich-Uetikon, 2001; Vol. 378, p 118.

(41) Gramlich, V.; Meier, W. M. *Zeitschrift Fur Kristallographie Kristallgeometrie Kristallphysik Kristallchemie* **1971**, *133*, 134.

(42) Pluth, J. J.; Smith, J. V. *J. Am. Chem. Soc.* **1980**, *102*, 4704.

(43) Koch, M. *OTOKO (modified from XOTOKO).*

(44) Coelho, A. A.; Cheary, R. W. *X-ray Line Profile Fitting Program (XFIT) v0.07.002* **1997**.

(45) Beale, A. M.; Sankar, G. *Proc. Indian Acad. Sci.-Chem. Sci.* **2003**, *115*, 525.

(46) NOTE: Design testing and modification of the hydrothermal cell performed by Sankar, G.; Sheehe, M.; O'Brien M

(47) Swaddle, T. W. *Coord. Chem. Rev.* **2001**, *219*, 665.

(48) Cotton, F. A.; Wilkinson, G. *Advanced Inorganic Chemistry*; Fifth ed.; John Whiley and Sons Inc, 1988.

(49) Huttig, G. F.; Moldner, H. *Zeitschrift Fur Anorganische Chemie* **1933**, *211*, 308.

(50) Laudise, R. A.; Ballman, A. A. *J. Phys. Chem.* **1960**, *64*, 688.

(51) Demianets, L. N.; Kostomarov, D. V.; Kuzmina, I. P.; Pushko, S. V. *Crystallogr. Rep.* **2002**, *47*, S86.

(52) Demianets, L. N.; Kostomarov, D. V. *Ann. Chim.-Sci. Mat.* **2001**, *26*, 193.

(53) Hasegawa, K. N., E.;Takata, M.;Sakata, M.;Togashi, N.;Yu, J.;Terasaki, O. *Japanese Journal of Applied Physics, Part 1* **1999**, *38*, 65.

(54) Tuilier, M. H.; Lopez, A.; Guth, J. L.; Kessler, H. *Zeolites* **1991**, *11*, 662.

(55) Flanigen, E. M.; Grose, R. W. In *Advances in chemistry Series*; Van Bekkum, H., Flanigen, E. M., Jansen, J., C, Eds. Washington DC, 1971; Vol. 101, p 76.

(56) Dwyer, J.; Karim, K. *J. Chem. Soc.-Chem. Commun.* **1991**, 905.

(57) Dwyer, J.; Dewing, J.; Karim, K.; Holmes, A. J.; Ojo, A. F.; Garforth, A. A.; Rawlence, D. J. In *Proceedings of the International Symposium*; Jacobs, P. A., Jaeger, N. I., Kubelkova, L., Wichterlova, B., Eds.; Elsevier Amsterdam: Prague, 1991, p 1.

(58) Hill, S. J.; Williams, C. D.; Duke, C. V. A. *Zeolites* **1996**, *17*, 291.

(59) Glatter, O.; Kratky, O. *Small Angle X-ray Scattering*; Academic Press: London, 1982.

Chapter 6

Synthesis of a microporous aluminophosphate with a hierarchical mesoporous structure

6.1 : Chapter overview

The synthesis of a highly crystalline microporous AlPO-5 with a hierarchical mesoporous structure has been attempted, using a simple single-stage one-pot hydrothermal synthesis method.

The resulting samples have then been subjected to a number of experimental tests to examine both the microporous crystalline and mesoporous structure of the samples. The generality of the procedure was then tested by adaptation to produce mesoporous AlPO-5 using different mesoporous templates and also mesoporous MeAPO-34.

These experiments will demonstrate that microporous AlPO materials can be synthesised with a mesoporous structure, using simple one-pot hydrothermal techniques and cheap 'off the shelf' surfactants for the generation of the mesopores. It is anticipated that this advance will open the door for the synthesis of many catalytically important AlPOs with improved properties such as high chemical throughput. Finally, a basic mechanism for the formation of these materials has been proposed.

6.2 : Introduction

AlPO-5 is a microporous molecular sieve with a topology (AFI) which is unique to the aluminophosphate family of materials. The framework consists of a series of large 1-dimensional 12-membered ring apertures (figure 6.1)[1]. Smaller 6 and 4-membered ring channels are also present and the system can be described in terms of the 12, 6 and 4-ring secondary building units (SBUs).

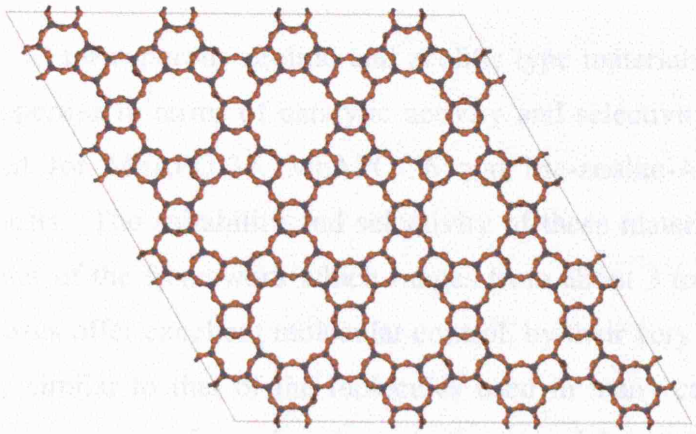

Figure 6.1: The structure of AlPO-5 topology showing the 12 membered ring one dimensional apertures.

The structure was originally solved for a single crystal sample, containing the tetrapropylammounium hydroxide SDA, and was found to be hexagonal and in the P6cc space group[2]. A subsequent analysis of neutron time of flight data then demonstrated that a calcined powder sample exists in the related P6/mcc space group[3]. Qui *et al*[4] have also demonstrated that the use of a fluorinated medium with the tetrapropylammounium hydroxide SDA significantly improves the quality of the AlPO-5 crystals, whilst retaining the P6cc space group.

6.2.1 : Formation of the microporous AlPO-5 phase

Although, as discussed in chapter 3, the synthesis of metal substituted AlPO-5 requires strictly controlled conditions, the synthesis of pure AlPO-5 is comparatively facile and can be achieved over a large range of conditions. Over 23 organic templates are known to facilitate the production of AlPO-5[5] and the resulting materials are generally highly crystalline and have good thermal stability.

A large degree of freedom is particularly desirable when considering a microporous AlPO to use for the novel introduction of hierarchical mesoporous domains, as the

formation of the microporous phase is far less likely to be affected by changes in the gel caused by the introduction of components to induce mesoporosity. AlPO-5 can therefore be considered an excellent 'test bed' for proving the principle of introducing mesoporosity into a microporous AlPO framework.

6.2.2 : The potential of micro and mesoporous materials

6.2.2.1 : The problem with micropores

The current 'crop' of microporous zeolitic and zeolitic type materials (such as AlPOs) exhibit unique properties in terms of catalytic activity and selectivity, some of which have been detailed for MeAPO-34, MeAPO-36 and Me-zeolite-A in the previous chapters of this thesis. The suitability and selectivity of these materials is determined by the pore diameter of the framework which ranges from about 3 to 20 Å. However, whilst these pore sizes offer excellent molecular control, by their very nature they are of a size that is very similar to that of the molecules used in many catalytic processes, reducing the mass transport of species through the material and limiting the rapid turnover desirable for commercial catalytic processes[6].

A number of routes have been adopted in an attempt to increase the catalytic performance of microporous materials. These include the synthesis of very small crystals which minimise the time the synthesis products spend in the micropores (the intra-crystalline diffusion path length)[7-10]. Small crystals also increase the microporous surface area available for reaction and can reduce coking in the reactor. Another method is to produce large pore zeolites such as UTD-1[11] and CIT-5[12], AlPOs such as VPI-5[13] and the gallophosphate ULM materials[14-16] (although the large nature of the pores may result in a reduction in the overall selectivity of the reactions.)

6.2.2.2 : The problem with mesopores

Another way to overcome the mass transport limitations of microporous materials is the introduction of purely mesoporous materials with 'tuneable' openings (20 – 150 Å). These materials were first synthesised by the Mobil petrochemical company in 1992[17] using the cationic long chain hexadecyltrimethylammonium ion. The final product (MCM-41) exhibits very high surface areas (600 – 1300 m^2/g) and it was suggested that the mesopores formed *via* a liquid crystal templating mechanism (see below).

A wide range of silicate structures can now be synthesised using either cationic surfactants similar to above, neutral surfactants, such as block copolymers[18,19] and 'gemini' (bridged diamine compounds)[20] and, more recently, anionic surfactants like aminosilanes[21] (see below for an introduction to surfactants and micelle formation). Post synthesis grafting and hydrothermal treatments have also been used to create new materials[22].

With their very high surface areas, these materials were first thought to offer wide implications for potential applications within the catalyst industry. However, it was found that they tend to exhibit either a very low catalytic activity or low hydrothermal stability, a factor believed to be strongly related to the amorphous nature of the walls of in these materials. For example, Corma *et al*[23] has compared the reactivity of MCM-41[17] with the zeolite USY under a number of different conditions and found MCM-41 to be 139 times less active than USY when cracking small molecules such as *n*-heptene. This low activity has been ascribed to the low number and weak acidity of Brønsted acid sites in MCM-41 compared to USY. With larger molecules (such as those present in gas oil) MCM-41 performed almost as well as USY due to the increased mass transport limitation in the microporous structure. Therefore, despite the low activity for smaller hydrocarbons, MCM-41 could play some part in the long chain stage of the catalytic cracking processes.

Upon further examination however, the hydrothermal stability of this material (and other mesoporous silicates) was found to be poor. The structure tends to collapse upon hydrothermal regeneration and the stability of the material can only be improved by reducing the amount of framework aluminium. This however further reduces the number of acid sites and therefore the materials activity.

From these results it can be seen that although the characteristics of these mesoporous materials indicate good potential for cracking large molecules, the lack of thermal stability makes commercial use difficult. Clearly the need for both a large number of strong acid sites and high thermal stability has to be addressed if these catalysts are to reach commercial potential.

There are a number of ways potentially to solve these issues; for example sulphanated zirconia has been used to increase the acidity of mesoporous materials[24] and zeolite-Y 'seeds' have been mixed with surfactant molecules to produce mesopores with a higher

acidity and hydrothermal stability approaching that of microporous zeolites, although these materials do still contain disordered walls[25,26].

6.2.2.3 : Mesoporous aluminophosphates

A brief overview of the mesoporous materials discussed so far shows that all are silicate based materials. Similar to the development of microporous materials, the synthesis of mesoporous aluminophosphate materials has, until recently, attracted far less attention. One of the reasons for this is that, despite the similarity of AlPO microporous structures to their silicate counterparts, translating the chemistry necessary for mesopores formation has proved far more difficult[27].

Many synthesis attempts have managed to produce AlPO materials with a mesoporous structure, but in most cases the organic could not be removed without collapse[28-30]. One of the earliest syntheses produced a lamellar mesostructured material (SCS-22) which, although thermally unstable, still retained some peaks at low scattering angles, indicating some mesoporosity[30]. An important step forward came in 1995 when Fyfe *et al*[31] synthesised mesostructured materials using the cationic trimethylammonium surfactant (C_nTMA) used in mesoporous silica synthesis. The cationic C_nTMA surfactant route has since been routinely utilised in the synthesis of mesoporous AlPOs systems.

Some of the best characterised materials containing significant long range order have been synthesised using similar techniques by Kimura *et al*[32-36]. The lamellar APW-1 and hexagonal APW-2 structures were synthesised from almost identical gels and it was found that a variation in conditions such as temperature and amount of template control which structure is formed (figure 6.2)[35]. APW-1 was found to contain an ordered crystalline framework, whilst APW-2's framework is amorphous. Upon calcination the APW-2 structure, despite substantial collapse, retains disordered mesopores of 16 – 39 Å[32,35,36]

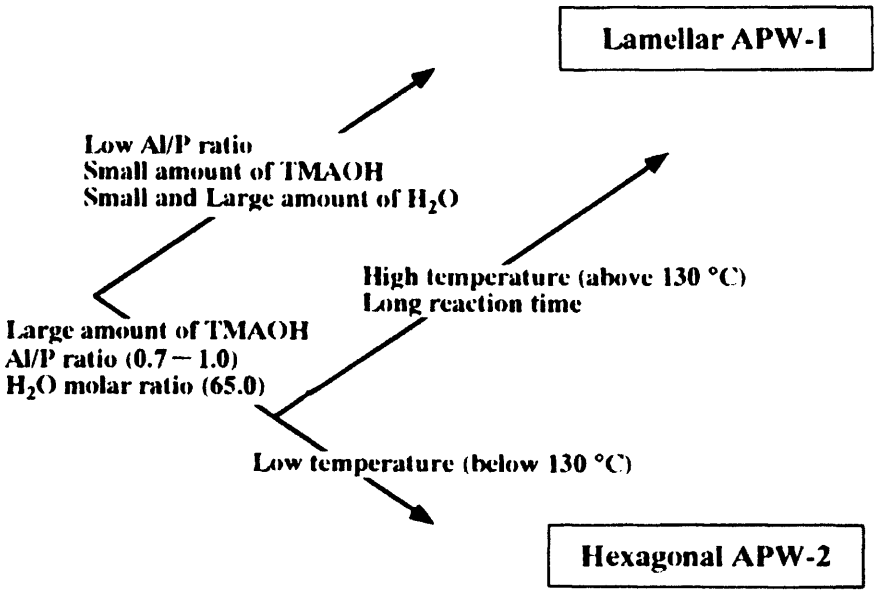

Figure 6.2: The variations in synthesis conditions which allow the formation of lamellar APW-1 and hexagonal APW-2. Reproduced from ref. 35.

Recently, other AlPO systems have been formed[37,38] and work has begun to focus on the insertion metals into the AlPO framework to improve catalytic activity. To date a number of substituted materials have been formed, including silicon (SAPO)[38-41], boron (BAPO)[42], iron (FeAPO)[43], zirconium (ZAPO)[44], chromium (CrAPO) and titanium (TAPO) systems[45].

Unfortunately, whilst the catalytic potential of these materials would appear to be very good, they tend to be even less stable than their silicate based counterparts with some samples even collapsing upon ion exchange[46].

However, despite these problems, some successful testing of catalytic reactivity has been achieved. For example, Kapoor and Raj[45] have shown mesoporous Ti-AlPOs to have high catalytic activity for olefin epoxidation and Fe-AlPO has been found useful the oxidation of cyclohexene and hydrogenation of nitro and carbonyl compounds[43,47]. Additionally, Kimura[48] has recently demonstrated that it is possible to thermally stabilise some of these structures by surface modification with organoalkoxysilanes, modifying the hydroscopic nature of the materials.

At this current stage in the development of mesoporous AlPOs the catalytic potential of the materials is clear. However, the inherent instability of these frameworks (as with silicates such as MCM-41) needs to be thoroughly addressed before any real industrial catalytic use can be realised.

6.2.3 : The generation of mesoporous in microporous materials

So far, the synthesis of microporous materials with properties more like mesoporous materials (i.e. mass transport) and mesoporous materials with properties more like microporous materials (i.e. high acidity/stability) have been examined.

An alternative route to achieving stable, highly active materials with large mass transport capabilities is to combine both mesopores and micorpores in a single material. An idealised structure of such a material was presented by Mann *et al*[49] (figure 6.3) for catalytic cracking reactions. It consists of mesoporous (and in this case macroporous) 1-dimensional channels with micropores emanating from their walls. Whilst idealised structures like this have yet to be achieved, there are currently a number of ways to introduce mesoporosity into microporous systems.

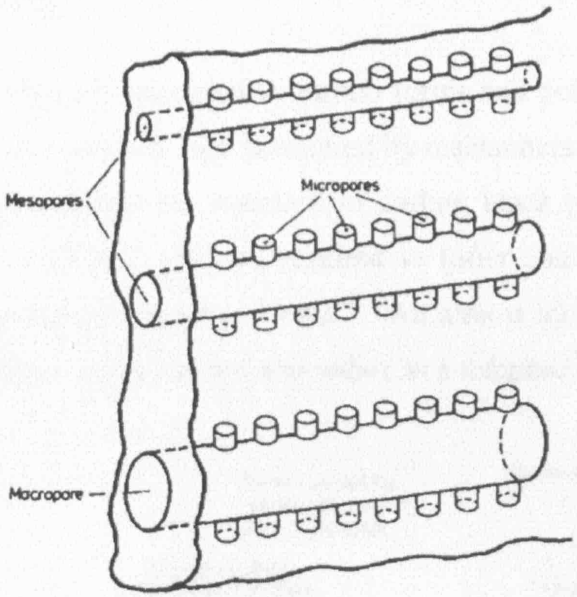

Figure 6.3: An idealised structure for a combined cracking material, containing microporous, mesoporous and macroporous regions. Reproduced from ref. 49.

As with the synthesis and catalytic testing of mesoporous materials, most work to date has focused on the synthesis of microporous zeolites with a hierarchical mesoporous structure rather than AlPO systems. There are two general synthesis routes that can be followed, either the post synthesis introduction of mesoporosity or the creation of mesopores during synthesis. Post synthesis treatments include steaming, acid/base leaching and various chemical treatments. However, these are beyond the scope of this thesis and details of these methods can be found in the review of van Donk *et al*[6].

The generation of a hierarchal microporous/mesoporous structure during synthesis has recently become one of the most popular methods for forming these materials. The technique generally requires the insertion of a 'template' into the microporous zeolite/AlPO gel with the dimensions of the mesopores (or indeed macropores) which are required.

It is useful to divide these inserted materials into those which can be considered to have a predetermined structure prior to synthesis, that cannot be easily altered by the synthesis conditions and those which must interact to form the templating structure (e.g. a micelle) within the gel, which can be affected by internal conditions such as pH, temperature and sheer rate (stirring). These two types of materials can then be referred to as 'hard' and 'soft' respectively.

6.2.3.1 : 'Hard' templating

'Hard' templates include materials such as carbon forms and polystyrene/latex spheres. The use of carbon in various forms was pioneered by researchers from Haldor Topsøe[50], who, for example, showed how the insertion of carbon black pearls (average particle diameter 12 nm) into a ZSM-5 solution resulted in (after calcination) ZSM-5 single crystals containing mesopores from 5 – 50 nm[51]. An almost identical method was also used to produce mesopores using carbon nanotubes as a template[52] (figure 6.4).

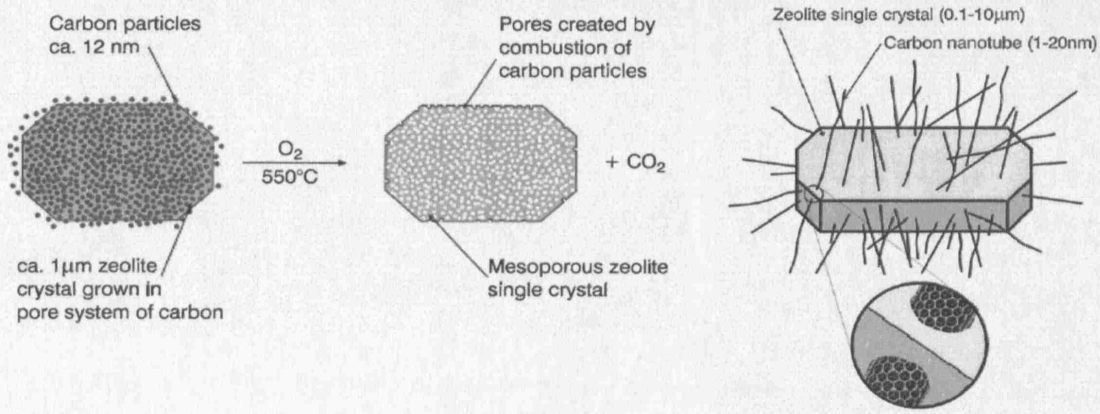

Figure 6.4: Two methods of producing mesopores using carbon black pearls (left) and carbon nanotubes (right). Reproduced from ref. 51 and ref. 52.

It is important to note here that there is a variation in size of the resulting mesopores and that these can be significantly different to the size of the template, demonstrating that

although the actual size of the 'hard' template is fixed (to ~ 12 nm), the interactions between the template and gel can be altered and mesoporous variation can be obtained.

Holland et *al*[53] used polystyrene (latex) spheres to synthesise macroporous spheres with zeolitic (ZSM-5) walls with up to 50 percent crystallinity and macropores averaging 250 nm. Recently Naydenov *et al*[54,55] demonstrated that similar methods can be employed for AlPO materials, synthesising AlPO-5 spheres with voids of macroporous dimensions by using hydrothermal treatment on aluminium impregnated resin beads (figure 6.5).

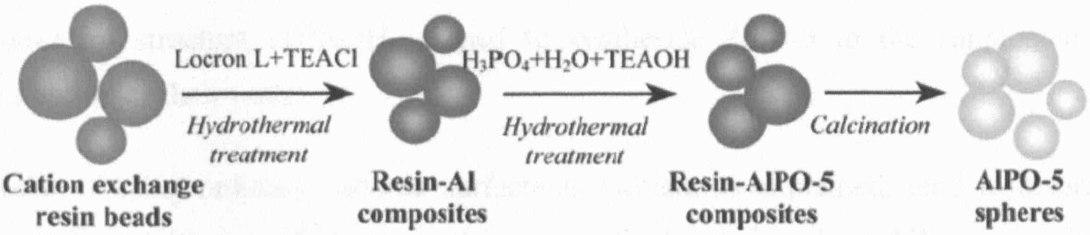

Figure 6.5: The synthesis procedure for forming microporous AlPO-5 with macroporous spherical void spaces. Reproduced from ref. 55.

Various other hard templates (such as starch[56] and wood[57]) have been used to form either meso or macroporous zeolites. These however are generally 2 step syntheses in which a pre-prepared zeolitic material is deposited onto the larger template structure. These methods are therefore synthetically closer to post synthesis treatments than true 'one pot' methods.

6.2.3.2 : 'Soft' templating

Soft templates tend to be surfactants, which must interact with each other to form the mesoporous template (e.g. a micelle) within the gel. To date, only a few examples of microporous materials containing mesoporous regions have been achieved using this method, which is at least partly due to the fact that initial synthesis attempts were not particularly successful. For example, Beck's[58] early work demonstrated that cationic surfactant molecules could form either microporous or mesoporous materials (depending on the length of the organic chain and temperature) but that in no circumstances were mixtures obtained. Another method explored was the introduction of a microporous SDA (e.g. TPAOH or alkaline metals) into a mesoporous gel containing cationic mesoporous templates. However, rather than producing the desired

product of mesopores with microporous walls, bulk meso or microporous phases or physical mixtures were produced[59,60].

Recently, Xiao *et al*[61] have successfully synthesised zeolite-β with a mesoporous hierarchical structure by mixing the cationic polymer polydiallyldimethylammonium chloride (PDADMAC) with microporous organic SDA TEAOH. The material has mesopores of 5-40 nm, in good agreement with the estimated size for the PDADMAC molecules. The material was also found to have a higher catalytic activity and longer catalyst life compared to normal zeolite- β. This reaction is particularly interesting as a variation in the microporous template can result in other zeolites with a mesoporous hierarchical structure (TPAOH is used to synthesise ZSM-5 in the supplementary information of their work).

Instead of using ordinary cationic surfactants (which, as explained, tend to result in mixed phases) Choi *et al*[62] have employed specifically designed amphilic organosilane surfactants (figure 6.6) to synthesise ZSM-5 containing a mesoporous hierarchy. These surfactants contain a quaternary ammonium group for facilitating zeolite-like surface ordering, an alkyl tail and an organosilane group to enhance the surfactant interactions with the zeolite as it forms. Finely tuned mesopores in the region 2 – 20 nm were introduced into the products and these were found to have very high catalytic activity compared to MCM-41, even though they had a significantly lower surface area.

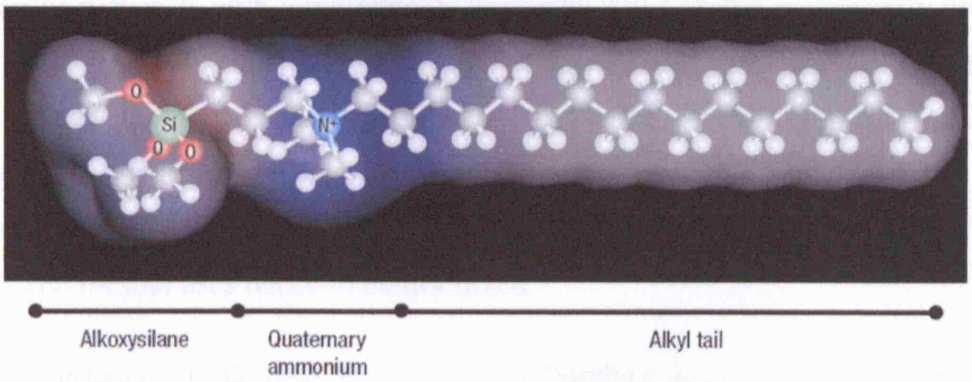

Figure 6.6: The organosilane surfactant used by Choi *et al* in the synthesis of mesoporous ZSM-5. Reproduced from ref. 63.

As Chmelka has stated 'Such hierarchical nano/mesoporous zeolites are anticipated to offer new flexibility in the design and engineering of increasingly sophisticated heterogeneous catalysts'[63]. The experience with microporous zeolites suggests that the

formation of microporous AlPO materials with a mesoporous hierarchy will also be a significant step towards greater catalytic versatility.

Until very recently such materials had not been successfully synthesised. However, during the writing of this, thesis Choi *et al*[64] have successfully adapted the organosilane surfactant synthesis route for the production of these AlPO materials. They have produced mesoporous AlPO-5 containing silicon and cobalt as well as AlPO-11 with crystalline walls and surface areas between 250 and 280 m^2g^{-1} for AlPO-5 (compared to a microporous surface area of 206 m^2g^{-1}). Whilst this is a significant step forward in the production of microporous AlPO materials with mesoporous hierarchy, the use of the silane moiety in the surfactant means that, even in the materials indicated as 'pure' AlPO-5, there is actually 0.05% molar percentage silicon, which is believed to come from substitution of the silane silicon atom into the framework. The work presented here differs significantly, as a neutral co-block polymer is used to create similar AlPO materials but with no substitution of the surfactant material into the framework, resulting in pure mesoporous AlPO-5. Additionally, the polymer utilised in these experiments is not specifically designed and is available 'off the shelf' in large quantities at relatively low cost.

6.2.4 : Surfactants and micelle formation.

From the previous section, it is clear that 'soft' templating methods for producing microporous materials with a mesoporous hierarchy will become increasingly important for the development for catalytic materials and a surfactant based soft templating route has been used in this work. A number of formation mechanisms for mesoporous systems from surfactant based gels have been proposed and are discussed below. However, before this the basic chemistry of surfactants and their interaction to form micelles and mesophases needs to be discussed.

The term surfactant is derived from the term '**Surf**ace **act**ive **agent**' and refers to a material which can significantly reduce the surface tension of a liquid or interfacial tension between liquids in very low concentrations. They do this by adsorbing at the interface between materials, at either the liquid-gas interface in water or at the liquid-liquid interface in an oil-water mix.

An example of the effectiveness of surfactants is the commercially available non-ionic surfactant Softanol-90[39], which can reduce the surface tension of water from 73 to 30 dynes/cm^{-1} in concentrations of just 0.005%, compared to a concentration of 40% for ethanol (a dyne is a unit of force used in the measurement of surfactant surface tension and is equal to 10^{-5} Newtons).

6.2.4.1 : Surfactant structure

The ability of surfactants to adsorb between interfaces such as oil and water comes from their amphiphilic nature, containing both a hydrophilic 'head' and hydrophobic 'tail'. The tail is generally a long carbon chain which can be either aliphatic or aromatic (or both) in nature and interacts only weakly with water. Conversely the head group interacts strongly with water and can be ionic, (anionic, cationic or zwitterionic) interacting *via* ion-dipoles or non-ionic and interacting *via* dipoles alone (table 6.1)[65,66].

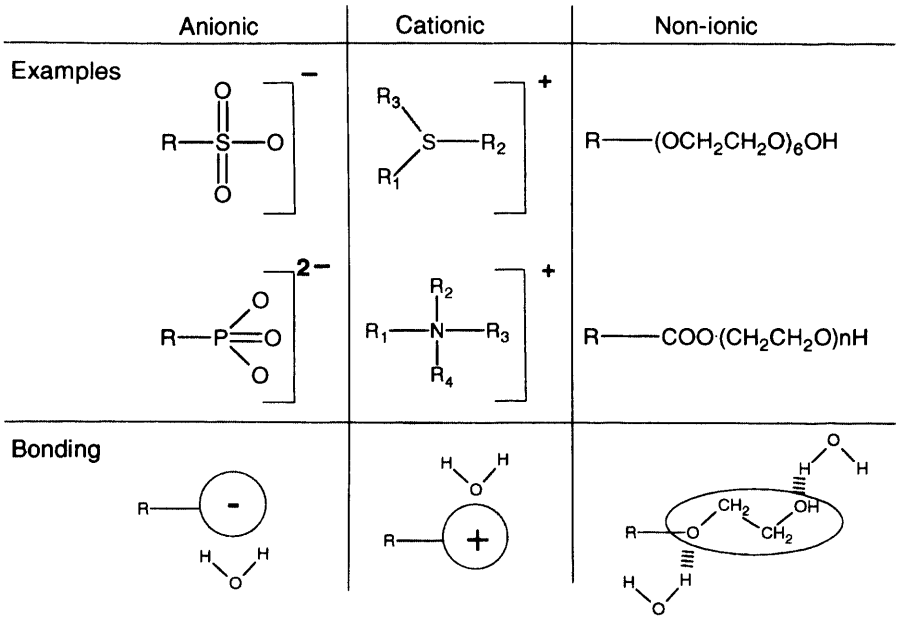

Table 6.1: Examples of surfactant head groups and how they interact with water. Note that R groups represent the tail of the systems. Zwitterionic surfactants contain both anionic and cationic parts depending on the conditions in the solution. Produced from details in refs. 65 and 66.

6.2.4.2 : Micelle formation

McBain[67] has previously described the orientation of surfactant molecules into self assembled aggregates (or micelles). At low concentrations surfactants are present as 'monomers' with no particular orientation at the interface. However, as the

concentration increases there is less and less room for adsorption at the interface and ordering occurs. At a particular concentration referred to as the 'critical micelle concentration' (CMC), no more adsorption at the interface can occur and therefore self assembly occurs. Here the hydrophilic heads create a surface in contact with water whilst the hydrophilic tails excluded water interacting with each other in the centre. The exact CMC of a system is dependant on a number of factors including the head group type, chain length and addition of salts or alcohols to the mix. Temperature is also an important factor and for ionic surfactants below a particular point (the Kraft temperature) no CMC exists and surfactant remains insoluble, whilst for non-ionic surfactants high temperatures result in a 'cloud point' resulting in partial separation of the system in water and micelle rich phases (see phase diagrams below).

6.2.4.3 : Micelle shape

The actual shape of a micelle in solution can vary considerably and is dependant on factors similar to the CMC, such as temperature, concentration, and type of surfactant. Generally, there are 3 basic types formed[65], spherical, rod-like and lamellar. For ionic micelles the number of surfactant molecules (aggregate number) is generally 50 - 100 and the diameter is approximately twice the length of the alkyl chain.

However, for non-ionic surfactants huge aggregation numbers and diameters of orders of magnitude greater than the alkyl chains have been identified. These can exist in a number of shapes including cylinders, disks and lamellar phases. A simple geometric model for the packing of the head and tail groups can be used to explain these structures. For example, if the relative size of a head group is large in comparison to the tail then a cone like shape is created and spherical packing occurs. However, if the head is relatively smaller then a truncated geometry occurs and a cylindrical micelle results[68]. These cylindrical micelles can exist in very long chains, for example Balzer[69] has identified micelles 3 nm in diameter and 219 nm in length, whilst Lin *et al*[70] has found structures 3-8 nm in diameter but up to 1000 nm in length.

These geometric considerations can the also be used to explain the variation in size of micelles as the size of the head group is varied. Any reduction in the size of the head group will allow more molecules to pack into the sphere increasing the micellar size

and, as indicated above, a further reduction would then lead to a preference for non-spherical structures[68].

6.2.4.4 : Liquid crystals

The micellular phases described so far can be described as being 'discrete' aggregates, existing as individual entities within the solution. However, under particular conditions (generally high concentration) connected assemblies of these aggregates can be formed with connections over macroscopic distances in 1, 2 or 3-dimensions. Examples of both discrete and connected structures are given in figure 6.7. The connected phases are referred to as 'liquid crystal like' as they behave as highly viscous fluids, but have some crystalline structure as detailed by X-ray diffraction[65].

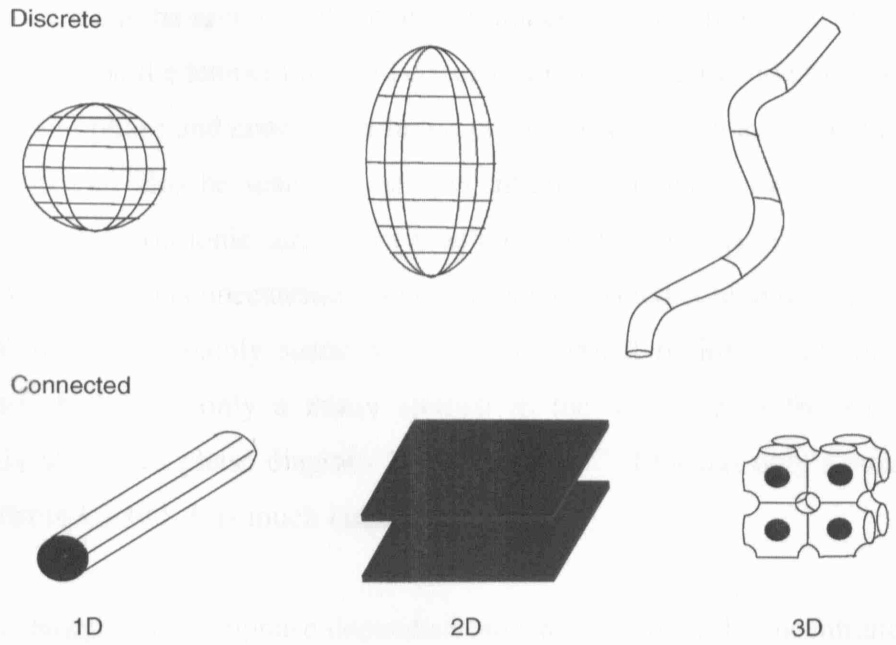

Figure 6.7: Example schematics of discrete and connected self-assembly structures. Reproduced from ref. 43.

6.2.4.5 : Phase diagrams

By considering phase diagrams for surfactant solutions it is possible to have some idea of what form of aggregation (or the mesophase type) is occurring in the solution. Figure 6.8 represents temperature/concentration phase diagrams of non-ionic surfactants containing 12 (left) and 16 (right) carbons in the tail and 8 ethyleneoxide units in the head (giving $C_{12}EO_8$ and $C_{16}EO_8$ respectively).

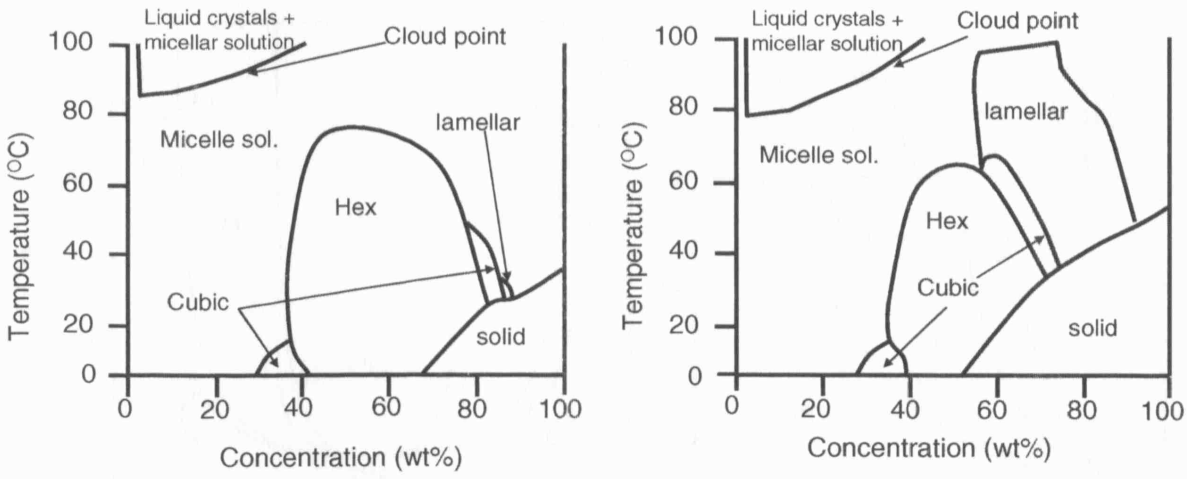

Figure 16.8: Phase diagrams for $C_{12}EO_8$ (left) and $C_{16}EO_8$ (right). Modified from ref. 68 and information from ref. 65.

From this plot it can be seen that there are a number of different phases surfactants can adopt depending on the temperature and concentration. These include the discontinuous micelle solution phase and continuous liquid crystal phases such as hexagonal, lamellar and cubic. It can also be seen that at concentrations above about 1 % and at high temperatures these non-ionic surfactants reach a 'cloud point'. Above this temperature (which is dependant on concentration) two layers are formed containing mainly water (a micelle solution) and mainly surfactant (a liquid crystal region). Additionally these figures also show that only a minor change in the structure of the surfactant can significantly affect the phase diagram. For example, $C_{12}EO_8$ has only a small lamellar phase, whilst in $C_{16}EO_8$ it is much larger.

As well as changes in mesophase dependant on temperature and concentration, Matsen and Bates[71,72] have also shown that at one concentration (in this case a melt) the mesophase can depend on length of the tail and head (figure 6.9).

The mesophase formed by a particular surfactant actually varies depending on this length and quantity of segregation between the head and tail (χN). However, this quantity of segregation is not well defined, being considered only strong, medium and weak. But as it should be similar for surfactants with similar head and tail groups the type of mesophase in a series of similar surfactants with different head and tail lengths will be dependant on the relative lengths of these.

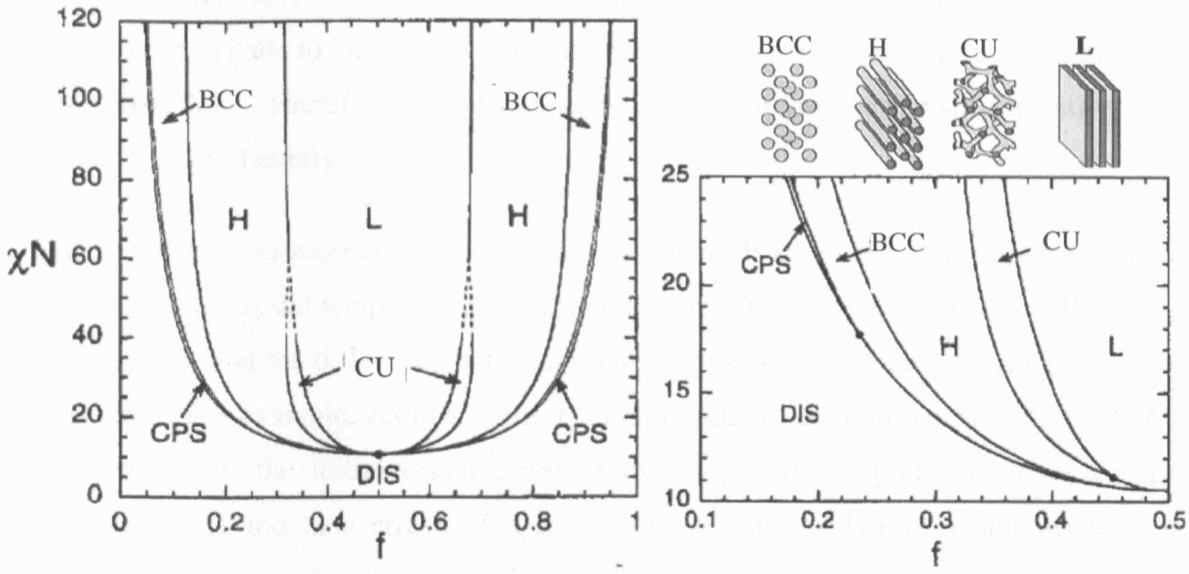

Figure 6.9: The phase diagram for di-block copolymers (left) and close up of a section of the diagram (right) with some representations of the potential phases. f = fraction of head compared to the tail. χN = segregation of the head and tail. Phases are L (lamellar), H (hexagonal packed cylinders), CU (bicontinuous cubic / Gyroid), BCC (bcc spheres), CPS (close packed spheres) and DIS (disordered). Modified from refs. 71 and 72.

Whilst these phase diagram are helpful to give some idea as to what is occurring during the formation of zeolitic microporous/mesoporous materials it should be noted that they will differ significantly at hydrothermal temperature and pressures and in 'real' gel systems, which contain many different interacting species not present in a standard surfactant-water mix.

6.2.5 : Mechanisms of mesopore formation.

The basics of surfactants and their formation into micelles and mesophases have now been discussed. A number of mechanisms of how these species then interact with gel species (such as silicates) to form mesoporous materials are now examined.

As very little work has been performed on combined micro/mesoporous materials there are currently no proposed unifying mechanisms as to how these materials form. The mechanisms discussed here are based on the knowledge from purely mesoporous materials such as MCM-41. Clearly, the problem of phase separation (section 6.2.3.2) for combined material synthesis using standard cationic surfactants indicates that these mechanisms may need to be significantly modified to account for these systems. It is

also noted that the recent success of the organosilane surfactant is partly attributed to the ability of the silane to enhance zeolite (and now AlPO) crystallisation in comparison to other materials. Therefore, the mechanism for organosilane surfactant formation may also differ significantly.

One of the earliest mechanistic proposals came from Beck *et al*[73] who suggested some form of liquid crystal templating mechanism for the formation of MCM-41. Effectively they suggest that the difference between microporous and mesoporous formation is one of timing. For example, zeolites form from an initial silica organisation, whilst MCM-41 forms from the initial organisation of micelles into a liquid crystal mesophase template (rods and then arrays of rods). However, as the liquid crystal structure is highly sensitive to the characteristics of the solution, the authors indicate that the mechanism can be driven either by the organisation of liquid crystals, around which the silica walls then grow, or in an opposite manner where the silicate anions control the formation of the liquid crystal arrays (figure 6.10).

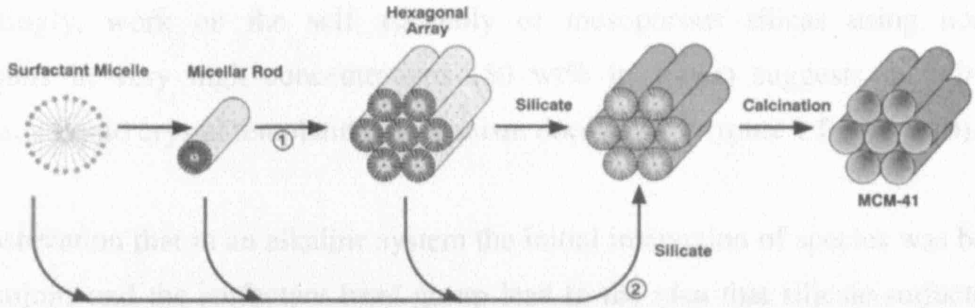

Figure 6.10: The formation of MCM-41 from the organisation of liquid crystals around which silica grows (1) or with silicate anions controlling the formation (2). Reproduced from ref 73.

In another paper the same group found that only when well defined liquid crystal hexagonal structures are formed, can MCM-41 be synthesised[58]. With small organic surfactants, micellular-like aggregates do not form to minimise hydroscopic interactions, and hence no MCM-41 forms. However, the larger surfactants form micellular aggregates of surfactant cations, which in combination with the anionic silicon species, generate a supramolecular structure resulting in mesoporous materials.

However, *in situ* NMR[74], SANS [75] and *in situ* ATR/FTIR studies[76] all suggest liquid crystal arrays do not form within gels at the low surfactant concentrations (~1% wt in water) used in the synthesis of MCM-41 (something that is also indicated by the phase

diagrams given above). It appears then, that in systems with low surfactant concentrations, formation proceeds by a mechanism very similar to the silicate (2) route suggested by Beck[73]. Here, randomly ordered rod like organic micelles interact with silicate species to form monolayers (2 or 3 deep) of silica encapsulation, these composites can then condense to form the long range MCM-41 ordered structure (figure 6.11) [74].

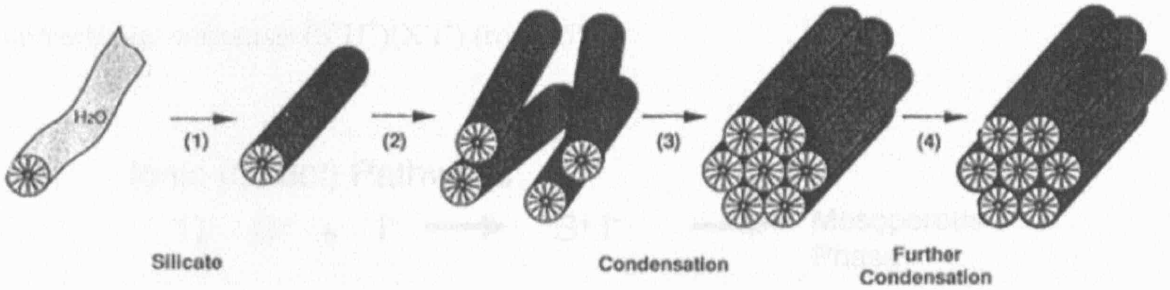

Figure 6.11: The formation of rod like micelles on which monolayers or silicate is deposited.(1). Condensation then occurs (2–4) resulting in the MCM-41 structure. Reproduced from ref. 74.

Interestingly, work on the self assembly of mesoporous silicas using non-ionic surfactants in very high concentrations (50 wt% in water) suggests that, in these systems, a liquid crystal templating mechanism does occur[77] (route 1 figure 6.10).

The observation that in an alkaline system the initial interaction of species was between silica anions and the surfactant head group lead to the idea that silicate-surfactant ion pairs assemble into molecular inorganic liquid crystals that undergo condensation[78]. Such matching of change density leads to the formation of mesoporous phases and the dynamic interaction of the ion pairs can direct the formation of different mesostructures.

The above theory can be extended to encompass cationic, anionic and non-ionic surfactant types. Here the formation of mesopores occurs as long as there is a complimentary electrostatic interaction between the charges. For ionic solvents, if the surfactant head groups (S) and inorganic ions (I) themselves have complementary electrostatic interactions, then direct co-condensation can occur (figure 6.12 routes 1 and 2)[79]. However, if the charges between the surfactant and inorganic are the same, counter-charged ions (X and M) must be present in stochiometric quantities to mediate condensation by creating a stable ion pair (routes 3 and 4).

When the formation of mesoporous phases from non-ionic surfactants was identified, the mechanism was extend to include S^oI^o type pairs, with hydrogen bonding between the inorganic and surfactant polymer chains being responsible for the attraction of silicon into monolayers[18]. It was noted that these non-ionic syntheses are generally performed in an acidic solution and Zhao *et al*[80] have shown that the concentration and identity of the acidic counter ion (X^-) can significantly alter the assembly process and so plays a vital role in the templating interaction. Therefore, the mechanism should more correctly be written as $(S^oH^+)(X^-I^+)$ (route 5).

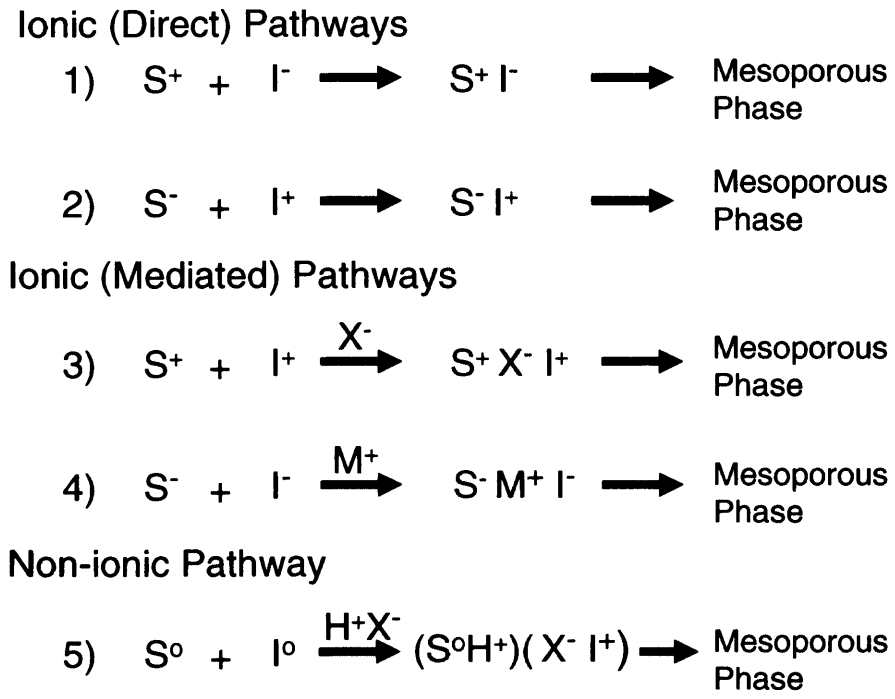

Figure 6.12: The formation of mesoporous phases *via* either direct ionic, mediated ionic or non-ionic (acidic anion supported) condensation. Surfactant head groups are (S), inorganics (I), counter charge ions (X and M) and the acidic cation (proton) (H).

6.2.6 : Aim of this work

The development of new heterogeneous catalysts with improved catalytic activity and better environmental safety is key to the future of the chemical and petrochemical industries. Currently there are a large number of microporous materials, based on either silicon and aluminium, phosphorus and aluminium or materials with additional substituted metals. In the previous chapters of this work some of their uses (e.g.

methanol to olefin conversion) have been discussed and the way in which some of these materials form has been examined.

However, despite the success of a number of these microporous materials, the pore size (as discussed above) limits the rate at which materials can pass through the system, resulting in slow mass transport. To overcome this problem a number of options have been explored, including the introduction of very small microporous materials and development of mesoporous materials. Whilst these materials have shown some potentially for good catalytic activity, a number of problems prevent these materials from being entirely commercially viable.

A different option is the introduction of a mixed crystalline microporous materials with hierarchical mesopores. To date this approach has been successfully achieved in only a few cases. The aim of this work is to continue the development of these systems to include the AlPO family of materials synthesised from commonly available surfactants.

The study is based on the large pore AlPO-5 material, due to the large number of synthesis conditions under which it can be synthesised. The development of a method for the introduction of a mesoporous structure is discussed and then a number of techniques are used to investigate the presence of mesopores. To indicate the generality of the procedure, the exact type of surfactant has been varied and the synthesis of another AlPO (MeAPO-34) attempted.

It is hoped that the development of this pure AlPO micro/mesoporous phase using non-ionic surfactants will open opportunities for the development of other catalytically interesting structures.

6.3 : Experimental

6.3.1 : Hydrothermal preparation of AlPO-5 materials

The synthesis procedure was based on the well known formation of AlPO-5. A general description for the formation of a standard mesoporous AlPO-5 material is detailed below (pure microporous phases were synthesised in an identical manner but without the surfactant). The surfactant used in these initial experiments is Brij-56, a neutral surfactant consisting of a poly(ethylene)oxide (PEO) block of ~10 units (the head group) and a saturated hydrocarbon chain of 16 carbons (the tail).

Gels were prepared to the following molar ratios:

1 H_3PO_4 : 1 $Al(OH_3)$: 0.74 TEAOH : 17.6 H_2O: 0.04 Brij-56

Initially a 9.5 wt % surfactant solution was made to act as the mesoporous template by dissolving 1.5g of Brij-56 (Sigma-Aldrich) in 15.78g of distilled water. In order to aid dissolution the Brij was heated up to give a liquid prior to addition to the water. Dissolution occurred over 20 – 30 minutes and required stirring and agitation. 3.47g of pseudoboehmite (Sasol) was then slowly added to the solution with stirring, and the resulting gel was left to stir for a further 15 minutes. It was noted that some of the pseudoboehmite had not entirely dissolved at this stage and remained as a powder at the bottom of the gel. To this semi-formed gel 3 ml of phosphoric acid (Sigma-Aldrich, 85% wt. in water) was added drop-wise with continued stirring. Upon addition the gel began to thicken and the remaining pseudoboehmite dissolves. After a further 10 minutes 5.15 ml of the microporous template tetraethylamine (Sigma-Aldrich, >99%) was added to the gel drop wise. At this point all of the remaining pseudoboehmite dissolved and the gel became quite thick and aerated (in some cases stirring by hand was required). The final gel was then stirred for a further 30 minutes to homogenise and then added to a Teflon lined autoclave and heated for 3 hours at 175°C.

On opening the autoclave the resulting solution was noted to contain a large portion of a waxy like organic substance, thought to be excess Brij. This was removed as much as possible using a spatula and the remaining white powder was separated from the

solution by centrifuge. XRD confirmed this white powder as AlPO-5 with a microporous structure. Note that a number of variations of this general mechanism were performed in the series of experiment, which are discussed in detail below.

6.3.2 : Characterisation techniques

6.3.2.1 : X-ray diffraction

XRD patterns of all samples were recorded using either the Bruker D4 diffractometer as described in detail in chapter 3 or a INEL angular dispersive detector with a cobalt K_α source (1.789007 Å). Low angle scans were performed on a Bruker D8 equipped with a special diffraction guard to allow data to be recorded at very low angles without interference of straight through beam from the X-ray source. Note that for ease of comparison, all XRD patterns are displayed at the cobalt wavelength, with those recorded using a copper source converted to the cobalt wavelength.

6.3.2.2 : Adsorption / desorption experiments

Adsorption and desorption measurements were performed on a Micrometrics Tristar 3000 which can measure down to pore volumes of 0.01 m^2/g. Nitrogen was used as the source gas and the experiments were performed at 77K. From the resulting isotherms surface areas and pore size were calculated using BET and BJH methods (see chapter 2). Samples were calcined before measurement by heating in air at 1°C per minute up to 550°C over a period of 8 hours.

6.3.2.3 : Aluminium nuclear magnetic resonance experiments

Aluminium nuclear magnetic resonance experiments (NMR) were performed on a Bruker MSL300 solid state spectrometer utilising magic angle spin (MAS).

6.3.2.4 : Transmission electron microscopy

Transmission electron microscopy was performed on a Fei Technai 20 FEG TEM operating at 200 kV.

6.4 : Results and discussion

Initially, the synthesis of purely microporous AlPO-5 and microporous AlPO-5 with a mesoporous hierarchy (from here on designated meso-AlPO-5) from identical gels with and without the mesoporous template is demonstrated. The materials are compared for microporosity and mesoporosity using a number of techniques and the structure of the materials is discussed. The rate of stirring and its effect on the formation of mesopores within the system is then examined. The use of two other Brij surfactants and their effect on the mesoporous structure is then examined and the synthesis of a meso-ZnAPO-34 is attempted. Finally, a mechanism for the formation of meso-AlPO formation is proposed.

6.4.1 : Comparison of AlPO-5 and meso-AlPO-5

Meso-AlPO-5 was synthesised using Brij-56 as the mesoporous template as discussed in the experimental section. As a control, pure AlPO-5 was also synthesised using an identical procedure but without the use of the Brij-56 template.

6.4.1.1 : Confirmation of microporosity

A comparison of the XRD of the samples (figure 6.13, left) reveals that both materials have an identical microporous structure. In order to check the stability of the pores on removal of the organics both samples were then calcined in air at 1°C / min to 550°C and left at this temperature for a period of 8 hours.

XRD of the samples after calcination (figure 6.13, right) revealed not only that (as expected) AlPO-5 had retained the microporous framework but that also the meso-AlPO-5 had remained microporous and no significant structural collapse had occurred. This confirms that the microporous structure is stable under standard synthesis conditions, and if mesoporisity is confirmed indicates that the structure is more stable than many of the purely mesoporous systems discussed in the introduction, which tended to collapse on organic removal.

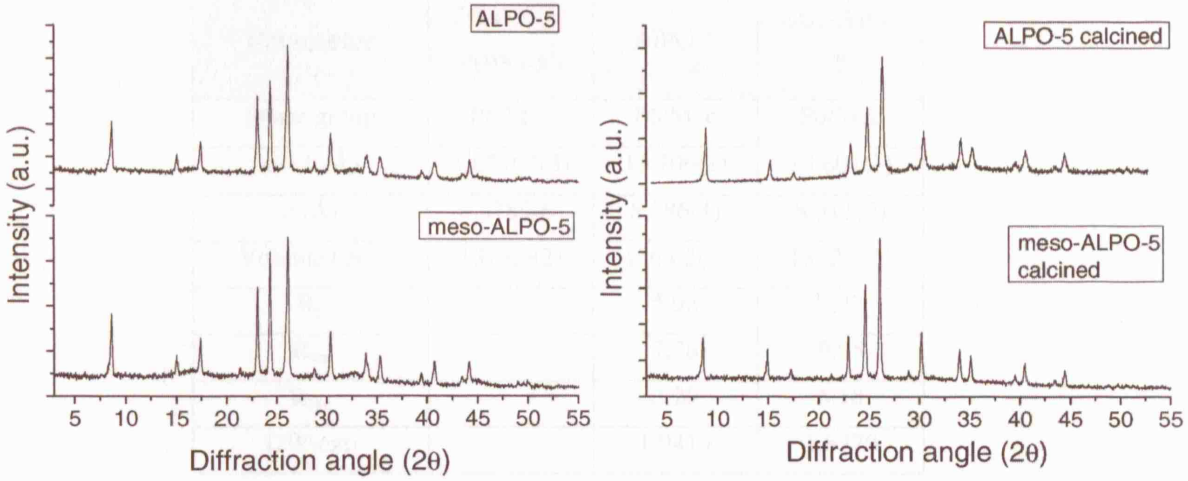

Figure 6.13: Comparisons of pure AlPO-5 and meso-AlPO-5 before and after calcination, revealing that the both have an identical structure and that the microporous structure remains stable after organic removal.

LeBail fits of the calcined samples (figure 6.14) reveal that both the pure AlPO-5 and meso-AlPO-5 exist in the same P6/Mcc space group as detailed previously by Richardson *et al* for other calcined AFI materials[3]. The unit cell parameters (table 6.2) show that pure AlPO-5 and the meso-AlPO-5 both have very similar unit cells with the meso-AlPO-5 having slightly contracted *a*, *b* and *c* parameters and smaller unit cell volume. Also both samples are slightly contracted compared to the values given by Richardson *et al*[3], possibly due to differences in synthesis procedure.

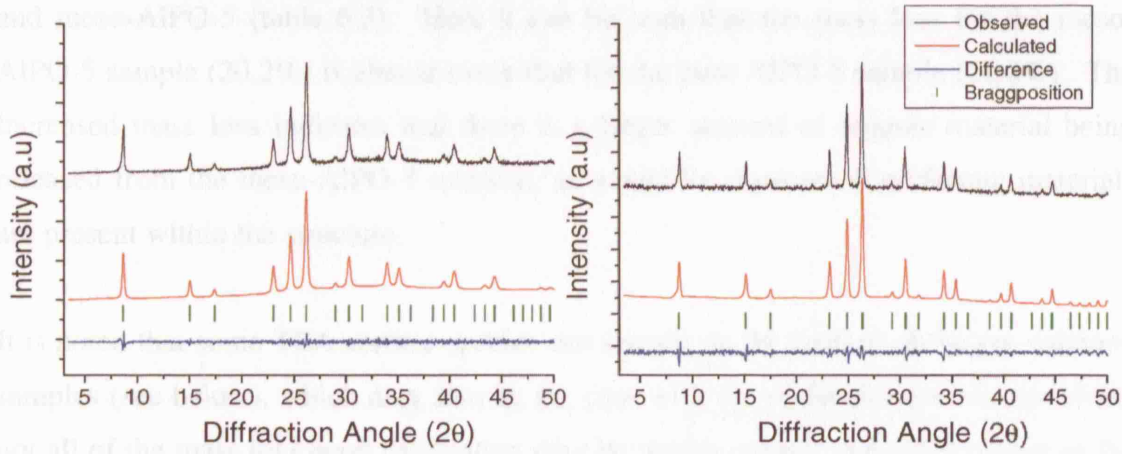

Figure 6.14: The LeBail fits for pure AlPO-5 and meso-AlPO-5, with the actual data, calculated data Bragg positions and the difference plots.

Parameter	'standard' AlPO-5[3]	AlPO-5	meso-AlPO-5
Space group	P6/Mcc	P6/Mcc	P6/Mcc
$a = b$ (Å)	13.7707(3)	13.706(1)	13.607(3)
c (Å)	8.3789(6)	8.386(1)	8.311(2)
Volume (Å^3)	1376.0(2)	1364.2(3)	1332.7(5)
R_p		5.98	7.27
R_{wp}		7.78	9.95
R_{exp}		3.20	6.18
DW-exp		1.9419	1.8779

Table 6.2: Fitting parameters for the pure AlPO-5 control sample and the meso-AlPO-5 sample.

6.4.1.2 : Confirmation of mesoporosity

The presence of the correct microporous structure of AlPO-5 has been confirmed in both the control material and in the material formed with the mesoporous Brij surfactant in the synthesis gel. To identify if the meso-AlPO-5 actually contains a mesoporous phase a number of techniques have then been utilised.

The first indication that mesoporosity has been introduced into the microporous structure comes from accurately measuring the mass loss upon calcination of AlPO-5 and meso-AlPO-5 (table 6.3). Here it can be seen that the mass loss for the meso-AlPO-5 sample (20.2%) is almost twice that for the pure AlPO-5 sample (11.4%). The increased mass loss indicates that there is a larger amount of organic material being released from the meso-AlPO-5 material, as would be expected if surfactant materials are present within the structure.

It is noted that some TEA surface species can remain on the surface of the pre-calcined samples (see below), which may also be the case with the surfactant species, therefore, not all of the mass loss upon calcination may be due to organic species occluded in the pores of the structure. However, it seems unlikely these surface species alone could account for a doubling in mass loss.

Sample	Mass pre-calcination (g)	Mass post-calcination (g)	% mass loss
meso-AlPO-5	0.5004	0.3995	20.16
AlPO-5	0.5054	0.4477	11.41

Table 6.3: Mass of pure AlPO-5 and meso-AlPO-5 before and after calcination and the calculated mass loss.

The BET isotherms for both the pure AlPO-5 and meso-AlPO-5 materials are shown in figure 6.15. The main difference between the isotherms is the substantially greater uptake of nitrogen for meso-AlPO-5 at relative pressures greater that 0.6, which is strongly indicative of increased internal volume due to mesoporosity, and is similar to uptakes observed by Choi *et al*[64] for organosilane synthesised AlPO-5 materials.

Due to the combination of microporous and mesoporous domains, classification of the BET isotherm according to IUPAC designation is difficult. However, the isotherms are very similar to the mesoporous ZSM-5 and zeolite-β observed by Xiao *et al*[61]. The meso-AlPO-5 isotherm is close to a type IV isotherm, which is indicative of mesoporistiy[81], whilst the AlPO-5 isotherm is much closer to type 1, indicative of microporosity. Both samples also contain hysteresis loops (larger in the mesoporous material) and whilst the effect of various factors on them is not well understood, both loops are similar to type H4, which is quantitatively indicative of narrow slit like pores[81].

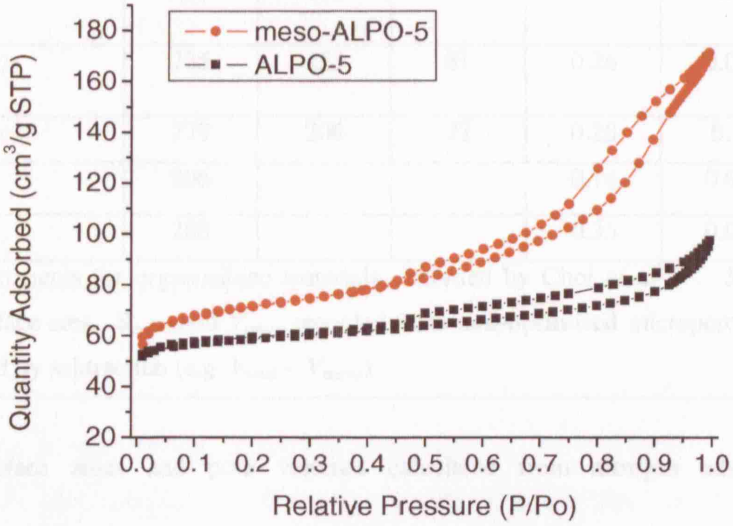

Figure 6.15: BET isotherms for AlPO-5 and meso-AlPO-5 recorded using nitrogen as the adsorptive.

The corresponding pore size distributions (PSD) (figure 6.16) calculated from the desorption profile using the BJH method give an indication of the mesopore size and distribution within each material. These confirm that meso-AlPO-5 contains mesopores with a relatively broad PSD with a modal value of 9.28 nm. By comparison (and as expected) the pure AlPO-5 material contains no mesoporosity over the same region. Note that in both samples there is a very sharp peak centred at approximately 3.8 nm, which has often erroneously been interpreted as true mesoporosity, but is in fact caused by the 'tensile strength effect' as discussed by Groen *et al*[82].

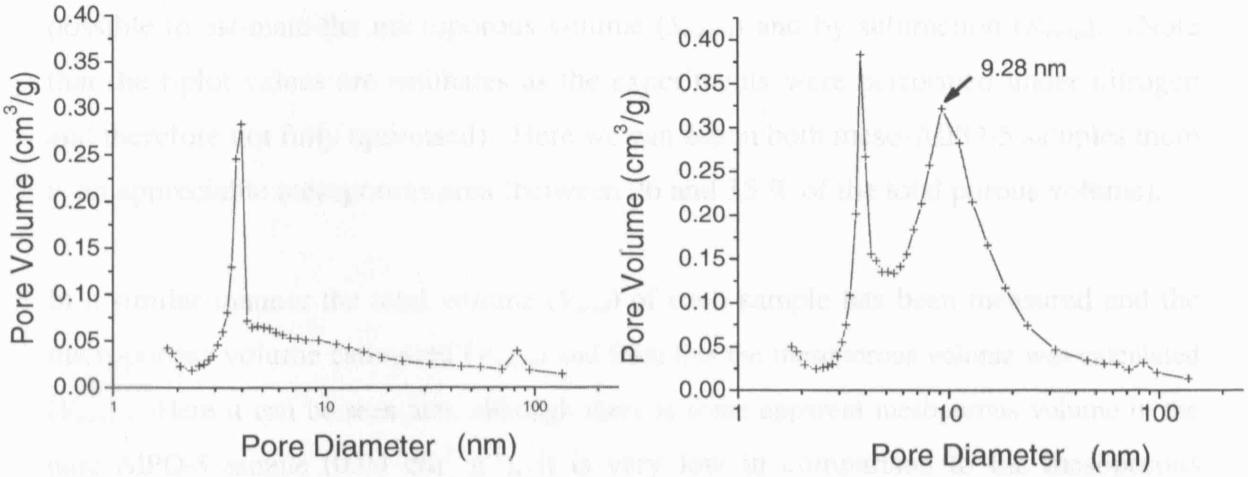

Figure 6.16: BJH desorption profiles for AlPO-5 (left) and meso-AlPO-5 (right).

Sample	S_{BET} (m^2g^{-1})	S_{micro} (m^2g^{-1})	S_{meso} (m^2g^{-1})	V_{total} ($cm^3\ g^{-1}$)	V_{micro} ($cm^3\ g^{-1}$)	V_{meso} ($cm^3\ g^{-1}$)
AlPO-5	180	145	35	0.11	0.07	0.04
meso-AlPO-5 (fast)	235	153	81	0.26	0.07	0.19
meso-AlPO-5 (slow)	279	206	72	0.28	0.1	0.18
AlPO-5*	206			0.14	0.09	0.05
meso-AlPO-5*	280			0.35	0.09	0.26

Notes: * = measurements for organosilane materials, recorded by Choi *et al*[64] . S_{BET} = Brunauer-Emmett-Teller surface area. S_{micro} and V_{micro} recorded from **non-optimised** microporous t-plots. S_{meso} and V_{meso} calculated by subtraction (e.g V_{total} - V_{micro}).

Table 6.4: Surface areas and pore volumes calculated from nitrogen adsorption/desorption measurements.

From the BET measurements, estimates of the surface area and pore size have been calculated and these are compared with similar recently synthesised materials (table 6.4). Note that the synthesis was repeated with both rapid and slow stirring of the gel and results for both of these are given. Further details about the effect of stirring are discussed below.

From these measurements it can be seen that the total BET surface area (S_{BET}) for meso-AlPO-5 synthesised using Brij-56 is comparable to the organosilane approach (235 and 279 $cm^3\ g^{-1}$ compared to 280 $cm^3\ g^{-1}$ respectively). From the microporous t-plots it is possible to estimate the microporous volume (S_{micro}) and by subtraction (S_{meso}). (Note that the t-plot values are estimates as the experiments were performed under nitrogen and therefore not fully optimised). Here we can see in both meso-AlPO-5 samples there is an appreciable mesoporous area (between 26 and 35 % of the total porous volume).

In a similar manner the total volume (V_{total}) of each sample has been measured and the microporous volume estimated (V_{micro}) and from this the mesoporous volume was calculated (V_{meso}). Here it can be seen that, although there is some apparent mesoporous volume in the pure AlPO-5 sample (0.04 $cm^3\ g^{-1}$), it is very low in comparison to the mesoporous sample (0.19 $cm^3\ g^{-1}$), and comparable with the AlPO-5 produced by Choi *et al* [64] (0.05 $cm^3\ g^{-1}$). However, the calculated mesoporous volume of both meso-AlPO-5 samples is slightly less than the organosilane material (0.19 compared to 0.26 $cm^3\ g^{-1}$), indicating slightly less mesopores in the Brij synthesised samples.

Whilst the calculated mesoporous surface areas and volumes are estimated, these results strongly indicate mesoporosity in the Brij synthesised samples in quantities comparable to, but slightly lower than the organosilane material of choi *et al*[64].

Further evidence for the presence of mesopores can be obtained by examining the very low angle X-ray diffraction. Using a specially modified plate it was possible to reduce the straight-through beam and record diffraction to very low angles on a standard Bragg-Brentano diffractometer. In order to ensure any signal is a result of the sample and not caused by the instrument (i.e. intensity increase due to straight-through beam and cut-offs due to the beam stop) the mesoporous sample was compared with a standard microporous sample. These measurements show that for the meso-AlPO-5 sample there is clearly a broad reflection at low 2θ centred at 0.85° 2θ. As this peak is

not present in the microporous sample (figure 6.17), this observation further supports the BET and calcination measurements, indicating mesopores with some regularity within the meso-AlPO-5 sample.

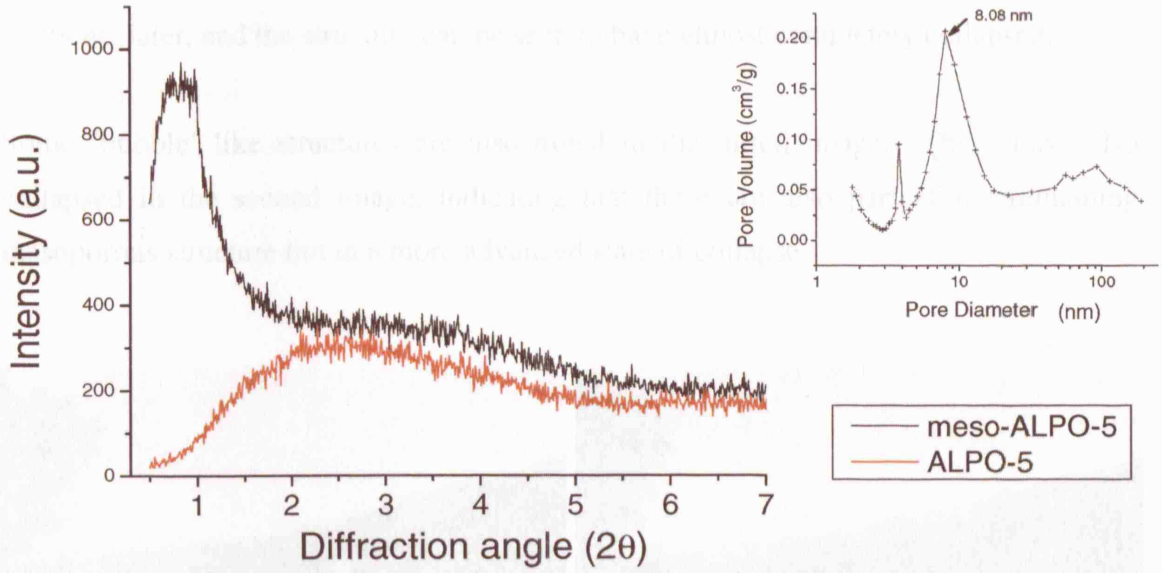

Figure 6.17: The low angle scans of meso-AlPO-5 and as a comparison pure AlPO-5 and the corresponding BJH desorption plot for the meso-AlPO-5 sample (inset).

For this meso-AlPO-5 sample the BJH desorption gives a broad PSD with a modal value at 8.1 nm (figure 6.17, inset), whilst calculations from the XRD indicate it to be 12 nm. The difference between these values indicates that whilst these methods can identify the presence of mesopores, exact size determination is not always easy. In particular at very large d-spacings, the broad nature of the data as well as any errors (such as constant 2θ shift) can have a pronounced effect. For example, the calculated XRD peak position for 8.1nm mesopores is 1.27° 2θ, and this is only 0.42° 2θ higher than the centre of the measured XRD peak position (0.85° 2θ). Therefore, from these results it is possible to conclude that the sample contains mesopores between 8 and 12 nm in size.

One of the most direct ways to identify if mesopores are present in a sample is to image the sample using transmission electron microscopy (TEM). Using this method the mesoporous structure of both zeolitic and AlPO based purely mesoporous samples have been recorded. However, when the meso-AlPO-5 sample was inserted into the electron beam, the sample was found to rapidly collapse. Initially, mesoporous regions were observed, but these collapsed very rapidly and before a full image could be recorded. In

figure 6.18 some parts of the mesoporous structure were successfully imaged having undergone partial collapse (left). The pores are needle-like with an approximate diameter of 10nm, which is in agreement with both the BET isotherm hysteresis type and the estimated pore size. The second image (right) was then recorded a few moments later, and the structure can be seen to have almost completely collapsed.

Some 'bubble' like structures are also noted in the initial image. These have also collapsed in the second image, indicating that these are also part of the remaining mesoporous structure but in a more advanced state of collapse.

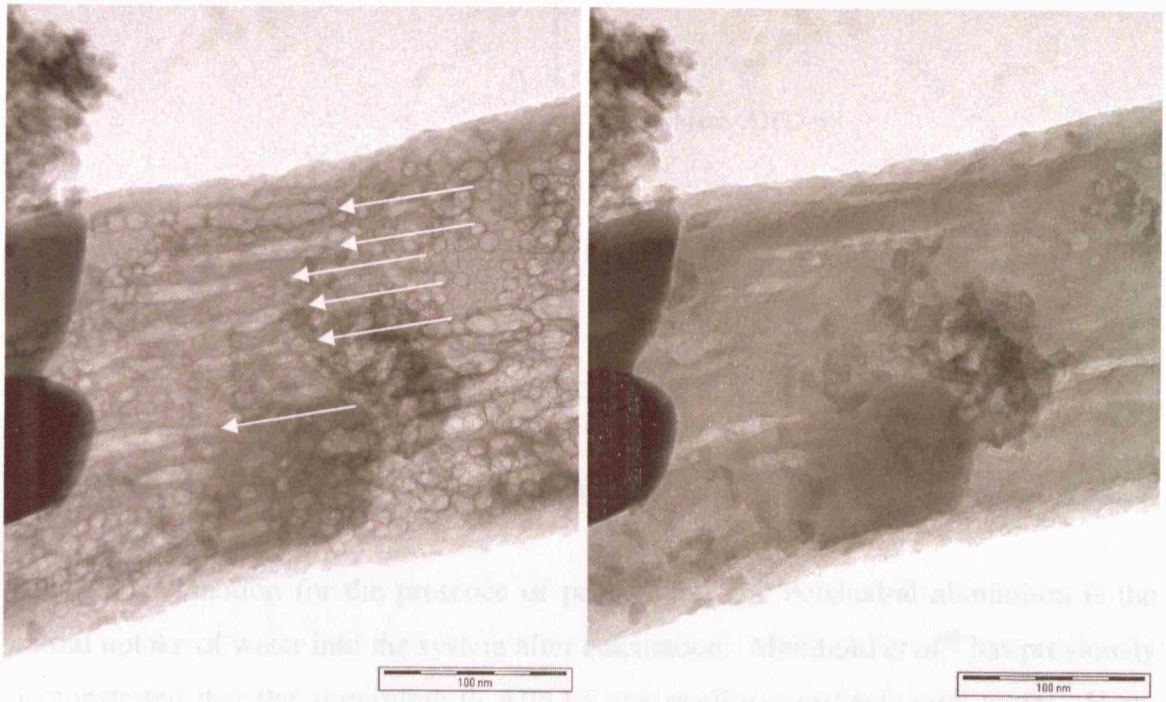

Figure 6.18: TEM images of meso-AlPO-5. The mesoporous structure rapidly collapses and only partials of the needle like pores could be imaged (left, pores marked with arrows). The collapse of the structure is apparent in the second image taken a few moments later (right). Here almost no meso structure is visible.

The final method used to examine these materials is ^{27}Al NMR. This method is useful as it can give some indication of the coordination of the aluminium within AlPO framework. The results for calcined pure AlPO-5 and meso-AlPO-5 (figure 6.19) show the presence of 3 peaks, at approximately 38 ppm, 6 ppm and -16 ppm.

The peaks at 38 ppm and -16 ppm are in the chemical shift region for tetrahedral and octahedral aluminium[83], whilst the shift at 6 ppm is in the region previously assigned to penta coordinated aluminium[84,85]. It is possible that the octahedral aluminium is a result of a partial collapse of the structure upon calcination. This seems unlikely however, as there is no appreciable degradation of the XRD signal after calcination. Additionally, upon collapse, these AlPO materials tend to form dense tetrahedral coordinated phases such as tridymite and berlinite and not octahedral systems (see below).

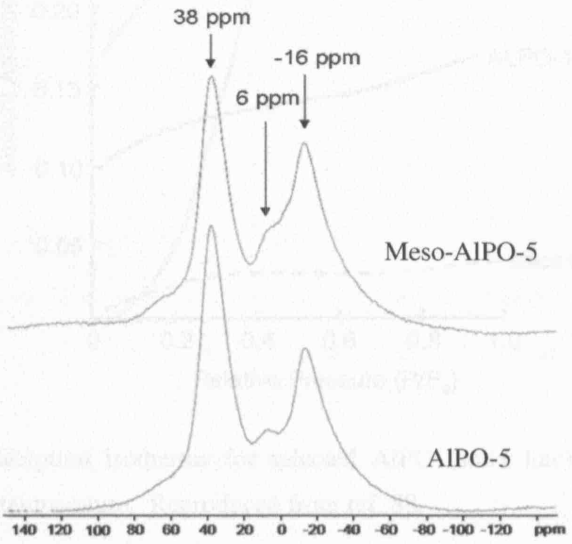

Figure 6.19: ^{27}Al NMR of meso-AlPO-5 and pure AlPO-5.

Another explanation for the presence of pentahedral and octahedral aluminium is the partial uptake of water into the system after calcination. Meinhold *et al*[86] has previously demonstrated that the aluminium in AlPO-5 can readily coordinate with water. Here, either two molecules can coordinate, leading to octahedral aluminium sites or one molecule coordinates, resulting in pentagonal sites.

As both samples had been previously calcined in order to remove the organic template, any water would also have been expelled from the framework. However, as the samples were then exposed to atmospheric moisture for a number of months prior to the NMR experiments, it is possible that the samples have re-hydrated.

Some aluminophosphates are known to exhibit hydrophilicity and in particular AlPO-5 (and to a lesser extent AlPO-20) is particularly hydrophilic, readily up taking water (figure 6.20)[87,88]. Therefore it appears that the samples have re-hydrated in the period

between calcination and the experiment, converting some aluminium sites from tetrahedral to octahedral.

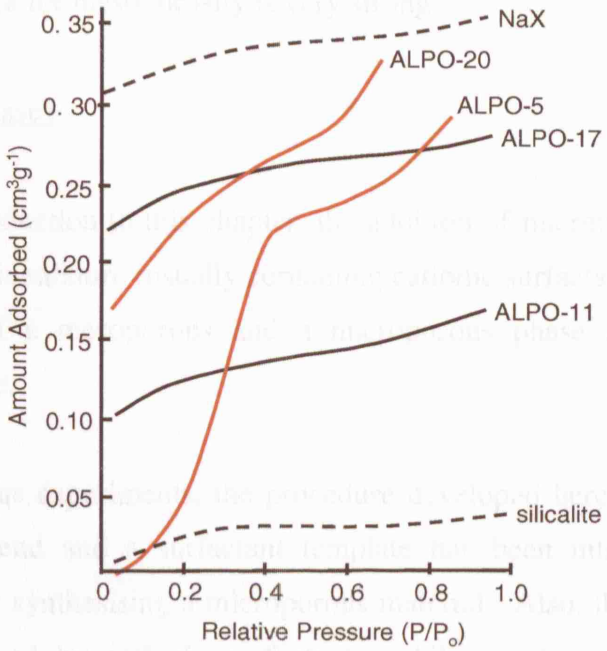

Figure 6.20: Water adsorption isotherms for selected AlPO (solid line) and zeolite (dashed line) molecular sieves at room temperature. Reproduced from ref. 88.

What is of particular interest in these measurements is the fact that the peak intensity ratio (tetrahdral:octahedral) of the meso-AlPO-5 sample (1:0.75) is noticeably higher than that of the pure AlPO-5 (1.0:0.58), indicating a greater uptake of water (figure 6.19). These results have two consequences: first they are consistent with a higher adsorption capacity and site availability bought about by the increased pore volume of a mesoporous material; second, they demonstrate the pores must be easily accessible to the external water molecules (i.e. they are not isolated and closed).

This experiment therefore supports the other work indicating that the meso-AlPO-5 samples contain mesopores and also shows that these are highly accessible to external molecules. Both of these properties are desirable for a successful catalytic material and suggest that mesoporous AlPOs formed using this synthesis method may exhibit improved activity over their pure microporous counterparts.

To summarise, in this section a combination of BET, low angle XRD, TEM and NMR has been used to identify the presence of a mesoporous region within the AlPO-5

material. Using each of these techniques alone on a single sample is not sufficient to confirm mesoporosity (for example very small crystallites can give false BET readings), however when used in combination with each other and when compared to a standard material, the evidence for mesoporosity is very strong.

6.4.1.3 : A mixed phase?

A stated in the introduction to this chapter, the addition of microporous templates to a mesoporous synthesis mixture (usually containing cationic surfactants) often results in a physical mixture of a mesoporous and a microporous phase and not the desired hierarchical structure.

Unlike those previous experiments, the procedure developed here has been developed from the opposite end and a surfactant template has been introduced into a well established route for synthesising a microporous material. Also, the majority of mixed phases were produced by cationic surfactants, whilst in this experiment a neutral surfactant has been used. The rationale behind this is that the charge on the cationic surfactant may be having a very strong directing effect on the aluminium and phosphorus species in the system, substantial enough to interrupt interactions with the microporous template. Therefore, by using a neutral template it is hoped that interaction with the microporous template can be achieved whilst retaining the structure direction of the macroporous template.

Despite these differences it is possible that a mixed phase is still occurring in the Brij system. To try and identify if this is occurring, a hydrothermal synthesis was performed under identical conditions used previously for the production of AlPO-5 and meso-AlPO-5, but without the micropore forming TEA organic.

An XRD of the resulting structure (figure 621, left) reveals that the dense phase material trydimite is formed. It is unlikely that this material contains any mesoporous phase, and this is confirmed by the BET results which give a total surface area of only 7.58 $m^2 g^{-1}$. As expected the BJH adsorption plot also confirms the collapse of the structure and when compared with compared to the Brij-TEA system no mesoporous region is observed (figure 6.21, right). Additionally, almost no sharp peak due to the tensile strength effect is observed, again expected as there is no microporous structure.

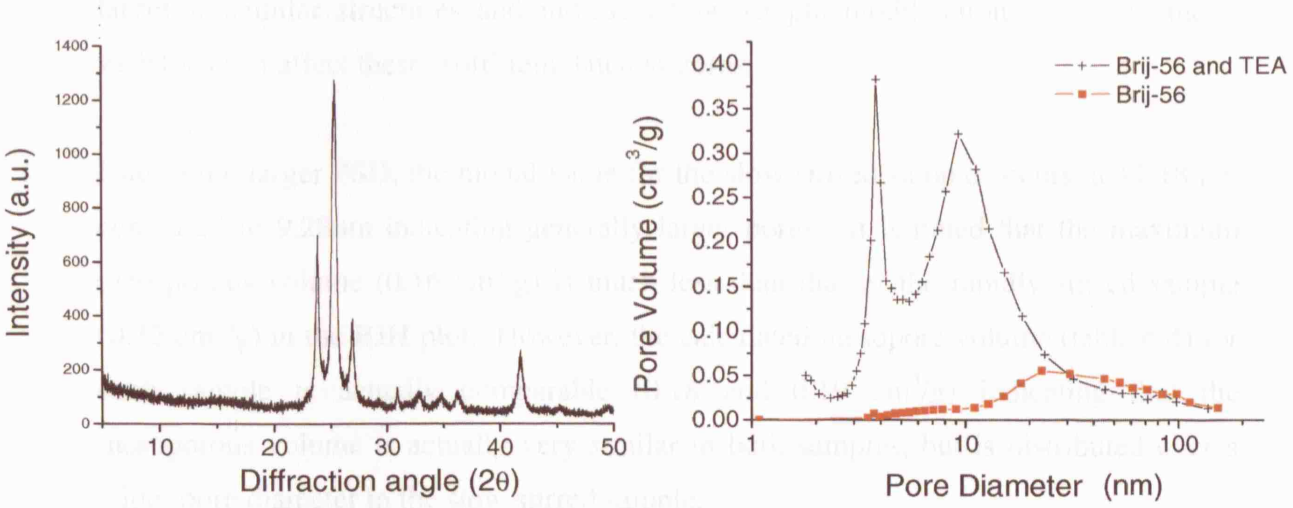

Figure 6.21: The XRD of a Brij-56 synthesis containing no TEA (left) and corresponding BJH PSD plot (right) compared with a standard Brij-56 TEA synthesis.

These results show that mesoporous regions cannot form from a gel that does not contain the microporous template. Although it is possible that a mesoporous region stabilised by the microporous structure could occur, this experiment does strongly indicate a hierarchical structure has most likely formed. It is also noted that if a supported structure has formed the close interaction of the two phases may make it impossible to easily distinguish the two and the properties of the material would most likely be close to that of an integrated material.

6.4.1.4 : The effect of stirring

During the course of the experiments detailed above it was also noted that the rate of stirring could have an effect on the mesopore distribution. In order to examine this further the rate of stirring was varied and the PSD of the samples compared.

Generally, a gel is rapidly stirred with a magnetic stirrer throughout the course of a reaction. However, when stirred very slowly (and only when necessary to allow dissolution of gel substituents) the meso-AlPO-5 materials are still formed. A comparison of the rapid and slow stirred samples (figure 6.22) shows that a wider PSD occurs in the slow stirred sample. It is proposed that this may be due to the reduced amount of shear stress on the gel, allowing surfactant molecules to group together into

larger micellular structures and indicates how simple modification of the synthesis variables can affect these 'soft' templated systems.

Due to the larger PSD, the modal value for the slow stirred sample occurs at 11.18 nm compared to 9.28nm indicating generally larger pores. It is noted that the maximum mesoporous volume (0.16 cm^3/g) is much less than that of the rapidly stirred sample (0.32 cm^3/g) in the BJH plot. However, the calculated mesopore volume (table 6.4) for each sample is actually comparable (0.18 and 0.19 cm^3/g) indicating that the mesoporous volume is actually very similar in both samples, but is distributed over a wider pore diameter in the slow stirred sample.

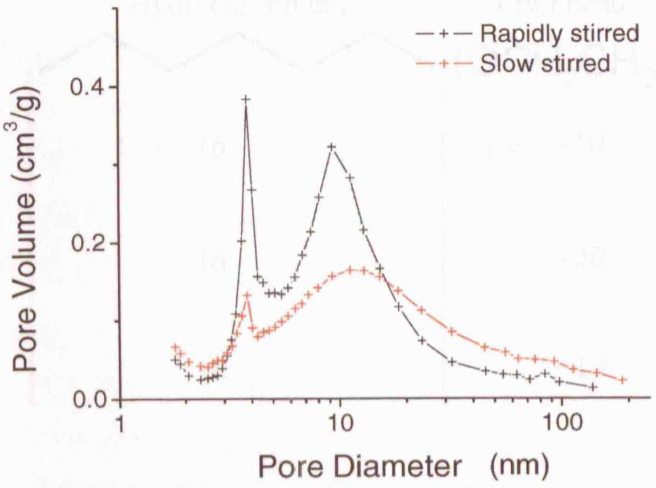

Figure 6.22: The BJH desorption pore size distribution for meso-AlPO-5 samples in which the gel was stirred slowly and rapidly.

Further experiments are currently underway to examine other effects such as temperature and pH and their effects on the gel.

6.4.2 : Generality of the procedure

In the previous section the formation of a mesoporous AlPO with a hierarchical microporous structure was attempted and successfully synthesised. Clearly, if this method is to become an important route for the production of such AlPO materials, it is necessary to see if it is more generally applicable. In this section, some initial experiments to examine both the usage of other Brij surfactants and the formation of other microporous-mesoporous materials are discussed.

6.4.2.1 : Other surfactants

As discussed in the experimental section, Brij-56 is a neutral surfactant consisting of a poly(ethylene)oxide (PEO) block (the head group) and a saturated hydrocarbon chain (the tail). In the case of Brij-56 the tail is 16 carbons long and the head is ~ 10 PEO units. In this experiment, the synthesis of meso-AlPO-5 has been attempted, using two other surfactants; Brij-76 which is almost identical in size to Brij-56, containing only an additional two carbons on the tail (figure 6.23) and Brij-58, with a much larger PEO head group (n = ~20).

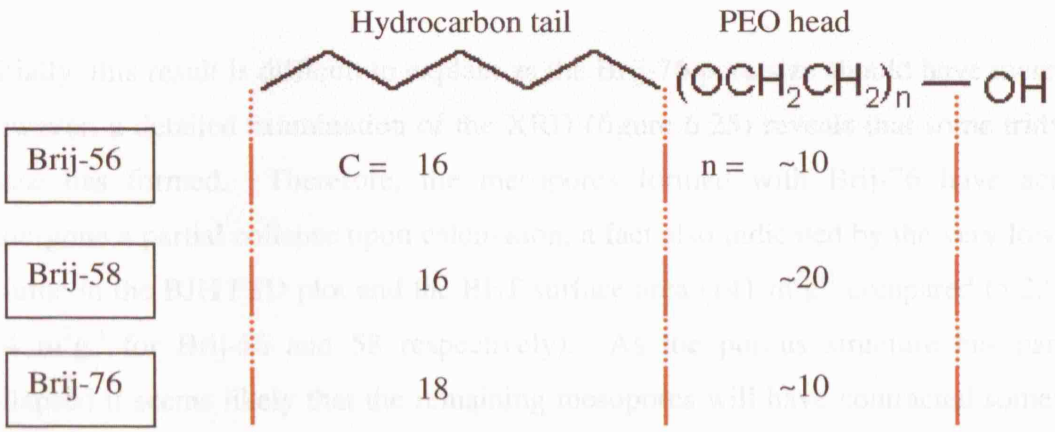

Figure 6.23: Comparison of the head and tail size of the various Brij surfactants used in the synthesis. C = carbon atoms, n = number of PEO units

In each case XRD indicated the formation of the micropores structure, whilst BET and BJH measurements indicated the formation of mesopores. If the structures of Brij-56 and Brij-76 are initially considered, the addition of two carbon atoms to the tail of Brij-76 would be expected to result in a slight increase in the diameter of any micelles formed and therefore a slight increase in the mesoporous diameter of the final structure. However, the BJH PSDs (figure 6.24) actually indicate that Brij-76 results in a decreased pore diameter of 8.09 nm compared to 9.28 nm.

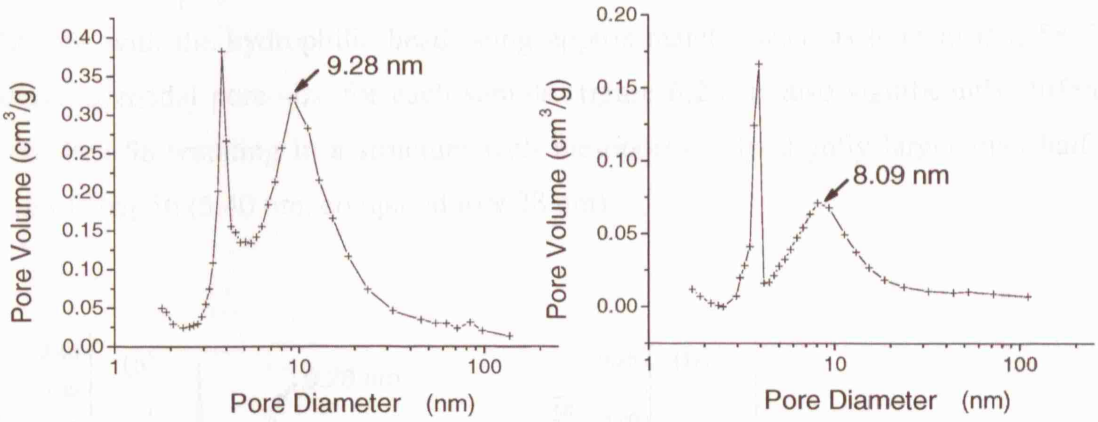

Figure 6.24: Comparison of the BJH pore size distributions for Brij-56 (left) and Brij-76 (right).

Initially, this result is difficult to explain as the Brij-76 pore size should have increased. However, a detailed examination of the XRD (figure 6.25) reveals that some tridymite phase has formed. Therefore, the mesopores formed with Brij-76 have actually undergone a partial collapse upon calcination, a fact also indicated by the very low pore volume in the BJH PSD plot and the BET surface area (141 m^2g^{-1} compared to 235 and 254 m^2g^{-1} for Brij-56 and 58 respectively). As the porous structure has partially collapsed it seems likely that the remaining mesopores will have contracted somewhat, resulting in the observed reduction in pore size for Brij-76. Considering that Brij-56 and -78 are very similar it is interesting that the final structure collapses upon calcination with one sample but not with the other. However, the reason for this remains to be examined.

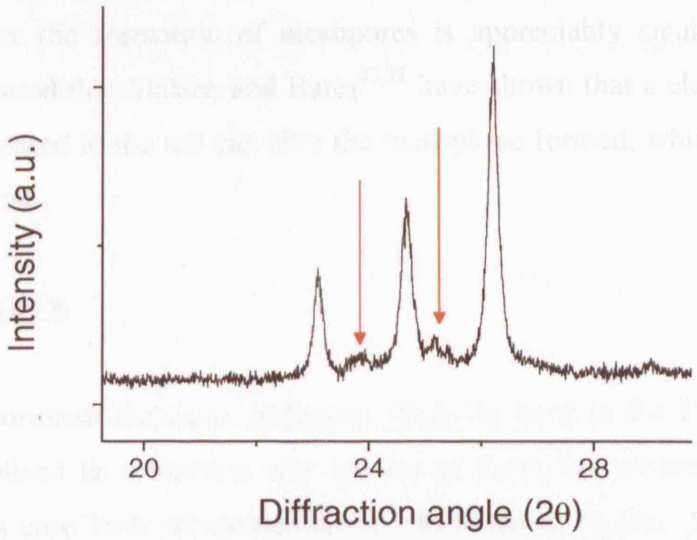

Figure 6.25: The XRD of Brij-76 after calcination with arrows marking the position of the forming trydimite dense phase.

In contrast to Brij-56 and Brij-76 there is a significant difference between Brij-56 and Brij-58, with the hydrophilic head being approximately twice as long in Brij-58. The resulting modal pore size for each sample (figure 6.26) is also significantly different, with Brij-58 resulting in a structure with mesopores only slightly larger than half the size of Brij-56 (5.40 nm, compared to 9.28 nm).

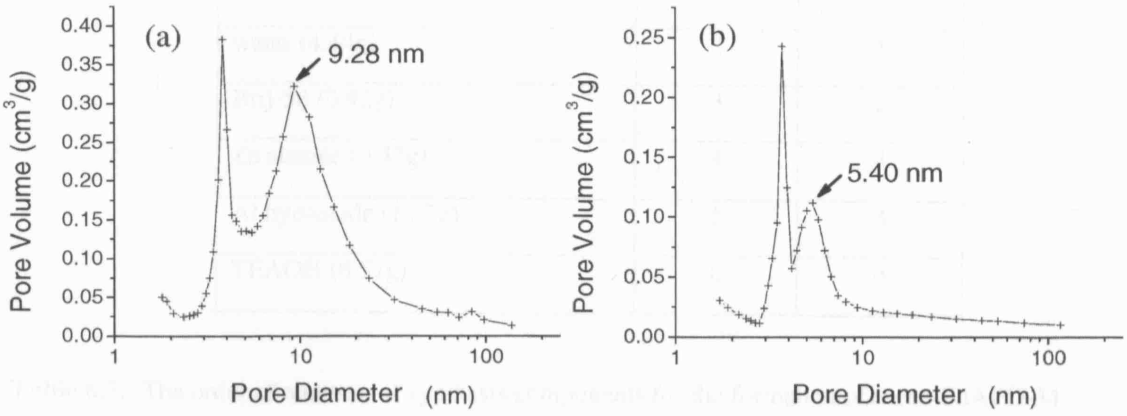

Figure 6.26: Comparison of the BJH pore size distributions for Brij-56 (left) and Brij-58 (right).

Unlike Brij-76 there is no sign of any structural collapse, therefore the most likely explanation for this change is the increased head group size of Brij-58. As described in the introduction, from geometric considerations an increase in head size will decrease the effective micelle size as less surfactant molecules can pack into the micelle sphere[68]. Therefore, as the head group of Brij-58 is twice as large as that in Brij-56 the micelle size available for the formation of mesopores is appreciably smaller. However, it should also be noted that Matsen and Bates[71,72] have shown that a change in the length of the head compared to the tail can alter the mesophase formed, which could also vary the size of the pores.

6.4.2.2 : Other AlPOs

In a further experiment the same surfactant (Brij-56) used in the formation of meso-AlPO-5 was utilised in a reaction mix known to form the microporous MeAPO-34 structure (in this case 10% substituted zinc). As noted in chapter 3, the formation of MeAPO-34 is far more susceptible to the formation of mixed phases than AlPO-5. Therefore two experiments were performed, one following the order of addition for a standard microporous AlPO-34 synthesis (procedure A), and the other following the

order for meso-AlPO-5 (procedure B) (table 6.5). Note that tetraethylammonium hydroxide (TEAOH) was used as the microporous SDA, aluminium hydroxide as the aluminium source and any additional components not in the original synthesis mixtures (e.g. zinc acetate in the Brij procedure) were added as necessary.

substituent (mass)	Procedure A order	Procedure B order
Phosphoric acid (3.38g)	1	5
water (4.44g)	2	1
Brij-56 (0.92g)	3	2
Zn acetate (0.43g)	4	4
Al hydroxide (1.37g)	5	3
TEAOH (6.57g)	6	6

Table 6.5: The order of addition of synthesis components for the formation of meso-ZnAPO-34.

Interestingly, the sample synthesised using the microporous procedure A failed to produce a phase pure MeAPO-34, with a number of unidentified impurities in the sample. However, the mesoporous procedure B successfully produced ZnAPO-34 and a comparison with a standard microporous material (formed using procedures in chapter 3) shows that the sample is directly comparable to standard microporous ZnAPO-34 (figure 6.27). Upon calcination the sample was found not to be particularly stable with considerable loss of the microporous structure. However, unlike the preparation of AlPO-5 with Brij-76, there appears to be no formation of a trydimite dense phases.

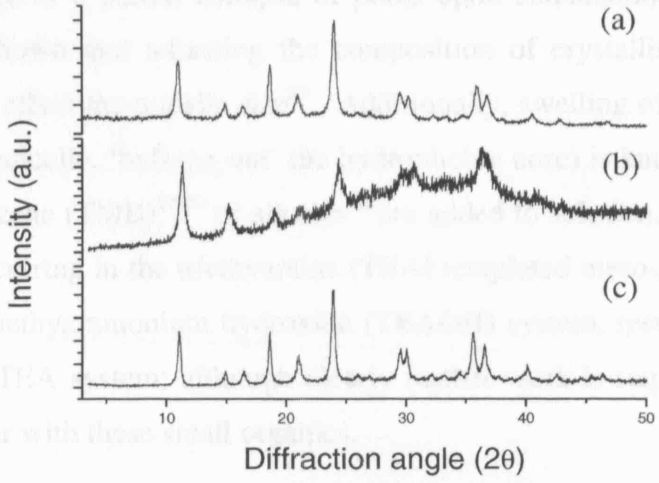

Figure 6.27: XRD patters of the synthesised meso-ZnAPO-34 before calcination (a), after calcination (b) and compared with standard ZnAPO-34 (c).

Despite this loss in crystallinity the sample was tested for its Adsorption / desorption ability and was found to be surprisingly porous. The total BET surface area remains very high (341 m^2g^{-1}) as was the remaining micropore area (265 m^2g^{-1}). By calculation, this leaves a mesopore surface area of 76 m^2g^{-1}, which is comparable with the meso-AlPO-5 samples (81m^2g^{-1}). The BJH PSD plot (figure 6.28) also indicates a high volume of mesopores with a narrow PSD. However, interestingly they are much smaller than those produced using the same surfactant for the AlPO-5 samples (3.09 nm compared to 9.28 nm).

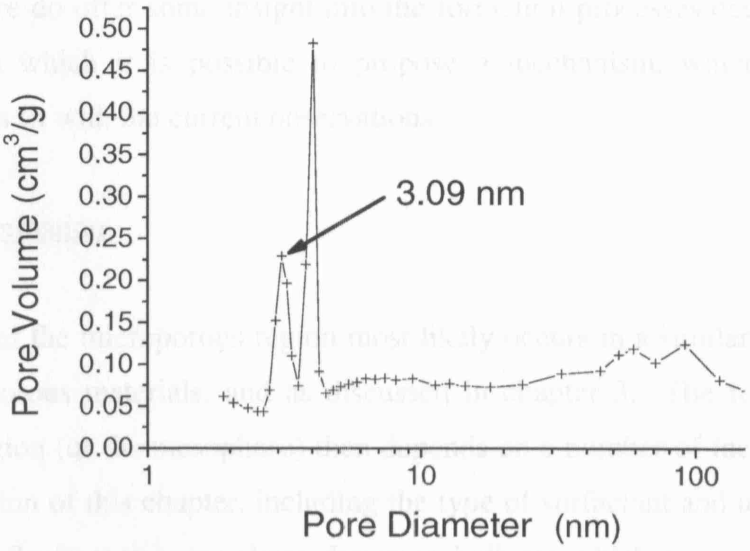

Figure 6.28: The BJH PSD plot for meso-ZnAPO-34.

The reason for such a small pore volume is currently not known, although it may be a simple consequence of a partial collapse of pores upon calcination. However, it has previously been shown that adjusting the composition of crystallisation variables in MCM-41 gels can affect the micelle size[89]. Additionally, swelling of micelles (where a species enters the micelle, 'bulking out' the hydrophobic core) is known to occur when 1,3,5 trimethylbenzene (TMB)[19,80] or alkanes[90] are added to solution. It is possible that this swelling is occurring in the triethyamine (TEA) templated meso-AlPO-5 formation, but not in the tetraethyammonium hydroxide (TEAOH) system, resulting in the larger pores seen in the TEA system; although clearly further work is required to see if this processes can occur with these small organics.

From this section of the work it can be seen that, whilst each product synthesised was not always stable and well crystalline, the potential for this procedure is clear.

Mesopores of different sizes can be introduced into an AlPO-5 structure using different Brij surfactants and the synthesis of other microporous AlPOs is also possible. Clearly some additional testing for the best synthesis conditions is required to produce the most stable systems. However, this route should be viable for the synthesis of many meso-AlPOs.

6.4.3 : Formation mechanism

Whilst these materials are currently only in their initial stage of development, the experiments here do offer some insight into the formation processes occurring in these materials, from which it is possible to propose a mechanism, which although not conclusive, does fit with the current observations.

6.4.3.1 : Pore formation

The formation of the microporous region most likely occurs in a similar fashion to that of pure microporous materials, and as discussed in chapter 3. The formation of the mesoporous region (or the mesophase) then depends on a number of factors as detailed in the introduction of this chapter, including the type of surfactant and temperature and concentration. Surfactant-water phase diagrams indicate which type of mesophase is formed by a particular surfactant at different concentrations and temperatures. Clearly, it is difficult to use these diagrams as a direct comparison for the more complicated gel systems utilised in these experiments; however it is possibly to estimate which structures may form.

For each of the experiments performed, a 10 % weight solution of surfactant in water was created, and whilst the phase diagram for each particular surfactant may vary, this clearly places the systems well within the discontinuous micelle in solution phase (figure 6.29). (Note that a phase diagram for Brij-56 $C_{16}PEO_{10}$ was not available so the diagram for $C_{16}PEO_8$, which is of a similar chain length, is reproduced here).

As described in the introduction, the exact form of micelle can be either spherical, cylindrical or lamellar and this is not currently known. Furthermore the experiments with Brij-58 suggest that it is possible to alter the micelle size by varying the head group size[68].

In order to form the open mesopores identified in this work, these discrete micelles in solution must undergo some form of ordering into a more continuous structure. Whilst the concentration of surfactant is to low for the spontaneous formation of an ordered liquid crystal mesophases to occur at low temperature, it can be seen (figure 6.29, red arrow) that as the temperature increases the cloud point of the surfactant will be reached. At this point, even at a concentration of 10 wt%, two phases form, one containing mainly liquid crystals and the other water with some micelles.

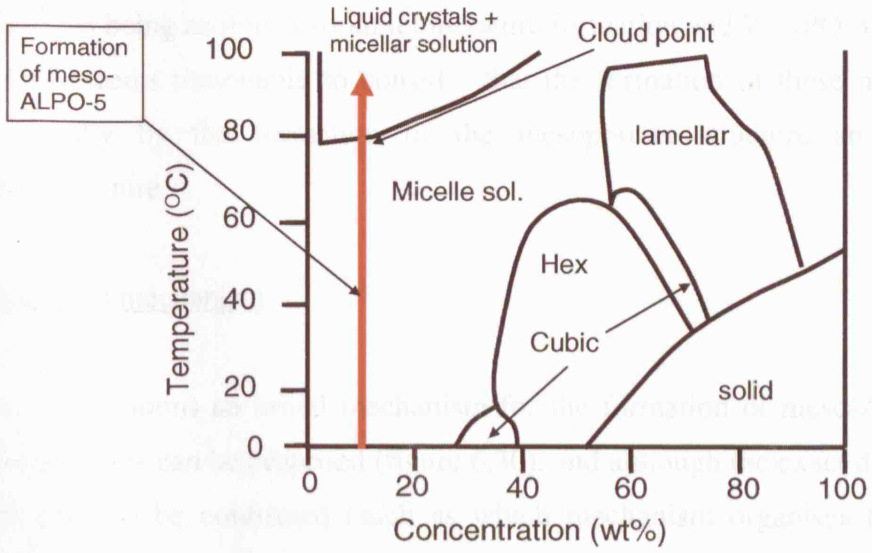

Figure 6.29: The phase diagram for $C_{16}PEO_8$ (very similar to Brij-56). The red arrow represents the formation of meso-AlPO-5 as the gel heats up. Diagram reproduced from refs. 65 and 68.

It is possible that it is this organisation of the micelles above the cloud point that result in the regular mesophase seen in other systems and suggests that, certainly in non-ionic systems, at elevated temperatures the formation of liquid crystals can occur in a similar manner to that proposed by Beck *et al*[73] (figure 6.10 mechanism 1). However, it is also reasonable that AlPO framework materials become H-bonded to the discrete micelles surface as they form[18] and that these may help to at least partially direct the structure in a manner more similar to mechanism 2 proposed by Beck *et al*[73] and Chen *et al*[74]. Clearly more experiments are required to identify which mechanism is dominant, although a combination of both may be ultimately responsible for the final structure (see mechanism below).

6.4.3.2 : Order of formation

During the formation of these materials there are two processes occurring, the formation of the micropores and the formation of mesopores. Potentially either could happen first during the formation mechanism. However, in the case of the non-ionic surfactants, micelle formation is not subject to a Kraft point and so micelle solutions can form at low temperatures. Therefore, micelles are present at the very early stages of the gel formation. Generally, most microporous materials require elevated temperatures to form (exceptions being zeolite-A room temperature formation and ZnAPO-34 formation at 40°C), so it seems reasonable to consider that the formation of these meso-AlPOs proceeds initially by the formation of the mesoporous structure and then the microporous structure.

6.4.3.3 : Proposed mechanism

From these observations an initial mechanism for the formation of meso-AlPOs from non-ionic surfactants can be proposed (figure 6.30), and although the exact details of the mechanism need to be confirmed (such as which mechanism organises the discrete micelles into organised units); it does offer some insight into the formation hierarchical materials.

In this mechanism, the 10 wt % solution of non-ionic surfactant results in the formation of micelles at low temperature in the gel, although their exact shape is currently unknown (for convenience they are represented as spheres in the figure). As the temperature increases some organisation of the micelles occurs (Beck's mechanism 2)[73] with AlPO framework materials building up on the micelle surface *via* hydrogen bonding[18] and growing in a manner similar to that described in chapter 3. At this stage the temperature is also high enough for microporous formation to begin. A further increase in the temperature results in the gel reaching the surfactant cloud point, and a more significant ordering of the micelles occurs forming a liquid crystal region (and a region containing some micelles in water), similar to Beck's mechanism 1[73]. Around these liquid crystalline regions microporous growth continues, becoming more rapid as the temperature reaches the hydrothermal levels generally associated with microporous AlPO formation. This results in the final material, which consists of an extended structure of microporous AlPO framework between the mesoporous liquid crystals.

Upon calcination the organics are then removed resulting in the open structure identified by BET, and containing micropores of ~ 1 nm and mesopores of ~10 nm.

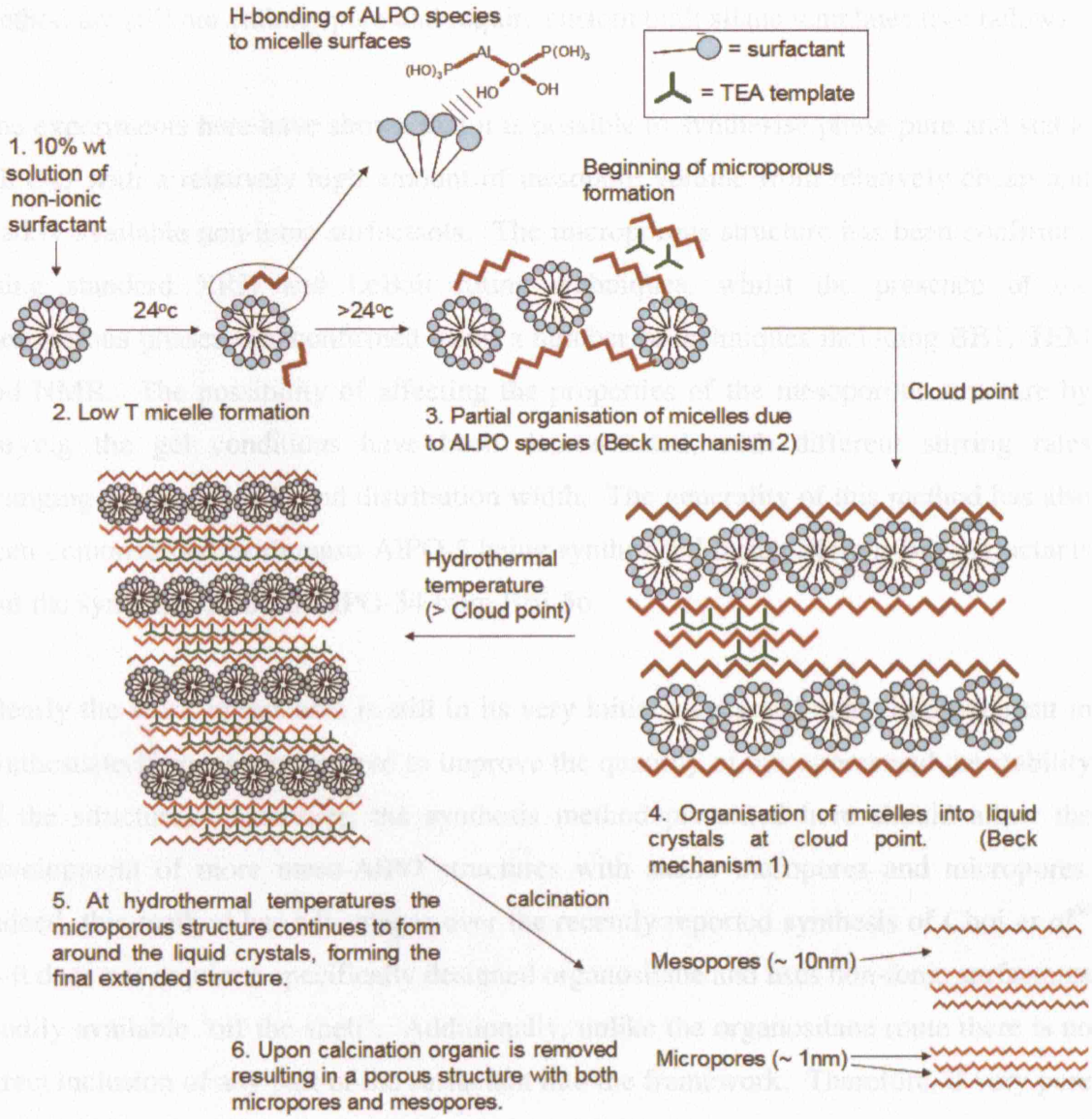

Figure 6.30: The proposed mechanism for the formation of microporous materials with a mesoporous structure such as meso-AlPO-5.

6.5 : Summary and conclusions

The intention of these experiments was to introduce a mesoporous hierarchical structure into a microporous AlPO framework. Until very recently (i.e. during the writing of this thesis) such materials had not been synthesised and those produced by Choi *et al's*[64] method are still not entirely pure and require custom built silane templates (see below).

The experiments here have shown that it is possible to synthesise phase pure and stable AlPO-5 with a relatively high amount of mesopore volume from relatively cheap and readily available non-ionic surfactants. The microporous structure has been confirmed using standard XRD and LeBail fitting techniques, whilst the presence of the mesoporous phases was confirmed using a number of techniques including BET, TEM and NMR. The possibility of affecting the properties of the mesoporous structure by varying the gel conditions have been demonstrated, with different stirring rates changing the modal PSD and distribution width. The generality of this method has also been demonstrated, with meso-AlPO-5 being synthesised from different Brij surfactants and the synthesis of meso-AlPO-34 from Brij-56.

Clearly the work in this area is still in its very initial stages and some improvement in synthesis techniques are required to improve the quantity of mesopores and the stability of the structures. However, the synthesis method presented here should allow the development of more meso-AlPO structures with stable mesopores and micropores. Indeed, this method has advantages over the recently reported synthesis of Choi *et al*[64] as it does not require a specifically designed organosilane and uses non-ionic surfactants readily available 'off the shelf'. Additionally, unlike the organosilane route there is no direct inclusion of any part of the surfactant into the framework. Therefore, if very pure materials are required (i.e. no silicon framework exchange), the method detailed here would be preferable.

From the experiments performed so far an initial mechanism for the formation of meso-AlPOs from non-ionic surfactants has also been proposed.

6.6 : Future work

As mentioned above this work is still in its very early stages. As such there are a large number of routes that future work could take.

One of the most important issues currently would be to attempt to increase the overall mesoporous volume of these materials. To this end, a series of temperature ramping experiments are planned in which is hoped it will be possible to order significantly more micelles before the onset of microporous crystallisation. Other synthesis variables such as exact gel composition, pH, metal sources and synthesis temperature and time may also be varied to increase the pore volume or change the exact PSD. These variations may also result in structures more stable towards calcination (particularly in the case of MeAPO-34).

With the materials already produced it would be desirable to try to improve the stability of the mesopores within the TEM electron beam in order to image the pores more thoroughly. This may possibly be achieved by packing the pores with a high atomic weight material to provide stability and good contrast with the AlPO framework. It would also be desirable to perform catalytic testing on the meso-AlPO-5 materials because as Choi *et al* have noted for meso-ZSM-5 'despite the significantly lower specific BET area, the mesoporous zeolite exhibited much higher catalytic activity than Al-MCM-41'[62].

Finally, the development of new materials can be progressed using the large number of other Brij and alternative non-ionic surfactant readily available from the chemical industry, and of course there are a huge number of potential micropores AlPO structures within which a mesoporous hierarchy may be developed.

6.7 : References

(1) Baerlocher, C.; McCusker, L. B.; Database of Zeolite Structures: http://www.iza-structure.org/databases/: 2005.

(2) Bennett, J. M.; Cohen, J. P.; Flanigen, E. M.; Pluth, J. J.; Smith, J. V. *Acs Symposium Series* **1983**, *218*, 109.

(3) Richardson, J. W.; Pluth, J. J.; Smith, J. V. *Acta Crystallogr. Sect. C-Cryst. Struct. Commun.* **1987**, *43*, 1469.

(4) Qiu, S. L.; Pang, W. Q.; Kessler, H.; Guth, J. L. *Zeolites* **1989**, *9*, 440.

(5) Oliver, S.; Kuperman, A.; Ozin, G. A. *Angew. Chem.-Int. Edit.* **1998**, *37*, 47.

(6) van Donk, S.; Janssen, A. H.; Bitter, J. H.; de Jong, K. P. *Catalysis Reviews-Science and Engineering* **2003**, *45*, 297.

(7) Bellussi, G.; Pazzuconi, G.; Perego, C.; Girotti, G.; Terzoni, G. *J. Catal.* **1995**, *157*, 227.

(8) Voogd, P.; Vanbekkum, H. *Applied Catalysis* **1990**, *59*, 311.

(9) Rajagopalan, K.; Peters, A. W.; Edwards, G. C. *Applied Catalysis* **1986**, *23*, 69.

(10) Haag, W. O.; Lago, R. M.; Weisz, P. B. *Faraday Discuss.* **1981**, 317.

(11) Freyhardt, C. C.; Tsapatsis, M.; Lobo, R. F.; Balkus, K. J.; Davis, M. E. *Nature* **1996**, *381*, 295.

(12) Yoshikawa, M.; Wagner, P.; Lovallo, M.; Tsuji, K.; Takewaki, T.; Chen, C. Y.; Beck, L. W.; Jones, C.; Tsapatsis, M.; Zones, S. I.; Davis, M. E. *J. Phys. Chem. B* **1998**, *102*, 7139.

(13) Davis, M. E.; Saldarriaga, C.; Montes, C.; Garces, J.; Crowder, C. *Nature* **1988**, *331*, 698.

(14) Ferey, G. *J. Fluor. Chem.* **1995**, *72*, 187.

(15) Ferey, G. *Chem. Mat.* **2001**, *13*, 3084.

(16) Loiseau, T.; Ferey, G. *J. Solid State Chem.* **1994**, *111*, 403.

(17) Kresge, C. T.; Leonowicz, M. E.; Roth, W. J.; Vartuli, J. C.; Beck, J. S. *Nature* **1992**, *359*, 710.

(18) Tanev, P. T.; Pinnavaia, T. J. *Science* **1995**, *267*, 865.

(19) Zhao, D. Y.; Feng, J. L.; Huo, Q. S.; Melosh, N.; Fredrickson, G. H.; Chmelka, B. F.; Stucky, G. D. *Science* **1998**, *279*, 548.

(20) Kim, S. S.; Zhang, W. Z.; Pinnavaia, T. J. *Science* **1998**, *282*, 1302.

(21) Che, S.; Garcia-Bennett, A. E.; Yokoi, T.; Sakamoto, K.; Kunieda, H.; Terasaki, O.; Tatsumi, T. *Nature Materials* **2003**, *2*, 801.

(22) Mokaya, R. *Angew. Chem.-Int. Edit.* **1999**, *38*, 2930.

(23) Corma, A.; Grande, M. S.; Gonzalez-Alfaro, V.; Orchilles, A. V. *J. Catal.* **1996**, *159*, 375.

(24) Xiao, F. S. *Top. Catal.* **2005**, *35*, 9.

(25) Liu, Y.; Zhang, W. Z.; Pinnavaia, T. J. *J. Am. Chem. Soc.* **2000**, *122*, 8791.

(26) Liu, Y.; Zhang, W. Z.; Pinnavaia, T. J. *Angew. Chem.-Int. Edit.* **2001**, *40*, 1255.

(27) Schuth, F. *Chem. Mat.* **2001**, *13*, 3184.

(28) Sayari, A.; Karra, V. R.; Reddy, J. S.; Moudrakovski, I. L. *Chem. Commun.* **1996**, 411.

(29) Feng, P. Y.; Xia, Y.; Feng, J. L.; Bu, X. H.; Stucky, G. D. *Chem. Commun.* **1997**, 949.

(30) Kraushaarczarnetzki, B.; Stork, W. H. J.; Dogterom, R. J. *Inorg. Chem.* **1993**, *32*, 5029.

(31) Fyfe, C. A.; Schwieger, W.; Fu, G.; Kokotailo, G. T.; Grondey, H. In *Symposium on Zeolites, Layered Compounds and Other Microporous Solids, 209th Natiional Meeting, Am. Chem. Soc.* Anaheim, California, 1995, p 266.

(32) Kimura, T.; Sugahara, Y.; Kuroda, K. *Chem. Commun.* **1998**, 559.

(33) Kimura, T.; Sugahara, Y.; Kuroda, K. *Chem. Lett.* **1997**, 983.

(34) Kimura, T.; Sugahara, Y.; Kuroda, K. In *11th International Zeolite Conference* Seoul, Korea, 1996, p RP45.

(35) Kimura, T.; Sugahara, Y.; Kuroda, K. *Chem. Mat.* **1999**, *11*, 508.

(36) Kimura, T.; Sugahara, Y.; Kuroda, K. *Microporous Mesoporous Mat.* **1998**, *22*, 115.

(37) Khimyak, Y. Z.; Klinowski, J. *Phys. Chem. Chem. Phys.* **2000**, *2*, 5275.

(38) Zhao, D. Y.; Luan, Z. H.; Kevan, L. *Chem. Commun.* **1997**, 1009.

(39) Zhao, X. S.; Lu, G. Q.; Whittaker, A. K.; Drennan, J.; Xu, H. *Microporous Mesoporous Mat.* **2002**, *55*, 51.

(40) Luan, Z. H.; Zhao, D. Y.; He, H. Y.; Klinowski, J.; Kevan, L. *J. Phys. Chem. B* **1998**, *102*, 1250.

(41) Chakraborty, B.; Pulikottil, A. C.; Das, S.; Viswanathan, B. *Chem. Commun.* **1997**, 911.

(42) Khimyak, Y. Z.; Klinowski, J. *J. Mater. Chem.* **2002**, *12*, 1079.

(43) Subrahmanyam, C.; Viswanathan, B.; Varadarajan, T. K. *J. Mol. Catal. A-Chem.* **2004**, *223*, 149.

(44) Lu, J. M.; Ranjit, K. T.; Rungrojchaipan, P.; Kevan, L. *J. Phys. Chem. B* **2005**, *109*, 9284.

(45) Kapoor, M. P.; Raj, A. *Appl. Catal. A-Gen.* **2000**, *203*, 311.

(46) Kron, D. A.; Holland, B. T.; Wipson, R.; Maleke, C.; Stein, A. *Langmuir* **1999**, *15*, 8300.

(47) Mohapatra, S. K.; Sahoo, B.; Keune, W.; Selvam, P. *Chem. Commun.* **2002**, 1466.

(48) Kimura, T. *Chem. Lett.* **2002**, 770.

(49) Mann, R. *Catal. Today* **1993**, *18*, 509.

(50) Carlsson, A.; Madsen, C.; Schmidt, I.; Houzvicka, J.; Jacobsen, C. J. H. European Patent, 1106575, 2001.

(51) Jacobsen, C. J. H.; Madsen, C.; Houzvicka, J.; Schmidt, I.; Carlsson, A. *Journal of the American Chemical Society* **2000**, *122*, 7116.

(52) Schmidt, I.; Boisen, A.; Gustavsson, E.; Stahl, K.; Pehrson, S.; Dahl, S.; Carlsson, A.; Jacobsen, C. J. H. *Chem. Mat.* **2001**, *13*, 4416.

(53) Holland, B. T.; Abrams, L.; Stein, A. *Journal of the American Chemical Society* **1999**, *121*, 4308.

(54) Naydenov, V.; Tosheva, L.; Sterte, J. *Microporous Mesoporous Mat.* **2003**, *66*, 321.

(55) Naydenov, V.; Tosheva, L.; Antzutkin, O. N.; Sterte, J. *Microporous Mesoporous Mat.* **2005**, *78*, 181.

(56) Zhang, B. J.; Davis, S. A.; Mann, S. *Chem. Mat.* **2002**, *14*, 1369.

(57) Dong, A. G.; Wang, Y. J.; Tang, Y.; Ren, N.; Zhang, Y. H.; Yue, J. H.; Gao, Z. *Adv. Mater.* **2002**, *14*, 926.

(58) Beck, J. S.; Vartuli, J. C.; Kennedy, G. J.; Kresge, C. T.; Roth, W. J.; Schramm, S. E. *Chem. Mat.* **1994**, *6*, 1816.

(59) Petkov, N.; Holzl, M.; Metzger, T. H.; Mintova, S.; Bein, T. *J. Phys. Chem. B* **2005**, *109*, 4485.

(60) Karlsson, A.; Stocker, M.; Schmidt, R. *Microporous Mesoporous Mat.* **1999**, *27*, 181.

(61) Xiao, F. S.; Wang, L. F.; Yin, C. Y.; Lin, K. F.; Di, Y.; Li, J. X.; Xu, R. R.; Su, D. S.; Schlogl, R.; Yokoi, T.; Tatsumi, T. *Angew. Chem.-Int. Edit.* **2006**, *45*, 3090.

(62) Choi, S. H.; Wood, B. R.; Ryder, J. A.; Bell, A. T. *J. Phys. Chem. B* **2003**, *107*, 1843.

(63) Chmelka, B. F. *Nature Materials* **2006**, *5*, 681

(64) Choi, M.; Srivastava, R.; Ryoo, R. *Chem. Commun.* **2006**, DOI: 10.1039/b612265e.

(65) Tadros, T. F. *Applied Surfactants: Principles and Applications*; First ed.; Wiley-VCH, 2005.

(66) Hummel, D. O. *Handbook of Surfactant Analysis*; Wiley, 2000.

(67) McBain, M. J. *Transactions of the Faraday society* **1913**, *9*, 99.

(68) Porter, M. R. *Handbook of Surfactants*; second ed.; Blackie Academic and Professional, 1994.

(69) Balzer, D. *Tenside, Surfactants, Detergents* **1991**, *28*, 419

(70) Lin, Z.; Scriven, L. E.; Davis, H. T. *Langmuir* **1992**, *8*, 2200.

(71) Matsen, M. W.; Bates, F. S. *Macromolecules* **1996**, *29*, 7641.

(72) Matsen, M. W.; Bates, F. S. *Macromolecules* **1996**, *29*, 1091.

(73) Beck, J. S.; Vartuli, J. C.; Roth, W. J.; Leonowicz, M. E.; Kresge, C. T.; Schmitt, K. D.; Chu, C. T. W.; Olson, D. H.; Sheppard, E. W.; McCullen, S. B.; Higgins, J. B.; Schlenker, J. L. *Journal of the American Chemical Society* **1992**, *114*, 10834.

(74) Chen, C. Y.; Burkett, S. L.; Li, H. X.; Davis, M. E. *Microporous Materials* **1993**, *2*, 27

(75) Glinka, C. J.; Nicol, J. M.; Stucky, G. D.; Ramli, E.; Margolese, D. I.; Huo, Q. S. In *Advances in Prorous Materials; Mater Res. Proc.*; Kormarneni, S., Smith, D. M., Beck, J. S., Eds. Pittsburgh, PA, 1995; Vol. 371, p 47.

(76) Calabro, D. C.; Valyocsik, E. W.; Ryan, F. X. *Microporous Materials* **1996**, *7*, 243.

(77) Attard, G. S.; Glyde, J. C.; Goltner, C. G. *Nature* **1995**, *378*, 366.

(78) Firouzi, A.; Kumar, D.; Bull, L. M.; Besier, T.; Sieger, P.; Huo, Q.; Walker, S. A.; Zasadzinski, J. A.; Glinka, C.; Nicol, J.; Margolese, D.; Stucky, G. D.; Chmelka, B. F. *Science* **1995**, *267*, 1138.

(79) Huo, Q. S.; Margolese, D. I.; Ciesla, U.; Feng, P. Y.; Gier, T. E.; Sieger, P.; Leon, R.; Petroff, P. M.; Schuth, F.; Stucky, G. D. *Nature* **1994**, *368*, 317.

(80) Zhao, D. Y.; Huo, Q. S.; Feng, J. L.; Chmelka, B. F.; Stucky, G. D. *J. Am. Chem. Soc.* **1998**, *120*, 6024.

(81) Sing, K. S. W.; Everett, D. H.; Haul, R. A. W.; Moscou, L.; Pierotti, R. A.; Rouquerol, J.; Siemieniewska, T. *Pure Appl. Chem.* **1985**, *57*, 603.

(82) Groen, J. C.; Peffer, L. A. A.; Perez-Ramirez, J. *Microporous Mesoporous Mat.* **2003**, *60*, 1.

(83) Kustanovich, I.; Goldfarb, D. *J. Phys. Chem.* **1991**, *95*, 8818.

(84) Fyfe, C. A.; Altenschildesche, H. M. Z.; Wong-Moon, K. C.; Grondey, H.; Chezeau, J. M. *Solid State Nucl. Magn. Reson.* **1997**, *9*, 97.

(85) Fyfe, C. A.; WongMoon, K. C.; Huang, Y. *Zeolites* **1996**, *16*, 50.

(86) Meinhold, R. H.; Tapp, N. J. *J. Chem. Soc.-Chem. Commun.* **1990**, 219.

(87) Szostak, R. *Molecular Sieves*; second ed.; Blackie Academic, 1998.

(88) Wilson, S. T.; Lok, B. M.; Messina, C. A.; Cannan, T. R.; Flanigen, E. M. In *Intrazeolite Chemistry*; Stucky, G. D., Ed.; American Chemical Society: Washington, 1983; Vol. 218, p 79.

(89) Corma, A. *Chemical Reviews* **1997**, *97*, 2373.

(90) Ulagappan, N.; Rao, C. N. R. *Chemical Communications* **1996**, 2759.

Chapter 7

Final Conclusions

During the course of this work the formation of a number of microporous materials and a hierarchical microporous and mesoporous material have been investigated.

The aim of the work on microporous materials was to use a combination of *in situ*, *ex situ* and experimental techniques to probe different parts of the formation processes of both zeolites and aluminophosphates. It is important to note that from the vast array of previous studies, a huge variety of mechanisms have been proposed for microporous materials. It seems likely that there is not one unifying mechanism for the formation of microporous materials and that variables ranging from different frameworks constitutions (e.g. aluminosilicate or aluminophosphate) to gel constituents (AlPO-34 gels with and without hydrofluoric acid) can alter the formation mechanism. Whilst this complicated situation may make the ultimate goal of rational design difficult or even unachievable, understanding each part of individual formation mechanisms is still essential, as it will allow us to more accurately control and improve current frameworks for industrial usage, as well as help lead towards new and catalytically interesting materials.

In chapter 3 the role of metal substitution and organic SDA conformation was examined in the formation of MeAPO-34 and AlPO-5 from similar gels. The need for a substituted metal to form MeAPO-34 (rather than AlPO-5) has been previously noted and in this work DFT calculations have shown that, unlike silicates, the early part of AlPO formation appears to be dominated by chains. In particular the addition of metal actually promotes the formation of chains rather than discreet SBU like units. Raman spectroscopy was then used to probe the interaction of the organic SDA with the gel and it was found that the substituted metal has a 'true templating' effect resulting in an interaction with the SDA and a change in SDA conformation. The formation of AlPO-5 primarily form a single organic conformation then indicates that the organic's role is somewhat more than space filling. However, as both MeAPO-34 and AlPO-5 can be formed from other SDAs, it is difficult to class its role as structure directing given the current criteria suggested by Davis and Lobo. Clearly these unique metal-organic interactions and changes in organic conformation can play a significant role in the gel

chemistry of porous materials and a greater understanding of how these affect the formation mechanisms of different systems is needed if greater reaction control is to be achieved.

In chapter 4 EDXRD was used to demonstrate the effect of different SDAs on the formation kinetics of a single AlPO framework (MeAPO-36). Crystallographic studies have then shown that the unit cell of the final material can also be subtly altered by these different SDAs, with the more bulky ECHA resulting in an expanded unit cell with a higher symmetry. Molecular size measurements where then used to confirm the larger volume of ECHA and these also indicated that TPA is very planar. Docking calculations have then shown that the planar nature of this molecule may result in highly ordered packing within the AlPO framework, resulting in the slower rate of formation of the TPA synthesised material. Both the expansion of the unit cell caused by synthesis with ECHA and the ordered packing of TPA appear to be a result of the need of these SDA molecules to try and charge balance the cobalt substituted framework. These effects are important as lower energy routes to microporous materials are desirable if commercial scale production is to be made as economically viable as possible.

Chapter 5 focused on the formation of the zeolitic material zeolite-A. Once again the effect of metal substitution was investigated, this time using a versatile SAXS/WAXS *in situ* setup. Initially an un-substituted system was investigated and a homogenous nucleation mechanism proposed that proceeds by agglomeration and solution species transport. A lack of intergrowth of the final crystalline product (as observed by SEM) indicates that dissolution and solution species transport is the primary mode of crystal growth. However, the insertion of germanium into the gel causes a more rapid crystallisation and results in larger amorphous aggregates. It seems therefore that germanium acts as a nucleation point and a stabiliser for the forming aggregates. This stabilisation effect then adjusts the formation mechanism, resulting in a greater preference for agglomeration of crystallites and therefore more crystal intergrowth in the final product. A greater understanding of how the gel composition can alter the processes within a general synthesis mechanism will therefore allow greater control over the final morphology of this and similar materials.

The final chapter of this work has focused on the formation of microporous AlPO-5 containing mesoporous apertures. Using simple and cheap 'off the shelf' charge neutral surfactants both AlPO-5 and MeAPO-34 have been successfully synthesised, with a reasonable degree of mesoporistiy (confirmed by a variety of techniques). Although still in its initial stages, this synthesis project may have important implications for the chemical industry as such materials, once fully optimised, should allow the reactivity of microporous frameworks to be combined with the high throughput of mesoporous frameworks. Additionally, this process has its advantages over other recent techniques in that it requires only readily available surfactants for mesoporous production and does not leave any 'residual' substitution within the final framework.

Appendix 1: DMOL cluster energies

Notes:

AlPO = no Zn in cluster

ZnAlPO = 1 Zn in cluster

2xZnAlPO = 2 Zn in cluster

3xZnAlPO = 3 Zn in cluster

When zinc is present it can be located in a number of different sites and when more than one zinc configuration has been tested each cluster in distinguished by the notation type I, II or III. In the branched systems either P or Al/Zn can be located at the branch point. These clusters have been tested in both configurations

Cluster type	Minimised energy (Hartrees)
Water	-76.4519271
Monomers	
zinc	-2082.924752
aluminium	-546.1415048
phosphorus	-644.626322
Dimers	
P-Al	-1114.54909
Zn-P	-2651.58763
Tetramers	
AlPO	-2152.68266
ZnAlPO type I	-3689.74302
ZnAlPO type II	-3689.74163
2xZnAlPO	-5226.66469
Hexamers	
AlPO	-3190.809217
ZnAlPO type I	-4727.896468
ZnAlPO type II	-4727.884851
ZnAlPO type III	-4727.874629
2xZnAlPO type I	-6264.833284
2xZnAlPO type II	-6264.829927
3xZnAlPO	-7801.671101
4-membered rings	
AlPO	-2076.22225
ZnAlPO	-3613.27649
2xZnAlPO	-5150.20675

Cluster type (cont.)	
6-membered rings	
AlPO	-3114.375167
ZnAlPO	-4651.437994
2xZnAlPO	-6188.390897
3xZnAlPO	-7725.22033
Branched 4-rings	
(with P at branch point)	
AlPO	-3114.349472
ZnAlPO type I	-4651.421878
ZnAlPO type II	-4651.408202
ZnAlPO type III	-4651.415827
(With Al/Zn at branch point)	
AlPO	-3114.352855
ZnAlPO type I	-4651.41155
ZnAlPO type II	-4651.403016
2xZnAlPO type I	-6188.384256
2xZnAlPO type II	-6188.380628
2xZnAlPO type III	-6188.378024
3xZnAlPO	-7725.210526
Fused 4-rings	
AlPO	-3037.893789
ZnAlPO type I	-4574.963993
ZnAlPO type II	-4574.945094
2xZnAlPO type I	-6111.904595
2xZnAlPO type II	-6111.905725
3xZnAlPO	-7648.734621

Appendix 2: Minimum energies SDA packing calculations

Note that all energies are in Kcal mol^{-1}

Individual template energies:	
TPA	-68.5653
DPBA	-33.0730
ECHA	-99.9062

Monte Carlo method

	No. of SDAs	Run 1	Run 2	Run 3	Run 4	Run 5	Average
TPA packing	1	-74.4729	-74.4711	-74.4729	-74.4721	-74.4727	-74.4723
	2	-114.102	-114.178	-113.88	-104.771	-113.699	-112.126
	3	-136.627	-138.109	-120.868	-136.202	-132.684	-132.898
DPBA packing	1	-67.893	-69.4126	-69.4126	-67.893	-69.3997	-68.8022
	2	-105.312	-99.5759	-98.5919	-105.023	-99.6812	-101.637
	3	-82.0751	-99.2083	-123.082	-127.715	-128.529	-112.122
ECHA packing	1	-92.599	-92.5991	-92.599	-92.5991	-93.0165	-92.6825
	2	-146.627	-143.967	-118.923	-148.589	-151.597	-141.941

Orientation method

		Orientation (as described in chapter 3)				
	No. of SDAs	YX	ZX	YX(45)ZX	YZ	YZ(45)ZX
TPA packing	1	-65.4146	-74.83	-65.4146	-78.041	-76.3776
	2	-103.412	-119.343	-105.573	-114.678	-114.678
	3	-122.75	-91.7531	-124.387	-131.051	-131.047
	4	-149.715	-88.0964	-142.951	15.3704	20.31568
DPBA packing	1	-66.5136	-66.1623	-66.5136	-56.8379	-56.8379
	2	-96.5715	-104.77	-95.6727	-89.5993	-67.3055
	3	-103.582	-131.866	-119.945	-119.953	-118.118
	4	-83.1228	-6.76482	-95.2775	-28.0779	-34.0569
ECHA packing	1	-47.9832	-89.1615	-47.9832	-57.4569	-82.2694
	2	-80.4059	-140.268	-58.3471	-134.177	-141.701
	3	-70.9204	16.31232	-17.1435	47.48874	29.98751
	4	62.85476	162.4302	60.76759	412.1975	133.7902
ECHA packing (expanded unit cell)	1	-68.9127	-86.7906	-51.1721	-35.6073	-82.2457
	2	-105.635	-138.054	-65.1568	-124.561	-114.49
	3	-72.014	14.74624	-26.6374	2.614101	-40.1122
	4	14.9489	152.1448	73.68281	56.32174	25.90885